MICROMECHANICS-BASED DESIGN OF FRC MATERIALS

from Microstructural Features to Structural Behavior

by

Yiping Geng

B.Eng. Tsinghua University, Beijing (July, 1985)
S.M.C.E. Massachusetts Institute of Technology (June, 1992)

Submitted to the
Department of Civil and Environmental Engineering in
Partial Fulfillment of the Requirements for the Degree of

DOCTOR OF SCIENCE
IN CIVIL AND ENVIRONMENTAL ENGINEERING

at the

Massachusetts Institute of Technology
October 1995

Signature of Author_____
Department of Civil and Environmental Engineering
October 1995

Certified by_____
Professor Christopher K.Y. Leung
Thesis Supervisor

Accepted by_____
Professor Joseph M. Sussman
Chairman, Departmental Committee on Graduate Studies

MICROMECHANICS-BASED DESIGN OF FRC MATERIALS
from Microstructural Features to Structural Behavior

by

Yiping Geng

Submitted to the Department of Civil and Environmental Engineering on October 5, 1995
in Partial Fulfillment of the Requirements for the Degree of
Doctor of Science in Civil and Environmental Engineering

Abstract

The thesis developed a micromechanics-based design and analysis methodology for discontinuous fiber reinforced brittle matrix composites. Unlike the traditional 'trial and error' approach, the new procedure aims at predicting the behavior of fiber reinforced composites and structures from microstructural features and micro-parameters, which enables engineers to design the material as well as the structural systems to satisfy a given performance requirement. By choosing the optimal combination of micro-parameters, composites with high performance/cost can be achieved.

Discontinuous fiber reinforced cementitious materials (FRC) is studied using the micromechanics-based design procedure. The research contains three part: microstructural study of the fiber/matrix interface, micromechanical modeling of microscopic deformation and failure mechanisms, and simulation of structural behavior using the micromechanics-based stress-displacement relation along the crack.

(a) The microstructural studies attempt to connect the change in interfacial properties of FRC during fiber pullout to the microstructural features of the interface using SEM and EDX. For the steel fiber/mortar interface, the rapid post-peak drop of the pullout force after total debonding is found to be due to abrasion of the calcium hydroxide crystal layer and a reduction of asperity on the mortar surface. For the nylon and polypropylene fiber/mortar interfaces, the flat post-peak behavior is caused by peeling of the fiber surface with very little damage on the mortar surface.

(b) Micromechanical models of steel FRC are established based on the observations of microstructural features. Two typical fiber pullout cases during crack opening are studied, straight fiber pullout under lateral compression and inclined fiber pullout with plastic deformation. Experimental study of straight fiber debonding and pullout under constant lateral stress verifies the debonding theory and provides the relation between lateral stress and interfacial parameters. A damage model is developed to count for the effect of variable lateral stress during fiber pullout, which agrees well with experimental results. Material variability is considered in the damage model for practical applications. Inclined fiber pullout under mixed mode crack opening is modeled. By employing the effect of lateral stress and constant spalling depth, the micromechanical model agrees well with experimental data under various loading histories and fiber inclination angles.

(c) Stress-displacement relations along Mode I crack are established based on the micromechanical models. A beam under four-point bending is studied using ADINA with strain-softening spring element along the mode I crack to simulate the post-peak behavior. The numerical solution agrees very well with the experimental data.

Thesis Supervisor: Dr. Christopher K.Y. Leung
Title: Assistant Professor of Civil and Environmental Engineering

ACKNOWLEDGMENTS

I would like to express the deepest appreciation to Professor Christopher K.Y. Leung, my thesis supervisor, for his guidance throughout this work. Without his support and advice, it would be impossible to have such a productive research program with several publications.

Also, I would like to thank my thesis committee members, Professors Ali S. Argon and Klaus-Jürgen Bathe at the Department of Mechanical Engineering and Professors Oral Buyukozturk and Jerome J. Connor at the Department of Civil and Environmental Engineering, for their illuminating guidance and caring mentorship, which nurtured not only my thesis, but also my whole career.

And thanks to Professor Deniele Veneziano, my academic advisor and Master's thesis supervisor, for his continuing support and encouragement during the past four years; to Dr. John T. Germaine, who help me generously on the experimental techniques; To Dr. Yiping Qiu and Professor Stanley Backer at the Department of Mechanical Engineering for their assistance on fiber testing, to Mr. Arthur P. Rudolph, Jr. and Mr. Steven W. Rudolph for their work on my experimental setups; and to all of my friends in the materials and structures group, Alex, Anthony, Benoit, Caterina, Darmadi (Lee), Doug, Hayat, Hong, Jinkoo, Jose, Josko, Leon, Miguel, Nathan, Oguz, Pat, Paul and Thanakorn (Pete) for the memorable time we had.

To Chunqing

CONTENTS

LIST OF FIGURES

LIST OF TABLES

PREFACE

Brittle materials, such as concrete and ceramics, have played an important role in modern industry because of their unique properties. For example, ceramic components are used in space shuttles to withstand extremely high and low temperatures; inexpensive concrete is used in buildings to hold tremendous compressive loads. Nevertheless, these brittle materials can fail easily and catastrophically. In order to overcome this shortcoming, fiber is added to control crack and improve post-cracking behavior.

The design of fiber reinforced composites involves two steps: selecting proper fiber and matrix; and determining the proportion and manufacturing techniques. Material engineers always face a dilemma when they choose the proportion. For example, when designing the windshield of an automobile, the engineer has to make sure that the proportion of fiber is not so low that the glass can easily fall apart during collision, nor so high that it creates manufacturing difficulties and increases costs.

The traditional design procedure for composites involves testing a series of specimens each of which corresponds to a different fiber/matrix proportion. The specimen that satisfies the performance/cost requirement best is used to determine the ideal proportion. This design procedure is very expensive in practice.

In this thesis, a new process, termed as the Micromechanics-Based Design and Analysis of fiber reinforced composites, is being developed. The new design procedure starts from microstructural study of fiber, matrix and interface, to micromechanical modeling of the microscopic deformation and failure mechanism. Ultimately, the composite structural behavior can be predicted by the micromechanics-based constitutive relation established along the crack.

With the micromechanical model, Engineers can design the material as well as the structural system to satisfy a given performance requirement. This provides more flexibility to the development of an optimal design with the highest performance/cost. In the future, engineers will be able to design a fiber reinforced composite by selecting proper fiber, matrix, proportion, and manufacturing process using a CAD/CAM program without entering a material testing laboratory.

Chapter 1. Introduction

1.1 FIBER REINFORCED CEMENTITIOUS MATERIALS

The application of fiber reinforced construction materials by our ancestors dated back to more than 3000 years ago. Exodus [1.1] may be the first document which recorded the usage of straw to increase the strength of bricks. Since the industrial revolution, asbestos cement became the first widely used composite with the invention of Hatschek (wet) and Magnani (semi-wet) processes in the end of the nineteenth century [1.2]. The application of asbestos fibers has been decreasing due to the health hazard and dwindling resource.

In the past several decades, technologies of composite materials have been advancing rapidly with the growth of a variety of engineering fields, especially the aerospace industry. A variety of fibers (steel, glass, polymer and carbon fibers), matrices (epoxies, thermosets, plastics and ceramics) and manufacturing methods (filament winding, pultrusion, molding and laminates) have been developed. Nowadays, with the continuing reduction of fiber cost, the demand of using recyclable materials [1.3] and the development of mixing technologies, fiber reinforced cementitious materials are becoming feasible to replace the plain concrete in civil engineering applications, especially in infrastructure construction and rehabilitation.

Fiber reinforced cementitious materials include fiber reinforced cement, fiber reinforced cement mortar, fiber reinforced concrete, and all other fiber reinforced hydraulic cement binders, as shown in Fig. 1.1. In the literature, either one or all of these composites can be abbreviated as FRC. The fibers used for reinforcement include metallic, synthetic, mineral and natural fibers, as shown in Fig. 1.1.

Although cementitious materials are economical, durable and have high compressive strength, they are very brittle and have low tensile strength and ductility. Unlike the high performance composite materials, such as metal matrix composites (MMC) and ceramic matrix composites (CMC), (which are designed to possess high strength and high ductility, and therefore, require high fiber volume fraction and continuous fiber), FRC materials are

generally not designed to increase material strength, even though tensile strength increases moderately.

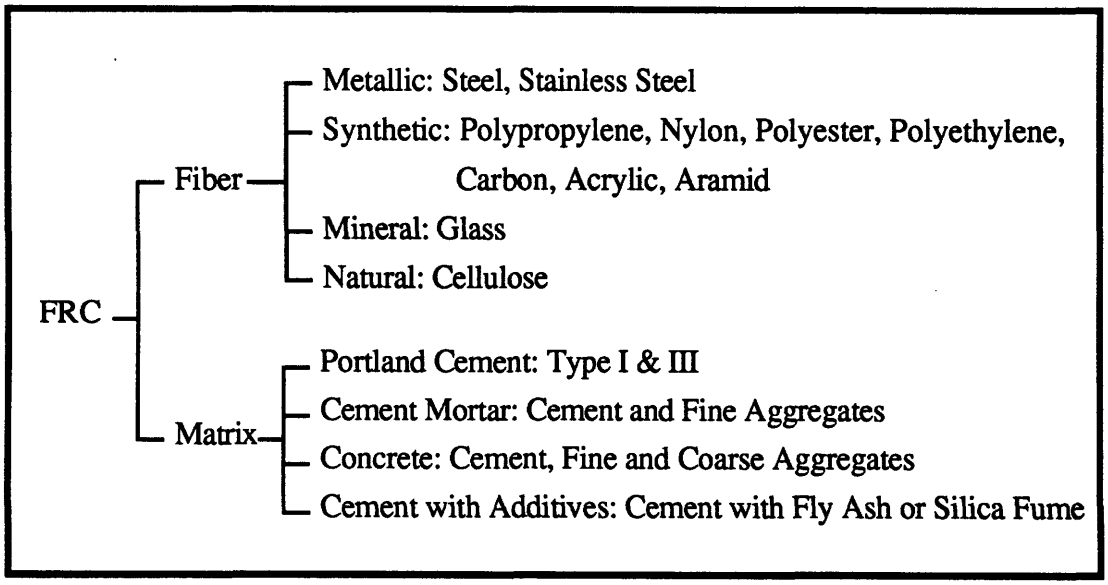

Figure 1.1 Fibers and Matrices used in FRC Materials

In practice, traditional reinforcing bars are used to achieve structural member strength and ductility. Nevertheless, concrete cracking and spalling can cause severe reinforcement corrosion problems, which requires significant and costly repair. Fibers are, therefore, added to the cementitious matrix, as a secondary reinforcement, to control cracking and increase ductility by the crack 'bridging effect'. In addition, the favorable ductile behavior of FRC can reduce the usage of shear reinforcements without jeopardizing the safety factors. For these purposes, discontinuous fibers of a relatively low volume fraction (1-5%) and short lengths are usually used, which are relatively easier to add into fresh concrete with little effect on workability.

1.2 HISTORICAL REVIEW

1.2.1 Steel Fiber Reinforced Concrete (SFRC)

Although fiber reinforcement is an ancient concept, Romualdi and Batson pioneered the modern research on SFRC in early 1960s [1.4]. Straight Steel fibers were first used in FRC composites to improve ductility and fracture toughness [1.5-1.6]. Typical volume fraction V_f used is below 2% and typical aspect ratio L_f/R_f (length/Radius) is about 60-100.

Difficulty of mixing and poor workability are the major problems with high fiber volume fraction and high aspect ratio. When V_f and L_f/R_f are high, fibers are clogged together (balling effect), making mixing very difficult.

With the development of water-soluble glue (to hold fibers together before mixing) and high-range water-reducing admixtures, mixing process and workability have improved significantly [1.7-1.8]. Various deformed shapes, such as: hooked, enlarged and crimped ends, irregular cross-section, have also been developed. Through plastic yielding during fiber pullout, deformed fibers are more effective than straight fibers in providing toughness, fatigue resistance, dynamic strength, and the reduction of shrinkage cracking and crack size [1.7-1.18]

Based on the research in the past two decades, ASTM and ACI have established standards and guidelines [1.19-1.20] for FRC. SFRC has been applied to a variety of structures, such as: nuclear reactor shielding, airport pavements, slabs, bridge decks, parking lots and dams [1.21-1.26]. Commercial products, such as Dramix fiber (Bekaert Fiber Technologies), are available for concrete reinforcement.

1.2.2 Synthetic Fiber Reinforced Concrete (SNFRC)

Synthetic fiber reinforcement was first reported by Goldfein in 1965 [1.27]. Two typical forms, monofilaments and fibrillated bundles, are generally available. Since late 1970s, SNFRC fibers are becoming popular for FRC due to their better post-peak behavior, impact load resistance and corrosion resistance (although they have creeping effect). SNFRC is also used to control cracking in the early stage of concrete hardening (less than 3 hours) [1.28].

ACI is drafting guidelines for SNFRC [1.29]. Typical fiber volume fraction is below 0.5%. In late 1970s, synthetic fibers were typically in the range of 300-400 denier. Nowadays, commercial products with higher aspect ratio (6-60 denier) are available. These finer fibers can achieve the reinforcement with even less volume fraction.

1.2.3 Other Fiber Reinforced Concrete

Other types of fibers are also available, such as glass fibers [1.30], carbon fibers [1.31] and many natural fibers [1.32]. Most of these fibers possess some superior properties, but also some limitations. Glass fiber strand with much smaller diameter is a health hazard in construction industry although it is not expensive. As a synthetic fiber, carbon fiber is too

expensive, making it impractical for FRC structures at the present stage. Natural fibers is less resistant to the alkaline environment in concrete. Therefore, these fibers are not used for general purpose. In the construction industry, steel and polymer fibers are the most widely used fibers by far.

1.2.4 Current Research Interest

There are a variety of interesting topics in the field of FRC materials. Several current research areas are listed:

(1). Development of efficient design procedures for the applications of FRC structural members, such as: beams, slabs, etc.

(2). Improvement of interfacial properties and bond using plasma treatment of fiber surface, etc.

(3). High strength FRC using silica fume and other admixture.

(4). Micro-fibers of micron-level diameters.

(5). Modeling fiber, matrix and interfacial degradation when FRC materials and structures are under dynamic loads.

This thesis focuses on the first topic, Micromechanics-Based Design Procedure.

1.3 THESIS OBJECTIVE

Traditionally, structural design starts from empirically determined stress-strain relations. When fibers are mixed into concrete (or other matrix types) to increase fracture toughness and ductility, the constitutive relation varies significantly depending on the volume fraction of fiber and other parameters. This makes it inefficient and expensive to design a fiber reinforced concrete member based solely on the experimental measurements.

The objective of the thesis is to develop a methodology for prediction of structural member behavior from the micro-parameters (properties of fiber and matrix, interface, fiber size, volume fraction, etc.). Through observation of microstructural features and modeling of microscopic deformation and failure mechanisms, the stress-strain curve can be related

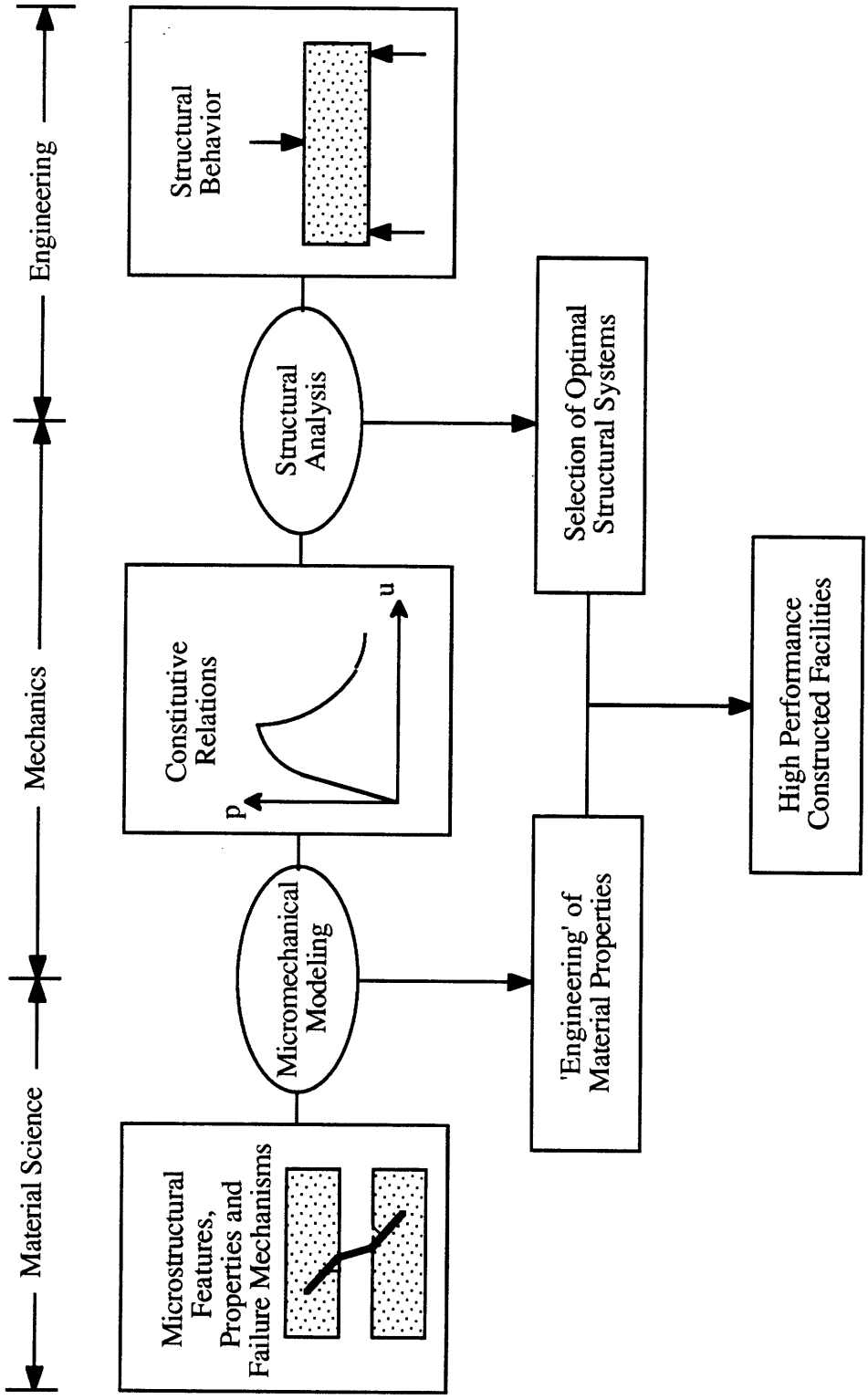

Figure 1.2 Micromechanics-Based Design and Analysis of FRC Materials and Structures

to the properties of fiber, matrix and fiber/matrix interface. With the micromechanical model, one can design the material as well as the structural system to satisfy a given performance requirement. This provides more flexibility to the development of an optimal design with the highest performance/cost, as shown in Fig. 1.2.

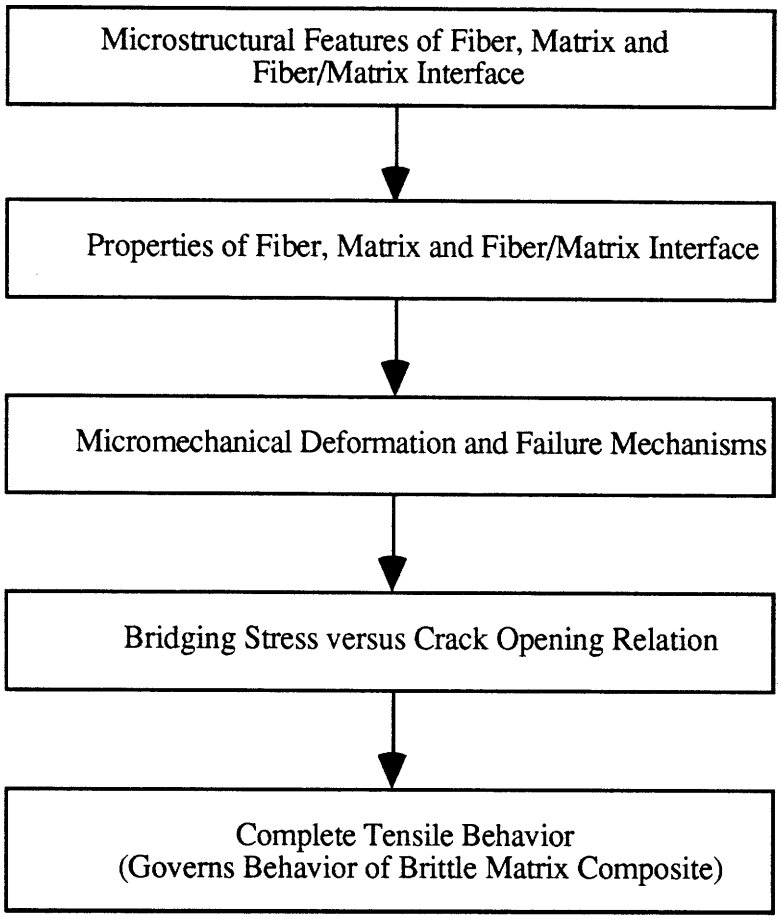

Figure 1.3 Approach of Micromechanical Modeling

In this thesis, steel fiber and cement mortar matrix are chosen to develop the micromechanics-based design procedure. Polypropylene and nylon fibers are investigated at some occasions for the purpose of comparison. For simplicity, straight fibers are studied, which can be extended to fibers of other shapes. Based on Fig. 1.2, the establishment of the design procedure involves a spectrum from material science to engineering structural analysis, which includes three fundamental steps:

(1). Microstructural study of interfacial feature: The microstructural study examines microscopic damages during the cracking process using modern technology, such as:

scanning electron microscopy (SEM) and energy dispersive X-ray analysis (EDX). The observation of microstructure evolution lays the foundation to establish the micromechanical models.

(2). Micromechanical modeling of failure mechanisms: Among the three steps, micromechanical modeling is the most important part to the development of a successful design procedure. A schematic approach for the micromechanical modeling of FRC is shown in Fig. 1.3. Cementitious materials are quasi-brittle, which fail by the propagation of pre-existing cracks. Given the micro-parameters of FRC, the relation of bridging force vs. crack opening can be solved by modeling microscopic deformation and failure mechanisms, such as fiber debonding, fiber bending, and matrix spalling (Fig. 1.4). With the bridging force-crack opening curve, macroscopic constitutive relation can be obtained by analyzing crack propagation and opening [1.33, 1.34]. Then the macroscopic behavior of structural members can be studied by the conventional numerical procedure.

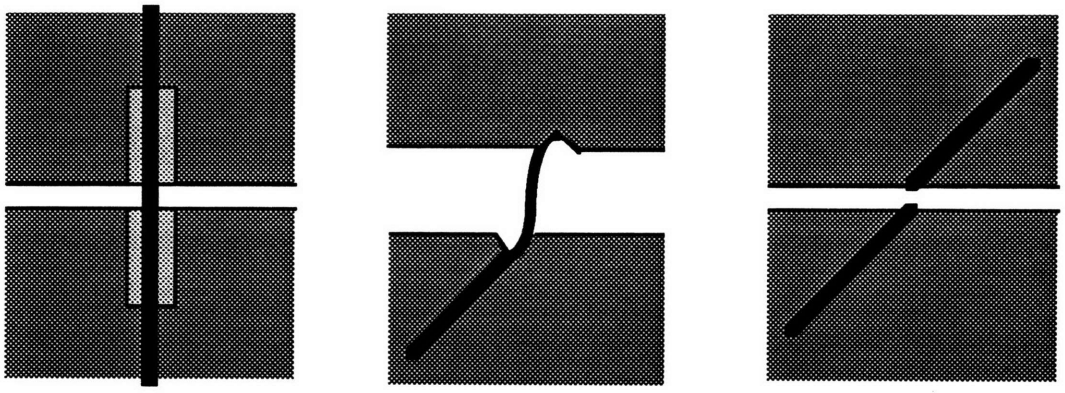

Figure 1.4 Failure Mechanisms

(3). Numerical Simulation of Structural Behavior: Let us examine a shear beam with crack deflecting during propagation. Fibers are pulled under two typical scenarios (Fig. 1.5): (a) fiber pullout under variable lateral compression, and (b) fiber pullout under mixed mode cracking. The crack bridging force of the two scenarios can be obtained by micromechanical modeling. The behavior of an FRC shear beam can, therefore, be predicted using the conventional FEM program, such as ADINA.

Using the micromechanics-based design and analysis methodology, which includes the above three steps, one can ultimately perform optimal design of composite materials and structures with minimal experimental work in the laboratory.

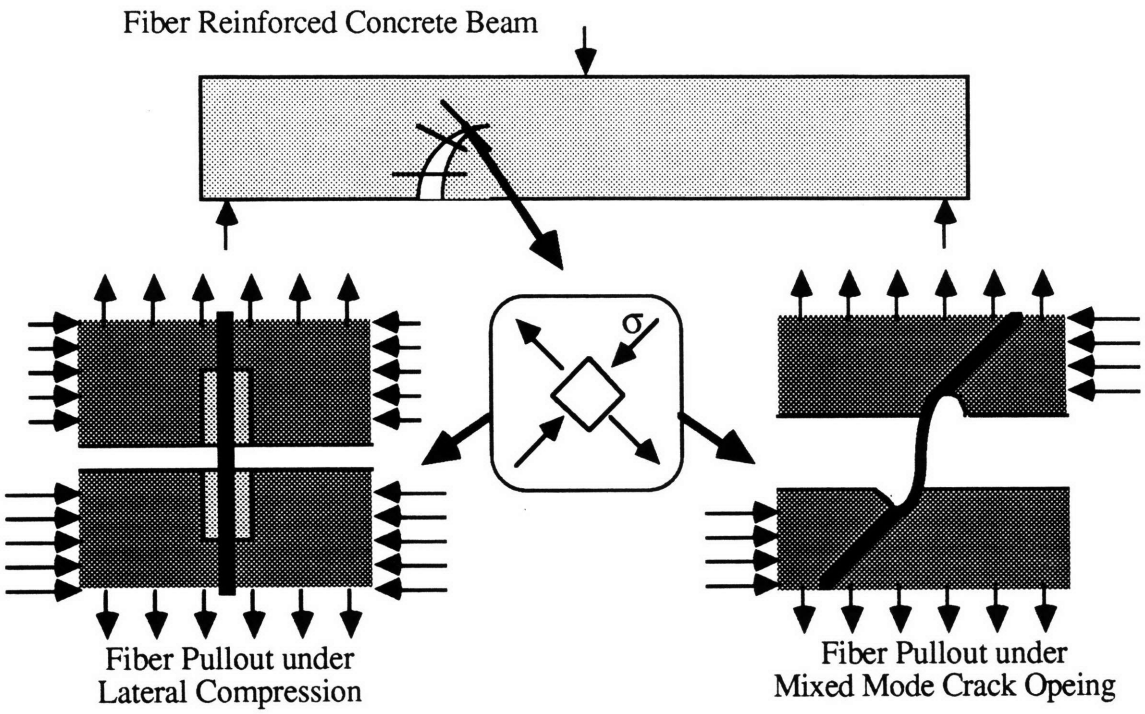

Figure 1.5 Failure of a Shear Beam

1.4 THESIS ORGANIZATION

Based on the objective and approach outline in Section 1.3, the thesis is divided into three parts (Fig. 1.6):

(1). Chapter 3 studied microstructural features of fiber/mortar interface. SEM and EDX analyses showed that the brittle calcium hydroxide layer at the steel/mortar interface is abraded during fiber pullout.

(2). Chapter 4 studied the effects of compressive stress on interfacial debonding strength and interfacial friction. The results validated not only the novel experimental procedure, but also the debonding theory developed by Leung and Li [1.35]; Chapter 5 developed a damage model to simulate the fiber pullout process under variable lateral

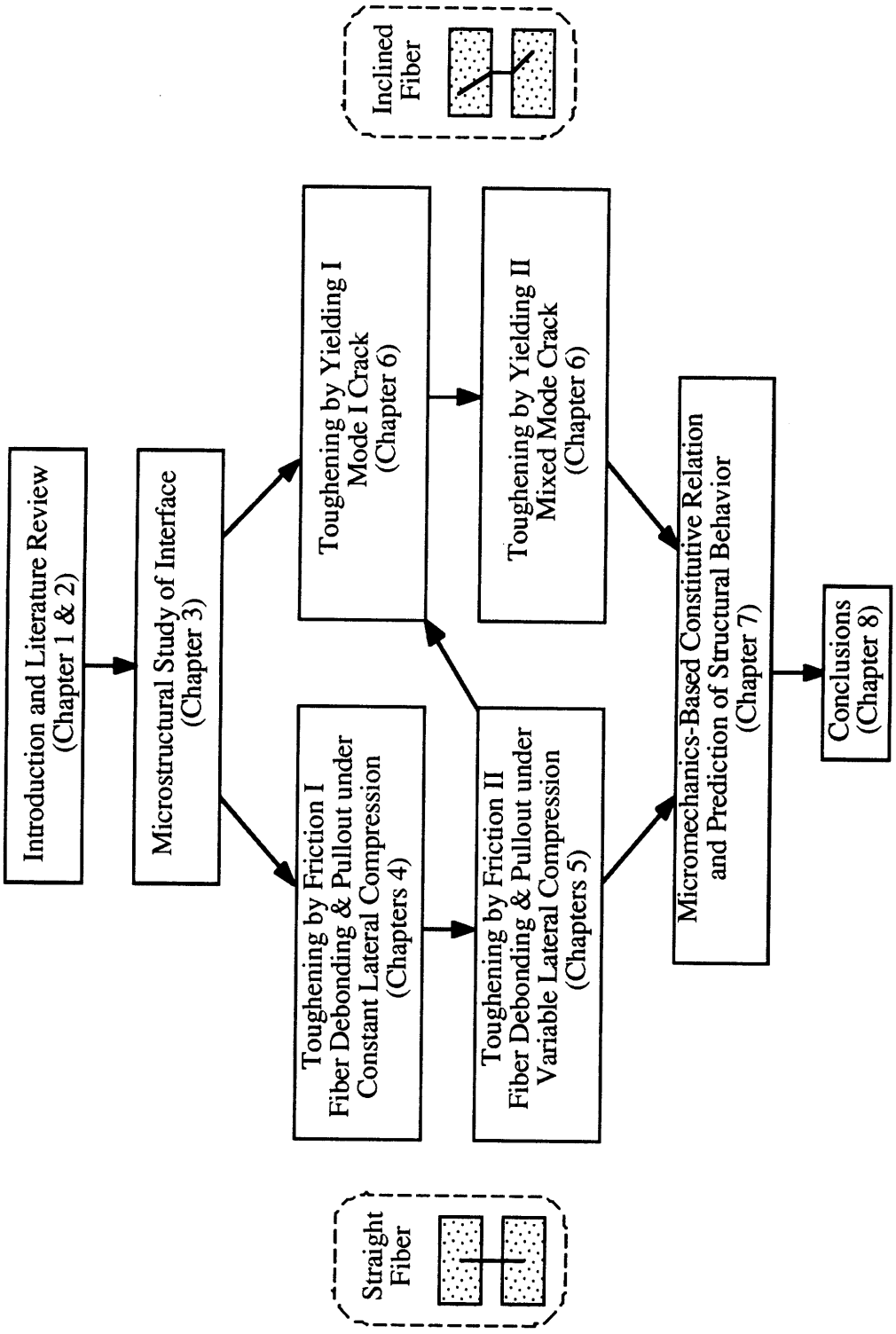

Figure 1.6 Thesis Outline

compressive stress. The model agrees well with the experimental results; Chapter 6 developed a modified experimental setup to test inclined fiber pullout with Mode I and mixed mode crack. Based on the experiment, a micromechanical model for the mixed mode cracking is established and the numerical simulation agrees well with the experimental results.

(3). Chapter 7 established the micromechanics-based constitutive relation (bridging force vs. crack opening) along the crack surface and performed numerical analysis (ADINA) to predict the behavior of an FRC member. Experiment was also performed to compare with the numerical results.

REFERENCES

1.1 *The Jerusalem Bible*, Reader's Edition, Doubleday & Company, Inc., Garden City, New York, Exodus, Chapter 5, verses 6 & 7 (1968)

1.2 Ryder, J.F., "Application of Fiber Cement." *RILEM Symposium 1975: Fiber Reinforced Cement and Concrete*, edited by A. Neville, Construction Press, Lancaster, pp. 23-25 (1975)

1.3 Wang, Y, A.-H. Zureick, B.-S. Cho, and D.E. Scott, "Properties of Fiber Reinforced Concrete Using Recycled Fibrs from Carpet Industrial Waste." Journal of Materials Science Vol. 29, No. 16, pp. 4191-4199 (1994)

1.4 Romualdi, J.P., and G.B. Batson, "Mechanics of Crack Arrest in Concrete." *Proceedings of ASCE*, Vol. 89, No. EM3, pp. 147-168 (1963)

1.5 Shah, S.P., and B.V Rangan, "Ductility of Concrete Reinforced with Stirrups, Fibers and Compression Reinforcements." ASCE Journal of the Structural Division, Vol. 96, No. 6, pp. 1167-1184 (1970)

1.6 Shah, S.P., and B.V Rangan, "Fiber Reinforced Concrete Properties." ACI Journal, Vol. 68, No. 2, pp. 126-135 (1971)

1.7 Ramakrishnan, V., T. Brandshaug, W.V. Coyle, and E.K. Schrader, "A Comparative Evaluation of Concrete Reinforced with Straight Steel Fibers and

Deformed End Fibers Glued together into Bundles." ACI Journal, Vol. 77, No. 3, pp. 135-143 (1980)

1.8 Ramakrishnan, V., W.V. Coyle, V. Kulandaisamy, and E.K. Schrader, "Performance Characteristics of Fiber Reinforced with Low Fiber Contents." ACI Journal, Vol. 78, No. 5, pp. 384-394 (1981)

1.9 Ramakrishnan, V., "Materials and Properties of Fiber Reinforced Concrete." *Proceedings of the International Symposium on Fiber Reinforced Concrete*, Oxford & IBH Publishing, New Delhi, pp. 2.3-2.23 (1987)

1.10 Batson, G., C. Ball, L. Bailey, E. Landers, and J. Hooks, "Flexural Fatigue Strength of Steel Fiber Reinforced Concrete Beams." ACI Journal, Vol. 69, No. 11, pp. 673-677 (1972)

1.11 Zollo, R.F., "Wire Fiber Reinforced Concrete overlays for Orthotropic Bridge Deck Type Loadings." ACI Journal, Vol. 72, No. 10, pp. 576-582 (1975)

1.12 Ramakrishnan, V., and C. Josifek, "Performance Characteristics and Flexural Fatigue Strength of Concrete Steel Fiber Composites." *Proceedings of the International Symposium on Fiber Reinforced Concrete*, Oxford & IBH Publishing, New Delhi, pp. 2.73-2.84 (1987)

1.13 Hashemi, H.N., M.D. Cohen, and T. Erturk, "Evaluation of Fatigue Damage on the Mechanical Properties of Fiber Reinforced Cement Pastes." Journal of Cement and Concrete Research, Vol. 15, No. 5, pp. 879-888 (1985)

1.14 Robins, P.J., and R.W. Calderwood, "Explosive Testing of Fiber-Reinforced Concrete." Concrete, Vol. 12, No. 1, pp. 26-28 (1978)

1.15 Suaris, W., and S.P. Shah, "Test Method for Impact Resistance of Fiber Reinforced Concrete." *Fiber Reinforced Concrete-International Symposium*, American Concrete Institute, SP-81, pp. 247-260 (1984)

1.16 Malmberg, B. and A. Skarendalh, "Method of Studying the Cracking of Fiber Concrete under Restrained Shrinkage." *RILEM Symposium 1987: Testing and Test Methods of Fiber Cement Composites*, Construction Press, Lancaster, pp. 173-179 (1978)

1.17 Swamy, R.N., and H. Stavrides, "Influence of Fiber Reinforcement on Restrained Shrinkage and Cracking." ACI Journal, Vol. 76, No. 3, pp. 443-460 (1979)

1.18 Dahl, P.A., "Influence of Fiber Reinforcement on Plastic Shrinkage and Cracking." *Brittle Matrix Composites*, edited by A.M. Brandt and I.H. Marshalls, Elsevier Applied Science, London, Vol. 1, pp. 435-441 (1986)

1.19 ASTM Standard A820-85, "Standard Specification for Steel Fibers for Use in Fiber Reinforced Concrete." American Society for Testing and Materials, Philadelphia (1985)

1.20 ACI Committee 544, "Design Consideration for Steel Fiber Reinforced Concrete." 544.3R-88, American Concrete Institute, Detroit (1988)

1.21 ACI Committee 544, "Guide for Specifying, Mixing, Placing, and Finishing Steel Fiber Reinforced Concrete." 544.3R-84, American Concrete Institute, Detroit (1984)

1.22 ACI Committee 544, "State-of-the-Art Report on Fiber Reinforced Concrete." 544.1R-82 (reapproved in 1986), American Concrete Institute, Detroit (1986)

1.23 ACI Committee 506, "State-of-the-Art Report on Fiber Reinforced Concrete." 506.1R-84, American Concrete Institute, Detroit (1984)

1.24 Lankard, D.R., "Fiber Concrete Application." *RILEM Symposium 1975: Fibre Reinforced Cement and Concrete*, edited by A. Neville, Construction Press, Lancaster, pp. 3-19 (1975)

1.25 Jonston, C.D., "Steel Fiber-Reinforced Concrete: Present and Future in Engineering Construction." Composites, Vol. 13, pp. 113-121 (1982)

1.26 Keer, J.G., "Fiber Reinforced Concrete." *New Reinforced Concretes: Concrete Technology and Design*, edited by R.N. Swanmy, Vol. 2, Surrey University Press, pp. 52-105 (1984)

1.27 Goldfein, S., "Fibrous Reinforcement for Portland Cement." Modern Plastics, Vol. 42, No. 8, pp. 156-160 (1965)

1.28 Zollo, R.F., "Collated Fibrillated Polypropylene Fibers in FRC." *Fiber Reinforced Concrete International Symposium*, SP-81, American Concrete Institute, Detroit, pp. 397-409 (1984)

1.29 ACI Committee 544, "Synthetic Fiber Reinforced Concrete (SNFRC)." ACI 544.1R-XX, TAC Submittal Draft 1 (1994)

1.30 Majumdar, A.J., "Some Aspect of Glass Fiber Reinforced Cement Research." *Symposium Proceedings on Advances in Cement-Matrix Composites*, Material Research Society, Pittsburgh (1980)

1.31 Akihama, S., T. Suenaga, and T. Banno, "Mechanical Properties of Carbon Fiber Reinforced Cement Composites." The International Journal of Cement Composites and Lightweight Concrete, Vol. 8, No. 1, pp. 21-33 (1986)

1.32 Aziz, M.A., P. Paramasivam, and S.L. Lee, "Prospects for Natural Fiber Reinforced Concrete in Construction." The International Journal of Cement Composites and Lightweight Concrete, Vol. 3, No. 2, pp. 123-132 (1981)

1.33 Marshall, D.B., B.N. Cox, and A.G. Evans, "The Mechanics of Matrix Cracking in Brittle-Matrix Fiber Composites." Acta Metall., Vol. 33, No. 11, pp. 2013-2021 (1985)

1.34 Leung, C.K.Y. and V.C. Li, "First-Cracking Strength of Short-Fiber Reinforced Ceramics." *Ceram. Eng. & Sci. Proc.*, Vol. 10, No. 9-10, pp. 1164-1178 (1989)

1.35 Leung, C.K.Y., and V.C. Li, "A New Strength-Based Theory for the Debonding of Discontinuous Fibers in an Elastic Matrix." Journal of Material Sciences, Vol. 26, pp. 5996-6010 (1991)

Chapter 2. Theoretical Background

For fiber reinforced concrete, the purpose of fiber addition is to increase the toughness and ductility, although the strength and modulus also increase moderately. Fiber volume fraction is, therefore, low. In addition, discontinuous fibers with random orientation are generally used in FRC, which is more difficult to model. In this chapter, relevant topics to the micromechanics-based design methodology and FRC materials are reviewed.

2.1 ELASTIC MODULUS

The modulus of elasticity of FRC materials obeys the rule of mixture before matrix cracking

$$E_c = \eta_1 \eta_2 E_f V_f + E_m V_m \tag{2.1}$$

where E_f and E_m are the elastic moduli of fiber and matrix respectively; V_f and V_m are the volume fractions of fiber and matrix respectively; η_1 is the efficient factor for fiber orientation and η_2 is the efficient factor for fiber length.

When fibers are aligned in the direction of loading, η_1=1. When fibers are randomly distributed, η_1=1/3 for 2-D case and η_1=1/6 for 3-D case [2.1]. For the case of composites under lateral constraint, η_1=3/8 for 2-D case and η_1=1/5 for 3-D case [2.2]. For continuous fibers, η_2=1. For discontinuous fibers, η_2<1 because a fiber carries less stress near the fiber end.

Since fiber volume fraction is generally less than 5% in FRC materials, the elastic modulus of FRC composites does not change significantly with fiber addition.

2.2 INTERFACIAL TRANSITION ZONE

In micromechanics-based design and analysis of FRC composites, the microstructural features of FRC (fiber, matrix and interface in particular) play an important role in developing the micromechanical models, estimating micromechanical parameters, analyzing

the structural behavior, and ultimately designing FRC composites with optimum energy absorption, ductility and tensile properties.

The microstructures near the fiber/cement paste, mortar or concrete interface are considerably different from the bulk matrix [2.3]. Pinchin and Tabor [2.4] studied cylindrical paste specimens with a steel wire embedded in the center. By splitting the specimen around the fiber, the tensile fracture surface near the fiber/paste (fiber/mortar) interface were studied by scanning electron microscopy (SEM), energy dispersive X-ray analysis (EDX) and X-ray diffraction (XRD). They found that the structure near the interface does not change appreciably for curing times greater than 7 days. XRD analysis indicated about 20-40% enrichment of calcium hydroxide (CH) within the cement matrix 10 μm from the interface. The indentation hardness tests showed a decrease in matrix strength within 0.75 mm from the fiber surface. Al Khalaf and Page [2.5] also investigated the interfacial zone between mild steel and Portland cement pastes and mortars by SEM. The cylindrical specimens, with upper half made of cement paste and low half made of steel, were loaded and broken under uniaxial tension. They found cohesive failure (fracture in the paste close to the interface) for young specimens and adhesive failure (fracture at the interface) for older ones. Al Khalaf and Page also identified a discontinuous CH layer (less than 1 μm) which replicated the topography of the steel surface, with the c-axis oriented normal to the steel surface. The CH exhibited a dendritic growth and in many cases crystal boundaries could be observed. In addition to the CH layer, there was frequent evidence of a calcium silicate hydrate (C-S-H) gel of various morphologies, and well developed crystals formed at different orientations. The C-S-H gel was not densely packed near the interface. Occasionally, the gel could be observed to adhere to the steel surface, but usually it was confined to the paste side of the interface.

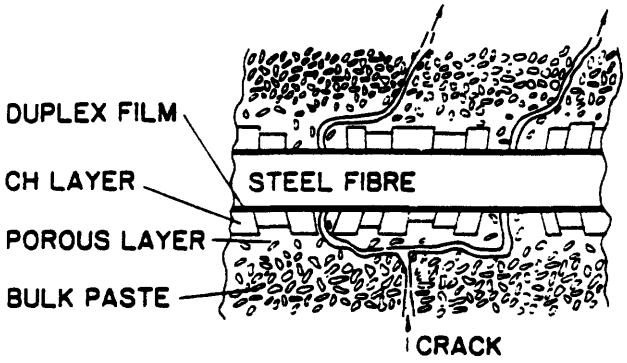

Figure 2.1 Interfacial Transition Zone at Fiber/Cement Interface

A more recent study by Bentur, et al. [2.6] concluded that the interfacial zone around steel fibers can be characterized by several layers (Fig. 2.1). The steel fiber surface is in contact with a thin duplex film layer (1 μm) consisting of a sub-layer of CH in direct contact with the steel and a single C-S-H sub-layer backing it. More than half of the area outside this duplex film is occupied by a thicker layer of dense CH crystals which is about 10 to 20 μm in thickness. The remaining area scattered among the dense CH crystals is a porous zone that contains some C-S-H gel and possibly some ettringite particles (AFt: calcium aluminum trisulfate). Around the thick CH layer is a distinct porous layer of C-S-H gel, and only beyond that porous layer is the bulk cement paste microstructure observed. The region surrounding the fiber thus contains a very porous and weak layer parallel to the fiber which extends at least 10 μm from the fiber surface. Wei, et al. [2.7] confirmed the presence of a weak interfacial zone by the hardness test.

Most of the available research work has focused on studying the interface prior to fiber pullout. In Chapter 3, the damage evolution during fiber pullout is studied microscopically.

2.3 FIBER DEBONDING AND PULLOUT THEORIES

2.3.1 Fiber Debonding

The purpose of the fiber pullout test is to determine interfacial properties governing the debonding/pullout behavior of fiber in a composite. In order to obtain useful quantitative information, a fiber debonding theory is required to (a) guide the extraction of interfacial parameters from the pullout test result, and (b) derive, based on the interfacial parameters, the fiber debonding/pullout behavior in an actual composite with a much higher fiber volume fraction than the pullout specimen. In the literature, various fiber debonding theories have been developed, with either the strength-based approach [2.8-2.13] or the fracture-based approach [2.14-2.19].

In the strength-based approach, debonding is assumed to occur when the interfacial shear stress (usually obtained from an approximate shear lag theory) reaches the interfacial shear strength τ_s. In the fracture-based approach, debonding is taken to occur as the energy release of the system during an incremental interfacial crack propagation is sufficient to overcome the interfacial fracture energy Γ.

Leung [2.19] showed that the same set of equations can be used to describe strength-based and fracture-based debonding if (a) debonding is assumed to occur as the interfacial shear stress reaches an effective interfacial strength τ_{eff} to be defined below, and (b) after debonding, the interfacial stress drops immediately to a constant interfacial friction value τ_i. The assumption of constant τ_i is reasonable during the debonding process when only part of the fiber/matrix interface has undergone debonding and there is relatively little sliding at the fiber/matrix interface. During fiber pullout, when the completely debonded fiber is sliding out of its groove, τ_i may change as a function of sliding distance s [2.20-2.22].

For strength-based debonding,

$$\tau_{eff} = \tau_i \tag{2.2}$$

For fracture-based debonding,

$$\tau_{eff} = \tau_i + \sqrt{\frac{E_f \Gamma (1-\alpha)\rho^2}{R_f}} \tag{2.3}$$

where $\alpha = E_f V_f / E_c$, $E_c = E_f V_f + E_m V_m$, and

$$\rho^2 = -\frac{2G_m E_c}{E_f V_f E_m \left[\dfrac{2\ln V_f + (1-V_f)(3-V_f)}{4(1-V_f)^2}\right]} \tag{2.4}$$

with E_f being the fiber Young's modulus, E_m the matrix Young's modulus, G_m the matrix shear modulus, V_f the fiber volume fraction and E_c the composite stiffness. Also, R_f is the fiber radius and ρ is a shear stress transfer parameter dependent on the fiber volume fraction as well as the stiffness values of the fiber and matrix phase. In the above expression for ρ, the presence of a compliant interphase around the fiber [2.6, 2.7] has been neglected. The incorporation of a compliant interphase will lead to a lower value of ρ and its effects on the determination of interfacial parameters will be discussed in Chapter 4.

For fracture-based debonding (Eq. 2.3), τ_i appears in the expression for τ_{eff} due to the following reason. Debonding at any point along the interface is accompanied by fiber/matrix relative sliding. The energy release of the system for the interfacial crack to propagate incrementally therefore consists of two components: (a) energy to overcome the frictional resistance to fiber/matrix relative sliding, and (b) energy for the creation of new interfacial crack surface, which is given by the second term in Eq 2.3. The detailed

derivation of Eq. 2.3 can be found in [2.19]. From Eqs. 2.2 and 2.3, it can be noted that if debonding is strength-based, τ_{eff} is a material property equal to τ_s. If debonding is fracture-based, τ_{eff} is a function of τ_i, Γ as well as the fiber size and volume fraction. In particular, for fixed R_f and V_f, the change in τ_{eff} should be the same as the change in τ_i as lateral stress is varied.

It has been discussed in [2.19] that for experiments carried out with one fiber size and one fiber volume fraction, it is impossible to distinguish between strength-based and fracture-based debonding because the experimental results can be fitted equally well with either theory. Without further knowledge about the debonding mode, it is more appropriate to interpret the data in terms of the effective interfacial shear strength τ_{eff}.

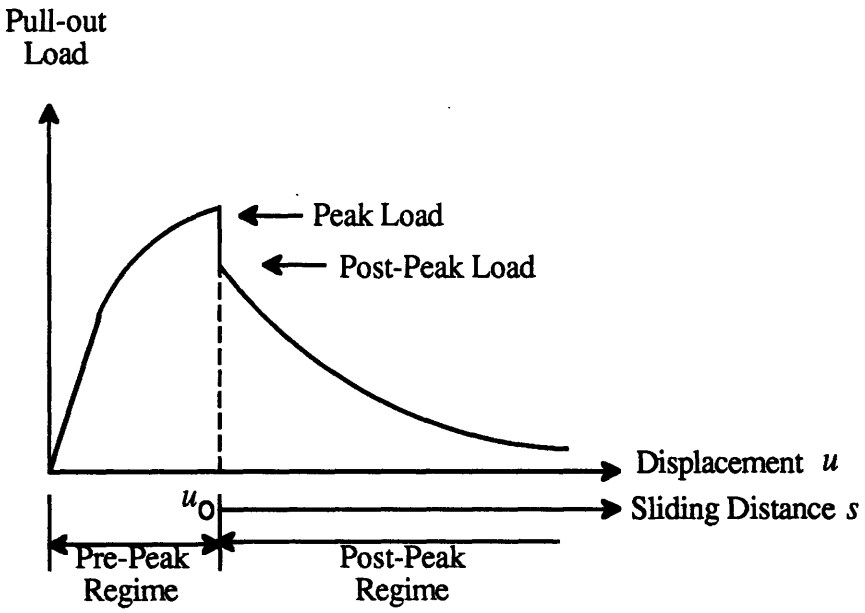

Figure 2.2 Typical Pullout Curve for a Single Fiber

If τ_{eff} is larger than τ_i, the pullout record for a single fiber will exhibit a sudden drop after the peak load is reached (Fig. 2.2). The drop is due to a snap-back behavior in the load vs. fiber displacement curve predicted theoretically by a debonding analysis [2.13, 2.19]. The point right after the drop corresponds to the completion of fiber debonding. Since τ_i is assumed to be constant up to this point, the post-peak fiber stress is equal to $2\tau_i L/R_f$, where L is the embedded fiber length. Once τ_i is determined from the post-peak load and ρ is calculated from the specimen and fiber sizes, τ_{eff} can be obtained by an iterative procedure based on a fiber debonding model developed by Leung [2.19]. The

peak fiber stress σ_{peak} is calculated from τ_i, ρ and assumed values of τ_{eff}. (Note: all the required equations and a flow chart for the computational procedure can be found in [2.19]) The value of τ_{eff} which gives the same value of σ_{peak} as the experimentally measured value is the required interfacial parameter.

In Chapter 4, fiber pullout test is performed under lateral stresses. The effect of lateral stress on τ_i and τ_{eff} at the onset of debonding is studied to provide more insight to the physical process during fiber debonding.

2.3.2 Fiber Pullout

The decrease of interfacial friction for steel FRC during the pullout stage has been widely observed [2.20-2.22]. By considering the decay of fiber misfit as a function of the sliding distance s, Naaman et al. [2.20] proposed the following empirical formula for the fiber pullout curve under zero lateral compressive stress

$$\tau_{i0}(s) = \tau_{i0}(0)\frac{\exp[-s^{\eta}] - \xi\exp[-L^{\eta}]}{1-\xi\exp[-(L-s)^{\eta}]}\frac{1-\exp\left\{\dfrac{-2\nu_f\mu(L-s)}{E_f r_f\left[\dfrac{1+\nu_m}{E_m}+\dfrac{1-\nu_f}{E_f}\right]}\right\}}{1-\exp\left\{\dfrac{-2\nu_f\mu L}{E_f r_f\left[\dfrac{1+\nu_m}{E_m}+\dfrac{1-\nu_f}{E_f}\right]}\right\}} \tag{2.5}$$

Where $s = u\text{-}u_0$ is the sliding distance after total debonding (i.e. the difference between the total displacement and the displacement at complete debonding, Fig. 2.2); L is the fiber embedded length; μ is the friction coefficient at the interface. The interfacial friction as a function of sliding distance can be considered as the product of three separate terms. In Eq. 2.5, the first term $\tau_{i0}(0)$ is the initial interfacial friction at the onset of total debonding (the subscript '0' in τ_{i0} represents a case with zero far field lateral stress). The second term, involving two empirical constants ξ and η, shows the decay of interfacial friction due to the reduction of fiber/matrix misfit. (Note: the misfit is originally a result of matrix shrinkage.) The third term accounts for the Poisson's effect. For steel fibers, where the interfacial friction is found to decrease rapidly with sliding, the Poisson's effect is relatively

unimportant compared with the misfit reduction. The third term in Eq. 2.5 can hence be effectively taken to be unity.

For polymer and other fiber types, there have been some fiber pullout models developed [2.23]. This thesis will focus on steel fiber only. In Chapter 5, the pullout behavior under variable lateral steel stress is studied.

2.4 INCLINED FIBER PULLOUT

Crack bridging by oblique fiber has been studied for various fiber and matrices. Piggott [2.24] studied the bending of brittle fibers in a rigid perfectly plastic matrix. In the model, the fiber is considered to be a flexible string with no bending stiffness. The fiber/matrix interfacial stress is assumed to have a magnitude equal to the yield strength of the matrix. Therefore, this model is only valid for cases with flexible fibers and matrix with very low yield stress and yield strain. However, with fitting parameters, it has been used successfully to fit experimental data of 0.76 mm glass fiber bundles embedded in brittle polyester resin.

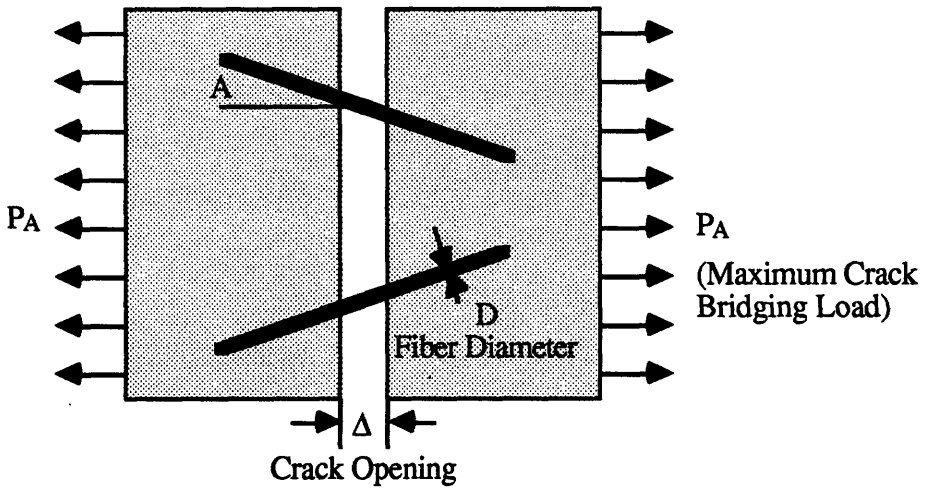

Figure 2.3 Test System for Oblique Fiber Composites [2.25]

Morton and Groves [2.25] analyzed the bridging effects of inclined ductile fibers in a yielding matrix by considering the bending of fiber across a crack (Fig. 2.3). In their work, interfacial shear stress is neglected and the reaction stress from the matrix on the

fiber is taken to be the matrix yield strength. With these simplified assumptions, the bridging stresses for a certain crack opening and fiber inclination angle are derived for two different cases: the case with the fiber remaining elastic and the case with plastic hinges formed in the fiber. The model tends to be in better agreement with experimental results at low fiber inclination angles. At higher angles, the discrepancy is attributed to extensive matrix yielding or matrix spalling that tends to relax the fiber.

The model of Li, et al. [2.26] assumes the presence of a frictional pulley at the exit point of the fiber into the crack and is only applicable to extremely flexible fiber with high failure strain. None of the above models can take into account the spalling of matrix below the fiber, which has been widely observed [2.25-2.28].

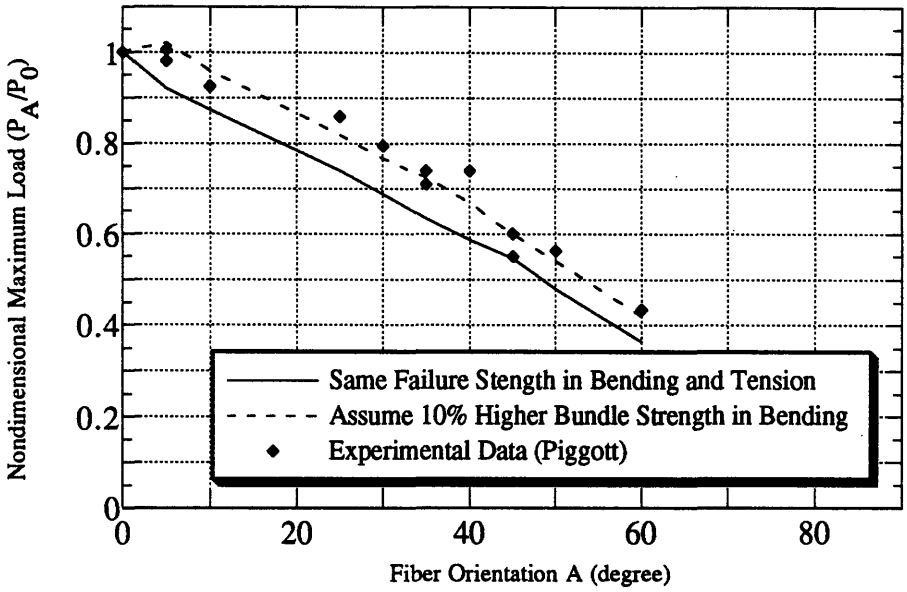

Figure 2.4 Comparison of Theoretical Model [2.29] with Experimental Data [2.24] (Glass Fiber Bundles)

By considering fiber debonding, fiber bending and rupture as well as matrix spalling, Leung and Li [2.29] studied brittle fiber reinforced brittle matrix composites. The fiber bending/matrix spalling mechanism is analyzed by treating the fiber as a beam bent on an elastic foundation with variable stiffness and the possibility of spalling. The foundation stiffness and spalling criterion are derived from a finite element analysis. Prediction of

maximum bridging stress for inclined fibers is in good agreement with the experimental results by Piggott [2.24], as shown in Fig. 2.4.

With a similar approach, Leung and Chi [2.30] studied ductile fiber reinforced brittle matrix composite by considering fiber yielding, instead of rupture. The model prediction of maximum crack bridging force in steel and other metallic fiber reinforced brittle matrix composites is found to be in reasonable good agreement with the experimental results of Morton and Groves [2.25]. Figure 2.5 shows the comparison of the results for steel fiber reinforced composite.

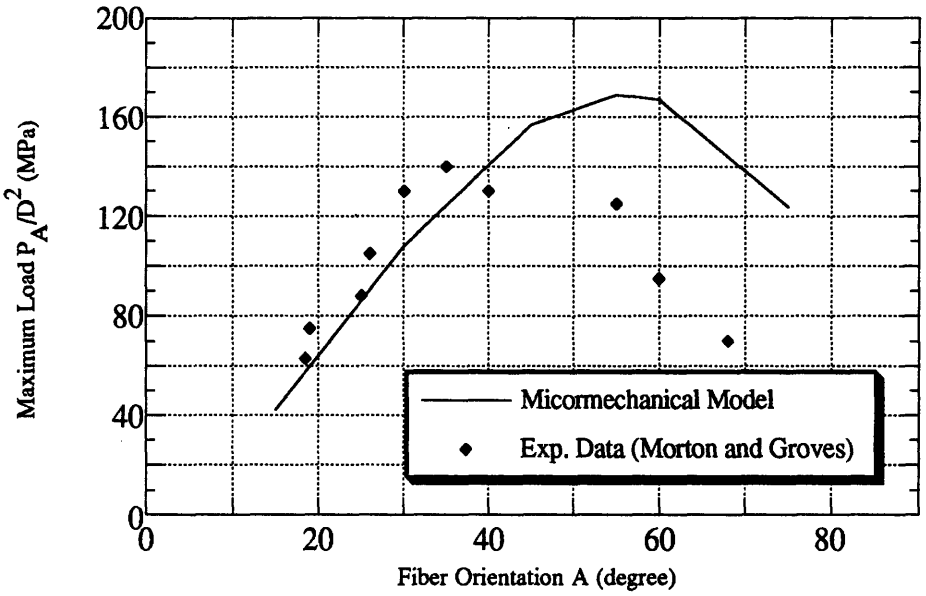

Figure 2.5 Comparison of Theoretical Model [2.30] with Experimental Data [2.25] (Steel Fibers)

Previous work has only covered the pullout of inclined fiber along a Mode I (opening mode) crack. In Chapter 6, the stress displacement relation along a mixed mode (opening mode and shear mode) crack is studied.

2.5 PREDICTION OF STRUCTURAL BEHAVIOR

Based on the stress-strain relation from bridging forces, structural behavior can theoretically be predicted directly through solving integral equations resulting from

propagation criteria of bridged cracks. Cases with simple geometry where Green's functions are available have been solved. These include the direct tensile specimen with internal cracks by Marshall et al. [2.31], beam under uniform moment by Dharini [2.32], double cantilever beam by Foote et al. [2.33] and the compact tension specimen [2.34].

For more general specimen and loading configurations, it is more convenient to obtain the constitutive relation first from the micro-parameters. Such a tensile constitutive relation, which includes both the rising and softening branch, can be implemented into the finite element programs for the derivation of structural component behavior. Two common ways of implementation, the discrete crack approach and the smear crack approach, have been developed.

In the discrete crack approach [2.35-2.37], a fictitious crack (with fiber bridging) is assumed to form once the tensile strength is reached at a certain point of the structure. The nodes on the two elements at the two sides of the crack are separated, with a softening spring introduced in between. The softening behavior of the spring corresponds to the decrease of fiber crack bridging stress with crack opening. Such a model is most convenient for cases with well-defined crack paths. Then, the finite element mesh can be arranged to have element boundaries along the expected crack direction and the plausible location of softening springs can be pre-determined.

In the smear crack approach [2.38-2.39], instead of introducing softening springs between separated nodes, cracking is assumed to produce a deformation smeared across an element. In such a case, the softening behavior of the elements is in terms of a stress-strain relation rather than a stress-displacement relation as in the softening spring. In the fixed multi-directional crack models [2.40], a new crack can be formed in a new direction when the principle stress directions change beyond a certain angle, with old cracks remaining in their original directions.

Both the discrete crack approach and the smeared crack approach have their advantages and disadvantages for a given application. In Chapter 7, only the discrete crack approach is used to simulate FRC member behavior.

REFERENCES

2.1 Cox, H.L., "The Elastic and Strength of Paper and other Fibrous Materials." British

Journal of Applied Physics, Vol. 3, pp. 72-79 (1952)

2.2 Krenchel, H., *Fiber Reinforcement.* Akademisk Forla Copenhagen (1964)

2.3 Mindess, S., "Interfaces in Concrete." *Materials Science of Concrete I*, Edited by Jan P. Skalny, The American Ceramic Society, Inc., Westerville, OH (1989)

2.4 Pinchin, D.J., and D. Tabor, "Interfacial Phenomena in Steel Fiber Reinforced Cement I: Structure and Strength of Interfacial Region." Cement and Concrete Research, Vol. 8, pp. 15-24 (1978)

2.5 Al Khalaf, M.N., and C.L. Page, "Steel/Mortar Interfaces: Microstructural Features and Mode of Failure." Cement and Concrete Research, Vol. 9, pp. 197-208 (1979)

2.6 Bentur, A., S. Diamond, and S. Mindess, "The Microstructure of the Steel Fiber-Cement Interface." Journal of Materials Science, Vol. 20, pp. 3610-3620 (1985)

2.7 Wei, S., J.A. Mandel, and S. Said, "Study of the Interface Strength in Steel Fiber-Reinforced Cement-Based Composites." ACI Journal, pp. 597-605 (1986)

2.8 Greszczuk, L.B., "Theoretical Studies of the Mechanics of the Fiber-Matrix Interface in Composites." *ASTM STP 452*, pp. 42-58 (1969)

2.9 Lawrence, P., "Some Theoretical Considerations of Fiber Pull-out from an Elastic Matrix." Journal of Materials Science, Vol. 7, pp. 1-6 (1972)

2.10 Takaku, A. and R.G.C. Arridge, "The Effect of Interfacial Radial and Shear Stress on Fiber Pull-out in Composite Materials." J. Phys., D: Appl. Phys., Vol. 6, pp. 2038-2047 (1973)

2.11 Gopalaratnam, V.S. and S.P. Shah, "Tensile Fracture of Steel Fiber Reinforced Concrete." ASCE J. Eng. Mech., Vol. 113, No. 5, pp. 635-653 (1987).

2.12 Hsueh, C-H., "Interfacial Debonding and Fiber Pull-out Stresses of Fiber-Reinforced Composites." Mat. Sci. & Eng., Vol. A123, pp. 1-11 (1990)

2.13 Leung, C.K.Y. & V.C. Li, "A New Strength-Based Theory for the Debonding of Discontinuous Fibers in an Elastic Matrix." J. Mat. Sci., Vol. 26, pp. 5996-6010 (1991)

2.14 Gurney, C. and J. Hunt, "Quasi-static Crack Propagation." *Proc. Roy. Soc., London*, Vol. A299, pp. 508-524 (1969).

2.15 Atkinson, C., J. Avila, E. Betz, & R.E. Smelser, "The Rod Pull-Out Problem, Theory and Experiment." J. Mech. Phys. Solids, Vol. 30, No. 3, pp. 97-120 (1982)

2.16 Stang, H., Z. Li, and S.P. Shah, "The Pull-out Problem: The Stress versus Fracture Mechanical Approach." ASCE J. Eng. Mech., Vol. 116, No. 10, pp. 2136-2150 (1990)

2.17 Gao, Y., Y.W. Mai, and B. Cotterell, "Fracture of Fiber-Reinforced Materials." J. Appl. Mech. and Phys. (ZAMP), Vol. 39, pp. 550-572 (1988)

2.18 Hutchinson, J.W. and H.M. Jensen, "Models of Fiber Debonding and Pullout in Brittle Composites with Friction." Mech .& Mat., Vol. 9, pp. 139-163 (1990)

2.19 Leung, C.K.Y., "Fracture-Based Two-Way Debonding Model for Discontinuous Fibers in Elastic Matrix." ASCE J. Eng. Mech., Vol. 118, No. 11, pp. 2298-2318 (1992)

2.20 Naaman, A.E., G.C. Namur, J.M. Alwan, and H.S. Najm, "Fiber Pullout and Bond Slip. I: Analytical Study." ASCE J. Struct. Eng., Vol. 117, No. 9, pp. 2769-2790 (1991a)

2.21 Naaman, A.E., G.C. Namur, J.M. Alwan, and H.S. Najm, "Fiber Pullout and Bond Slip. II: Experimental Verification." ASCE J. Struct. Eng., Vol. 117 No. 9, pp. 2791-2808 (1991b)

2.22 Naaman, A.E. and S.P. Shah, "Pull-out Mechanism in Steel Fiber-Reinforced Concrete." ASCE J. Struct. Div., Vol. 102, No. 8, pp. 1537-1548 (1976)

2.23 Wang, Y., V.C. Li, and S. Backer, "Tensile Properties of Synthetic Fiber Reinforced Mortar." Cement and Concrete Composites, Vol. 12, No. 1, pp. 29-40 (1990)

2.24 Piggott, M.R., "Toughness in Oblique-Stressed Fibrous Composites." J. Mech. Phys. Solids, Vol. 22, pp. 457-468 (1974)

2.25 Morton, J., and G.W. Groves, "The Cracking of Composites consisting of Discontinuous Ductile Fibers in a Brittle Matrix--Effect of Fiber Orientation." J. Mat. Sci., Vol. 9, pp. 1436-1445 (1974)

2.26 LI, V.C., Y. Wang, and S. Backer, "Effect of Inclining Angle, Bundling and Surface Treatment on Synthetic Fiber Pull-out from a Cement Matrix." Composites, Vol. 21, No. 2, pp. 132-140 (1990)

2.27 Becker, P.F., E.R. Fuller, and P. Angelini, "Matix-Grain-Bridging Contributions to the Toughness of Whisker-Reinforced Ceramics." J. Am. Ceram. Soc., Vol. 74, No. 9, pp. 2131-2135 (1991)

2.28 Cai, H, K.T. Faber, and E.R. Fuller, "Crack Bridging by Inclined Fibers/Whiskers in Ceramic Composites." J. Am. Ceram. Soc. (1992)

2.29 Leung, C.K.Y. and V.C. Li, "Effect of Fiber Inclination on Crack Bridging Stress in Brittle Fiber Reinforced Brittle Matrix Composites." JMPS, Vol. 40, No. 6, pp. 1333-1362 (1992)

2.30 Leung, C.K.Y. and J. Chi, "Derivation of Crack Bridging Force in Random Discontinuous Fiber Composites through Micromechanics." in press ASCE J. Eng. Mech. (1995)

2.31 Marshall, D.B., B.N. Cox, and A.G. Evans, "The Mechanics of Matrix Cracking in Brittle-Matrix Fiber Composites." Acta Metall., Vol. 33, No. 11, pp. 2013-2021 (1985)

2.32 Dharini, L.R., "Analysis of a Ceramic Matrix Composite Flexure Specimen." *ASTM STP*, Vol. 1080, pp. 87-97 (1990)

2.33 Foote, M, Y.W. Mai, and B. Cotterell, "Crack Growth Resistance-Curves in Strain-Softening Materials." J. Mech. Phys. Solids, Vol. 34, No. 6, pp. 593-607 (1986)

2.34 Cox, B.N., and D.B. Marshall, "Stable and Unstable Solutions for Bridged Cracks in Various Specimens." Acta Metall. Mater., Vol. 39, No. 4, pp. 579-589 (1991)

2.35 Hillerborg, A., "Analysis of One Single Crack." *Fracture Mechanics of Concrete*, ed. F.H. Wittmann, Elsevier Science, Amsterdan, pp. 223-249 (1983)

2.36 Ingraffea, A.R., and V. Saouma, "Numerical Modeling of Discrete Crack Propagation in Reinforced and Plain Concrete." *Fracture Mechanics of Concrete: Structural Applications and Numerical Calculations*, ed. G. Sih and A. DiTommaso, Martinus Nijhoff, pp. 171-225 (1984)

2.37 Gustafsson, P.J., "Fracture Mechanics Studies of Non-yielding Materials like Concrete." *Report TVBM-1007*, Div. of Building Materials, Lund Institute of Technology, Sweden (1985)

2.38 Bazant, Z.P., and B.H. Oh, "Crack Band Theory for Fracture of Concrete." ***RILEM** Mat. & Struct.*, Vol. 16, pp. 155-177 (1983)

2.39 Rots, J.G., and R. de Borst, "Analysis of Mixed-mode Fracture in Concrete." ASCE J. Eng. Mech., Vol. 113, No. 11, pp. 1739-1758 (1987)

2.40 de Borst, R., and P. Nauta, "Non-orthogonal Cracks in a Smeared Finite Element Model." Eng. Computations, Vol. 2, pp. 35-46 (1985)

Chapter 3. Interfacial Damage Evolution

SYNOPSIS

This study attempts to connect the change in interfacial properties of FRC during fiber pullout to the microstructural features of the interface. The microstructural features of fiber (steel, nylon and polypropylene)/mortar interfaces are examined during fiber debonding and pullout. Since fiber pullout is found to be sensitive to lateral compression, microscopic studies are carried out on fibers pulled out with and without lateral compression. SEM and EDX analyses are performed at four different stages: (a) before debonding, (b) right after debonding, (c) at small sliding distance, and (d) at large sliding distance.

For the steel fiber/mortar interface, it is found that the mortar surface (interfacial transition zone) is subjected to abrasion while the steel surface is subjected to plastic deformation. The rapid post-peak drop of the pullout force at early sliding distance is due to the grinding effect, which leads to a reduction of asperity on the mortar surface. EDX analysis on mortar interface shows that the ratio of calcium/silicon count first increases within a short sliding distance and decreases thereafter, indicating a process of CH layer abrasion and C-S-H layer exposure. Application of lateral compressive stress accelerates the abrasion process.

For the nylon and polypropylene fiber/mortar interfaces, the fiber surface peels and the matrix surface experiences very little damage. Nylon fiber surface swells and peels with short whiskers on the surface increasing the post-debonding pullout force. The polypropylene fiber surface peels and is plowed with long whiskers and long scratch lines leading to slow decrease in the post-peak pullout force. With lateral compression applied to the mortar during fiber pullout, the abrasion and peeling effects are more severe. Holes may form on the polypropylene surface over the longer sliding distance. The ratio of calcium/silicon count on the mortar surface by EDX does not show obvious trends with sliding distance indicating that the mortar surface experiences very little damage.

3.1 INTERFACIAL MICROSTRUCTURES

The performance of fiber reinforced concrete (FRC) is strongly affected by the fiber debonding/pullout behavior [3.1-3.3]. For different fibers, the pullout curves may exhibit totally different trends. For example, the interfacial friction, which is very sensitive to interfacial microstructures, may either decrease rapidly (steel FRC [3.4, 3.5]) or increase slightly (synthetic FRC [3.6]) after total debonding. In order to understand the variation of interfacial friction during fiber debonding and pullout, it is necessary to investigate microstructural features at the interface, especially the damage evolution of the microstructure during fiber pullout.

3.1.1 Steel Fiber/Concrete Interface

It has been found that the microstructure near the cement paste, mortar or concrete interface is considerably different from the bulk matrix [3.7-3.11]. An SEM study by Bentur, et al. [3.10] concluded that the interfacial transition zone (Section 2.2) around steel fibers can be characterized by several layers (Fig. 3.1). The steel fiber surface is in contact with a thin duplex film layer (1 μm) consisting of a sub-layer of CH (calcium hydroxide) next to the steel and a C-S-H (calcium silicate hydrate) sub-layer. More than half of the area outside this duplex film is occupied by a thicker layer of dense CH crystals which is about 10 to 20 μm in thickness. The remaining area scattered among the dense CH crystals is a porous zone that contains some C-S-H gel and possibly some ettringite particles (AFt: calcium aluminum trisulfate). Around the thick CH layer is a distinct porous layer of C-S-H gel, and only beyond that porous layer is the bulk cement paste microstructure observed. The region surrounding the fiber thus contains a very porous and weak layer parallel to the fiber which extends at least 10 μm from the fiber surface.

Although the microstructure of the fiber/mortar interface has been reasonably understood, the microstructural change of interface during the fiber pullout process, due to interfacial debonding and friction, are known in considerably less detail. To the author's knowledge, only Pinchin and Tabor [3.12] attempted to explain the decrease in interfacial friction of steel fiber/mortar during the pullout process based on the surface compaction of hydrated cement paste, a phenomenon observed by Soroka and Sereda [3.13].

Pinchin and Tabor attribute the significant friction decrease during a small amount of steel fiber pullout to densification or compaction, but not to wear, on the mortar surface.

They argued that the compaction during fiber pullout occurs on a very fine scale in the order of 0.1-0.3 μm near the embedded steel fiber and is difficult to detect. Since their conclusions are based on the final stage of the pullout test, i.e., at total fiber pullout, it may not reflect the whole pullout process.

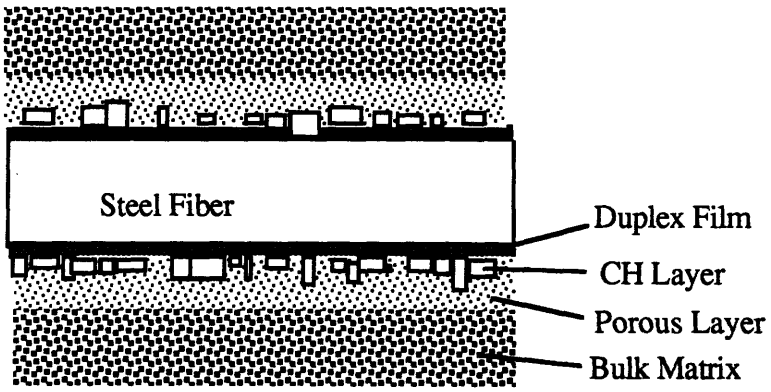

Figure 3.1 Microstructure of the steel fiber/cement interface

3.1.2 Polymeric Fiber/Concrete Interface

Polymeric fibers have high yield strength, but unlike steel fiber, they have lower elastic moduli and transverse strengths than cementitious materials. Therefore, the interfacial damage mechanism of polymeric fiber/mortar is different from that of steel fiber/mortar. Several researchers [3.6, 3.14-3.18] have studied polymeric FRC's.

Polypropylene fiber was the first synthetic polymer fiber applied to concrete in the forms of monofilament or fibrillated film. Baggott and Gandhi [3.16] studied continuous monofilament polypropylene fiber (340 μm) reinforced cement beam under tensile load. They observed defects of up to 10 μm in size on the polypropylene fiber interface. One typical damage observed was the chiseling out of a long shaving of fiber by matrix particles (Fig. 3.2).

The application and study of nylon FRC are not as extensive as polypropylene FRC although nylon fiber exhibits good toughness and durability. Wang, et al. [3.6] investigated the nylon/cement interface and observed peeling and fibrillation at the fiber surface (Fig. 3.3). They concluded that the increased interfacial friction during fiber pullout is due to the increase in surface abrasion.

In this chapter, the interfacial microstructures and the damage evolution of steel, nylon and polypropylene FRC's are investigated with scanning electron microscopy (SEM) and energy dispersive X-ray analysis (EDX). By comparing the interfacial microstructural evolution of the three types of FRC, different interfacial damage mechanisms are observed.

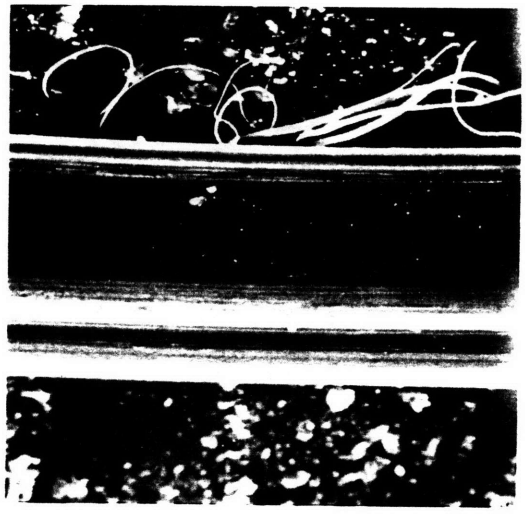

Figure 3.2 Shaving on Polypropylene Fiber (Diameter = 340 μm) [3.16]

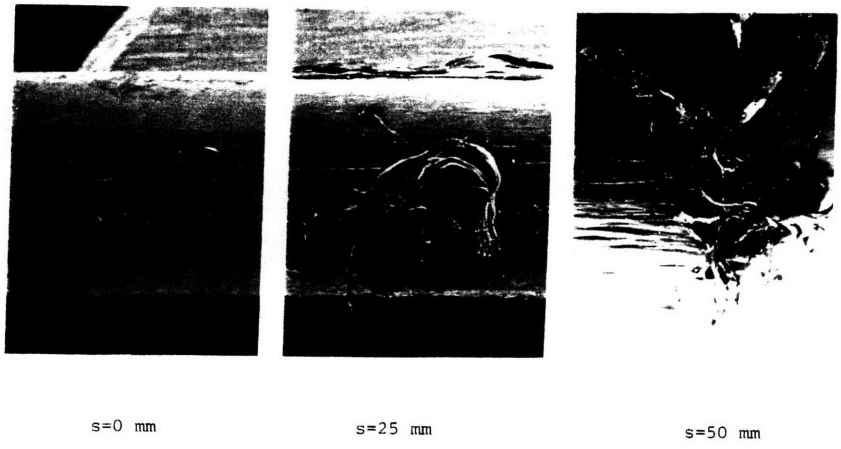

Figure 3.3 Peeling and Fibrillation on Nylon Fiber [3.6]
(Diameter = 500 μm, s = Sliding Distance)

3.2 EXPERIMENTAL PROCEDURE

3.2.1 Specimen Preparation

The specimen for the measurement of interfacial properties consists of a single fiber embedded in a rectangular block of mortar. The dimension of the specimen is shown in Fig. 3.4.

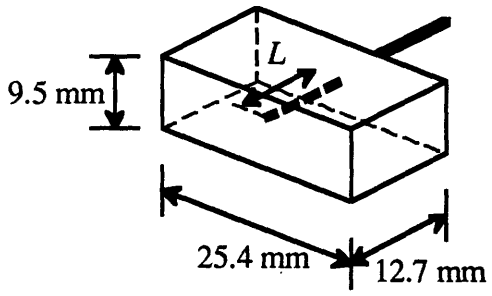

Figure 3.4 Single Fiber Pullout Specimen (Embedded Length L = 10 mm)

The fibers used include: (a) steel wire (low carbon and cold drawn steel, the straight part of the Dramix ZL30/.50, Bekaert Fiber Technologies), (b) nylon monofilament (nylon 66, Dupont Co.), and (c) polypropylene monofilament (relaxed low draw, Albany International Research Co.). The steel fiber is 0.5 mm in diameter. The nylon and polypropylene monofilaments (0.5 mm in diameter) are 2143 deniers and 1549 deniers, respectively. The Young's Moduli and tensile strengths of fibers are obtained from tensile tests (Fig. 3.5 and Tab. 3.1). The clean surfaces of the virgin fibers are shown in Fig. 3.6.

Table 3.1 Coefficients of Cement Mortar and Fibers

	Diameter (mm)	Young's Modulus (GPa)	Tensile Strength (MPa)	Other Strength (MPa)
Cement Mortar	---	22.3	3.6 (splitting)	40 (Compressive)
Steel Fiber	0.5	200	1242	1040 (yield)
Nylon Fiber	0.5 (equivalent)	6 [3.14-3.16]	451	---
Polypropylene Fiber	0.5 (equivalent)	4 [3.14,3.15]	391(10mm/min) 462(50mm/min)	---

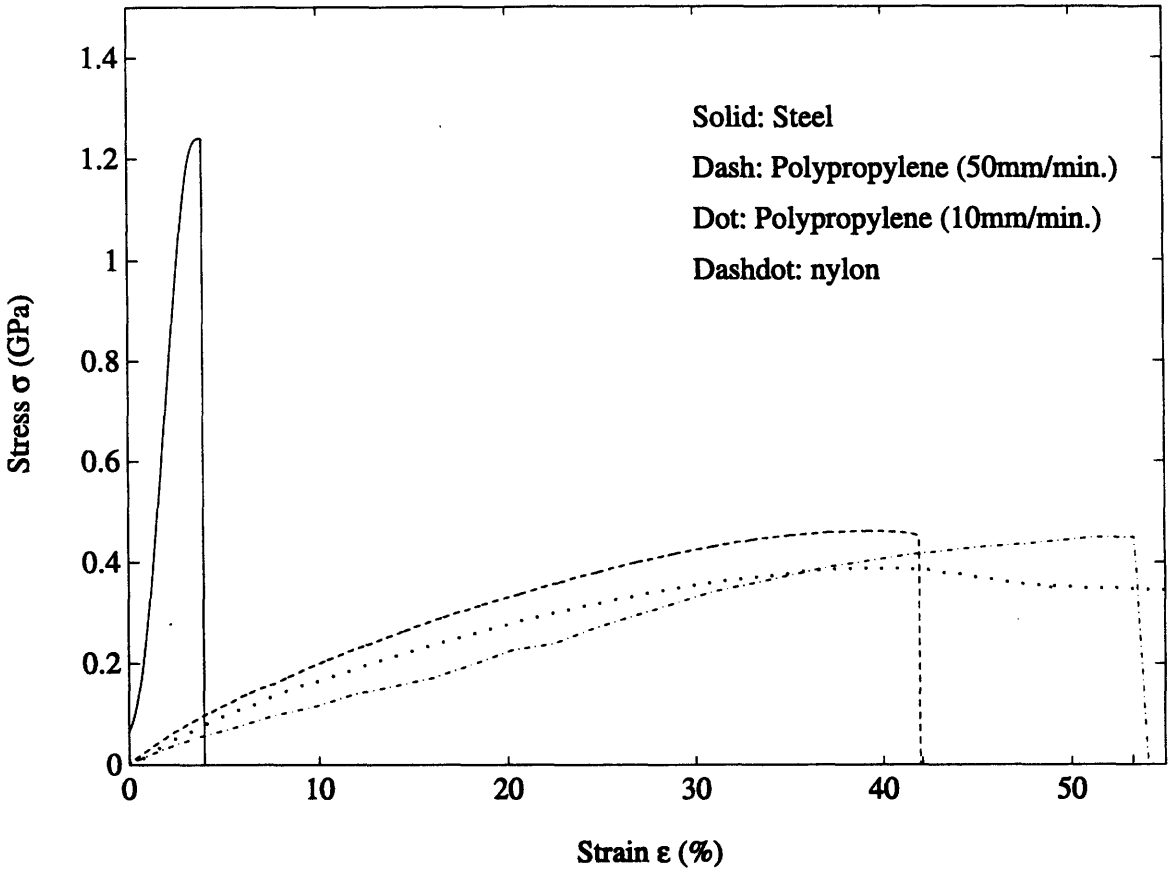

Figure 3.5 Fiber Tensile Curves

Specimens are cast in a brass mold shown in Fig. 3.7. To prepare pullout specimens for interfacial property measurements, one end of each fiber is first embedded into a Plexiglas block of the same size as the pullout specimen. The blocks are then put into the brass mold and mortar is cast to make the specimen.

It should be mentioned that demoulding oil is applied to all the interior surfaces of the mold as well as surfaces of the Plexiglas blocks that may come into contact with mortar. The purpose of this is to allow easy removal of mortar from the mold and the Plexiglas blocks. In applying the oil, extra care is taken to make sure that the fiber will stay clean from oil contamination. The embedded length of fiber in the mortar specimen (which is the same as the length of fiber protruded from the Plexiglas block) is controlled to be $L = 10$ mm.

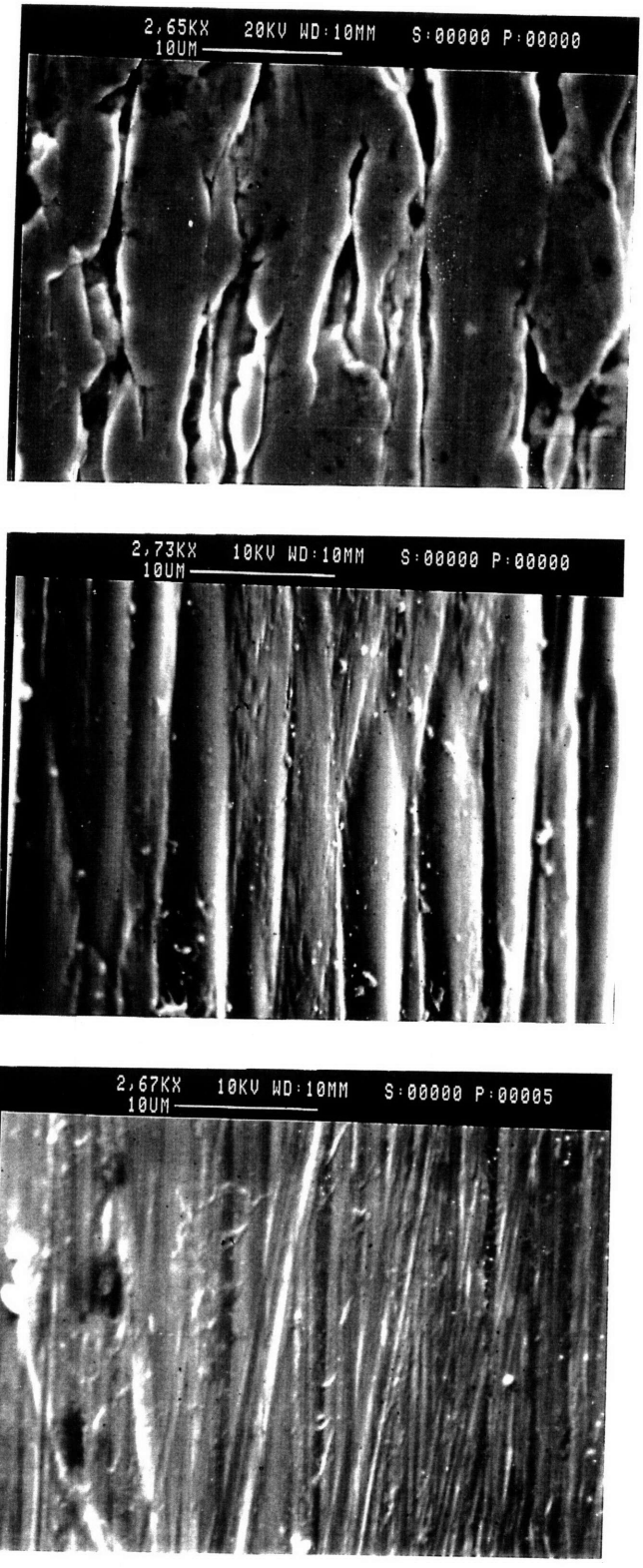

Figure 3.6 Clean Fiber Surfaces

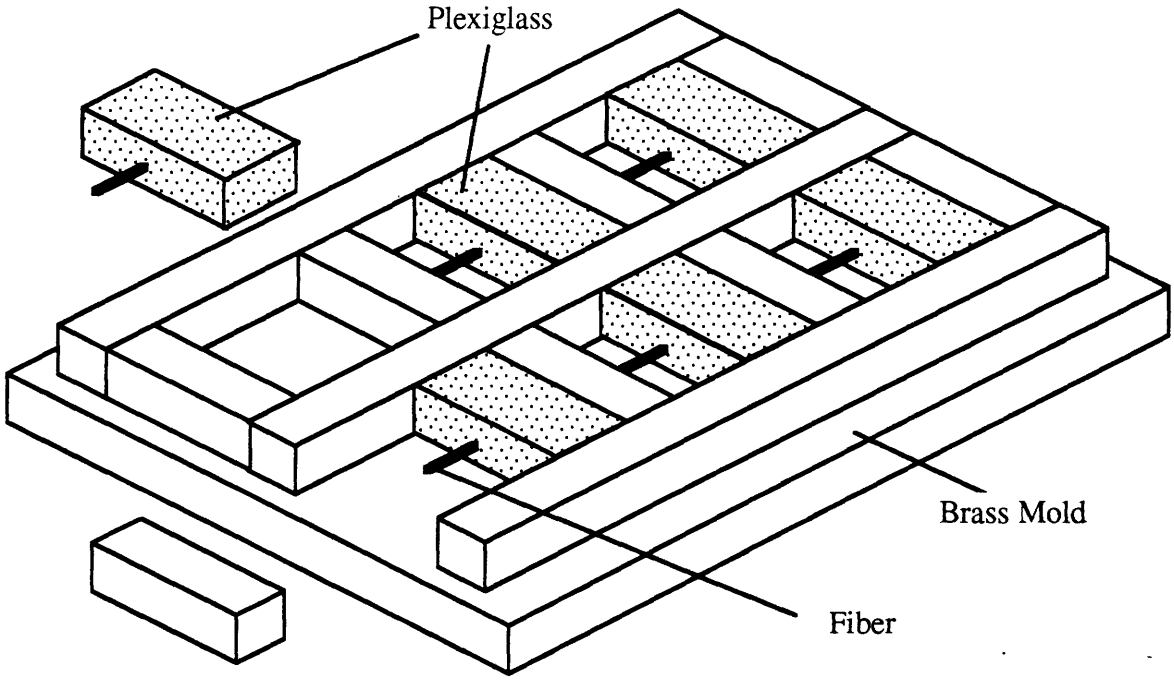

Figure 3.7 Brass Mold for Pullout Specimens

Mortar used in this investigation is made from type III Portland cement and mortar sand. A water/cement/sand ratio of 0.5:1:2 is employed. A sieve of grid size 2.362 mm is used to screen out larger aggregates in the sand. Cement and sand are dry-mixed for 3 minutes and then mixed with water for 6 minutes. Water is added with three equal quantity at 2-minute intervals. After casting, the mold is vibrated on a shaking table to remove pores in fresh mortar. The vibration takes roughly 9 minutes. The specimens are then kept moist at room temperature (about 25°C) for 24 hours before they are demouled and put into a water bath for further curing. Pullout tests are performed with saturated surface dry (SSD) specimens at the age of 7 days. The compressive and splitting tensile strengths of the mortar at 7 days, obtained from cylindrical specimens, are 42 MPa and 3.6 MPa respectively. Other material properties are listed in Table 3.1.

3.2.2 Experimental Setup

A 2-D loading device is designed to perform the fiber pullout test (Fig. 3.8). Loads can be applied in two orthogonal directions: the pullout direction (along the fiber) and the lateral direction (perpendicular to the fiber). The part of the pullout specimen with the embedded fiber is glued to an L-shape specimen holder while the pulled end of the fiber is held tightly by a grip. The holder and grip are connected to the load cells (Data Instruments) through

hardened steel rods. A linear variable differential transformer (LVDT, Lucas Schaevitz) is used to measure the fiber sliding history. The LVDT and its core are mounted on the L-shape specimen holder and the fiber grip, respectively.

Loading is applied by turning a nut against a reaction block on the end of each loading chain. In the pullout direction, the nut behind the reaction block is driven by a motor through gears and the loading is displacement-controlled to enable the measurement of

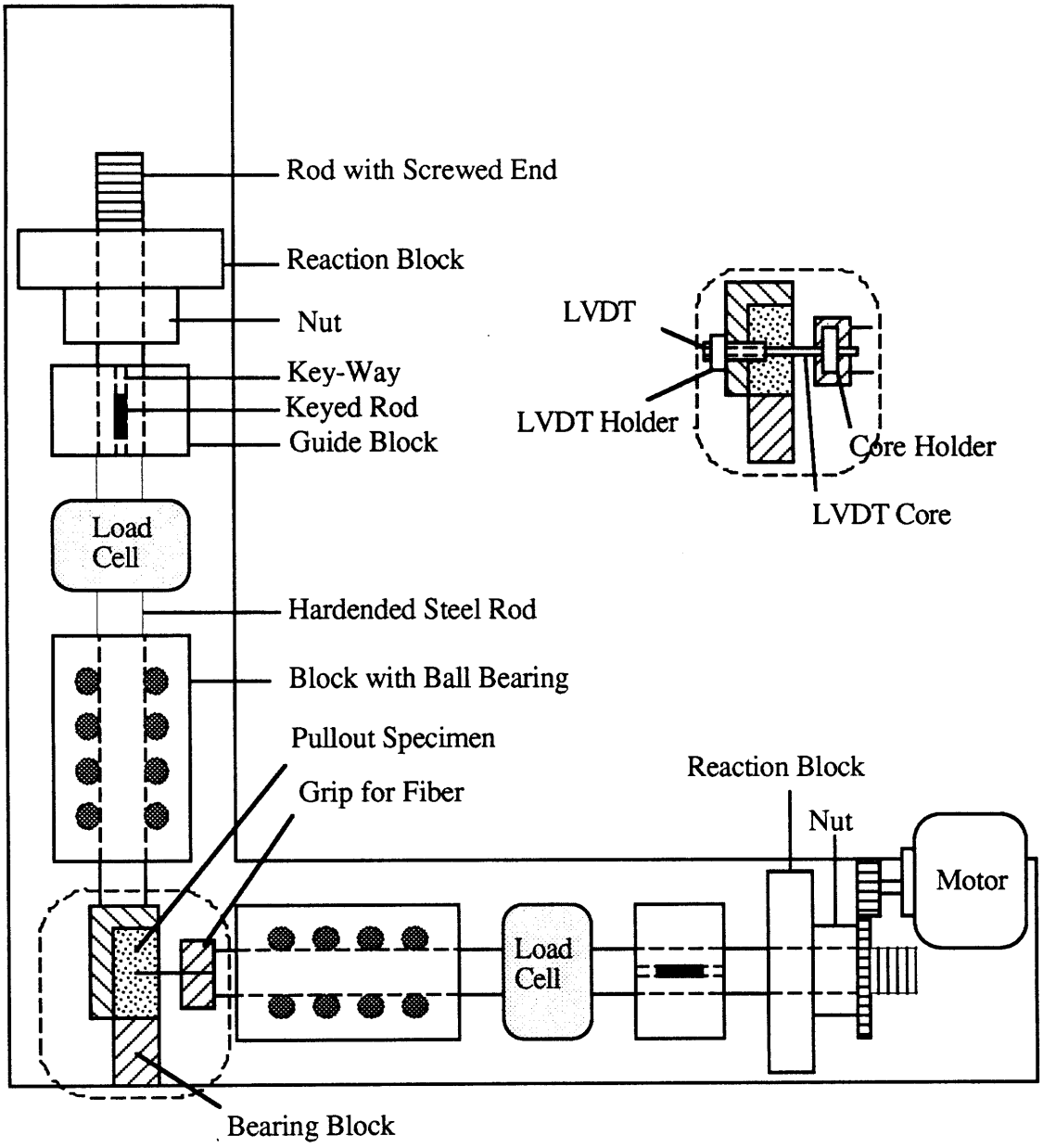

Figure 3.8a Plan View of the 2-D Fiber Pullout Device

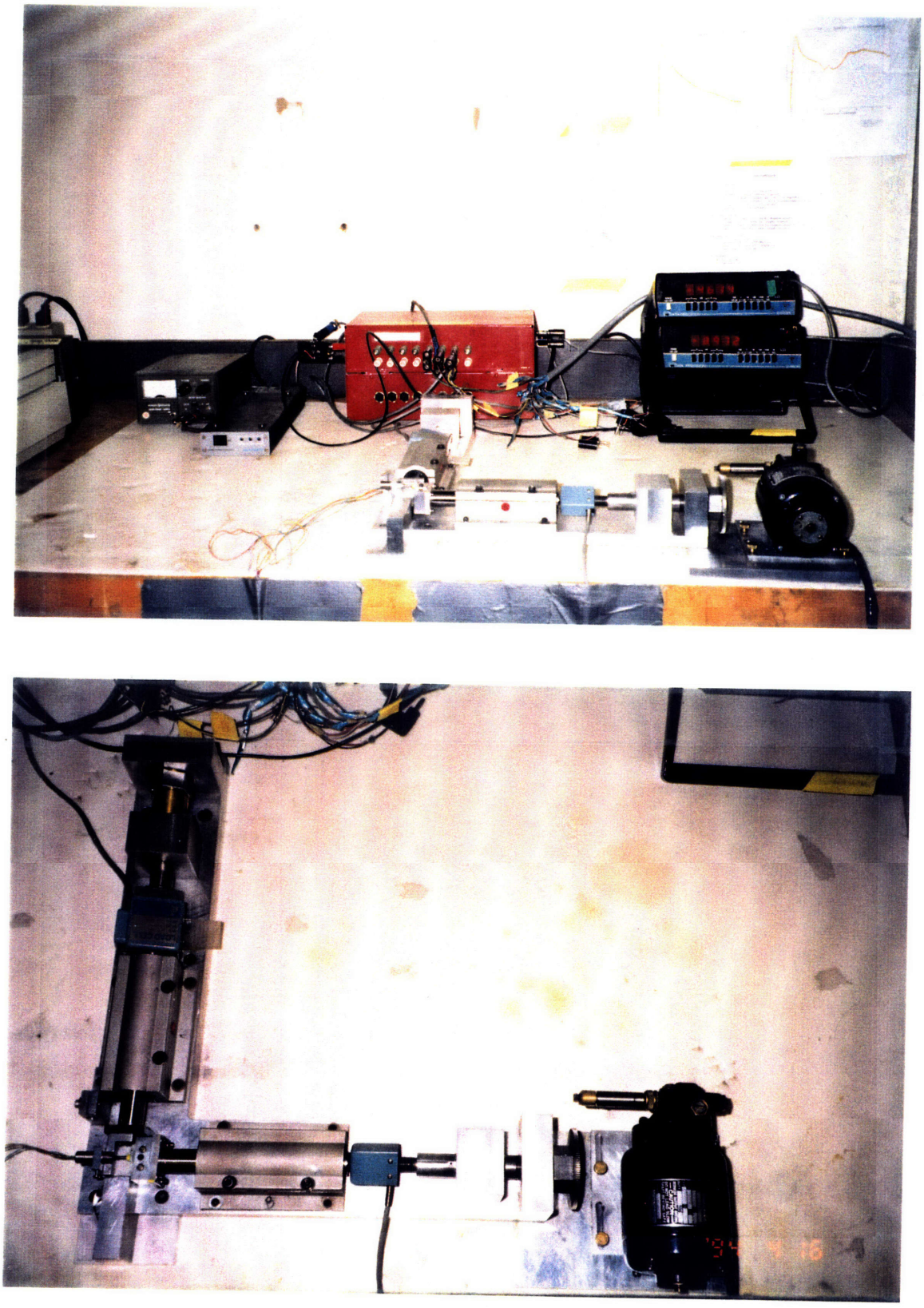

Figure 3.8b Experimental Setup of the 2-D Device

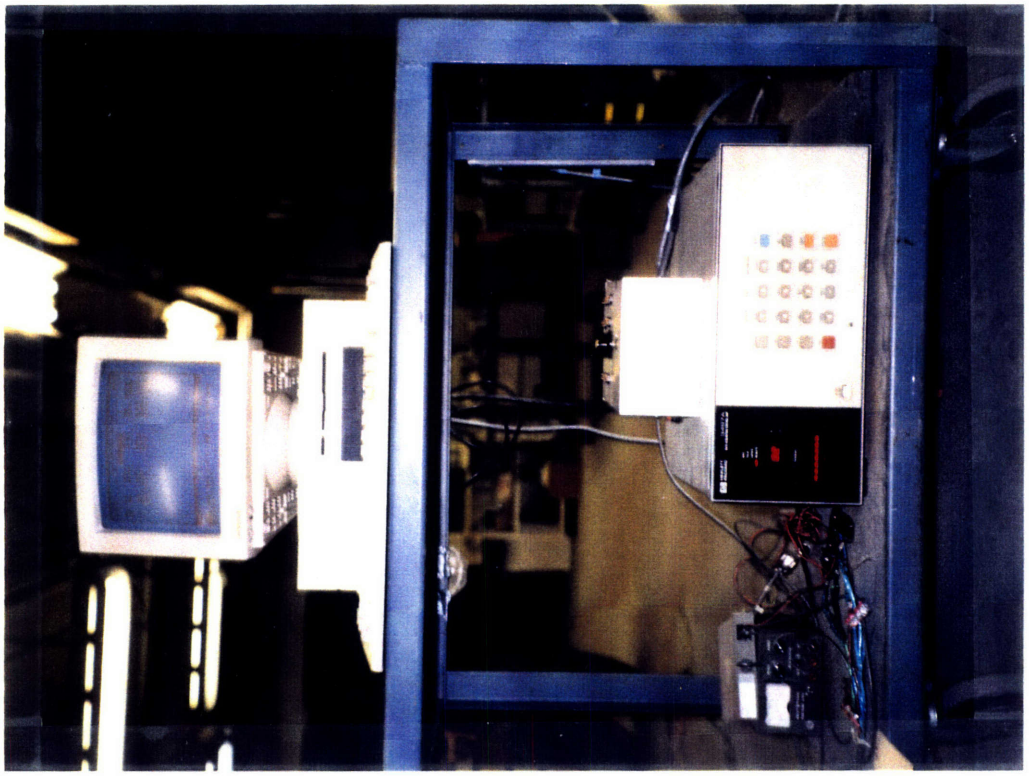

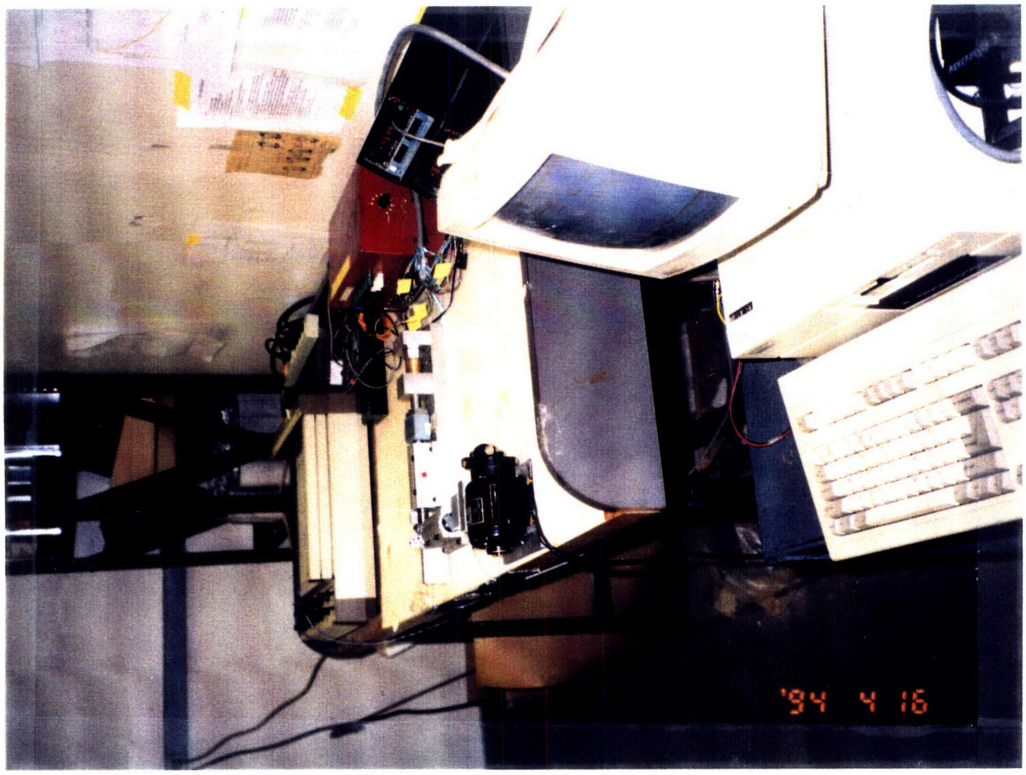

Figure 3.9 Data Acquisition System

post-peak softening behavior. The loading rate is 2.65 μm/sec (0.159 mm/min). The friction caused by the ball bearing is very small (less than 1.4 N) and is deducted from the measured pullout load. In the lateral direction, the nut in front of the reaction block is turned manually to the prescribed lateral compression.

During the experiment, output from both load cells as well as the LVDT are recorded in an IBM compatible computer through a HP data logger (Fig. 3.9). The output from the load cell in the fiber direction and the LVDT are also simultaneously plotted on a Gould X-Y plotter (Fig. 3.9).

3.2.3 Testing Procedure

Two sets of specimens are tested with zero lateral compression and a constant lateral compressive stress (σ_c = 20 MPa). At different stages of pullout (Fig. 3.10a), interfacial examinations are carried out: (a) before debonding (sliding distance s = 0), no pulling is required, (b) right after debonding (very small sliding distance), (c) pullout 1 mm (s = 1 mm), and (d)pullout 10 mm (s = 10 mm)

To examine the interface at a given stage, the test is stopped after reaching that particular stage. The tested specimen is then removed from the loading system and split by three point bending (Fig. 3.10b) to expose fiber/mortar interfaces. In order to identify the microstructural features of the fiber/mortar interfaces at each stage of pullout, the fiber and mortar groove surfaces are gold-coated for SEM analysis. SEM and EDX are carried out near the fiber embedded end and the mortar groove exit since these locations generally experience the most interfacial interactions (Fig. 3.10c).

3.3 EXPERIMENTAL RESULTS AND DISCUSSION

Figure 3.11 shows the typical pullout curves (fiber stress vs. displacement at the pulling end of the fiber) for steel, nylon and polypropylene fibers. Compared with the tensile strengths of the fibers (Table. 3.1), the peak loads are much lower. Therefore, fibers can be considered within their elastic ranges except that damage may occur at the fiber surface. The post-peak pullout behavior shows different trends for different fibers: (a) steel fiber pullout -- decreases rapidly, (b) nylon fiber pullout -- increases slowly, and (c) polypropylene fiber pullout -- decreases slowly. With lateral compression, the peak

pullout load increases. However, for the steel fiber, the post-peak load drop also becomes more rapid.

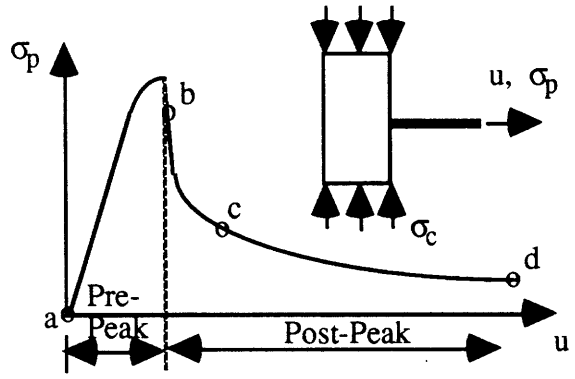

(a) Load to Certain Stage

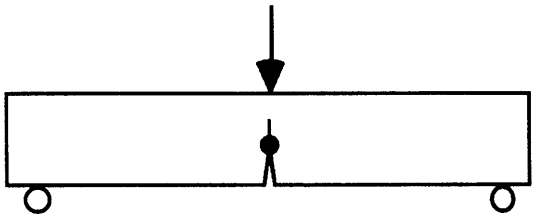

(b) Split the Specimen after Loading

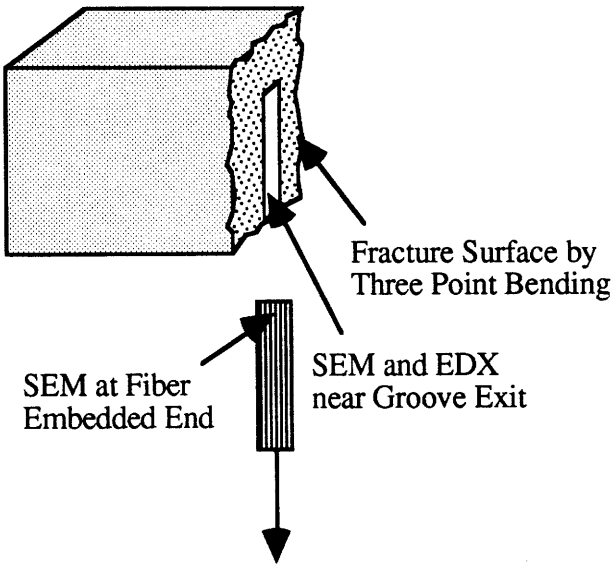

(c) Observe Area of Interest

Figure 3.10 Testing Procedure

3.3.1 Steel Fiber/Mortar Interface

Figure 3.12 shows the mortar surface when pullout is under zero lateral compression. Each micrograph in the figure corresponds to one of the four pullout stages.

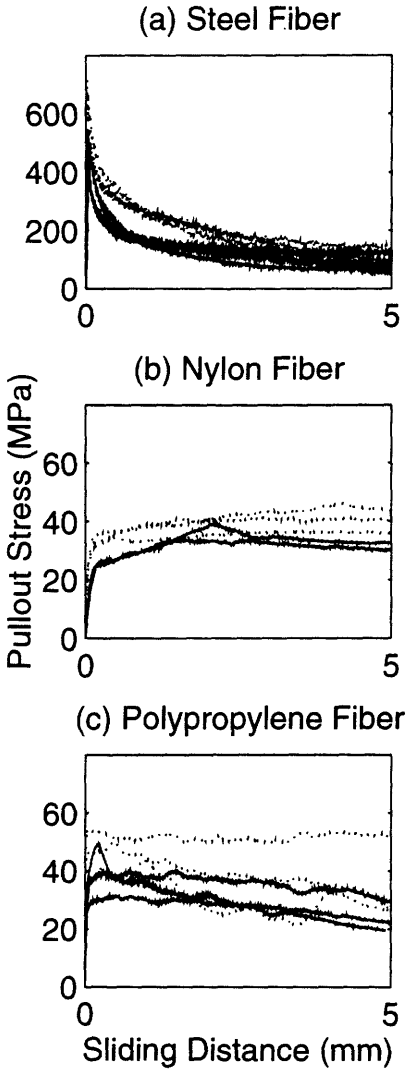

Figure 3.11 Typical Pullout Curves (Solid: $\sigma_c = 0$; Dotted: $\sigma_c = 20$ MPa)

At stage (a), the interface is separated by tensile debonding. Most of the mortar surface (Fig. 3.12a) follows the topology of the steel surface (Fig. 3.13a). On a very small portion of the surface, cement mortar pieces (CH crystals and C-S-H fibrous blocks) are spalled from the matrix and adhered to the steel surface , similar to the observation of Bentur, et al. [3.10] and Pinchin and Tabor [3.12]. The result indicates that interfacial fracture usually occurs along the steel/mortar interface, but occasionally occurs within the interfacial transition zone where the tensile strength of the mortar is less than the chemical bond at the interface.

At stage (b), shear debonding can also result in some failure inside the matrix, leading to the presence of mortar particles on the steel surface (Fig. 3.13b), although most of the debonded surface is on the steel fiber/mortar interface. A small amount of sliding grinds the spalled mortar pieces to small particles of up to 2 μm in size (Figs. 3.12b & 3.13b).

The irregular spalled mortar pieces are ground to much smaller particles under further pullout at stages (c) and (d) and becomes more regular in their shapes (Fig. 3.12c & d). The decrease of particle size is more rapid in the early sliding stage, which agrees well with the rapid initial decrease of the post-peak pullout curves. At the final stage (d), both the mortar surface and the steel surface (Figs. 3.12d & 3.14a) are smoothened. On the mortar surface, cracks are filled with very fine particles and only the scratch lines can be observed. The steel surface experiences plastic yielding during fiber pullout, similar to the observation of Banthia et al. [3.21].

The same observation is repeated for the case with lateral compression (Fig. 3.15). At stage (a), surface compaction due to compression can be observed in a small portion of the surface (white spots). By comparison of mortar surface at stages (b) and (c) for the cases with and without compression in Figs. 3.12 & 3.15, one can observe that the particle size decreases more rapidly when compression is applied. The lateral compression accelerates the abrasion process due to severe grinding. At stage (d), the steel surface exhibits scratch lines (Fig. 14b) which indicates more surface yielding.

In order to quantify the surface damage, energy dispersive X-ray analysis (EDX) is carried out. Since the mortar surface is relatively smooth and the analyzed area is roughly 0.06 mm^2, the EDX analysis can provide reasonable results. Figure 3.16 shows a typical X-ray spectrum. From the ratio of the area under the Ca and Si peaks on the X-ray spectrum, one can deduce the change in CH/C-S-H on the matrix surface during the fiber debonding/pullout process. The areas are calculated by first removing the effect of the

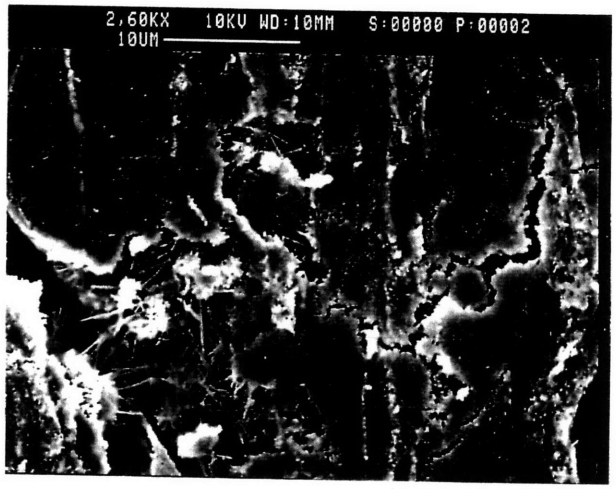

(a) Tensile Debonding

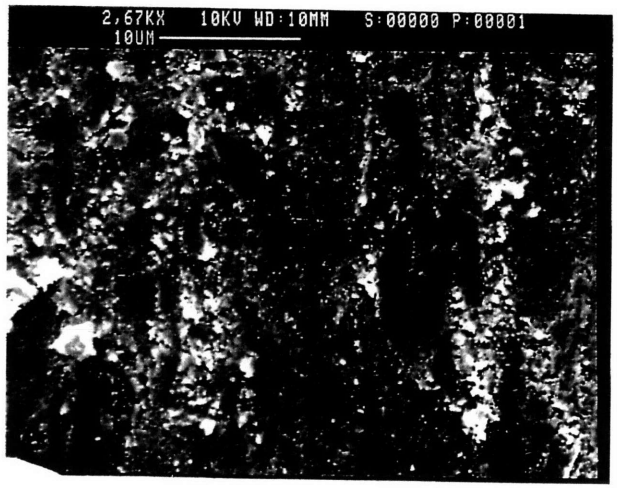

(b) Shear Debonding

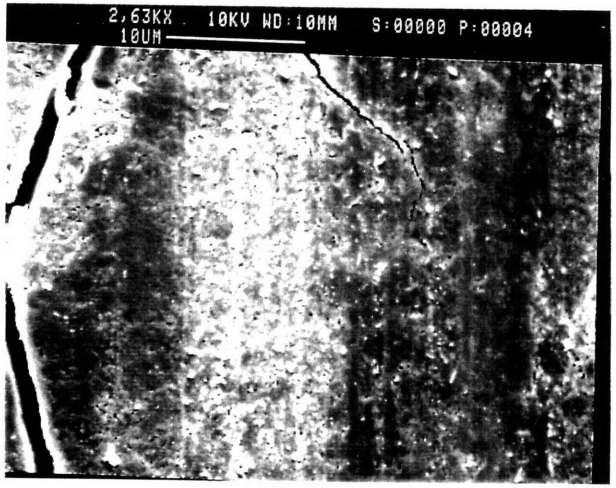

(c) Pullout 1 mm

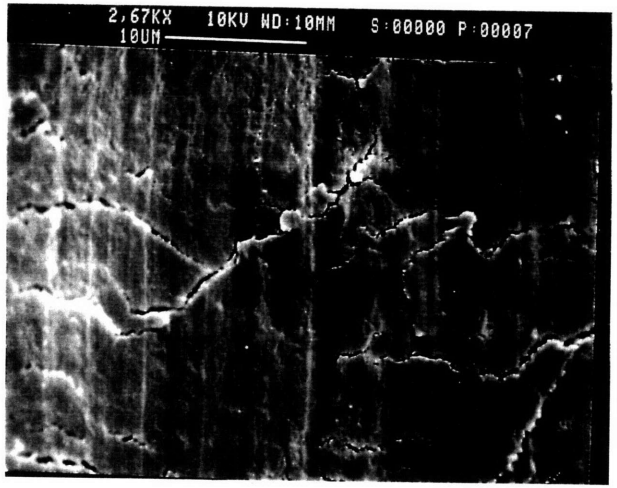

(d) Pullout 10 mm

Figure 3.12 Mortar Surface at Steel/Mortar Interface under no Compression ($\sigma_c = 0$)

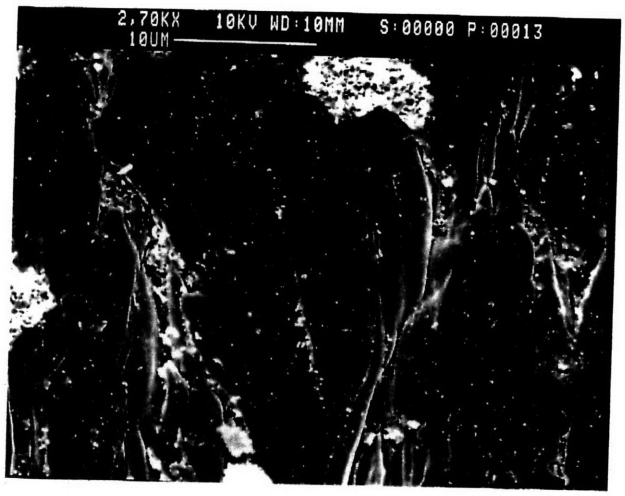

(a) Tensile Debonding

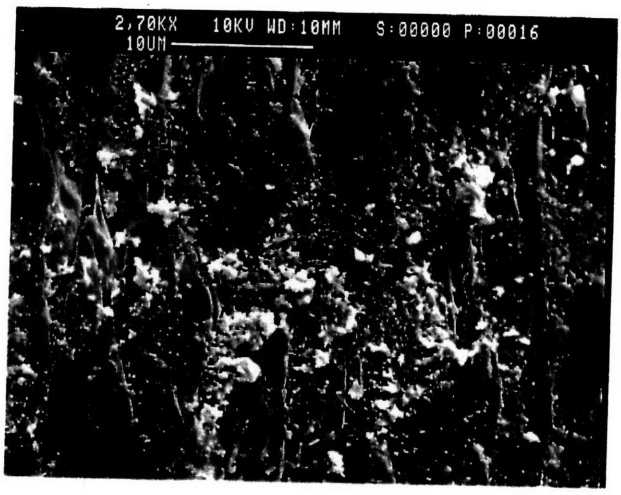

(b) Shear Debonding

Figure 3.13 Steel Surface at Steel/Mortar Interface at Stages (a) and (b) under no Compression ($\sigma_c = 0$)

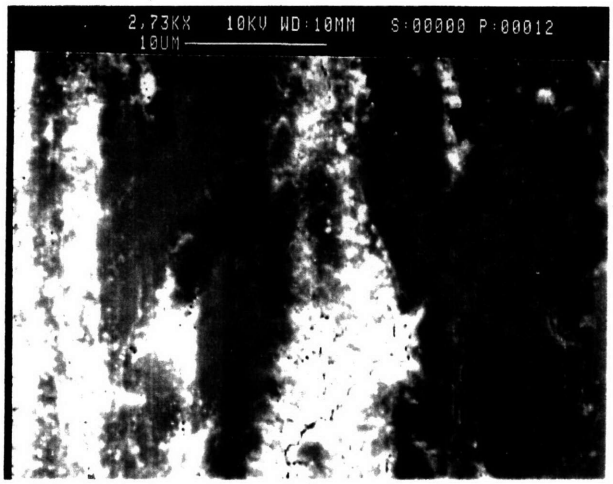

(a) $\sigma_c = 0$

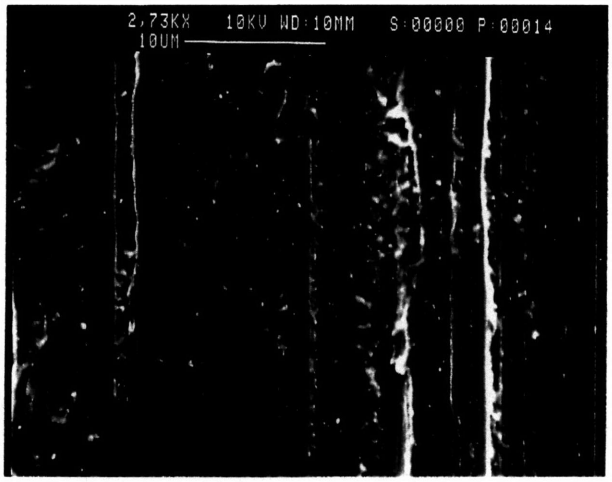

(b) $\sigma_c = 20$ MPa

Figure 3.14 Steel Surface at Steel/Mortar Interface at Stage (d)

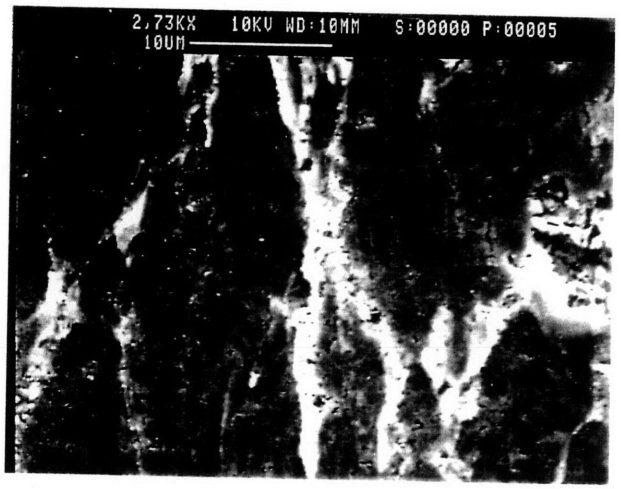

(a) Tensile Debonding

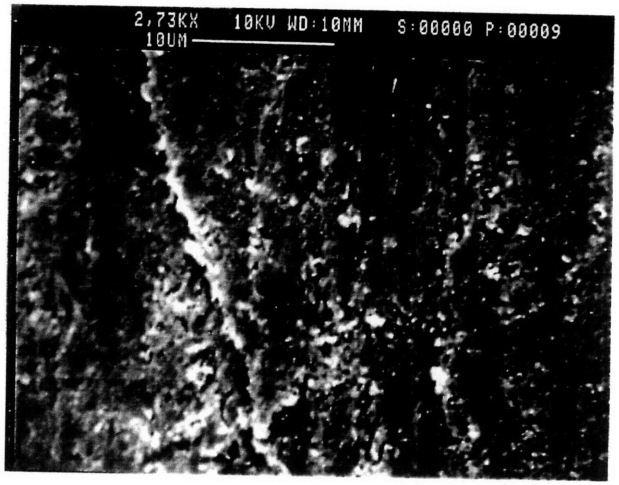

(b) Shear Debonding

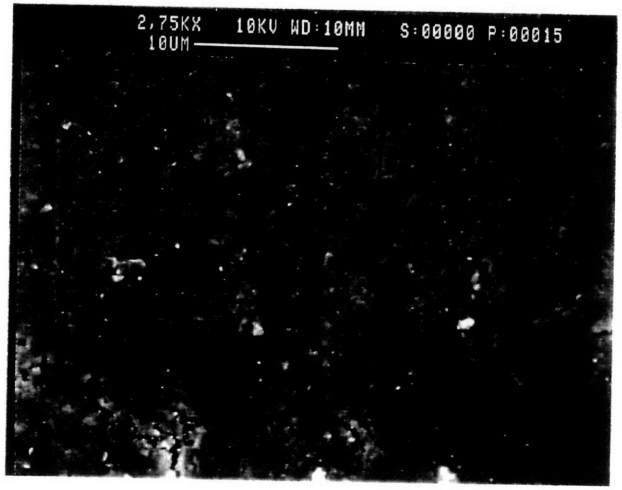

(c) Pullout 1 mm

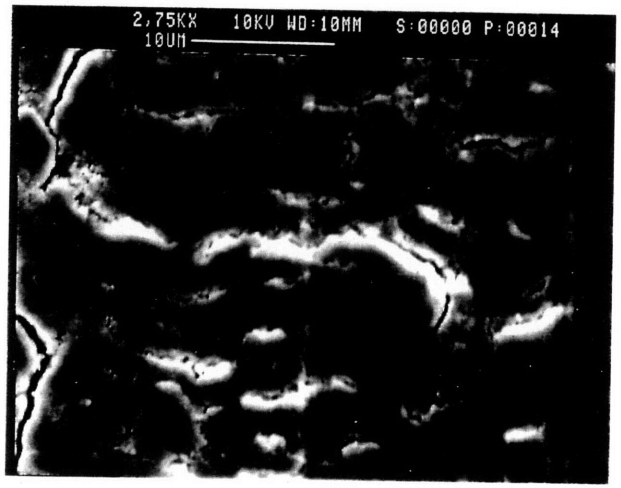

(d) Pullout 10 mm

Figure 3.15 Mortar Surface at Steel/Mortar Interface under Compression (σ_c = 20 MPa)

background and the neighboring peaks. Figure 3.17 shows the Ca/Si ratio at the four pullout stages for mortar surface. The Ca/Si ratio at the steel/mortar interface increases in the first three stages and decreases at the last stage. Based on the SEM observations in Figs. 3.12 & 3.15, there are two possible contributions to the increase and the decrease:

(1). Debonding occurs preferentially in the weak area at the interface or in the matrix, where the brittle CH phase is rich. In the early pullout stages, the brittle CH phase is crushed when it interacts with the steel surface and is smeared over the matrix surface, leading to an increase in the Ca/Si ratio.

(2). The decrease of the Ca/Si ratio can be attributed to abrasion. On further fiber sliding, the crushed CH phase is ground into much finer particles and partly swept into the pores and cracks on the mortar surface, hence exposing the underlying C-S-H phase. This process can reduce the calcium count and increase the silicon count.

One can see in Fig. 3.17 that debonding and an inevitable small amount of sliding at stage (b) increases the Ca/Si ratio. Further sliding to stage (c) leads to crushing and smearing of the CH phase, which increases the Ca/Si ratio. After very long sliding distance (stage (d)), sweeping and cleaning of the CH phase occurs, thus decreasing the Ca/Si ratio.

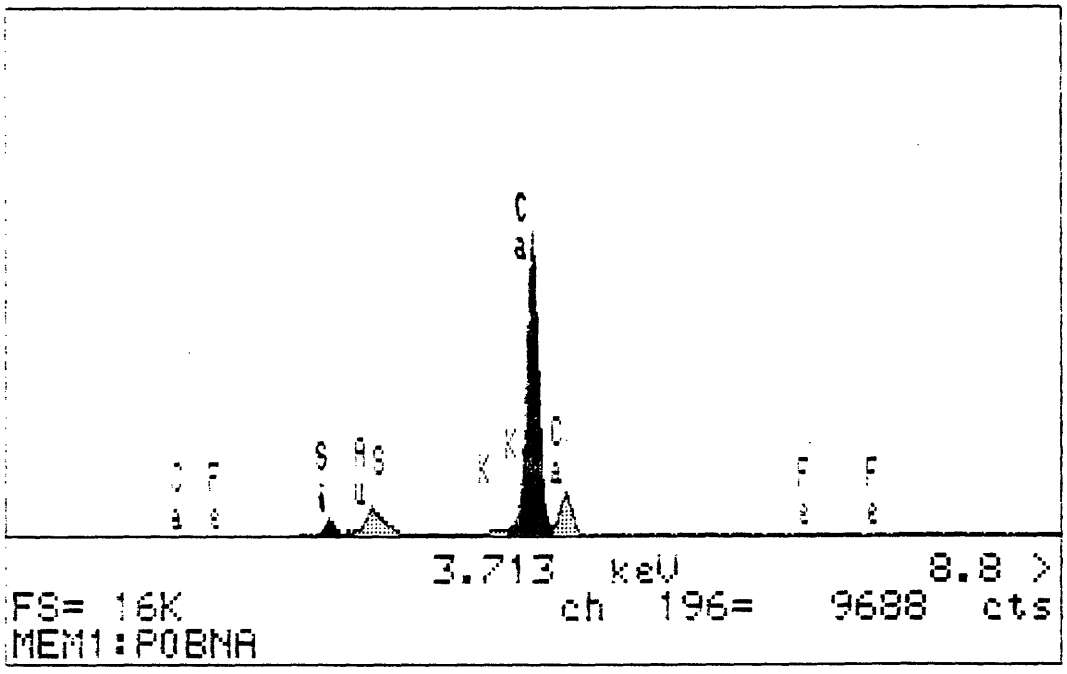

Figure 3.16. X-Ray Spectrum

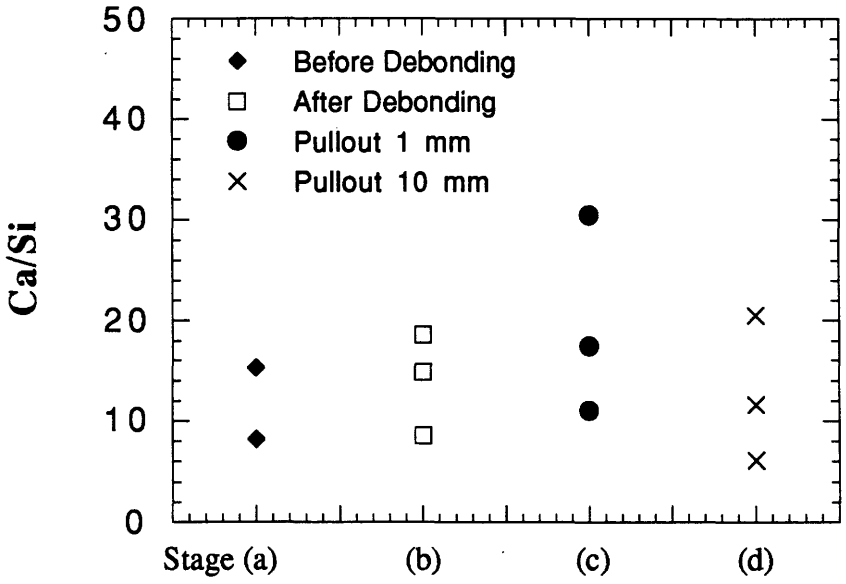

(a) $\sigma_c = 0$

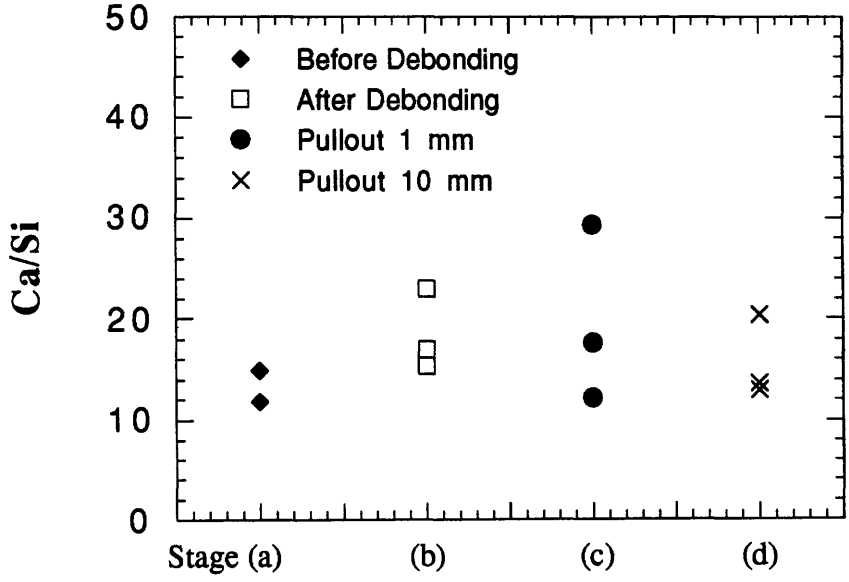

(b) $\sigma_c = 20$ MPa

Figure 3.17 Ca/Si Ratio at Mortar Surface of Steel/Mortar Interface

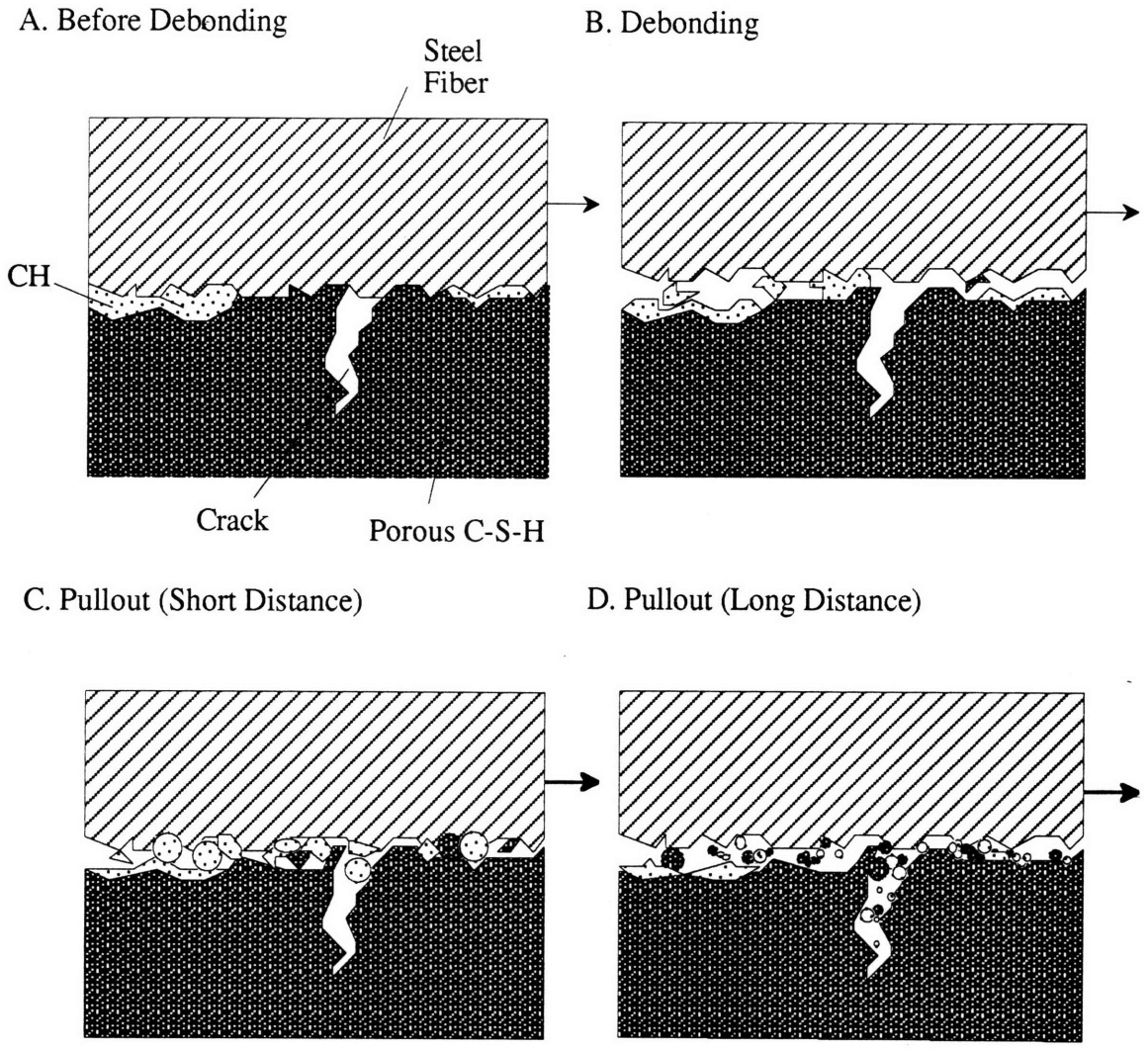

Figure 3.18 Damage Evolution at Steel Fiber/Mortar Interface

The results of EDX cannot be explained solely by the surface compaction mechanism proposed by Pinchin and Tabor [3.12]. In Fig. 3.17, the Ca/Si ratio remains the same for the cases both with and without compression at stage (a). Since the fiber is not pulled at stage (a) and no abrasion can take place, one can conclude that surface compaction will not alter the Ca/Si ratio. Nevertheless, the Ca/Si ratio during fiber sliding varies significantly for cases both with and without compression, which confirms that the surface microstructure (the compliance layer in the interfacial transition zone) changes significantly during fiber sliding. This microstructural evolution is caused by the surface grinding and abrasion.

Based on microscopic observation and EDX analysis, the pullout process can be characterized by a simple model in Fig. 3.18. Brittle CH crystal is first abraded followed

by abrasion of C-S-H gel. This process results in a change of Ca/Si ratio on the surface due to the grinding and sweeping of CH phase into pores and cracks.

3.3.2 Polymeric Fiber/Mortar Interface

Unlike the steel/mortar interface, the mortar surfaces at the nylon/mortar and polypropylene/mortar interfaces have little damage (Fig. 3.19), similar to the observation of Chan and Li [3.22]. The EDX analysis shows no trend of Ca/Si variation (Figs. 3.20 & 3.21), which indicate that the interfacial transition zone is intact. Similar to the observation in [3.6] and [3.16], the polymeric fiber surface experiences peeling, especially at the fiber embedded end or over a long sliding distance. The data scattering of the Ca/Si ratio for polypropylene fiber under compression at stage (d) (Fig. 3.21b) is consistent with randomness of the pullout curves at long sliding distance (Fig. 3.11).

During mixing of nylon FRC, cement particles can penetrate into the rough surface of the nylon fiber to form hydrogen bond. The hardened mortar can either tear away some of the nylon surface or spall from the matrix and adhere to the fiber. The low asperity polypropylene fiber has less peeling because of the weaker van der Waals bonds at the interface. After total debonding, the stiffer mortar surface causes surface peeling in both nylon fiber (Fig. 3.22a) and polypropylene fiber (Fig. 3.23a). For both nylon and polypropylene fiber FRC's, friction plays a dominant role in the interfacial resistance.

Since nylon fiber is hydrophilic, water may penetrate into the nylon surface and causes fiber swelling. The increase of the fiber radius due to peeling and swelling causes a significantly higher interfacial compression and increases the post-debonding load over sliding distance. On the other hand, the polypropylene fiber is hydrophobic. The surface is plowed with long whiskers and the long scratch lines. The scratch lines (Fig. 3.23a) are similar to those on steel fiber surface caused by surface hardening. The lower surface asperity of the polypropylene fiber results in the post-debonding decrease and randomness of pullout load.

When the fiber is pulled under compression over a long distance (10 mm), severe peeling and shaving are observed on the nylon fiber surface (Fig. 3.22b) and black holes are observed on the polypropylene surface (Fig. 3.23b). These black holes are similar to those observed on a thin polymer film failed in tension. The polypropylene fiber surface is subjected to shear load by the mortar matrix (surface stretch microscopically) during pullout. Under the low pulling rate and the long pullout distance, the fiber surface undergoes significant molecular alignment and creeping which results in a pseudo

volumetric increase. In order to maintain a constant volume, small holes are generated by the Poisson's effect, i.e., the surface ligaments get thinner and break into small holes.

3.4 CONCLUSIONS

The microstructural features of the steel, nylon and polypropylene fiber/mortar interfaces during fiber debonding and pullout are studied. Mortar abrasion is found to be a major mechanism accounting for damage at the steel fiber/mortar interfacial zone. The damage at the nylon and polypropylene fiber/mortar interfaces is mainly due to fiber surface peeling while the mortar surface experiences very little damage. By applying lateral compression to the mortar during fiber pullout, the abrasion effect becomes more severe for steel fibers. In both nylon and polypropylene, peeling becomes more significant and black holes can occur on the polypropylene surface.

To increase interfacial friction (and hence increase toughness and ductility), additives is a feasible mean to reduce or eliminate the weak interfacial transition zone for the steel FRC, while surface roughening is a feasible mean to increase interfacial interaction for polymer FRC.

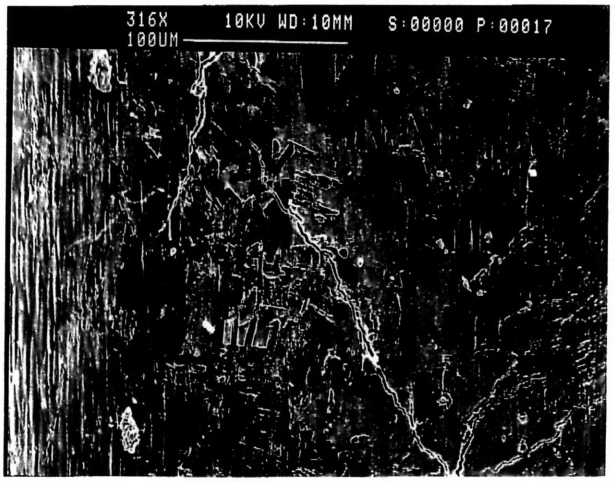

Figure 3.19 Mortar Surface at Nylon Fiber/Mortar Interface
(σ_c = 20 MPa, Pullout 1 mm)

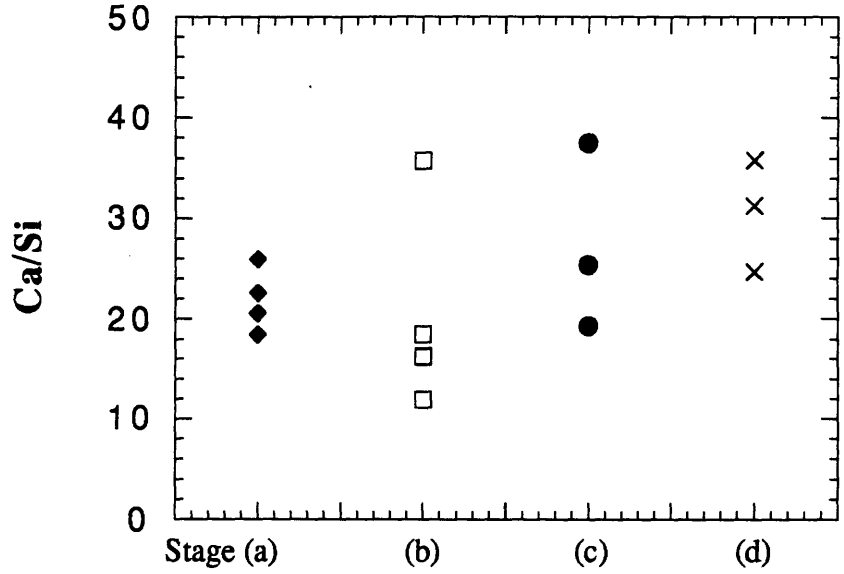

(a) $\sigma_c = 0$

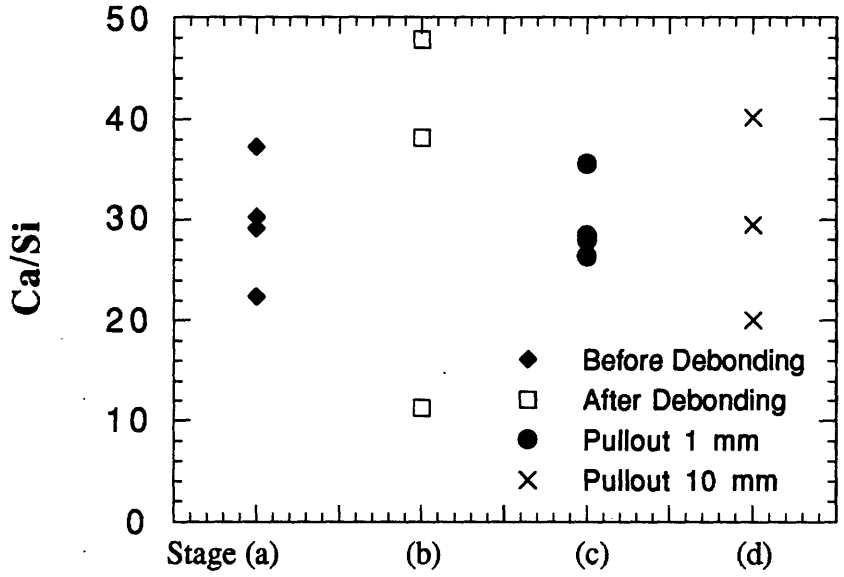

(b) $\sigma_c = 20$ MPa

Figure 3.20 Ca/Si Ratio at Mortar Surface of Nylon/Mortar Interface

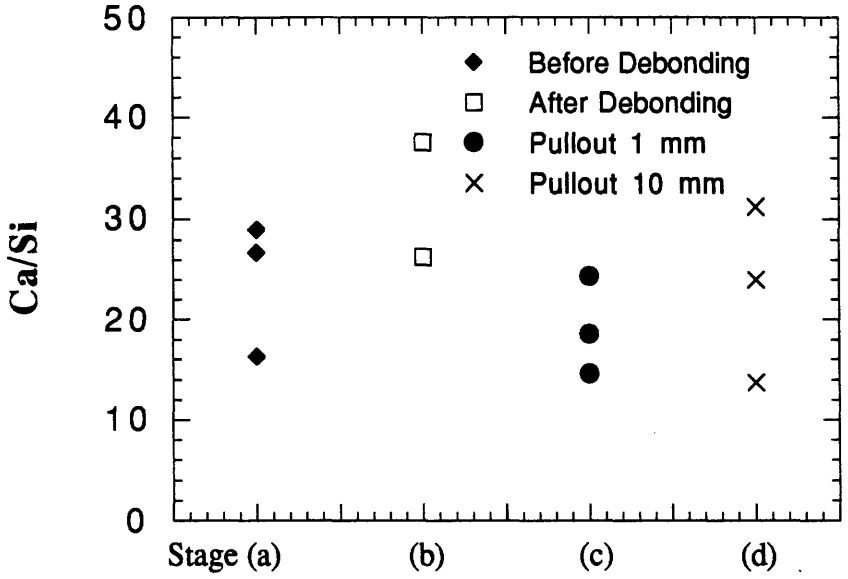

(a) $\sigma_c = 0$

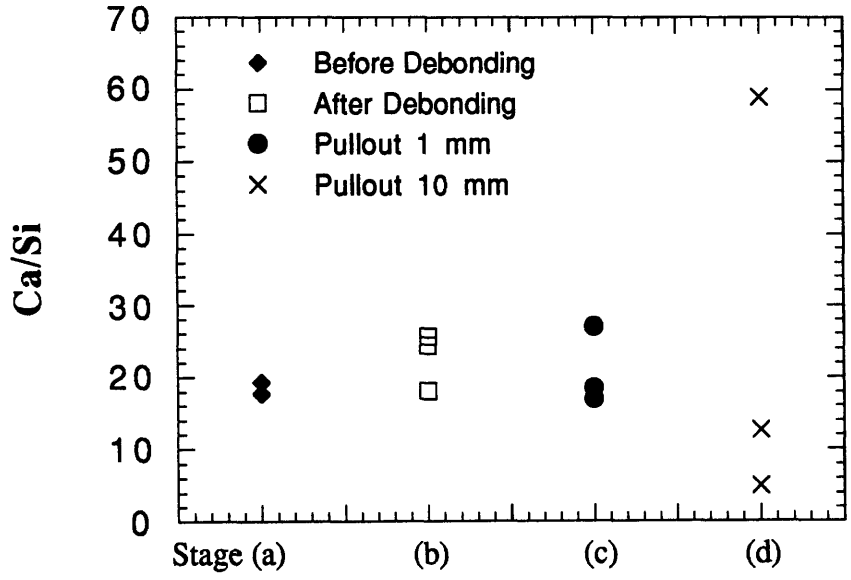

(b) $\sigma_c = 20$ MPa

Figure 3.21 Ca/Si Ratio at Mortar Surface of Polypropylene/Mortar Interface

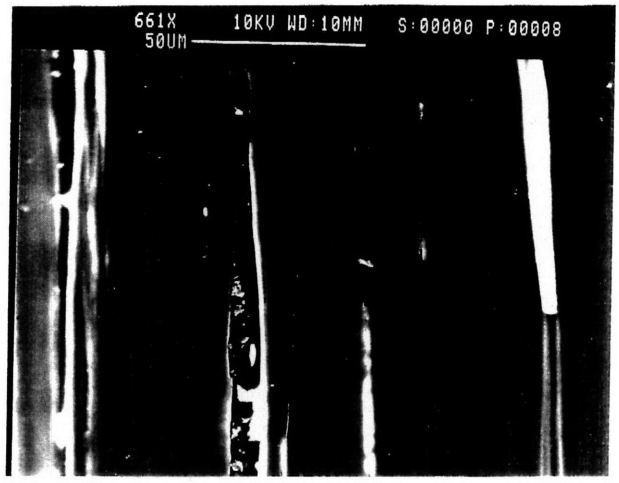

(a) $\sigma_c = 0$

(b) σ_c = 20 MPa

Figure 3.22 Nylon Surface (Pullout 10 mm)

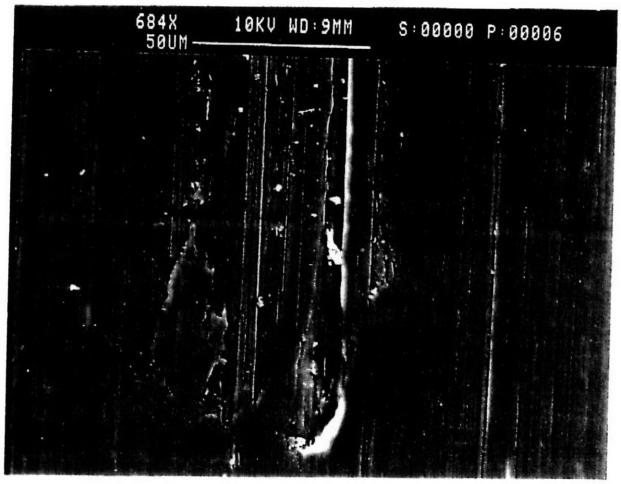

(a) $\sigma_c = 0$

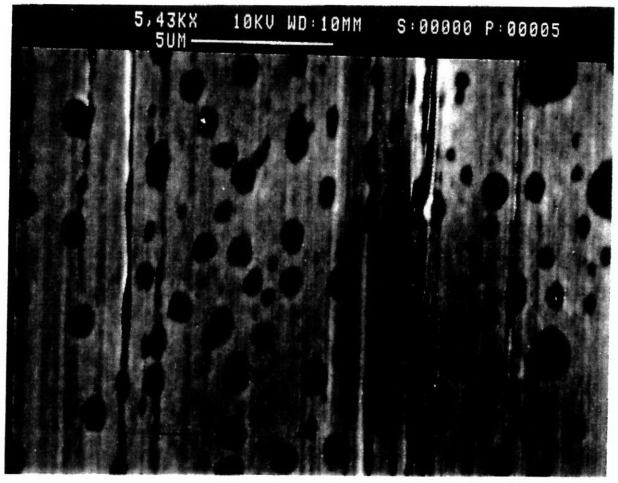

(b) $\sigma_c = 20$ MPa

Figure 3.23 Polypropylene Surface (pullout 10 mm)

REFERENCES

3.1 Shah, S.P., and C. Ouyang, "Mechanical Behavior of Fiber-Reinforced Cement-Based Composites." J. Am. Ceram. Soc., Vol. 74, No. 11, pp. 2927-2938 (1991)

3.2 Bentur, A., and S. Mindess, *Fiber Reinforced Cementitious Composites*. Elsevier, New York (1990)

3.3 Li, V.C., and C.K.Y. Leung, "Theory of Steady State and Multiple Cracking of Random Discontinuous Fiber Reinforced Brittle Matrix Composites." ASCE J. Eng. Mech., Vol. 118, No. 11, pp. 2246-2264 (1992)

3.4 Naaman, A.E., and S.P. Shah, "Pull-out Mechanism in Steel Fiber-Reinforced Concrete." ASCE J. of Structural Division, Vol. 102, pp. 1537-1548 (1976)

3.5 Leung, C.K.Y., and Y. Geng, "Effect of Lateral Stress on the Debonding and Pull-out of Steel Fiber in a Cementitious Matrix." *ACI Special Publication on Interfaces in Cementitious Materials*, edited by O. Buyukozturk and M. Wecheratana (1994)

3.6 Wang, Y., V.C. Li, and S. Backer, "Analysis of Synthetic Fiber Pull-out from a Cement Matrix." *Bonding in Cementitious Composites*, edited by S. Mindess and S.P. Shah, Materials Research Society Symposium Proceedings, Pittsburgh, PA, Vol. 114, pp. 159-165 (1988)

3.7 S. Mindess, "Interfaces in Concrete." *Materials Science of Concrete I.* Edited by Jan P. Skalny, The American Ceramic Society, Inc., Westerville, OH (1989)

3.8 Pinchin, D.J., and D. Tabor, "Interfacial Phenomena in Steel Fiber Reinforced Cement I: Structure and Strength of Interfacial Region." Cement and Concrete Research, Vol. 8, pp. 15-24 (1978)

3.9 Al Khalaf, M.N., and C.L. Page, "Steel/Mortar Interfaces: Microstructural Features and Mode of Failure." Cement and Concrete Research, Vol. 9, pp. 197-208 (1979)

3.10 Bentur, A., S. Diamond, and S. Mindess, "The Microstructure of the Steel Fiber-Cement Interface." Journal of Material Science, Vol. 20, pp. 3610-3620 (1985)

3.11 Wei, S., J.A. Mandel, and S. Said, "Study of the Interface Strength in Steel Fiber-Reinforced Cement-Based Composites." ACI Journal, pp. 597-605 (1986)

3.12 Pinchin, D.J., and D. Tabor, "Inelastic Behaviour in Steel Wire Pull-out from Portland Cement Mortar." Journal of Materials Science, Vol. 13, pp. 1261-1266 (1978)

3.13 Soroka, I., and P.J. Sereda, "The Structure of Cement-Stone and the Use of Compacts as Structural Models." *Proceedings of the 5th International Symposium on the Chemistry of Cement*, Tokyo, Vol. 3, pp. 67-73 (1968)

3.14 Hannant, D.J., *Fiber Cements and Fiber Concretes.* John Wiley and Sons, New York (1978)

3.15 Dave, N.J., and D.G. Ellis, "Polypropylene Fiber Reinforced Cement." The International Journal of Cement Composites, Vol. 1, pp. 19-28 (1978)

3.16 Baggott, R., and D. Gandhi, "Multiple cracking in aligned polypropylene fiber reinforced cement composites." J. of Material Science, Vol. 16, pp. 65-74 (1981)

3.17 Rice, E.K., G.L. Vondran, and H.O. Kunbargi, "Bonding of Fibrillated Polypropylene Fibers to Cementitious Materials." *Bonding in Cementitious Composites*, edited by S. Mindess and S.P. Shah, Materials Research Society Symposium Proceedings, Pittsburgh, PA, Vol. 114, pp. 145-152 (1988)

3.18 Peled, A., H. Guttman, and A. Bentur, "Treatments of Polypropylene Fibers to Optimize their Reinforcing Efficiency in Cement Composites." Cement and Concrete Composites, Vol. 14, pp. 277-285 (1992)

3.19 Balaguru, P.N., and S.P. Shah, *Fiber Reinforced Cement Composites.* McGraw-Hill, Inc., New York, pp. 108-109 (1992)

3.20 Moncrieff, R.W., *Man Made Fibers.* 6th Edition, John Wiley & Sons, New York, p. 653 (1975)

3.21 Banthia, N., J.-F. Trottier, M. Pigeon, and M.R. Krishnadev, "Deformed Steel Fiber Pullout: Material Characteristics and Metallurgical Process." *High Performance Fiber Reinforced Cement Composites*, edited by H.W. Reinhardt and A.E. Naaman, E&FN Spon, London (1992)

3.22 Chan, Y-W, and V.C. Li, "Effect of Plasma Treatment on Fiber/Cement Interface Properties." *Proc. of 1st International Conference on Composite Engineering*, pp. 293-294 (1994)

Chapter 4. Effect of Lateral Stress on Interfacial Parameters

SYNOPSIS

The experimental setup developed in Chapter 3 is used to study the effect of lateral stresses on fiber debonding and pullout.

Steel fiber reinforced mortar specimens were tested in detail. With lateral compression, both the initial interfacial friction and the effective interfacial shear strength are found to increase. A higher lateral compression, however, also results in a more rapid decrease in the interfacial friction during fiber pullout. Therefore, while lateral compression can significantly increase the peak pullout load, the energy absorption capability (denoted by the area under the pullout curve) does not increase to the same degree. Qualitatively, lateral tension imposes opposite effects to lateral compression. Quantitatively, a small lateral tension can result in changes in interfacial properties comparable in magnitude to those caused by a much higher lateral compression. Therefore, although the lateral tension that can act on a fiber is limited by the low tensile strength of the matrix, it may still impose a noticeable effect on the fiber debonding/pullout behavior.

Polypropylene and nylon fibers are also tested. It is found that the energy absorption of polymer fiber pullout is about 2/3 that of steel fiber, although the peak load of polymer fiber is about an order lower (1/10) than that of steel fiber.

4.1 LATERAL COMPRESSION AND LATERAL TENSION

Fiber debonding and pullout is usually studied with the fiber pullout test, in which one or more fibers embedded in the matrix is pulled and the load vs. displacement curve is recorded. Almost all the reported pullout tests in the literature are carried out under zero far-field lateral stress (Note: far-field here refers to stresses not induced by local effects such as shrinkage of matrix around the fiber). However, when failure involves shear cracks or splitting cracks, significant lateral compression are acting on the crack bridging fibers (Fig. 4.1a and 4.1b). Also, at the bottom of slabs under biaxial bending, crack

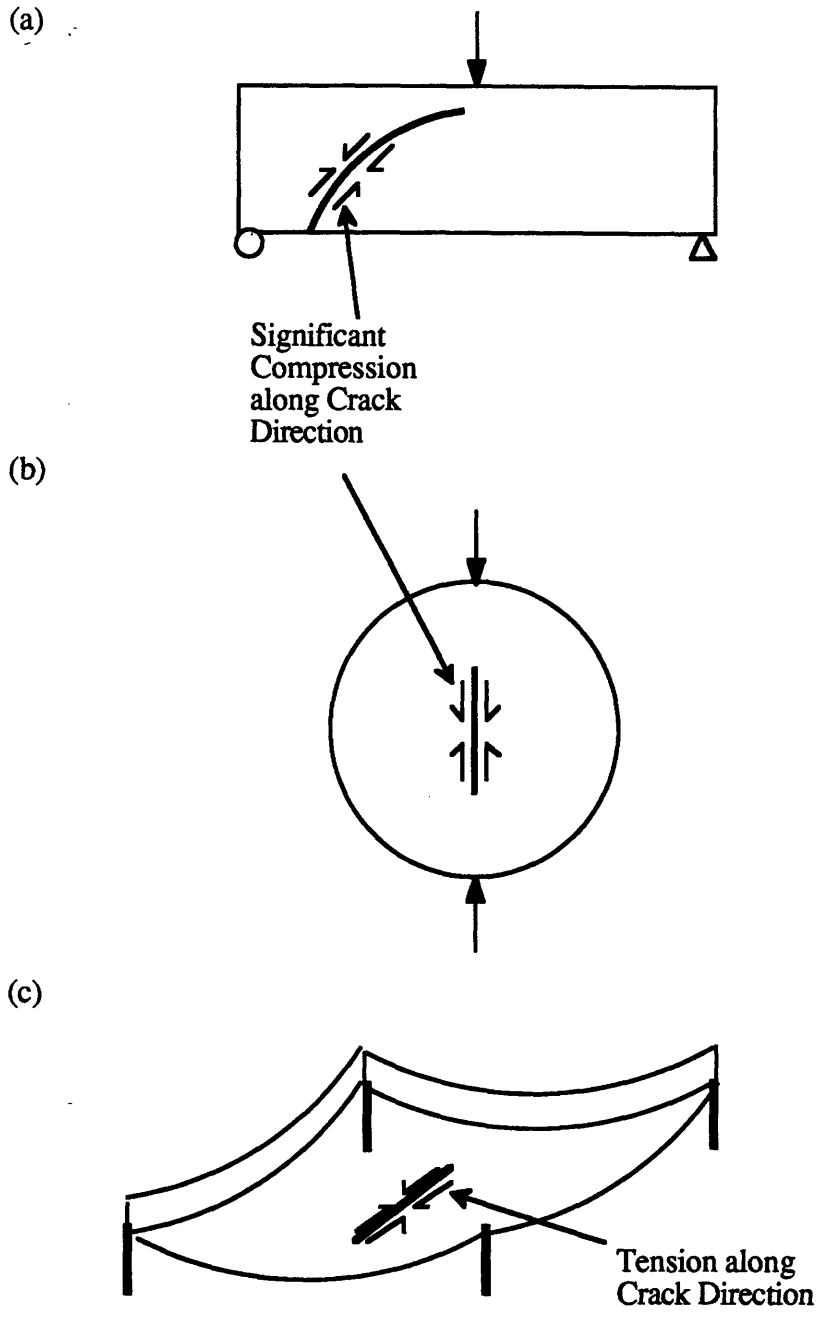

Figure 4.1 Crack Propagation Involving Lateral Stresses Parallel to Crack

bridging fibers can be under significant tension (Fig. 4.1c). The effect of lateral stresses on fiber debonding and pullout should therefore be studied.

A significant increase in interfacial friction with uniform radial stress has been reported by Tabor and Pinchin [4.1]. Effects of lateral tension, however, has never been studied. Also, in most practical situations, such as those shown in Fig. 4.1, significant lateral

compression is only present along one direction perpendicular to the fiber. The major objective of this chapter is to investigate the effect of lateral compression (along one direction) on the debonding and pullout behavior of fibers in a mortar matrix. Experimental results show that both the interfacial friction and effective interfacial strength can vary significantly with lateral stresses. Therefore, to properly model fiber debonding and pullout in composites under general loading conditions, the effects of lateral stresses need to be incorporated.

4.2 EXPERIMENTAL RESULTS AND DATA INTERPRETATION

The 2-D setup described in Section 3.2 is used to perform the pullout tests. The specimen preparation and the testing procedure have already been described in Chapter 3. Three sets of tests are performed: (a) steel fiber pullout under compression, (b) steel fiber pullout under tension, and (c) polymer fiber pullout under compression.

4.2.1 Steel Fiber under Compression

For steel fiber, two sets of specimens, with the embedded fiber lengths of 5 and 10 mm respectively are tested under lateral compression. The lateral compressive stresses applied are 0, 10, 20 and 30 MPa. It should be mentioned that the load in the lateral direction only varies by very small amounts during fiber pullout and can be considered constant for all purposes. The pullout curves under four lateral compressive stress levels are shown in Figs. 4.2a and 4.2b for embedded lengths of 5 mm and 10 mm respectively.

(1). Interfacial friction at the on set of debonding τ_i: After the fiber is completely debonded, post-peak fiber pullout curves can occur with or without the stick-slip effect, as shown in Fig. 4.3. It should be noted that the stick-slip behavior is not a material behavior but depends on loading system stiffness and loading rate. However, based on a simple spring-mass model for the stick-slip phenomenon [4.2], it can be shown that τ_i obtained from the midpoint represents the kinetic value. At the stick stage, stress increases slowly (upward solid lines) and the friction is static. At the slip stage, stress decreases suddenly (downward dash dot) and the friction is kinetic. For a case without stick-slip, the interfacial friction τ_i is simply obtained from the fiber stress level right after the unstable post-peak load drop. For a case with stick-slip, τ_i is obtained from the stress level corresponding to the midpoint of the first stick curve (Fig. 4.3). The initial interfacial friction for each test are calculated as described above, and shown in Fig. 4.4a.

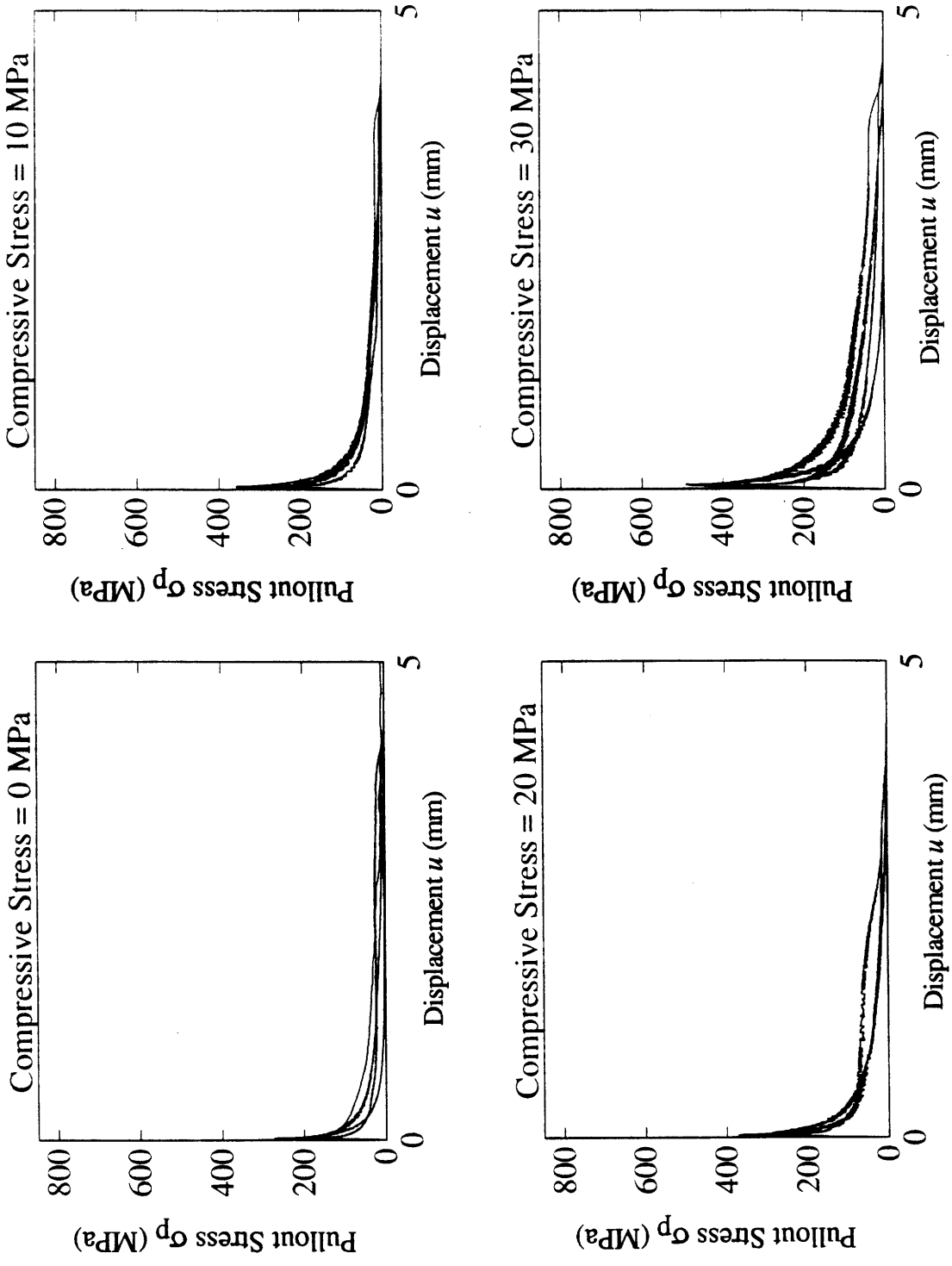

Figure 4.2a Experimental Pullout Curves for an Embedded Length of 5 mm (Steel Fiber)

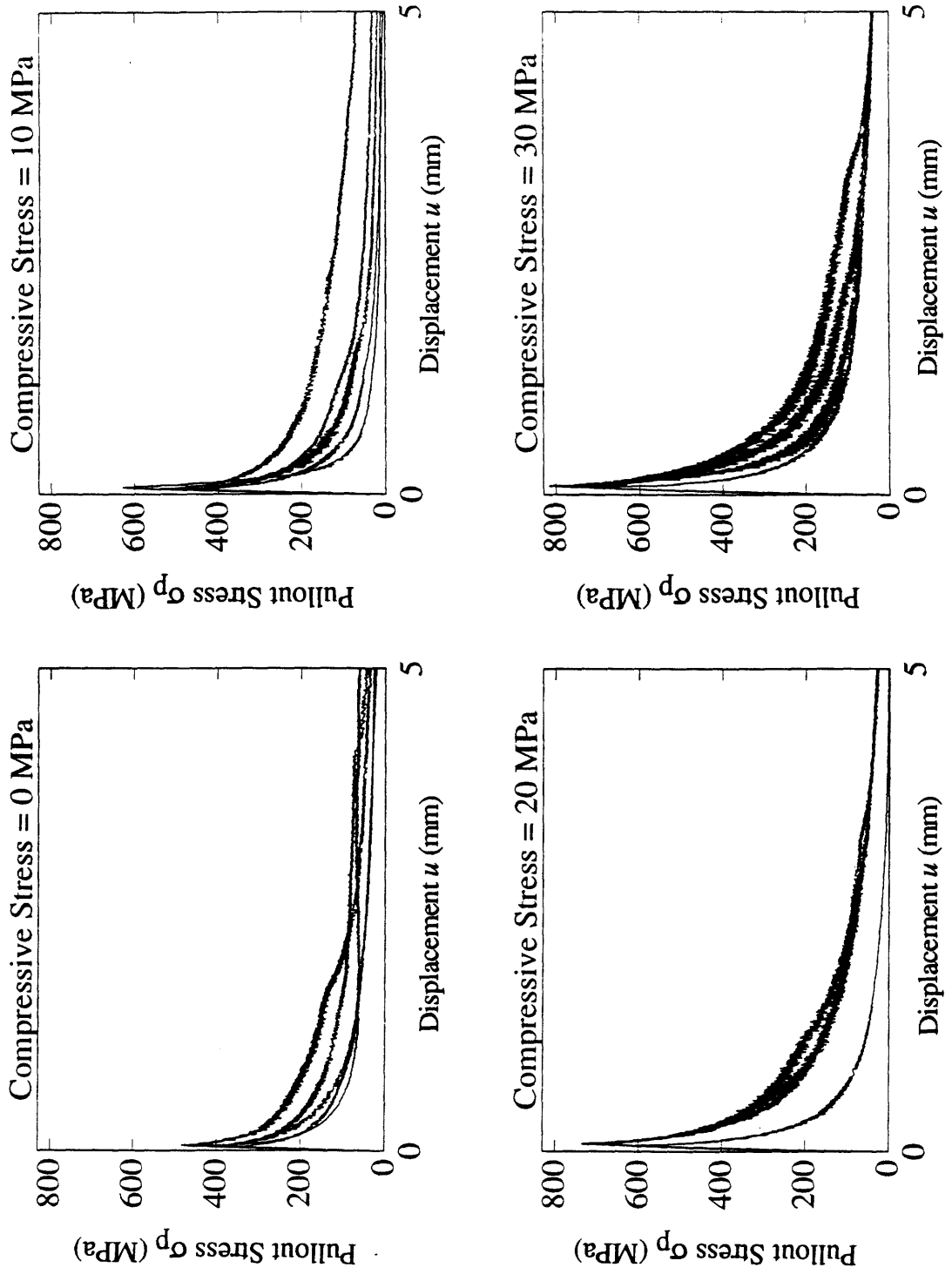

Figure 4.2b Experimental Pullout Curves for an Embedded Length of 10 mm (Steel Fiber)

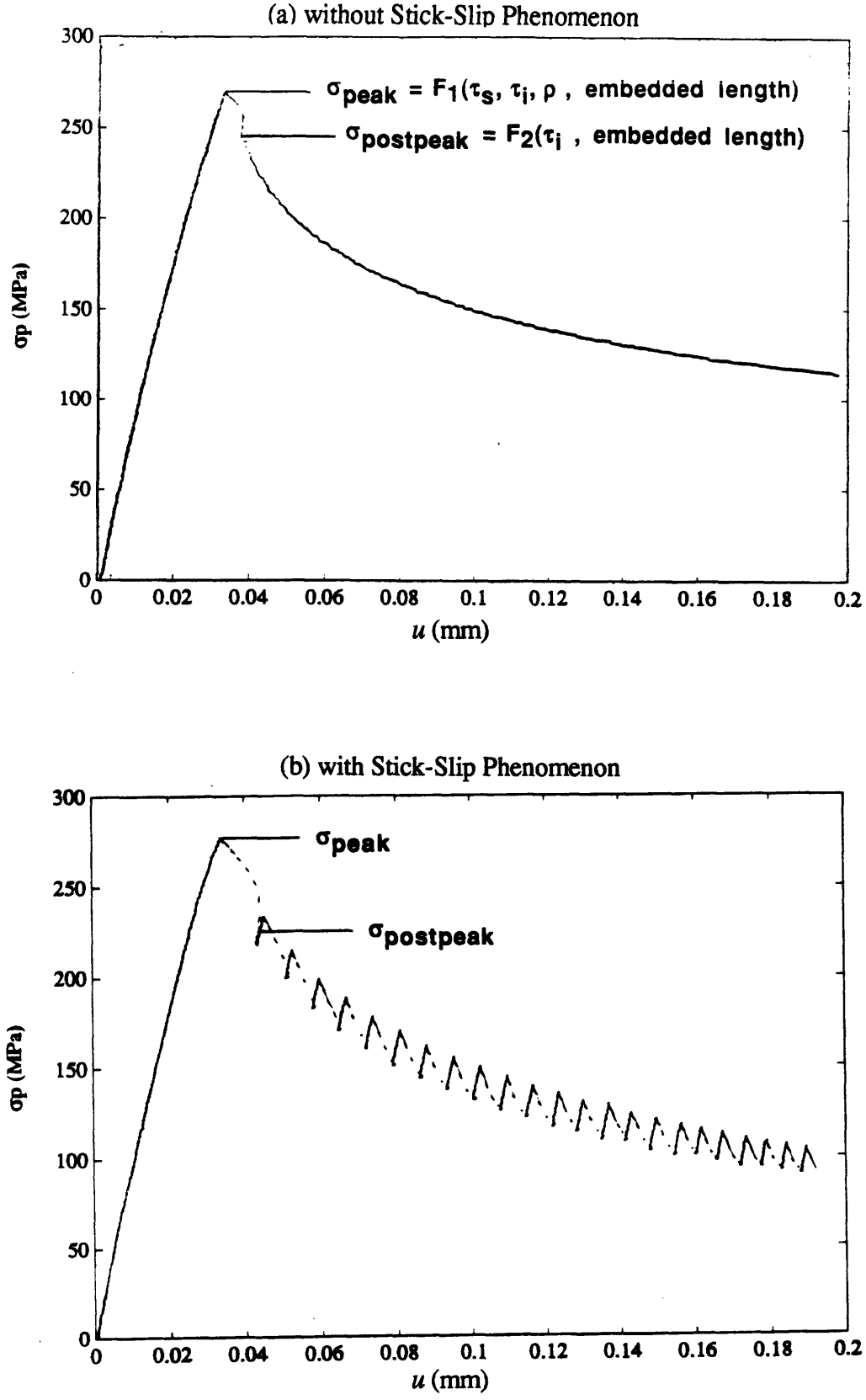

Figure 4.3 Typical Results of Steel Fiber Pullout

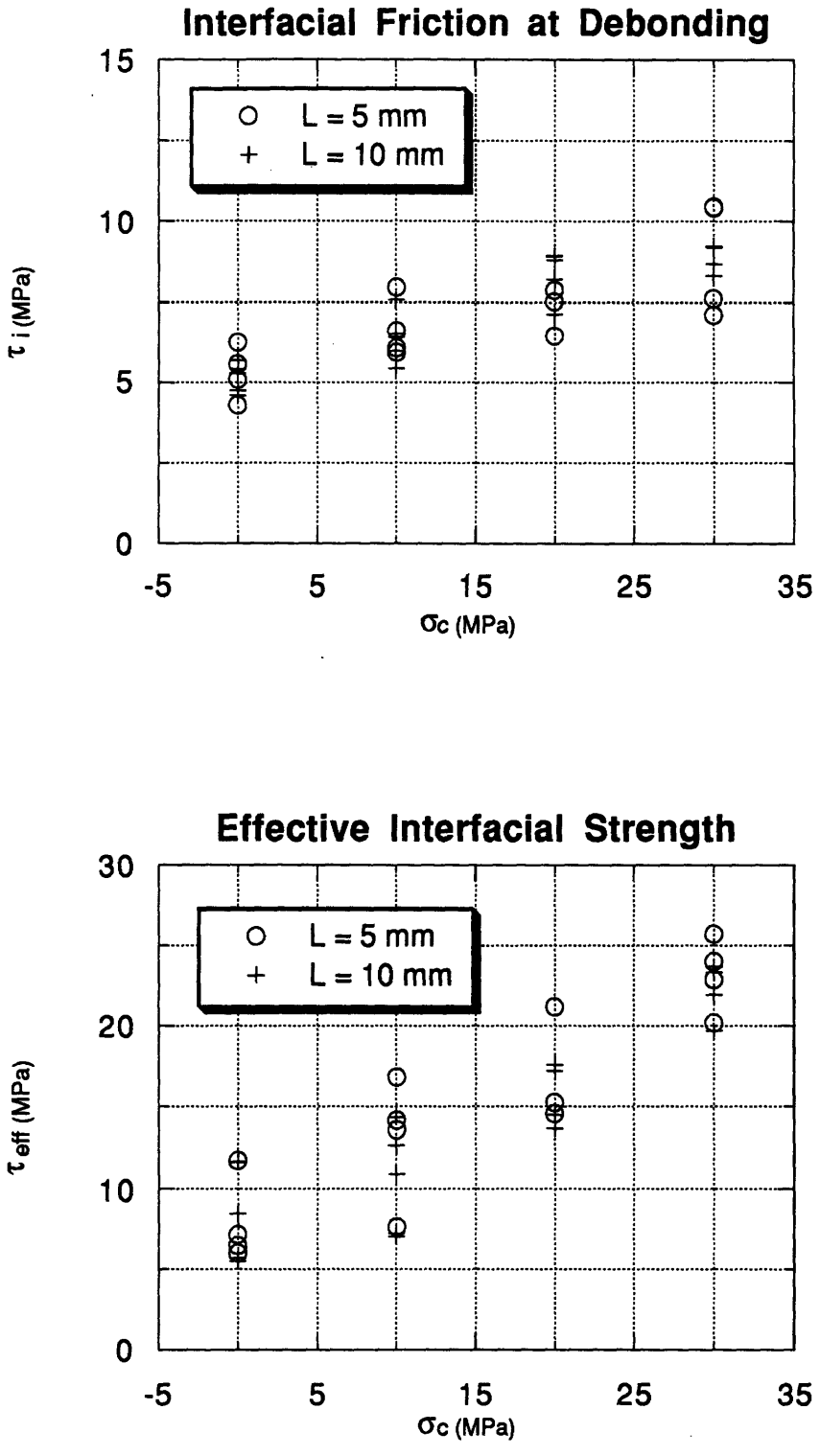

Figure 4.4 Interfacial Friction and Effective Interfacial Strength vs. Lateral Compression (Steel Fiber)

(2) Effective interfacial strength τ_{eff}: In the above test, the measured displacement, especially in the pre-peak stage, contains error from the setup deformation. This prohibits the estimation of ρ from the initial slope of the pullout curve as carried out in [4.5]. Here, ρ is derived from Eq. 2.4, assuming the absence of a compliant interphase between the fiber and the matrix

$$\rho^2 = -\frac{2G_m E_c}{E_f V_f E_m \left[\frac{2\ln V_f + (1-V_f)(3-V_f)}{4(1-V_f)^2}\right]} \tag{2.4}$$

with the fiber volume fraction derived from an approximate geometry in Fig. 4.5 ($Vf = \pi R_f^2/H^2$), we obtain $\rho = 0.255$ from Eq. 2.4 given above. After τ_i and ρ are obtained, τ_{eff} can be determined from an iteration scheme described in Section 2.3.1. The effective shear strength (assume $\rho = 0.255$) for each test are calculated and shown in Fig. 4.4b. Both τ_i and τ_{eff} increase with lateral compressive stress σ_c.

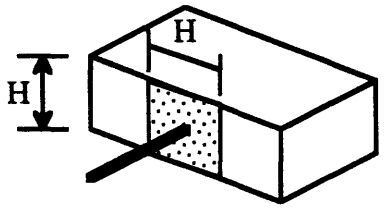

Figure 4.5 Approximate Geometry for Calculation of Fiber Volume Fraction

It should be noted that τ_i and τ_{eff} for all cases are significantly higher than the macroscopic tensile strength of mortar, which is around 3.6 MPa. Failure, however, is still found to occur along the fiber/matrix interface. This is because the high shear stress is only acting on a very small volume of mortar around the fiber (several times the fiber size or a few mm). The local tensile strength in the small volume of material is much higher than the commonly reported tensile strength that is measured with specimens of over 75 mm in size, which contains much larger flaws.

It should also be noted that the debonding model (Section 2.3.1) is developed for the axisymmetric case. When lateral stress is applied in one direction, the debonding is theoretically non-axisymmetric in nature. However, since the general trends for pullout curves are the same with and without lateral compression, the axisymmetric theory is applied to the extraction of interfacial behavior for all cases.

(3). Post-peak interfacial friction $\tau_i(s)$: In the post-sliding regime, as observed by Naaman and other investigators [4.3-4.4], the interfacial friction is found to decrease with sliding distance. In this chapter, we simply obtain $\tau_i(s)$ for various lateral stress levels by dividing the load at a given sliding distance by the surface area of fiber still in its groove. (Note: $\tau_i(0)$, the initial interfacial friction before sliding occurs, has been referred to simply as τ_i.)

$$\tau_i(s) = \frac{R_f}{2(L-s)}\sigma_p(s) \tag{4.1}$$

where σ_p is the fiber stress at the pulling end, L is fiber embedded length, s is the sliding distance of the pulling end, and R_f is the fiber radius. The fiber deformation is negligible.

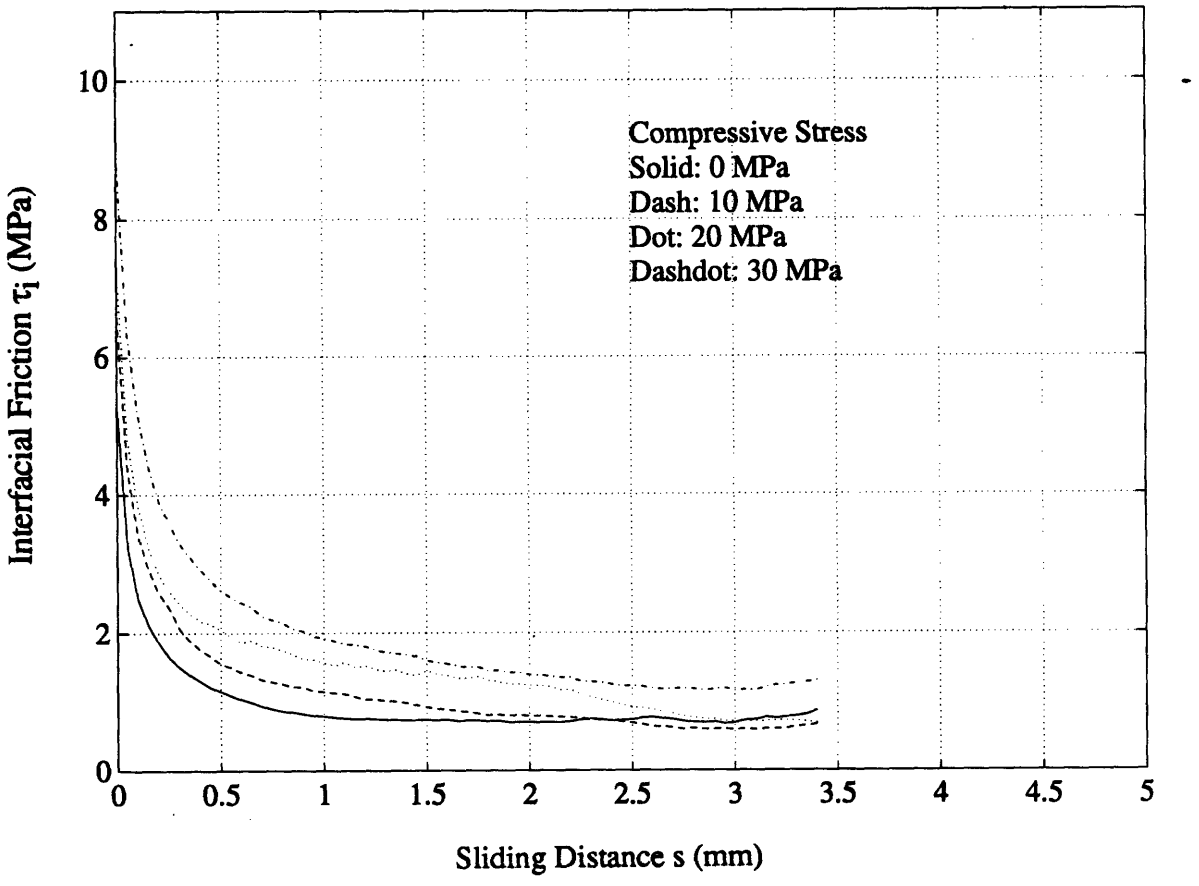

Figure 4.6a Average Interfacial Friction vs. Sliding for Different Values of Lateral Compression (Steel Fiber Embedded Length L = 5 mm)

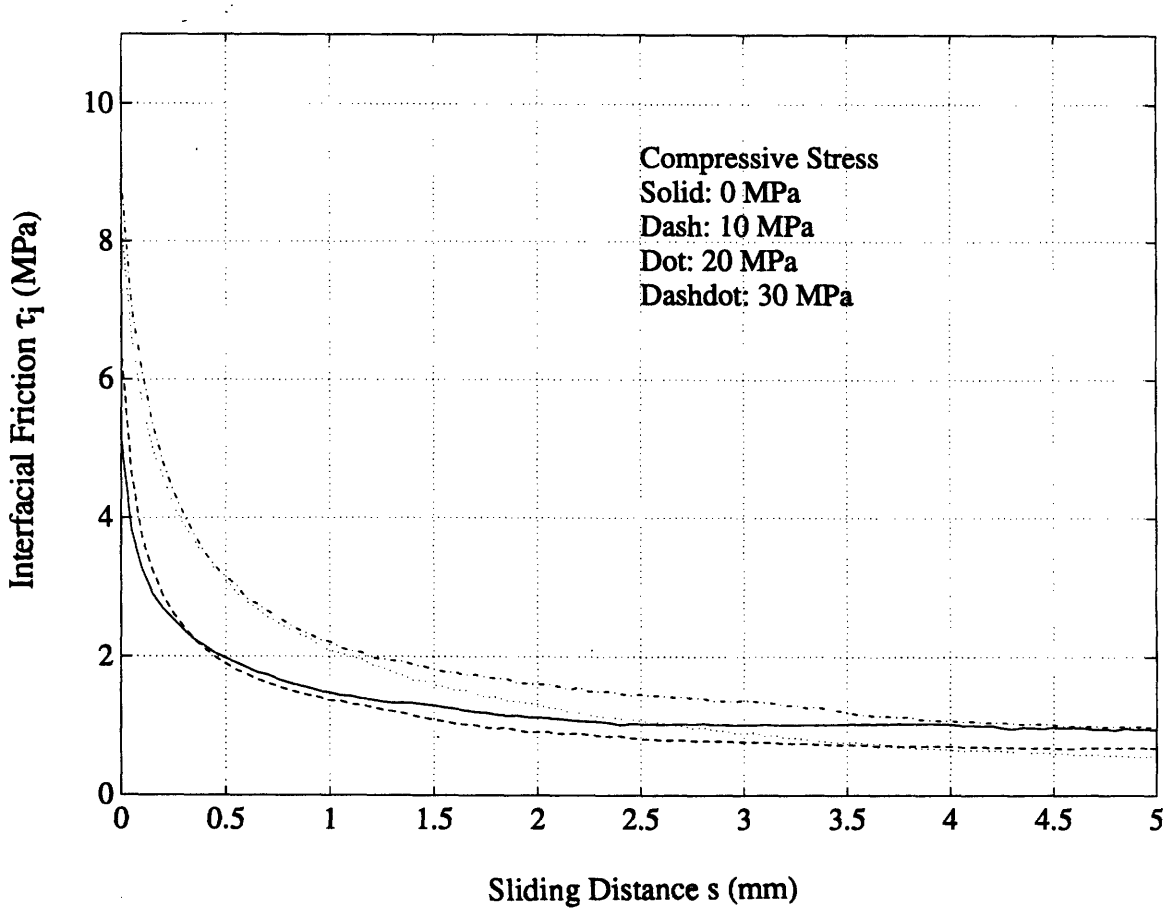

Figure 4.6b Average Interfacial Friction vs. Sliding for Different Values of Lateral Compression (Steel Fiber Embedded Length L = 10 mm)

For fiber pullout under zero lateral compression, stick-slip effect occurs in less than half of the tests. When lateral compression is applied, the probability of stick-slip effect increases. Almost all the pullout curves under 30 MPa compression have stick-slip drop. Therefore, the stick-slip effect is more common in cases with high lateral compression. In Fig. 4.6a and 4.6b, $\tau_i(s)$ curves for various lateral compression levels (obtained as the average of several tests at each compression level) are shown.

4.2.2 Steel Fiber under Tension

In another series of experiments, the effect of lateral tension on debonding/pullout behavior is studied. Since two different batches of mortar are employed for specimens tested under lateral tension and lateral compression, the results are separately presented. Results for zero lateral tension and 1 MPa tension for both 5 mm and 10 mm embedded length are shown in Fig. 4.7.

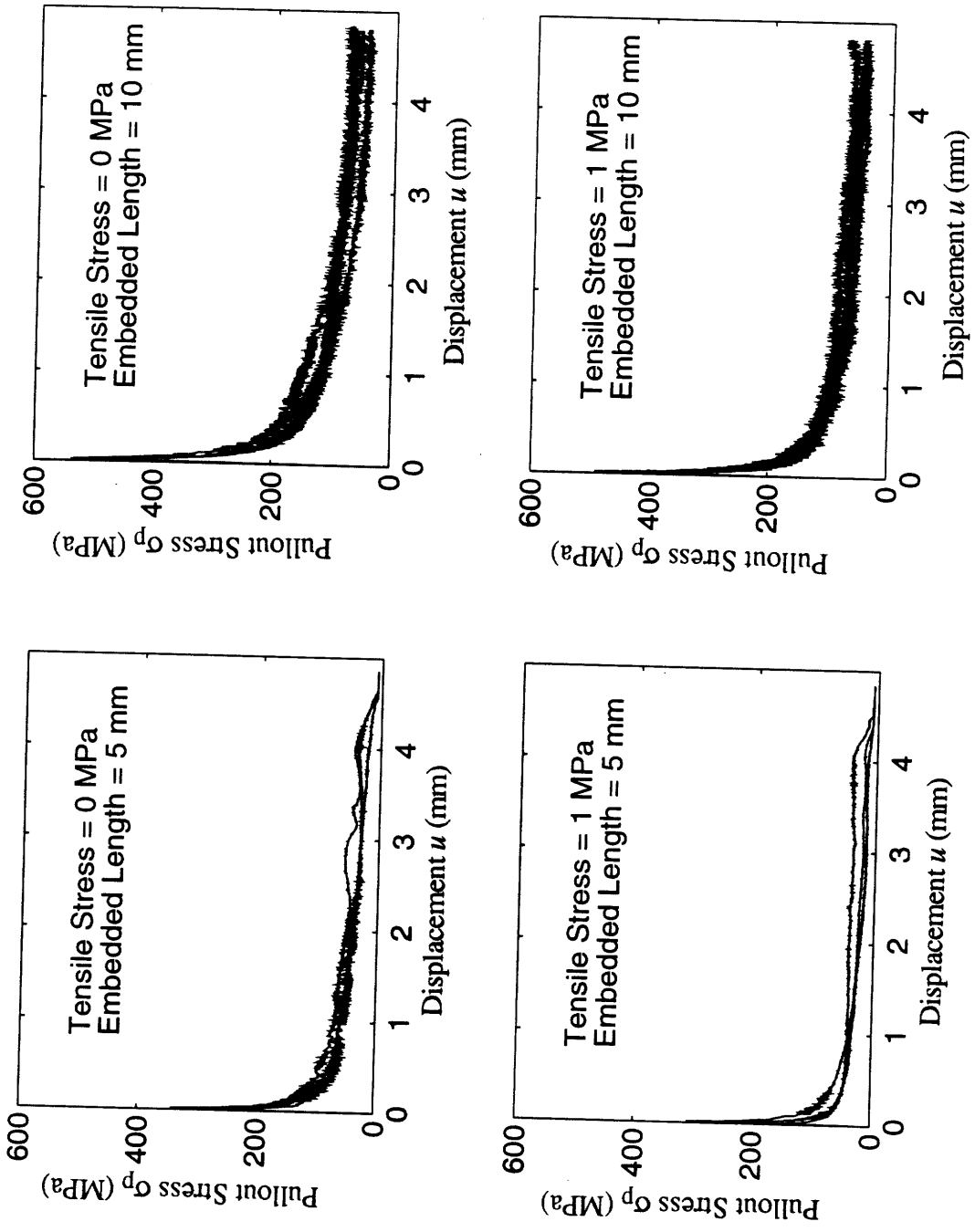

Figure 4.7 Fiber Pullout Curves for Zero and 1 MPa Lateral Tension (Steel Fiber)

It is interesting to note that for all cases with lateral tension, no measurable unstable drop in the pullout curve can be observed after σ_{peak} is reached. In other words, σ_{peak} and $\sigma_{postpeak}$ are essentially the same, indicating that τ_i and τ_{eff} are identical when 1 MPa lateral tension is applied. In Fig. 4.8a and 4.8b, average $\tau_i(s)$ curves are plotted for zero and 1 MPa lateral tension. Crosses on the y-axis indicate the value of $\tau_i(0)$. The uplifting of the $\tau_i(s)$ curves for 5 mm embedded length at long sliding distance is due to experimental variations.

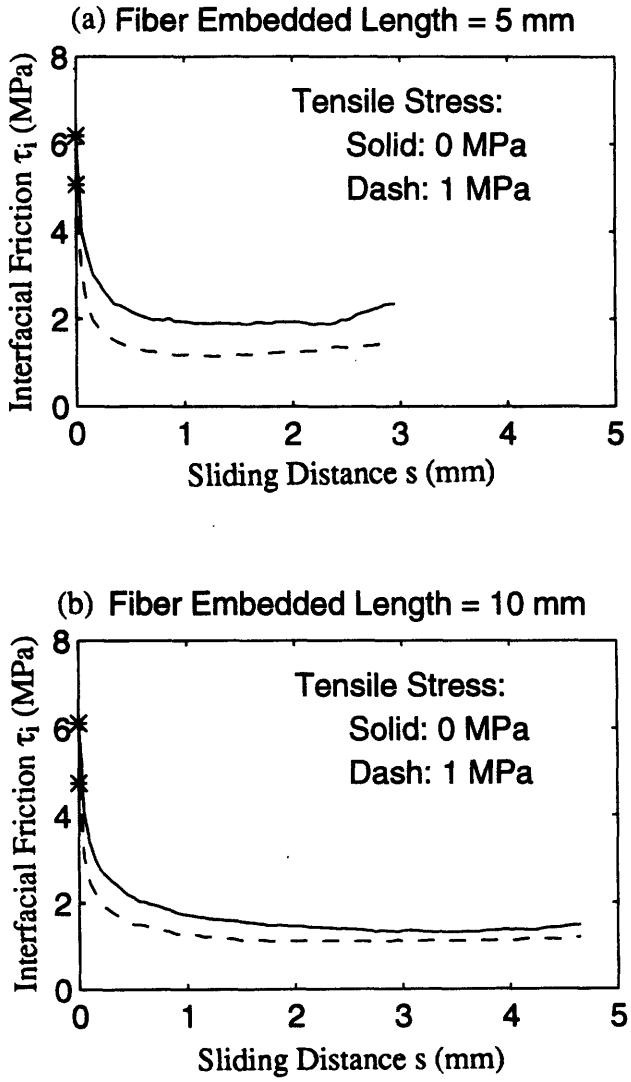

Figure 4.8 Average Interfacial Friction vs. Sliding Distance for Zero and 1 MPa Lateral Tension (Steel Fiber)

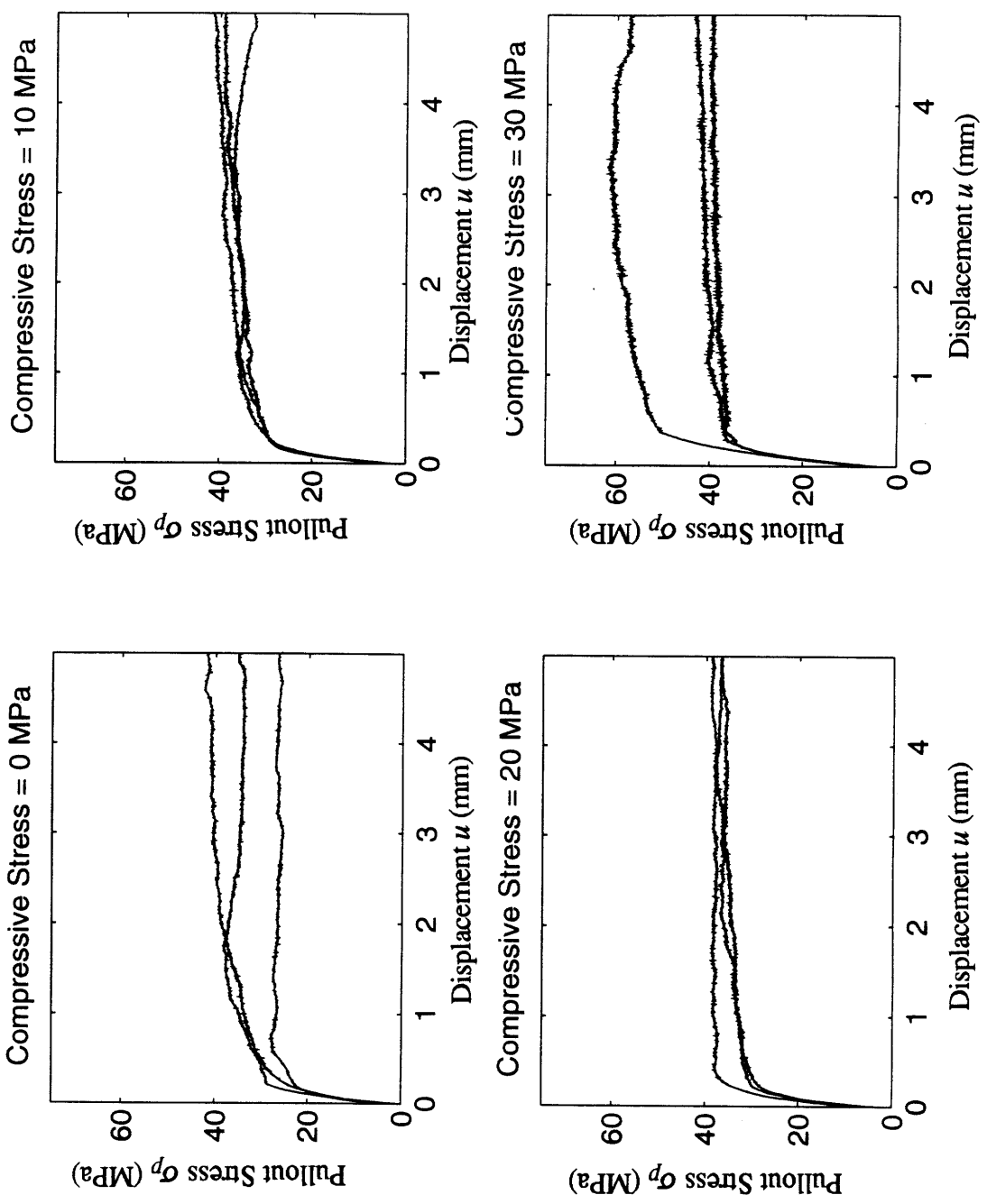

Figure 4.9 Experimental Pullout Curve for an Embedded Length of 10 mm (Nylon Fiber)

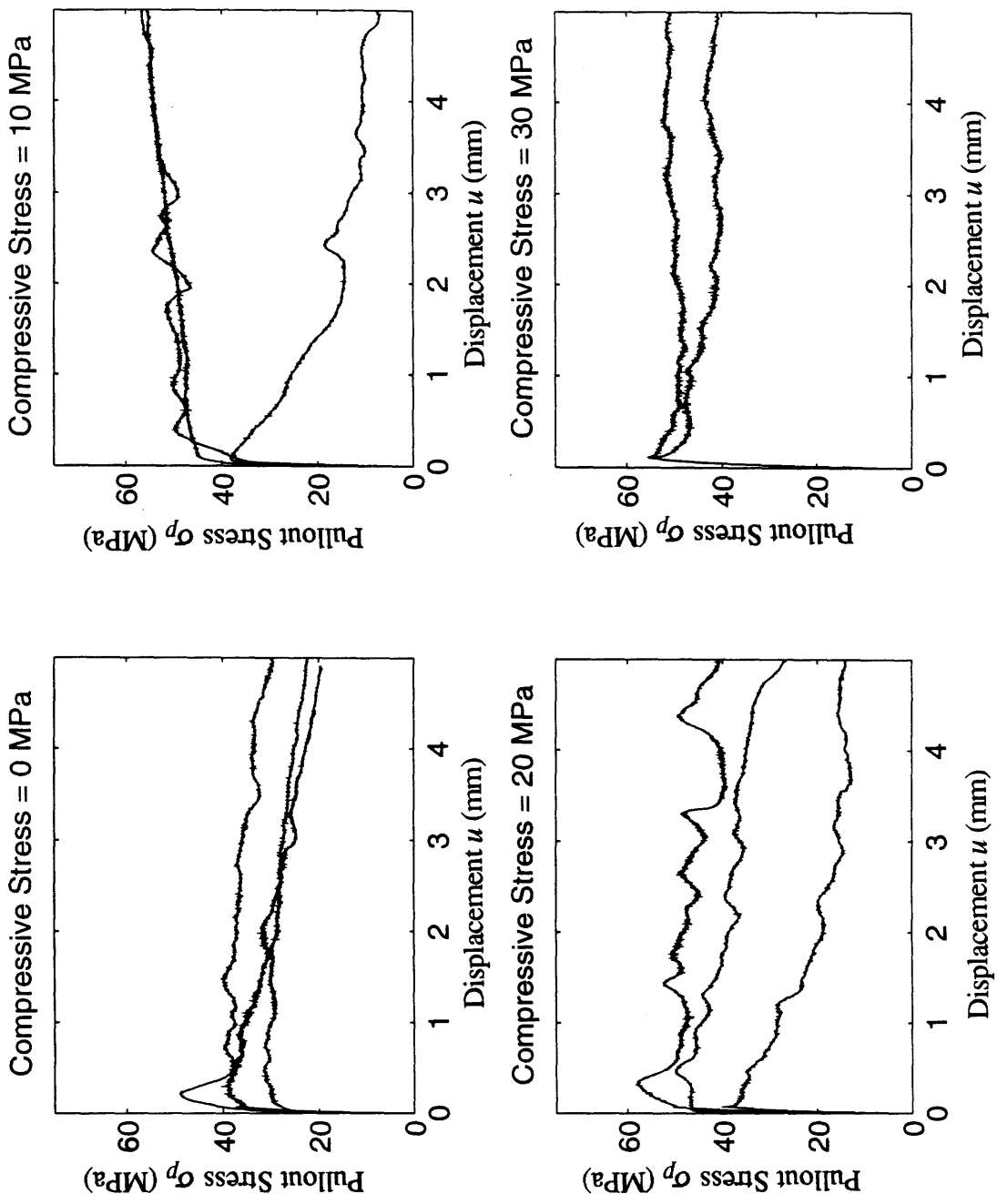

Figure 4.10 Experimental Pullout Curve for an Embedded Length of 10 mm (Polypropylene Fiber)

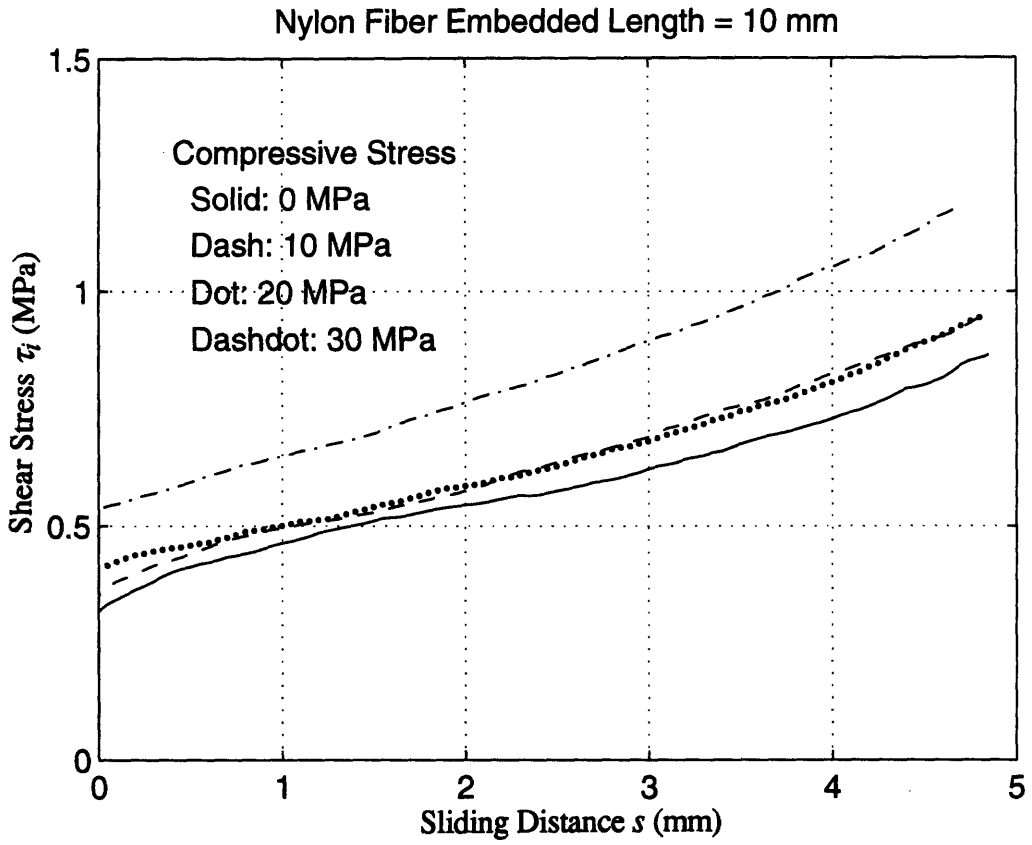

Figure 4.11 Average Interfacial Friction vs. Sliding Distance for Different Values of Lateral Compression (Nylon Fiber)

4.2.3 Polymer Fiber under Compression

For the purpose of comparison, nylon and polypropylene fibers, with embedded length of 10 mm, are tested under the lateral compressive stresses of 0, 10, 20 and 30 MPa (Figs. 4.9 and 4.10. Similar to the observation in Chapter 3, the post-peak load of nylon fiber

curves increases slowly, while the post-peak load of polypropylene fibers decreases slowly with randomness.

In Figs. 4.11 and 4.12, average $\tau_i(s)$ curves are plotted for each lateral tension. For both nylon and polypropylene fibers, $\tau_i(s)$ increases with sliding distance. However, the effect of lateral compression on $\tau_i(s)$ is insignificant.

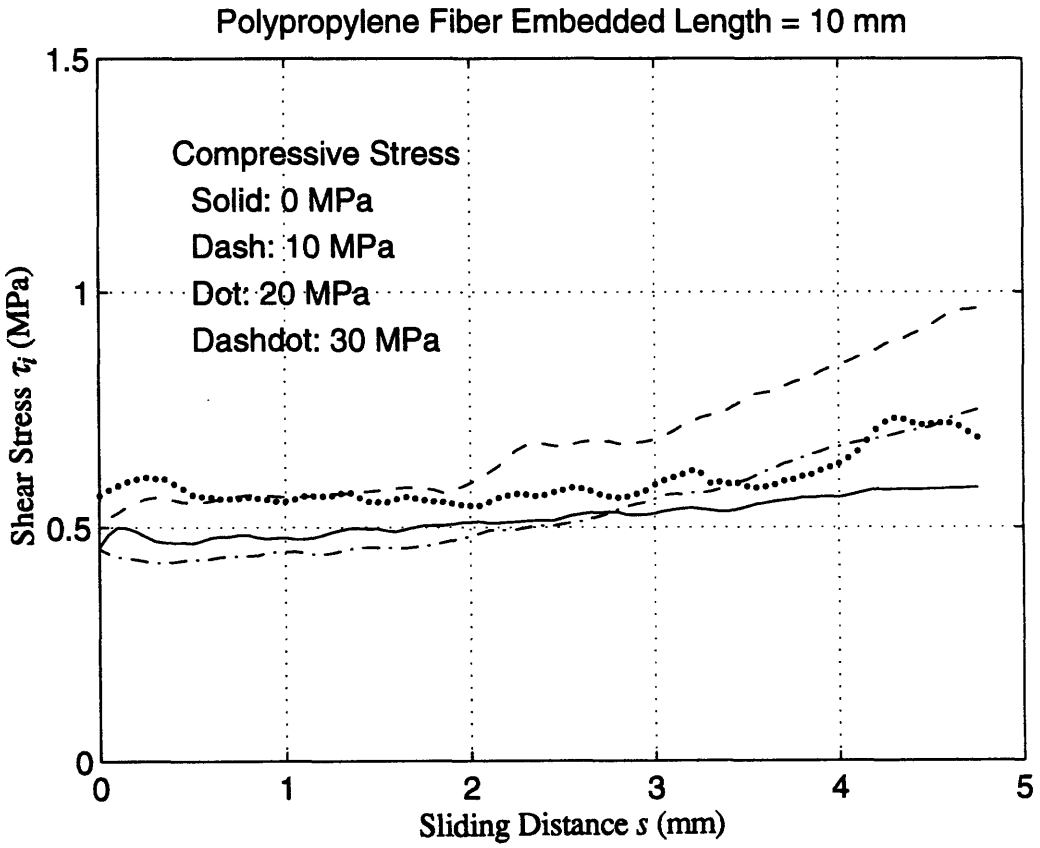

Figure 4.12 Average Interfacial Friction vs. Sliding Distance for Different Values of Lateral Compression (Polypropylene Fiber)

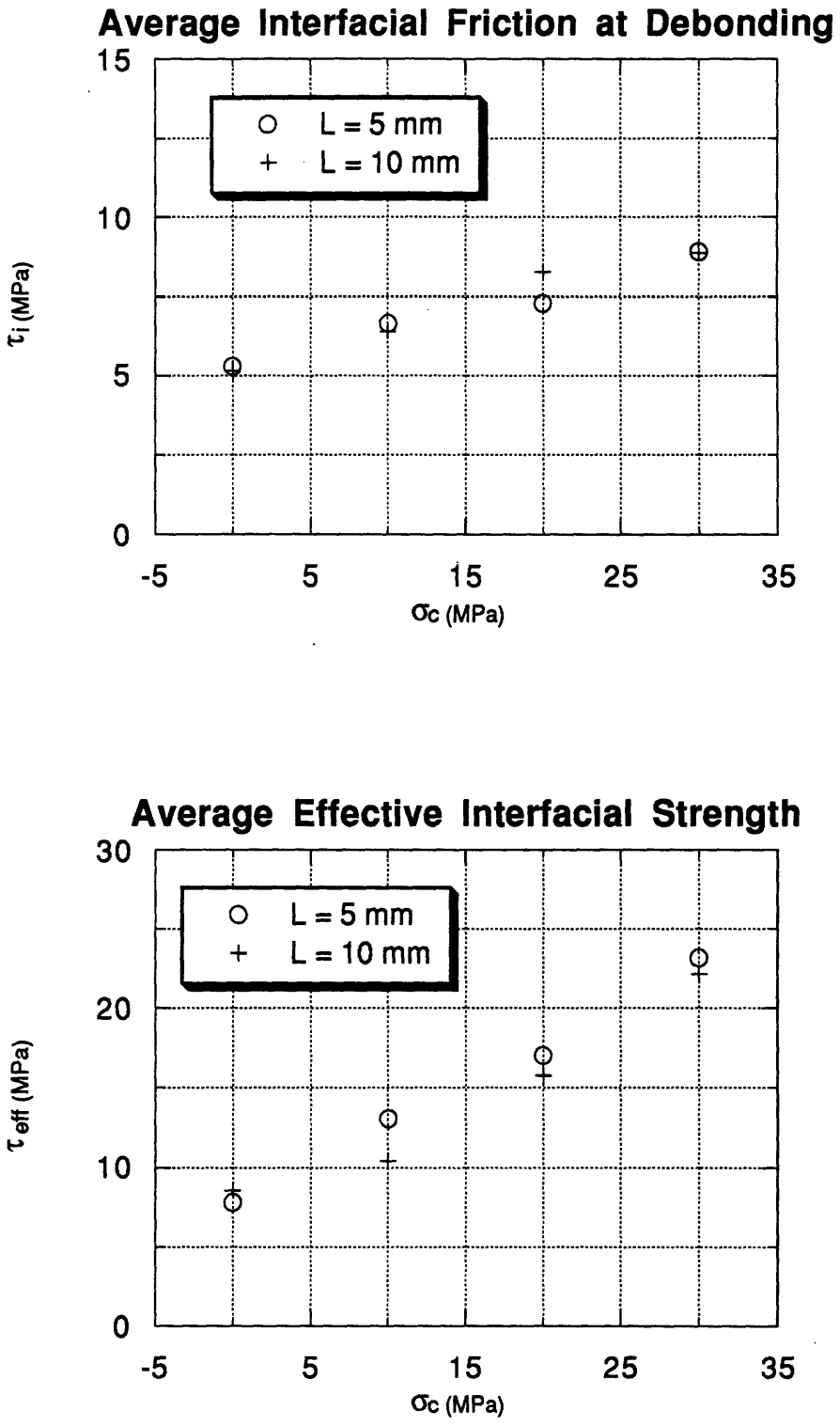

Figure 4.13 Average Interfacial Friction and Effective Interfacial Strength vs. Lateral Compression

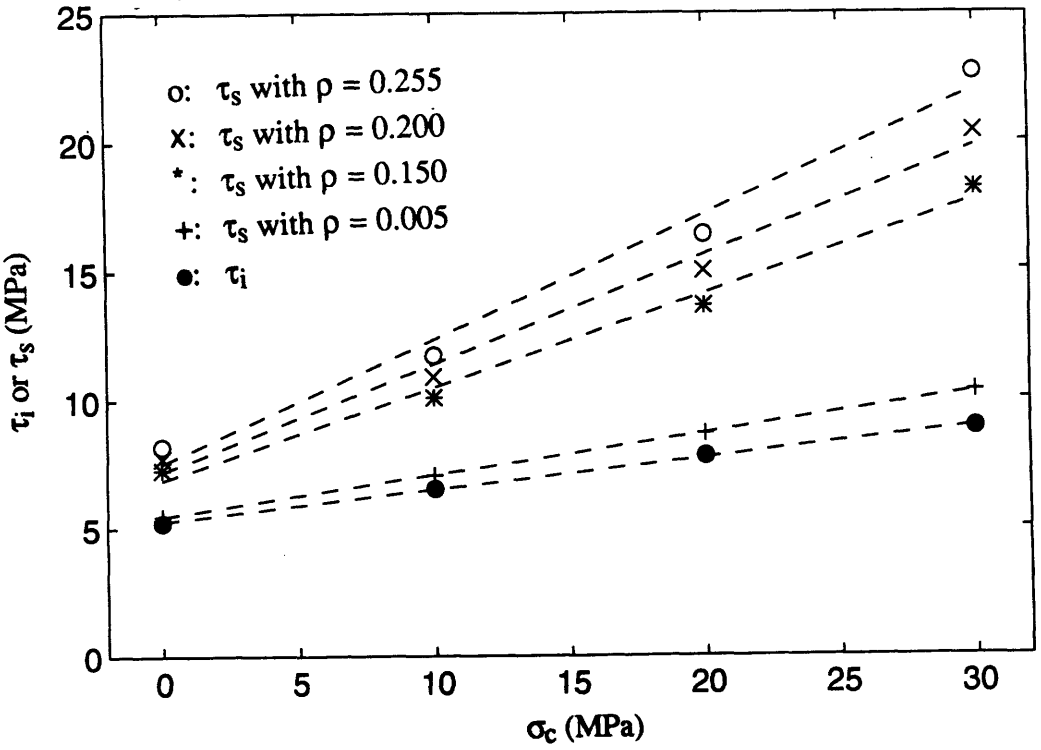

Figure 4.14 Effect of ρ on Effective Interfacial Strength

4.3 DISCUSSION

4.3.1 Debonding under Lateral Compression

The average values of initial interfacial friction and the effective shear strength for each compression level are shown in Fig. 4.13. The agreement of results obtained from two different embedded lengths verify the validity of the experimental approach and the interfacial parameter extraction technique. τ_i increases with lateral stress as expected due to the proportionality of kinetic friction with normal compressive stress at the interface. It is, however, interesting to find that τ_{eff} also increases with lateral compression and is actually increasing at a high rate than τ_i.

Since the determination of τ_{eff} relies on the value of ρ, and ρ is obtained as an upper bound by neglecting the plausible presence of a compliant interphase, τ_{eff} values as a function of lateral compression σ_c have also been calculated using lower values of ρ. The results are shown in Fig. 4.14. It is clear from Fig. 4.14 that a lower value of ρ will lead to lower values of τ_{eff} as well as a lower slope of τ_{eff} vs. σ_c. However, even with ρ as low

as 0.005, which corresponds to the presence of an extremely compliant interphase, τ_{eff} is still found to increase at a higher rate with applied compression than τ_i. This trend is therefore a real material behavior. If interfacial debonding is strength-governed, this implies the interfacial strength increases linearly with lateral compression (Eq. 2.2). If interfacial debonding is fracture-governed, the interfacial fracture energy is shown to increase linearly with lateral compression (Eq. 2.3).

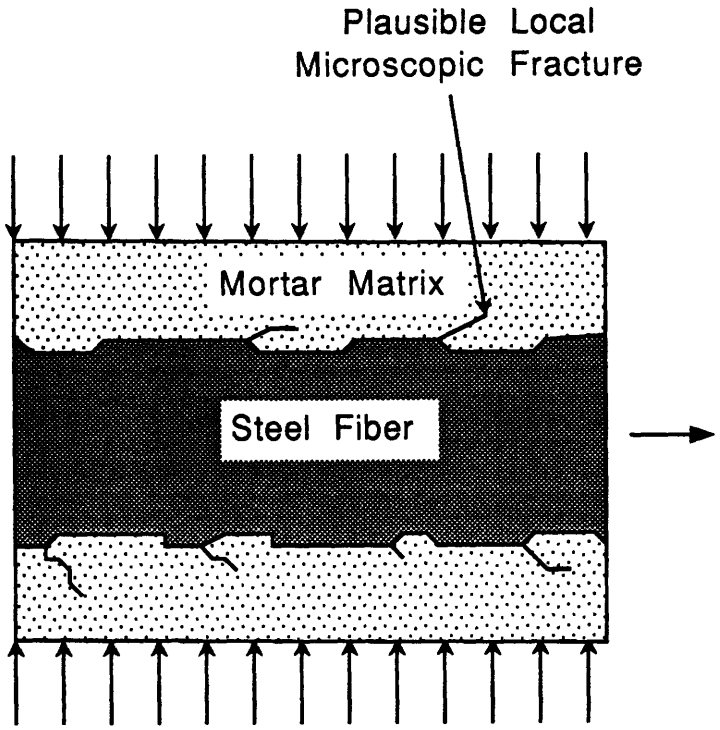

Figure 4.15 A Simple Model for the Microscopic Fracture Involved in Fiber Debonding

The increase in pre-sliding interfacial resistance (i.e., interfacial strength or interfacial fracture energy, depending whether debonding is assumed to be strength-based or fracture-based) with lateral compression can be explained qualitatively with the help of a simple model shown in Fig. 4.15, which shows a fiber with a rough surface embedded in a quasi-brittle matrix.

In order for the fiber to slide relative to the matrix, the mechanical interlock (due to surface roughness) has to be overcome by local microscopic fracture in the matrix. The presence of lateral compression make it more difficult for such local fracture to occur and hence increase the pre-sliding interfacial resistance. Qualitative evidence to support the proposed mechanism can be observed on SEM micrographs of a clean fiber surface before

the fiber is embedded into mortar (Fig. 4.16a) and a fiber surface right after debonding (Fig. 4.16b). Details of SEM specimen preparation can be found in Chapter 3 on a thorough SEM study which includes some work on EDX analysis of the fiber/mortar interface during fiber debonding/pullout.

From Fig. 4.16a, it is obvious that the fiber surface is rough and it is possible for hydrated cement particles to get caught in the 'troughs' on the rough surface. The debonded fiber surface in Fig. 4.16b confirms this point of view. While most of the debonded fiber surface is clean, there are cement particles stuck on the fiber surface which have been sheared off by rough edges as the fiber slides relative to the matrix surface.

4.3.2 Pullout under Lateral Compression

At higher values of lateral compression, the initial interfacial friction is higher (as shown in Fig. 4.4). However, with a higher lateral compression, the pullout resistance will also decrease more rapidly with fiber sliding. In Fig. 4.6a and 4.6b, $\tau_i(s)$ curves for different lateral compression can be observed to cross over each other, indicating a lower pullout resistance for a higher lateral compression beyond a certain sliding distance. The decrease of interfacial friction with sliding, as well as the increasing rate of decay with lateral compression, can be explained by the 'abrasion and grinding effect' discussed in Chapter 3.

The sliding of steel fiber can abrade the cement matrix, thus increasing the size of the cement matrix groove. Moreover, the mortar particles, formed as a consequence of matrix abrasion, are subsequently ground into smaller sizes and act as small 'ball bearings' to reduce the interfacial frictional coefficient. Micrographs shown in Fig. 4.16c and d, which shows the steel surface after 1 mm and 10 mm of fiber sliding respectively, provides visual proof of the abrasion effect. Compared with Fig. 4.16b which shows the steel fiber right after debonding, it is clear that the mortar particle size is significantly reduced with sliding. Indeed, after 10 mm of sliding, the particles become very fine and almost unnoticeable on the scale of the micrograph. Under higher interfacial normal compression, the abrasion and grinding effects become more significant. Fig. 4.17 shows the steel surface after 1 mm of sliding under 20 MPa of lateral compression. Comparing Fig. 4.16c for the same sliding distance without lateral compression, the surface looks much cleaner for higher compression, implying that the surface mortar particles have already been ground to much finer sizes.

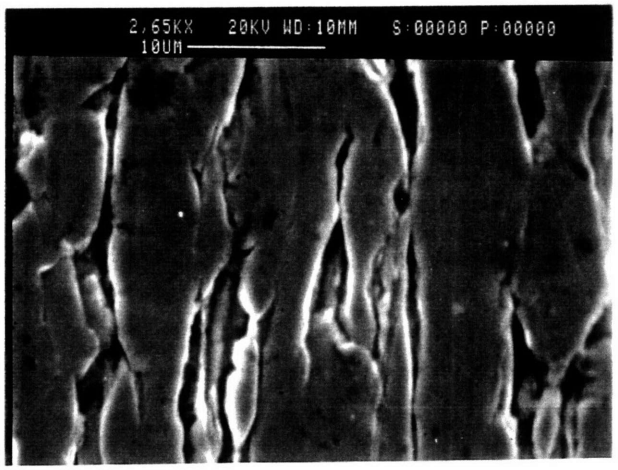

(a) Clean Surface

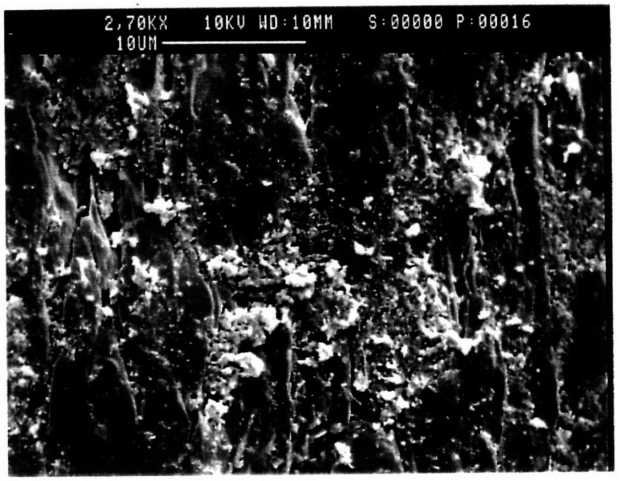

(b) After Debonding

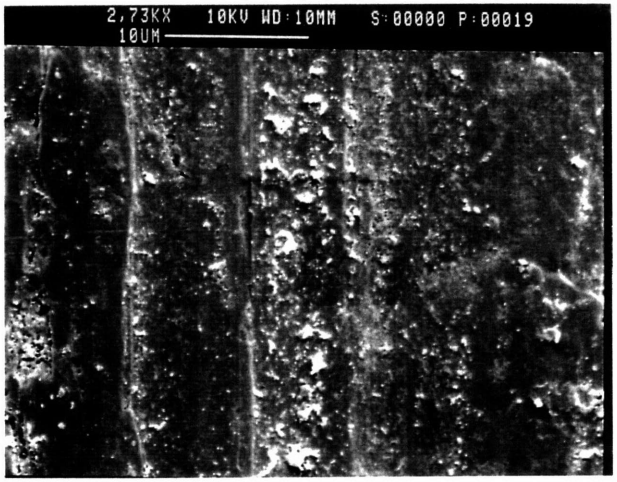

(c) 1 mm Sliding

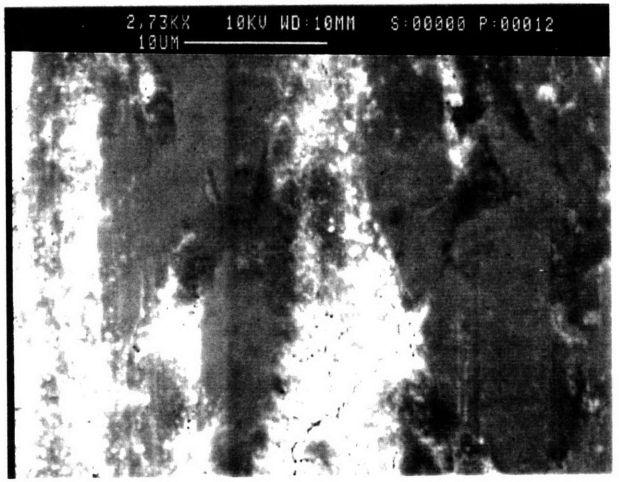

(d) 10 mm Sliding

Figure 4.16 Steel Surface under Zero Lateral Compression

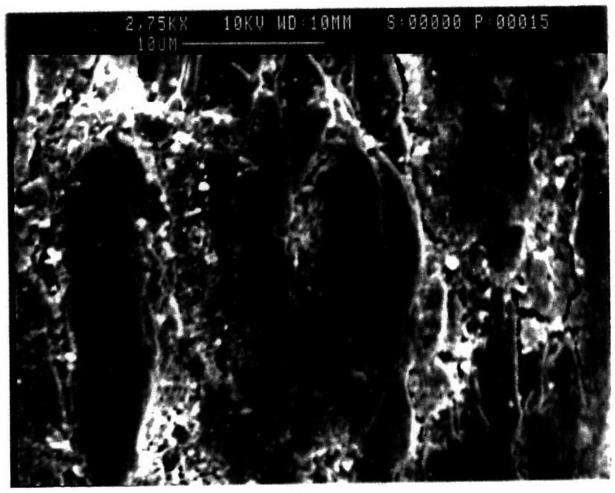

Figure 4.17 Steel Surface after 1 mm Sliding under 20 MPa Lateral Compression

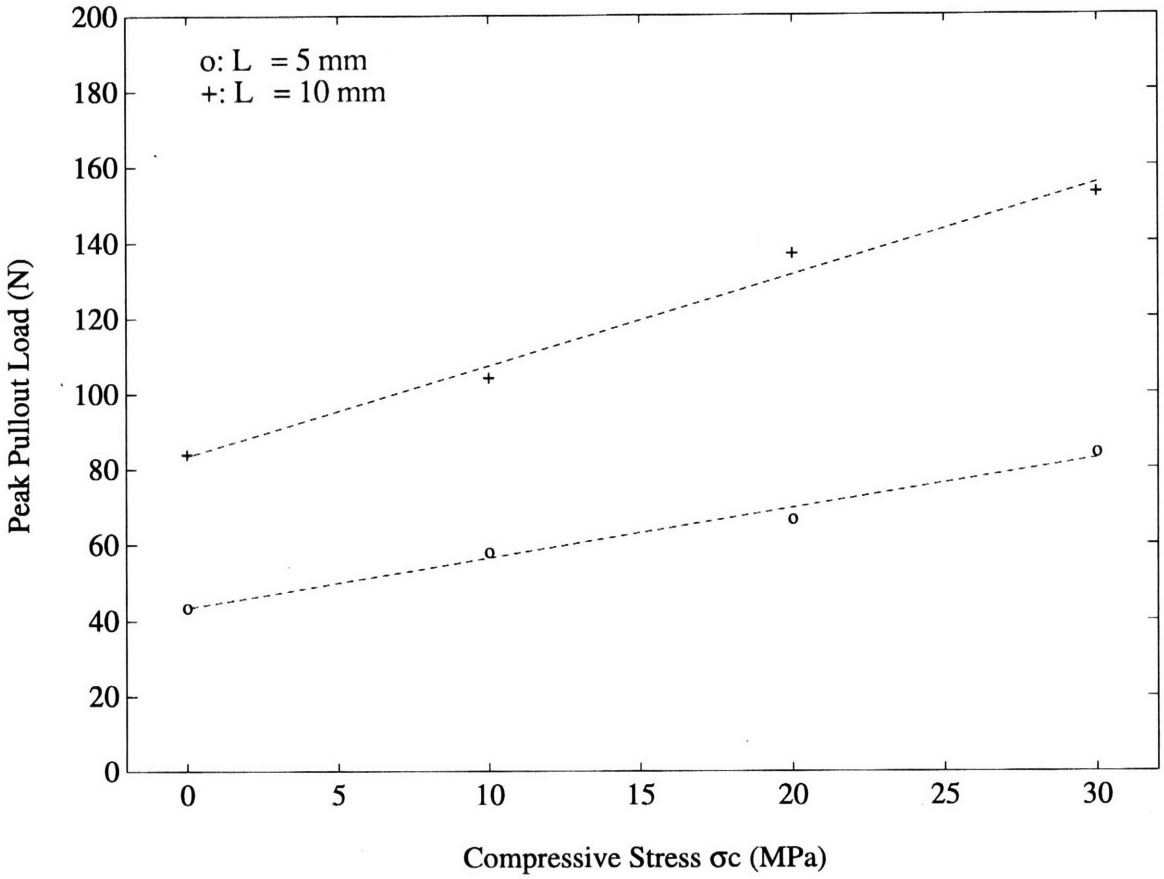

Figure 4.18 Peak Pullout Load vs. Lateral Compression (Steel Fiber)

4.3.3 Peak Load and Energy Absorption under Lateral Compression

The behavior of steel fiber reinforced concrete with lateral compression acting on fibers can be best illustrated by Fig. 4.18 and 4.19, which shows respectively the increase of peak pullout load and total energy absorption (up to a sliding distance of 5 mm) with lateral compression. As shown in Fig. 4.18, the peak pullout load of a fiber can be significantly increased by the presence of lateral compression. A compressive stress of 30 MPa can almost double the peak pullout load. A high peak pullout load implies high resistance to initial crack propagation and hence significant improvement in the strength of the composite. On the other hand, due to the higher rate of drop of post-peak interfacial friction with lateral compression, the increase of energy absorption with lateral stress is not as much as that of the peak pullout load (Fig. 4.19). The toughness improvement of steel fiber reinforced concrete is therefore not very drastic even when there is high lateral compression acting on the fibers.

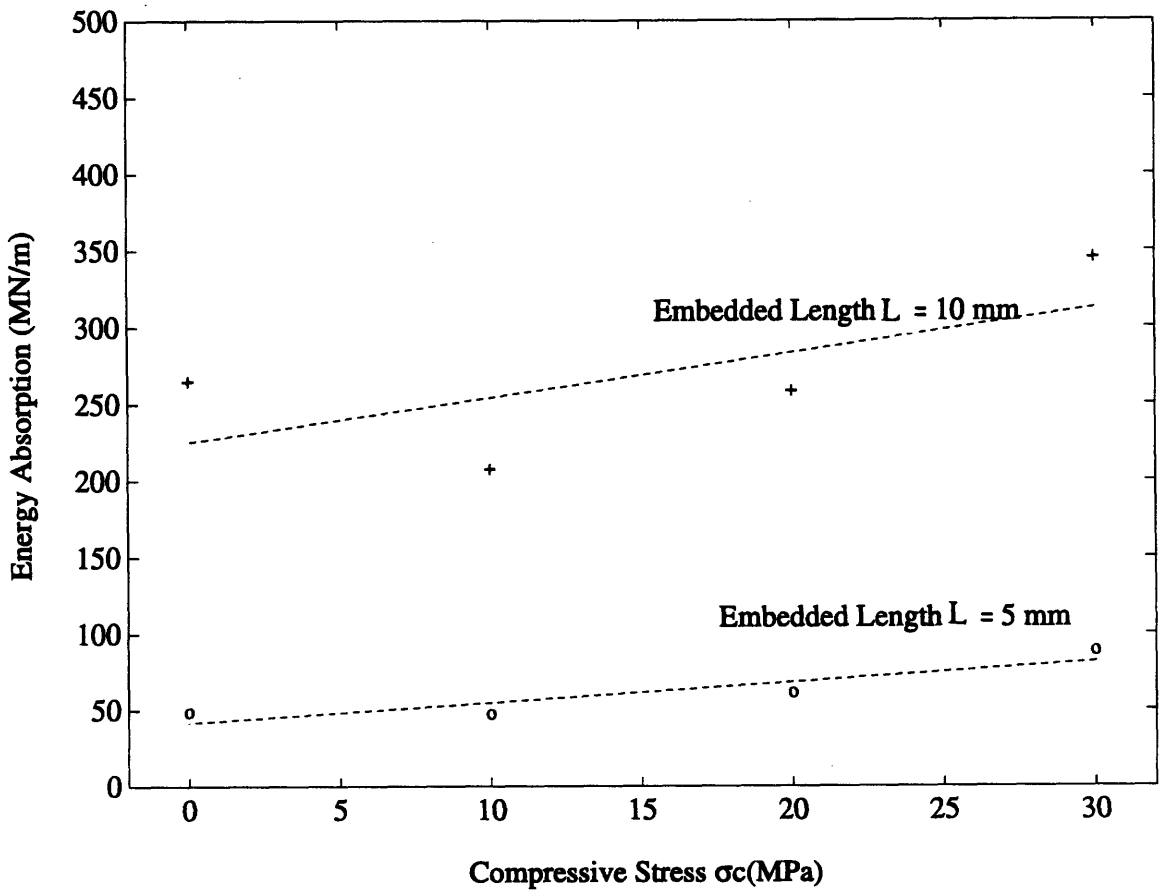

Figure 4.19 Energy Absorption up to 5 mm Sliding Distance vs. Lateral Compression (Steel Fiber)

Figures 4.20 and 4.21 shows the comparison of steel, nylon and polypropylene fiber pullout with 10 mm embedded length. For polymeric fibers, the peak loads is extremely low and do not increase significantly with compressive stress. However, the energy absorption (areas under pullout curves up to sliding distance s = 5 mm) does increase with compressive stress.

Although the peak loads of polymeric fibers are one order lower than those of steel fibers (about 1/10 that of steel fibers), the energy absorption has the same order of those of steel fibers (only 2/3 that of steel fibers). This is due to the trend of increasing interfacial friction for polymer fibers.

4.3.4 Debonding/Pullout under Lateral Tension

For the case with no applied lateral stress, the values of $\tau_i(0)$ obtained from this batch of specimens (Fig. 4.8), are slightly higher than those obtained from the previous batch (Fig. 4.5). The difference is within experimental variation. With 1 MPa of applied lateral tension, $\tau_i(0)$ drops to roughly 80% of its value at zero lateral stress. Compared with results in Fig. 4.13, which shows a roughly 35% increase of $\tau_i(0)$ with 10 MPa of lateral compression, it can be stated that $\tau_i(0)$ is more sensitive to lateral tension than lateral

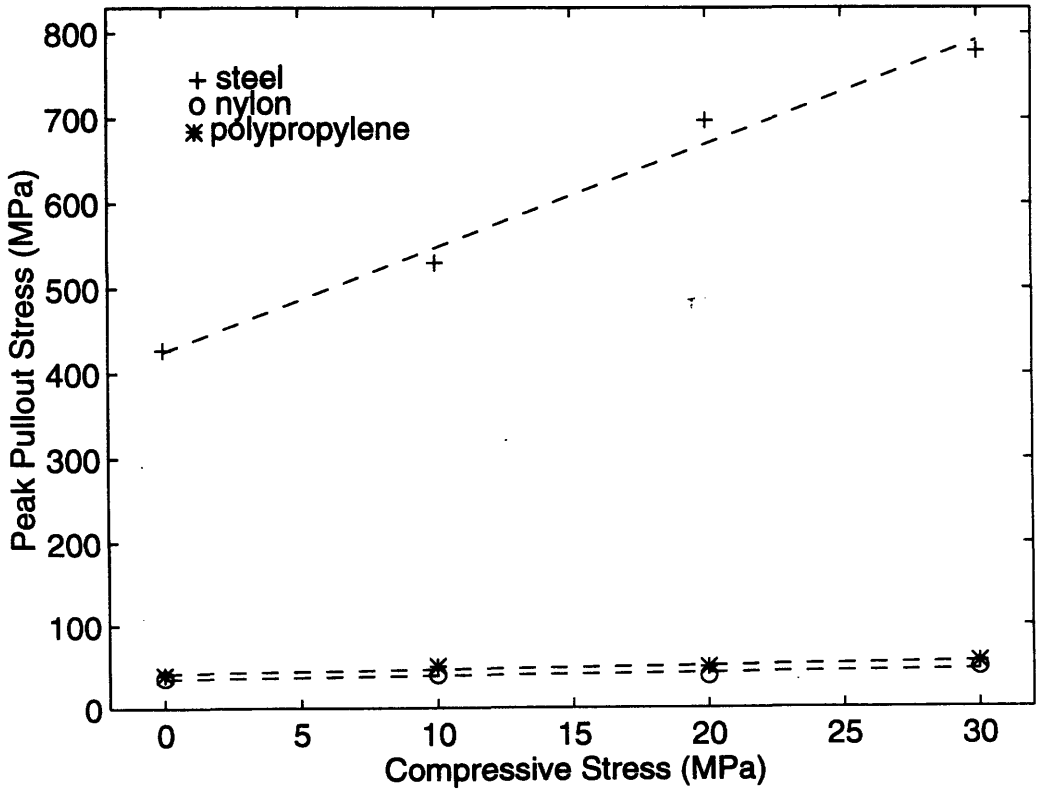

Figure 4.20 Comparison of Peak Loads

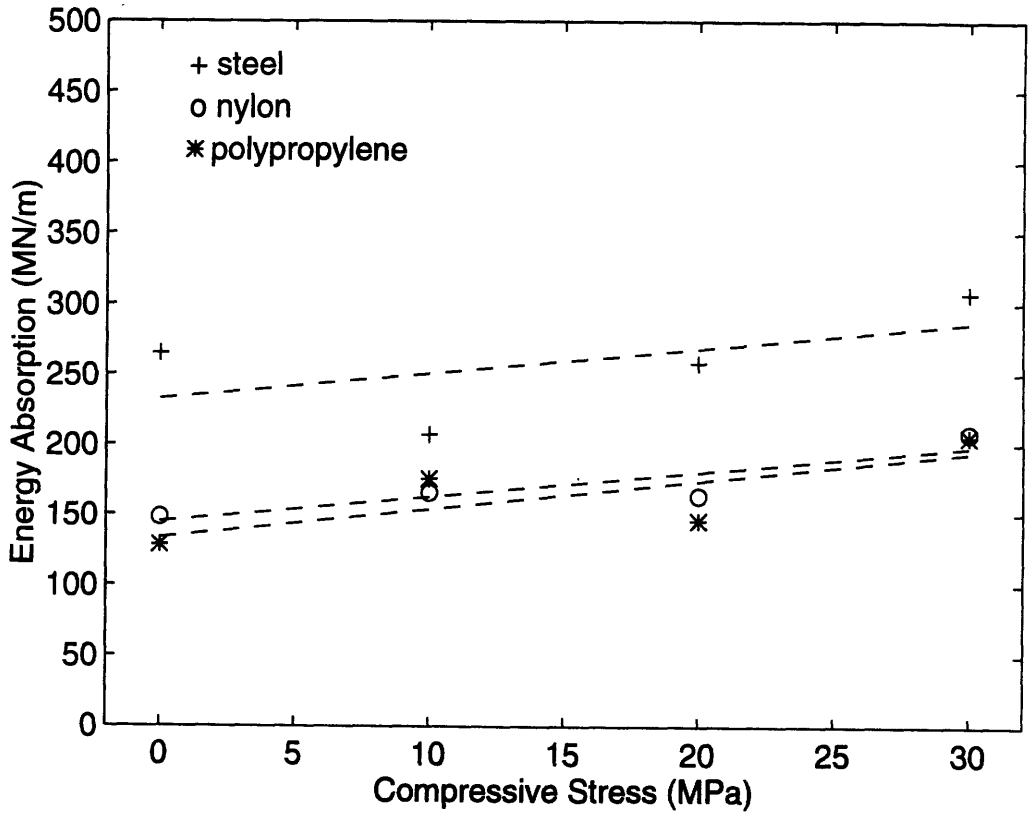

Figure 4.21 Comparison of Energy Absorptions

compression. Assuming τ_{eff} to be the same as $\tau_i(0)$ for the case with 1 MPa tension (as explained above), one can draw a similar conclusion for τ_{eff}. From Fig. 4.8b, the decrease of τ_i with s is found to be slower for the case with lateral tension. This trend is not obvious in Fig. 4.8a, where experimental verifications has led to significant increase of interfacial friction at larger sliding distance. Also, by comparing Figs. 4.8a and 4.8b with Figs 4.6a and 4.6b, lateral tension is found to have a much higher effect on the fiber pullout behavior than lateral compression.

To summarize, one can conclude that the qualitative effects of lateral tension on fiber debonding and pullout are opposite to those for lateral compression. Quantitatively, however, a small lateral tension may have comparable effect (in terms of the change in magnitude of interfacial parameters) to a much higher compression. Therefore, although the lateral tension that can act on fibers in practical situations is limited to a relatively low value below the tensile strength of mortar, it may still impose a noticeable effect on fiber debonding/pullout behavior.

4.4 CONCLUSIONS

The investigation establishes the sensitivity of steel fiber debonding behavior to both applied lateral compression and tension. Both the effective interfacial strength and initial interfacial friction are found to increase with applied lateral compression. Interestingly, the rate of increase in effective interfacial strength is higher than that for the initial interfacial friction. During fiber pullout, the rate of drop in interfacial friction is found to increase with lateral compression. As a result, while lateral compression can significantly increase the peak pullout load, the energy absorbed is not increased to the same degree. The effect of lateral tension is qualitatively opposite to that of lateral compression. However, quantitatively, the debonding/pullout behavior is much more sensitive to lateral tension than compression. Although polymer fiber specimens are only studied for the purpose of comparison, they shows reasonably good properties, such as similar energy absorption level of steel fiber specimens.

REFERENCES

4.1 Pinchin, D.J., and D. Tabor, "Interfacial Contact Pressure and Friction Stress Transfer in Steel Fibre Cement." *Testing and Testing Methods of Fibre Cement Composites*, edited by R.N. Swamy, pp. 337-344 (1975)

4.2 Bowden, F.P. and D. Tabor, *The Friction and Lubrication of Solids*. Clarendon Press, Oxford, pp. 104-111 (1986)

4.3 Naaman, A.E., Namur, G.C., Alwan, J.M. & Najm, H.S. "Fiber Pullout and Bond Slip. II: Experimental Verification." ASCE J. Struct. Eng., Vol. 117, No. 9, pp. 2791-2808 (1991)

4.4 Naaman, A.E. and Shah, S.P. "Pull-out Mechanism in Steel Fiber-Reinforced Concrete." ASCE J. Struct. Div., Vol. 102, No. 8, pp. 1537-1548 (1976)

4.5 Li, Z., Mobasher, B. & Shah, S.P. "Characterization of Interfacial Properties in Fiber Reinforced Cementitious Composites." J. Am. Ceram. Soc., Vol. 74, No. 9, pp. 2156-2164 (1991)

Chapter 5. Fiber Pullout under Variable Compressive Stress

SYNOPSIS

The behavior of steel fiber pullout and the decay of interfacial friction under far field uniaxial lateral compressive stress σ_c depends on the decays of both the residual interfacial friction τ_{i0} (or misfit) and the interfacial friction coefficient $\bar{\mu}$ (surface asperity). This work proves experimentally that, for a given interface, a unique relationship exists between τ_{i0} and $\bar{\mu}$, which is independent of the histories of sliding distance s and lateral compressive stress σ_c, i.e. independent of the interfacial abrasion rate during the fiber pullout process. Based on the above observation, a damage model, which evaluates the residual interfacial friction τ_{i0} only, is developed to predict the pullout curves under variable lateral compressive stress. Using a forward difference formula and a τ_{i0} vs. $\partial\tau_{i0} / \partial s$ plot with a shifting scheme, one can predict the decay of interfacial friction when variable lateral compressive stress exists. Experimental verification shows that the model predicts the pullout curves under variable compressive stress well. A modified shifting scheme is developed to account for material variability and can be applied to practical problems without generating new τ_{i0} vs. $\partial\tau_{i0} / \partial s$ plots.

5.1 VARIABLE COMPRESSIVE STRESS

Fiber pullout is an important mechanism governing the fracture toughness of fiber reinforced composites. A typical fiber pullout curve consists of an initial rising part followed by a softening behavior (Fig. 2.2). In composites with low fiber volume fractions where multiple cracking is not achieved, the pre-peak behavior determines the first cracking strength of the composite while the post-peak behavior governs the energy absorption and hence the fracture toughness of the composite. At ultimate failure of concrete structures (Chapter 7), crack openings at the millimeter level are not uncommon. The determination of post-peak fiber pullout behavior (up to several mm's) is therefore important to quantify the energy absorption capability of the material when ultimate failure occurs.

The bridging stress depends on various micromechanisms including fiber debonding/pullout, fiber bending, fiber snubbing and matrix local spalling. This chapter focuses on the modeling of fiber pullout behavior and Chapter 6 will focus on fiber bending under mixed mode crack opening. Models for the other major mechanisms can also be found in [5.1] for debonding, [5.2] for fiber snubbing, and [5.3-5.4] for fiber bending and matrix local spalling.

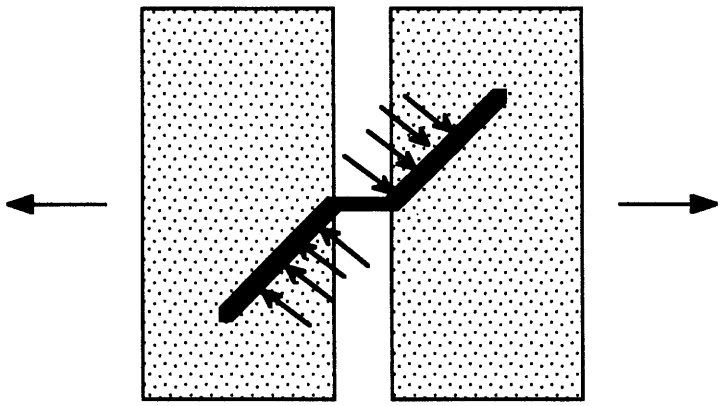

Figure 5.1 Inclined Fiber Pullout under Lateral Compression

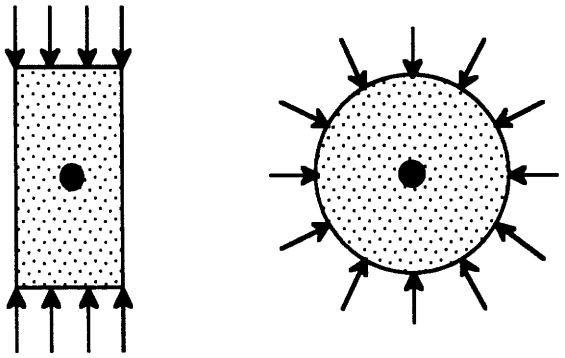

(a). Leung & Geng (b). Pinchin & Tabor

Figure 5.2 Two Testing Specimens with Different Lateral Compressive Stresses

Fiber pullout under zero far-field stress have been studied by Naaman, et al. [5.5-5.7] and reviewed in Section 2.3.2. However, fiber pullout in real structures can occur under the presence of lateral stresses (Fig. 4.1). Moreover, the lateral stress may vary as the crack opening increases (Fig. 5.1). Pinchin and Tabor [5.8] are the first to investigate the effect of lateral compressive stress. They tested steel wire pullout from a cement cylinder under uniform lateral stress. For the more practical case in Fig. 4.1, Leung and Geng [5.9] studied the fiber pullout under constant uniaxial lateral compressive stress and tension

(Chapter 4). Note that the experimental results are obtained with stresses applied along one direction perpendicular to the fiber (Fig. 5.2a) instead of uniform compressive stress (Fig. 5.2b) as in Pinchin and Tabor [5.8]. Fiber pullout with lateral stress along a single direction is more representative of practical situations involving shear cracks or splitting cracks, where cracks are moving along the direction of compressive principal stress.

From Fig. 4.13 in Chapter 4, one can see that the interfacial friction at the onset of debonding (s=0) is linearly dependent on the far field compressive stress and can be expressed as

$$\tau_i(0)|_{\sigma_c} = \tau_{i0}(0)|_{\sigma_c=0} + \bar{\mu}(0)\sigma_c(0) \tag{5.1}$$

where $\tau_i(0)$ is the interfacial friction under lateral compressive stress at s=0; the argument in the parentheses is the sliding distance s=0; $\tau_{i0}(0)$ is the initial interfacial friction under zero lateral compressive stress; σ_c is the lateral compressive stress; and $\bar{\mu}$ is the effective frictional coefficient (average over fiber surface). For the material composition tested in Fig. 4.13, $\tau_{i0}(0)$ = 5.263 MPa and $\bar{\mu}(0)$ = 0.123.

From Fig. 4.6, once can also see that increasing lateral compressive stress increases the initial interfacial friction but also leads to a more rapid decrease in interfacial friction with sliding. No attempt, however, was made in Chapter 4 to model the post-peak softening behavior and its sensitivity to lateral stress. The major objective of the present investigation is to develop a model for the pullout behavior of steel fibers from cementitious matrices, under any arbitrary variation of lateral compressive stresses.

5.2 PHYSICAL BASIS OF DAMAGE-BASED PULLOUT MODEL

Scanning electron microscopy (SEM) studies in Chapter 3 [5.10] indicated that the decrease in interfacial friction during fiber pullout is due to two mechanisms: (a) abrasion of the matrix surface, leading to reduction of misfit (or residual stress) between fiber and matrix groove, and (b) smoothening of both the cement and steel surfaces, leading to a reduction in frictional coefficient between the two surfaces. Both the above damage mechanisms are found to be more significant with increasing lateral compressive stress. To develop a model applicable to any lateral compressive stress history, the interfacial friction at any sliding distance, $\tau_i(s)$ can be considered to be composed of two separate parts at sliding distance s:

$$\tau_i(s) = \tau_{i0}(s) + \bar{\mu}(s)\sigma_c(s) \tag{5.2}$$

where $\tau_{i0}(s)$ is the residual friction due to fiber/matrix misfit, $\bar{\mu}(s)$ is an effective frictional coefficient, and $\sigma_c(s)$ is the lateral compressive stress. Note that both the residual friction and the effective frictional coefficient are functions of not only the sliding distance s but also the lateral compressive stress history $\sigma_c(s)$ during the sliding process (when $s = 0$, Eq. 5.2 reduces to Eq. 5.1) . To determine how τ_{i0} and $\bar{\mu}$ varies with σ_c and sliding distance s, pullout tests can be carried out under constant lateral compressive stress with interval unloading. (In Fig. 5.3 in next section, τ_{i0} can be calculated from the pullout load after unloading and $\bar{\mu}$ can be obtained from the load drop after unloading.) Since the removal of matrix in the groove and the smoothening of groove surface occurs simultaneously, it is postulated that $\bar{\mu}$ is a single-valued function of τ_{i0}, regardless of the lateral compressive stress history. Based on the experimental results, (a) a relation between τ_{i0} and $\bar{\mu}$, and (b) damage equations for τ_{i0} in terms of σ_c and s, can be obtained by empirical fitting. By differentiating the damage equations, $\partial\tau_{i0} / \partial s$ is obtained as a function of σ_c and τ_{i0}. The rate of damage with sliding, is hence expressed in terms of the applied lateral compressive stress and the current 'state' of the interface. Under any arbitrary lateral compressive stress history, the residual friction $\tau_{i0}(s)$ is then given by:

$$\tau_{i0}(s)|_{\sigma_c(s)} = \tau_{i0}(s)|_{\sigma_c(0)} + \int_0^s \frac{\partial\tau_{i0}}{\partial\xi}|_{\sigma_c(\xi),\tau_{i0}(\xi)}\, d\xi \tag{5.3}$$

Once $\tau_{i0}(s)$ is known, $\bar{\mu}(s)$ can be found from the $\bar{\mu}$ vs. τ_{i0} relation. The interfacial friction under the current lateral compressive stress level, $\tau_i(s)$, is calculated from Eq. 5.2.

5.3 EXPERIMENTAL PROCEDURE AND RESULTS

The experimental setup is a 2-D biaxial loading device described in detail in Chapter 3 (Fig. 3.8a). The size of the mortar specimen embedded with 10 mm steel fiber is shown in Fig. 3.4. The material properties are listed in Table 5.1.

Table 5.1 Coefficients of Cement Mortar and Steel Fiber

	Specimen Size (mm)	Young's Modulus (GPa)	Tensile Strength (MPa)	Other Strength (MPa)
Cement Mortar	25.4x12.7x9.5	22.3	3.6 (Splitting)	40 (Compres.)
Steel Fiber	0.25 (Radius)	200	1242	1040 (Yield)

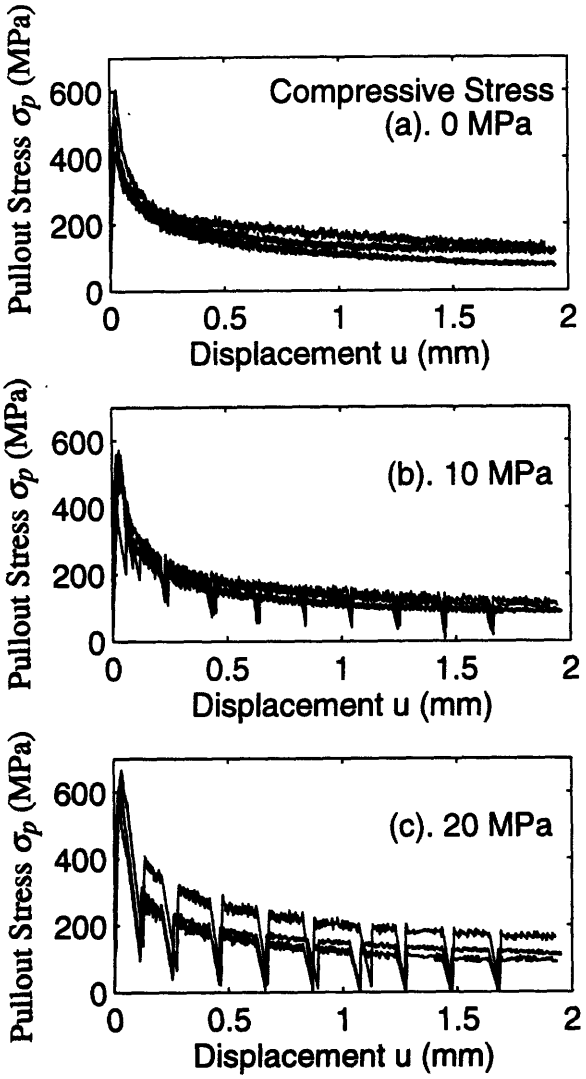

Figure 5.3 Pullout Test with Loading and Unloading of Lateral Stress
(First Series of the Experimental Tests)

Three series of experiments are carried out. In the first series, three sets of specimens are tested (Fig. 5.3) under uniform lateral compressive stresses of σ_c = 0, 10 and 20 MPa, respectively. For cases with non-zero σ_c, the pulling of the fiber is stopped at approximately every 0.2 mm after total debonding (s = 0). At each stop, the lateral stress is unloaded to zero. After recording the residual pulling load, the specimen is reloaded laterally before the fiber is further pulled out. The interfacial friction τ_i and interfacial

residual friction τ_{i0} are calculated respectively from the fiber stresses at points before and after unloading of lateral stress, by:

$$\tau_i(s) = \frac{R_f}{2(L-s)}\sigma_p(s) \tag{4.1}$$

where σ_p is the fiber stress at the pulling end (Chapter 4). In Fig. 5.4, each symbol type corresponds to one pullout curve. Figures 5.4a and 5.4b shows data points for the τ_i (larger value) and τ_{i0} (lower value) vs. s at each unloading point when lateral stresses are applied (10 and 20 MPa).

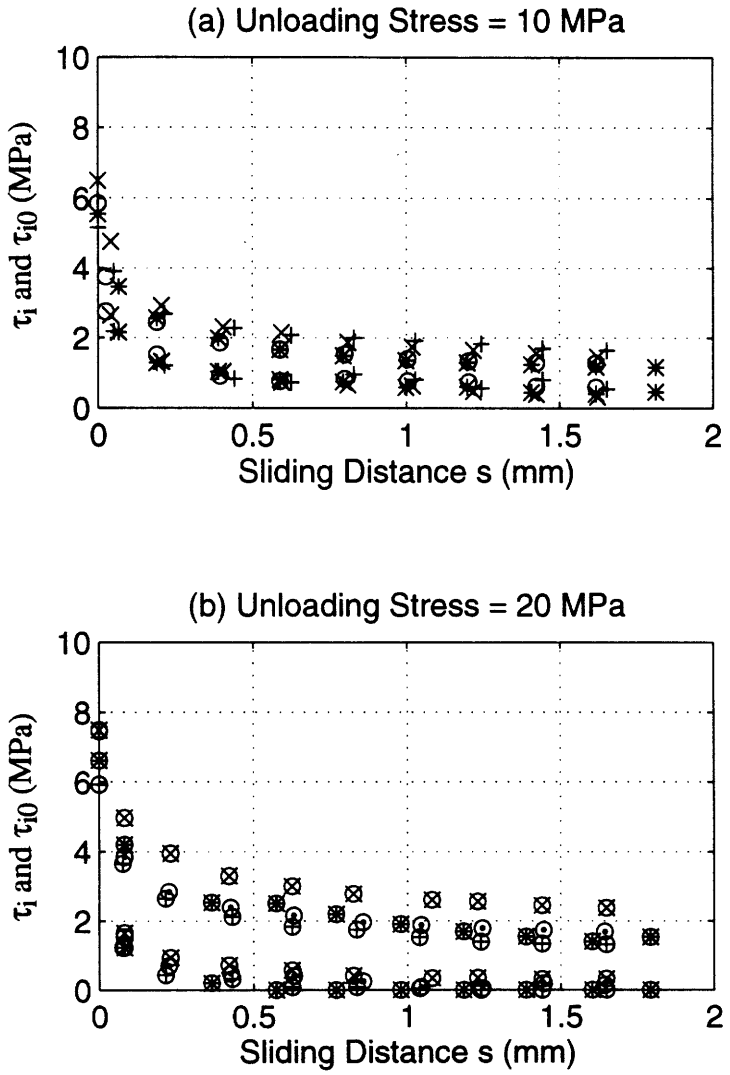

Figure 5.4 Interfacial Friction τ_i and Residual Friction τ_{i0} vs. Sliding Distance s

The second and third series of experiment (Figs. 5.19 and 5.20) were carried out to measure the pullout behavior of fibers under variable lateral compressive stress. The loading history employed and the results will be described in Section 5.5.3 on the verification of the fiber pullout model.

5.4 MODELING OF PULLOUT BEHAVIOR

5.4.1 Interfacial Residual Friction τ_{i0} and Effective Friction Coefficient $\bar{\mu}$

From the results of τ_i vs. s and τ_{i0} vs. s in Fig. 5.4, the effective friction coefficient $\bar{\mu}$ can be calculated from $\bar{\mu} = (\tau_i - \tau_{i0})/\sigma_c$. For each unloading point, $\bar{\mu}$ as a function of τ_{i0} is then plotted in Fig. 5.5. Note that identical symbols in Figs. 5.4 and 5.5 indicate data points from a single experimental pullout curve.

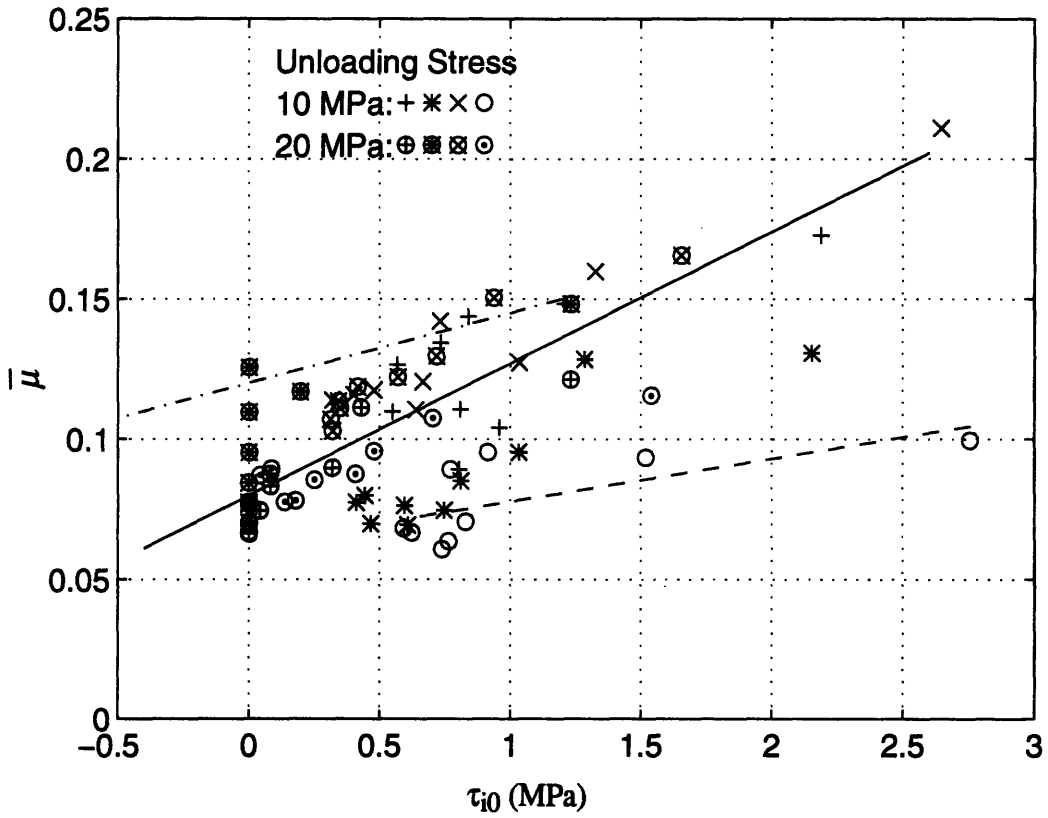

Figure 5.5 Relation of $\bar{\mu}$ vs. τ_{i0}

Figure 5.5 shows that regardless of loading history (sliding distance and lateral stress), all the data points for $\bar{\mu}$ and τ_{i0} appear to follow a linear relationship. This is consistent

with our postulation of a one-to-one relation between $\bar{\mu}$ and τ_{i0}. It is found that the outlying points are mainly from two particular tests, denoted by symbols 'o' and '◆'. The two exceptions may be due to different initial interfacial conditions resulted from mishandling during specimen mixing. The test with symbol 'o', which follows the dashed line, may be affected by the interface contamination with the demoulding oil, which reduces the surface roughness $\bar{\mu}$ to a higher extent than the residual friction τ_{i0}. The test with symbol '◆', which follows the dashdotted line, may be affected by the presence of a highly porous interfacial transition zone, which leads to a higher reduction in the residual friction τ_{i0} than the surface roughness $\bar{\mu}$.

From Fig. 5.5, the relation of $\bar{\mu}$ and τ_{i0} can be expressed empirically as:

$$\bar{\mu}(s) = \frac{\tau_{i0}(s)}{\tau'} + \mu' \tag{5.4}$$

where $\tau' = 21.28$ MPa reflects the rate of surface roughness decay with misfit; $\mu' = 0.08$ is the friction coefficient at the moment when the misfit layer is totally abraded (i.e. when $\tau_{i0} = 0$).

After the misfit (and τ_{i0}) reaches zero, further abrasion under lateral compressive stress will lead to the formation of a gap at the interface after unloading σ_c. In this model, τ_{i0} is allowed to decrease to a negative value. Negative τ_{i0} does not exist physically, but it represents a misfit (or gap) which has to be considered in the calculation of τ_i using Eq. 5.2 when lateral compressive stress is present and the gap can be closed. Substitute Eq. 5.4 into Eq. 5.2

$$\tau_i(s) = \left[1 + \frac{\sigma_c(s)}{\tau'}\right]\tau_{i0}(s) + \sigma_c(s)\mu' \tag{5.5}$$

Since the parameters τ' and μ' are known, τ_i is determined by τ_{i0} solely in Eq. 5.5. When τ_{i0} is negative, the $\bar{\mu}$ vs. τ_{i0} relation in Fig. 5.5 is assumed to follow a straight line extrapolated from the positive values, therefore, Eqs. 5.4 and 5.5 still apply. Then, if τ_i calculated from Eq. 5.5 is below zero, it means that the compressive stress is not high enough to close the gap and the interfacial friction τ_i should be set to zero.

5.4.2 History Dependent Residual Interfacial Friction

When the lateral compressive stress $\sigma_c(s)$ is given, one can see that the only unknown in Eq. 5.5 is τ_{i0}, which depends on loading history. For an incremental sliding Δs, τ_{i0} can

be obtain by the first order forward difference from the previous value and its changing rate based on Eq. 5.3

$$\tau_{i0}(s+\Delta s)|_{\sigma_c(s+\Delta s)} = \tau_{i0}(s)|_{\sigma_c(s)} + \frac{\partial \tau_{i0}}{\partial s}|_{\sigma_c(s+\Delta s),\tau_{i0}(s)}\,\Delta s \tag{5.6}$$

The first term in Eq. 5.6 can be obtained from previous increment step. When $s = 0$, the first term is the initial residual friction, and can be obtained by equating Eqs. 5.1 and 5.5, which gives alternative expressions for the interfacial friction at $s = 0$

$$\tau_{i0}(0)|_{\sigma_c(0)} = \frac{\tau_{i0}(0)|_{\sigma_c(0)=0} + [\bar{\mu}(0) - \mu']\sigma_c(0)}{1 + \dfrac{\sigma_c(0)}{\tau'}} \tag{5.7}$$

Where $\tau' = 21.28$ MPa, $\mu' = 0.08$ from Fig. 5.5 and Eq. 5.4; for the first series of the test in Fig. 5.3, when lateral stress $\sigma_c(0) = 0$, the initial interfacial friction at the onset of debonding $\tau_{i0}(0) = 5.3020$ MPa from Fig. 5.6 and the initial interfacial friction coefficient $\bar{\mu}(0) = 0.0745$ from Eq. 5.4, which is different from Fig. 4.13 because of material variability. When lateral stress $\sigma_c(0)$ is not zero, the initial residual friction varies (Eq. 5.7) as shown in Fig. 5.7. The effect of material variability is more significant when lateral stress is large.

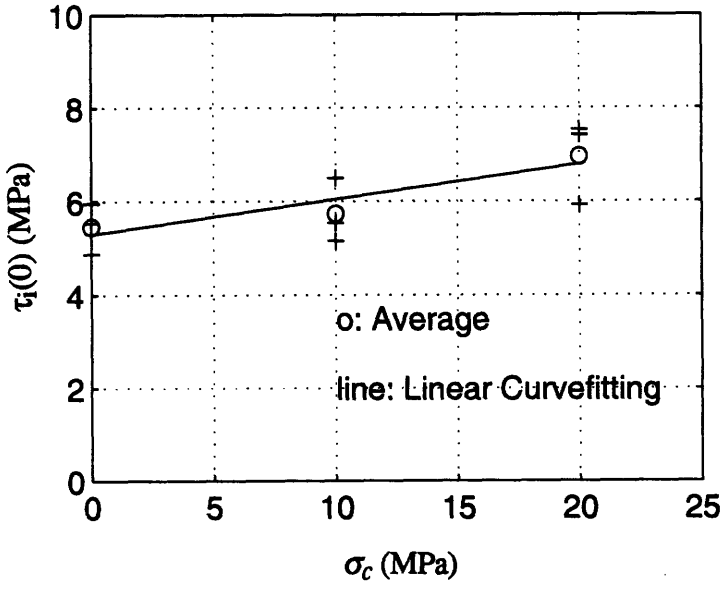

Figure 5.6 Interfacial Friction vs. Lateral Compression at the onset of Debonding (From Post-peak Pullout Load at $s = 0$)

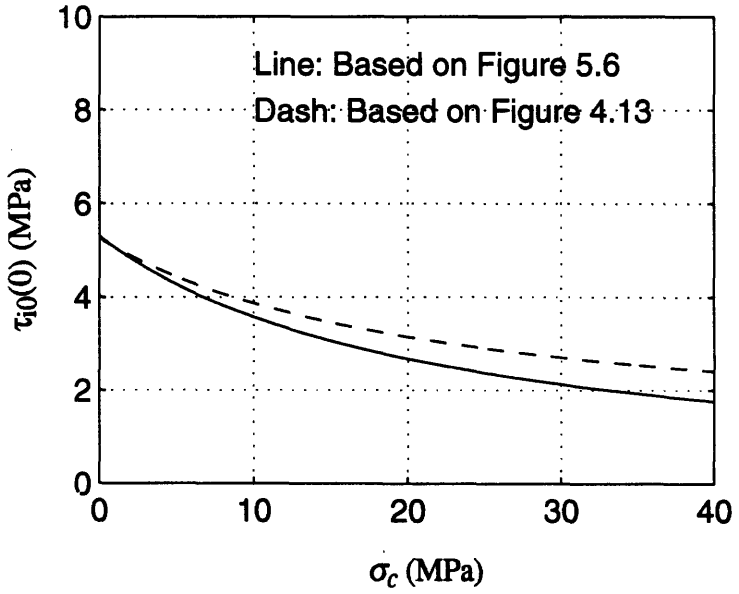

Figure 5.7 Interfacial Residual Friction τ_{i0} vs. Lateral Compressive Stress σ_c

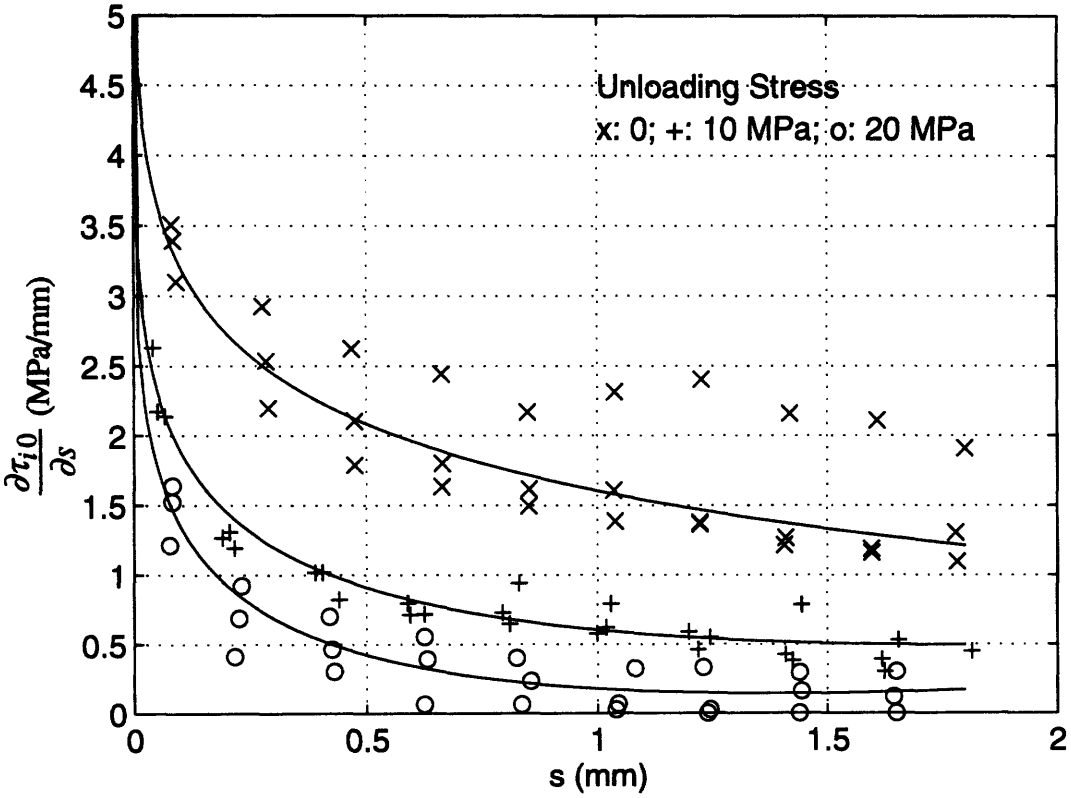

Figure 5.8 Fitting Experimental Data by Modified Naaman's Formula

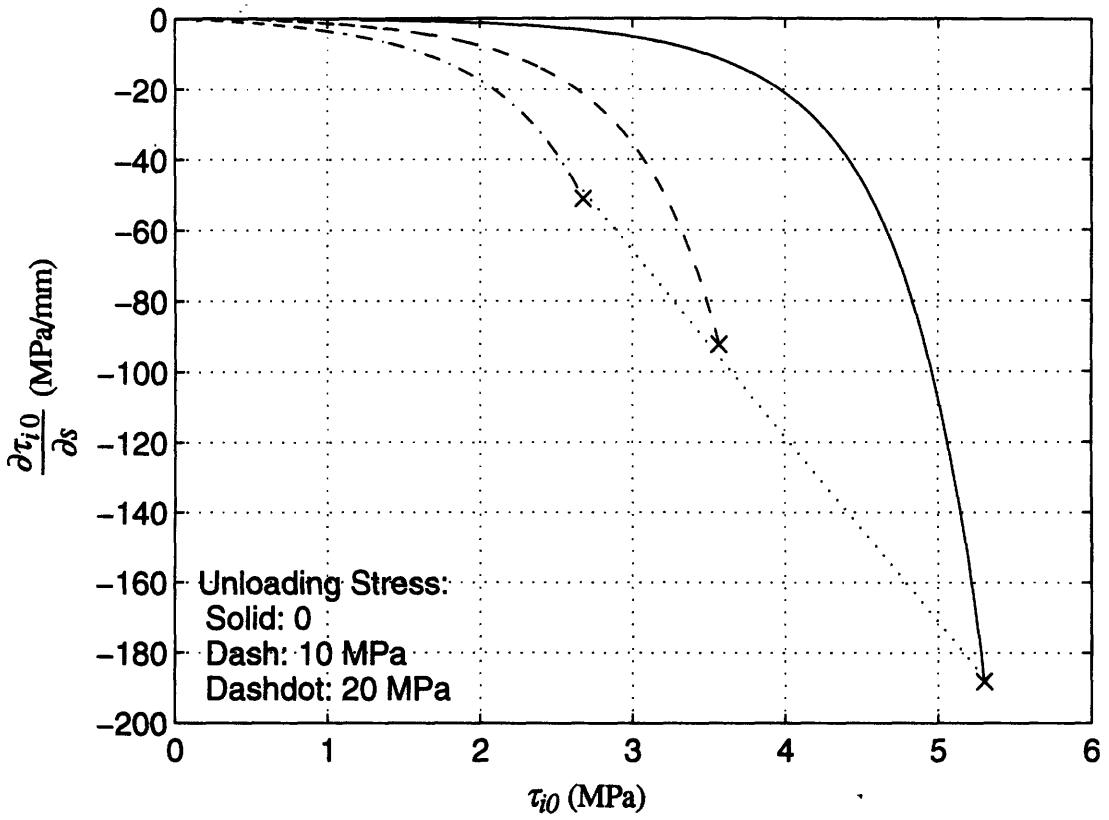

Figure 5.9 $\partial \tau_{i0} / \partial s$ vs. τ_{i0} curves under Different Lateral Compressive Stress σ_c

To evaluate the second term in Eq. 5.6, τ_{i0} is first obtained as a function of s and differentiated to get $\partial \tau_{i0} / \partial s$. Figure 5.8 shows the data for $\tau_{i0}(s)$ under different lateral compressive stress (taken from Figs. 5.3 and 5.4) together with the fitting curves. The data are first fitted with a high order polynomial for each pullout curve, then average the polynomials, and finally fitted the average polynomial with Naaman's formula (Eq. 2.5), with two modifications, (a) the Poisson's ratio term taken to be unity, and (ii) the addition with a linear term to obtain better fits.

$$\tau_{i0}(s) = \tau_{i0}(0)\frac{\exp[-s^{\eta}] - \xi \exp[-L^{\eta}]}{1 - \xi \exp[-(L-s)^{\eta}]} + \alpha s + \beta \qquad (5.8)$$

where α, β, ξ, η are fitting coefficients. $\xi = 1.0$ and $\eta = 0.2$ are constants under different compressive stresses. By differentiating the modified Naaman's formula (Eq. 5.8), $\partial \tau_{i0} / \partial s$ vs. τ_{i0} under different compressive stress are obtained and plotted in Fig. 5.9. The starting point is the point where sliding starts at total debonding (symbol 'x'). The x-coordinate (τ_{i0} value) of this point is calculated from Eq. 5.7 (Solid line in Fig. 5.7).

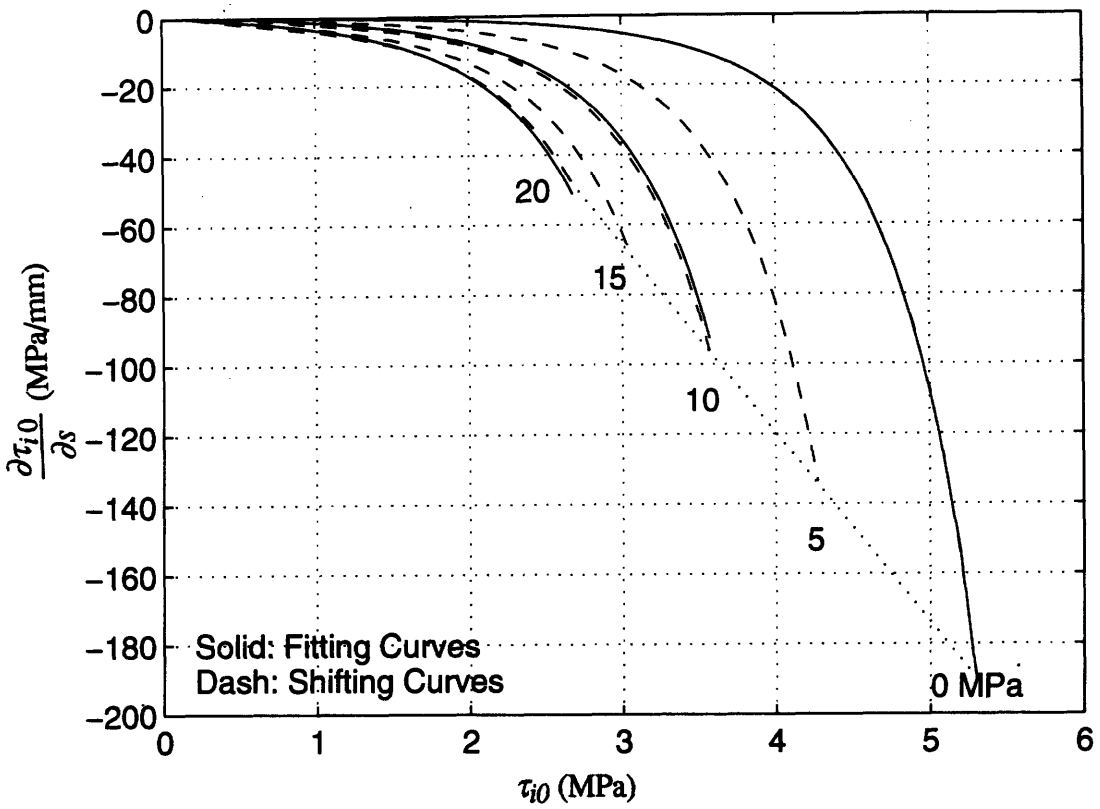

Figure 5.10 A Shifting Scheme for $\partial \tau_{i0} / \partial s$ vs. τ_{i0} curves under Different Lateral Stress

From Fig. 5.9, it is observed that the curves for the three compressive stresses follow very similar shapes. The curve for $\partial \tau_{i0} / \partial s$ under finite compressive stress can then be obtained by shifting the curve corresponding to zero lateral compressive stress. The shifting is done in the following manner illustrated in Fig. 5.10. In Fig. 5.9, a straight line of slope $k = 54$ mm^{-1} is drawn from the starting point of the zero compressive stress curve (dotted line in Figs. 5.9 and 5.10). For the curve corresponding to a finite compressive stress σ_c, the starting point is the intersection of $\tau_{i0}(0)$ from Eq. 5.7 and the dotted line in Fig. 5.10. By shifting the zero compressive stress curve horizontally until it pass through the intersecting point, the curves (dashed lines) under different compressive stress are obtained.

The curve shifting scheme described above overestimates $\partial \tau_{i0} / \partial s$ in the late pullout stage, when both τ_{i0} and $\partial \tau_{i0} / \partial s$ become small. A modification is therefore made when $\tau_{i0}(s) < 1$ MPa. In this regime, $\partial \tau_{i0} / \partial s$ is described by a straight line between points A and B (Fig. 5.11), where point A is the interception of the experimental fitting curves on the τ_{i0} axis (solid lines)

$$\tau_{i0}(\infty) = 0.8MPa - 0.033\sigma_c(s) \tag{5.9}$$

and point B is the upper bound of the late pullout stage τ_B = 1 MPa. The value of $\partial\tau_{i0} / \partial s$ at the upper bound is obtained from the shifted curve when $\tau_{i0}(s)$ = 1 MPa. Figure 5.11 shows that the modification (dashed lines when τ_{i0} < 1 MPa) represents the experimental fitting curves (solid lines) well. The expressions of the whole modified shifting scheme is given as following: for $\sigma_c(s) = 0$, which is equivalent to the modified Naaman's formula

$$\frac{\partial\tau_{i0}}{\partial s}\Big|_{\sigma_c=0} = F(\tau_{i0}) \tag{5.10a}$$

And for $\sigma_c(s) > 0$ (compressive stress), which is the modified shifting scheme

$$\frac{\partial\tau_{i0}}{\partial s}\Big|_{\sigma_c} = \begin{cases} F(\tau_{i0} - \tau_{shift}), & if\ \tau_B \le \tau_{i0}(s) \le \tau_{i0}(0) \\ \dfrac{\tau_{i0}(s) - \tau_{i0}(\infty)}{\tau_B - \tau_{i0}(\infty)} F(\tau_B - \tau_{shift}), & if\ \tau_{i0}(\infty) \le \tau_{i0}(s) \le \tau_B \\ 0, & if\ \tau_{i0}(s) > \tau_{i0}(\infty) \end{cases} \tag{5.10b}$$

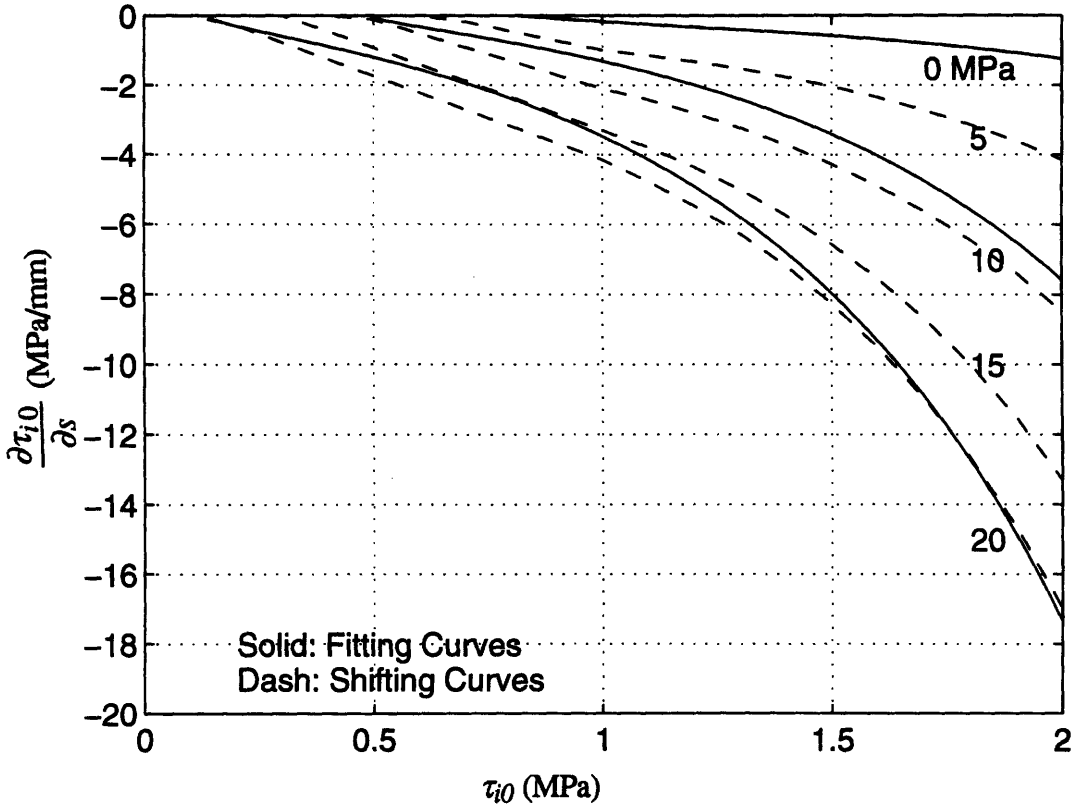

Figure 5.11 Modification of the Shifting Scheme at Late Pullout Stage

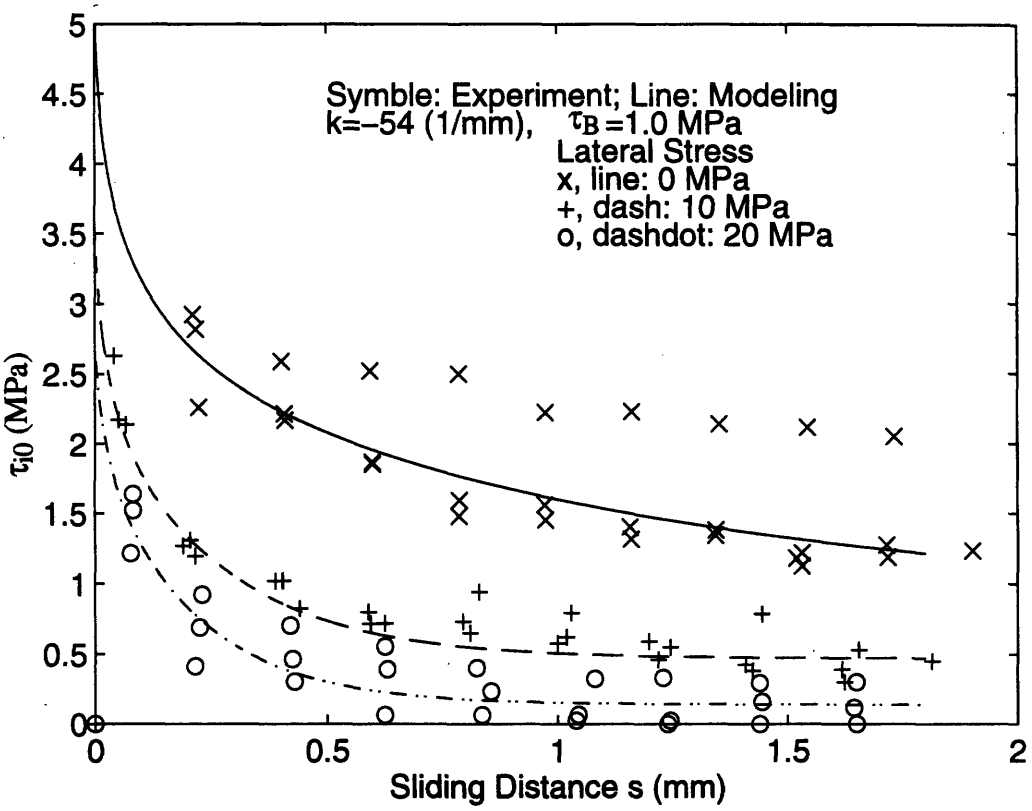

Figure 5.12 Back-fitting Interfacial Residual Friction

Where τ_{shift} is the magnitude of curve shifting along the τ_{i0} axis determined by slope k and $\tau_{i0}(0)$ in Eq. 5.7. $\tau_{i0}(\infty)$ and τ_B are the lower and upper bounds of the late sliding stage.

In order to verify the validity of the shifting scheme, Eq. 5.6 is used to calculate the τ_{i0} vs. s relation under 0, 10 and 20 MPa compressive stress. Comparison between the predicted curve and experimental results (from Figs 5.3 and 5.4) shows very good agreement (Fig. 5.12).

5.5 DISCUSSION AND EXPERIMENTAL VERIFICATION

5.5.1 Calculation of $\tau_{i0}(s)$

Figure 5.13 shows two cases for calculating $\tau_{i0}(s)$. For incremental sliding Δs along Path A, the first term in Eq. 5.6 can be taken from the previous increment $\tau_{i0}(s)$. Since the second term in Eq. 5.6 depends on $\partial\tau_{i0} / \partial s$, when $\sigma_c(s) = \sigma_1$ changes to $\sigma_c(s+\Delta s) = \sigma_2$, $\tau_{i0}(s)$ determines $\partial\tau_{i0} / \partial s$ from the curve corresponding to $\sigma_c(s+\Delta s)$ along Path A.

For the other case, when σ_c increases, $\tau_{i0}(0)$, the starting point for a particular $\partial\tau_{i0} / \partial s$ vs. τ_{i0} curve, decreases. As a result, when σ_c increases in the early pullout stage, a value for $\partial\tau_{i0} / \partial s$ may not exist at the value $\tau_{i0}(s)$ for the shifting curve $\sigma_c(s+\Delta s) = \sigma_2$. In such cases, $\partial\tau_{i0} / \partial s$ is taken as the initial value of the new curve under $\sigma_c(s+\Delta s)$ by Eq. 5.7 (Path B in Fig. 5.13).

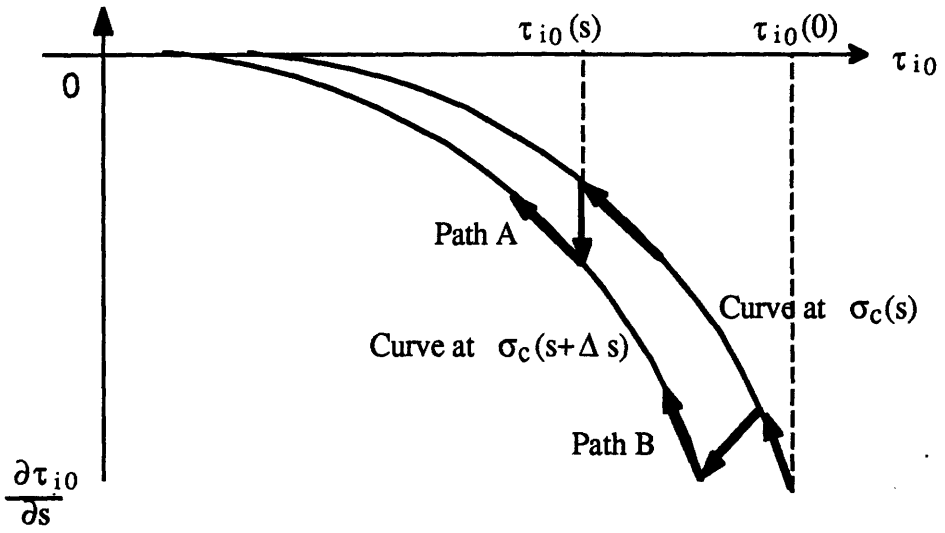

Figure 5.13 Determination of $\partial\tau_{i0} / \partial s$ by $\sigma_c(s)$ and $\tau_{i0}(s)$

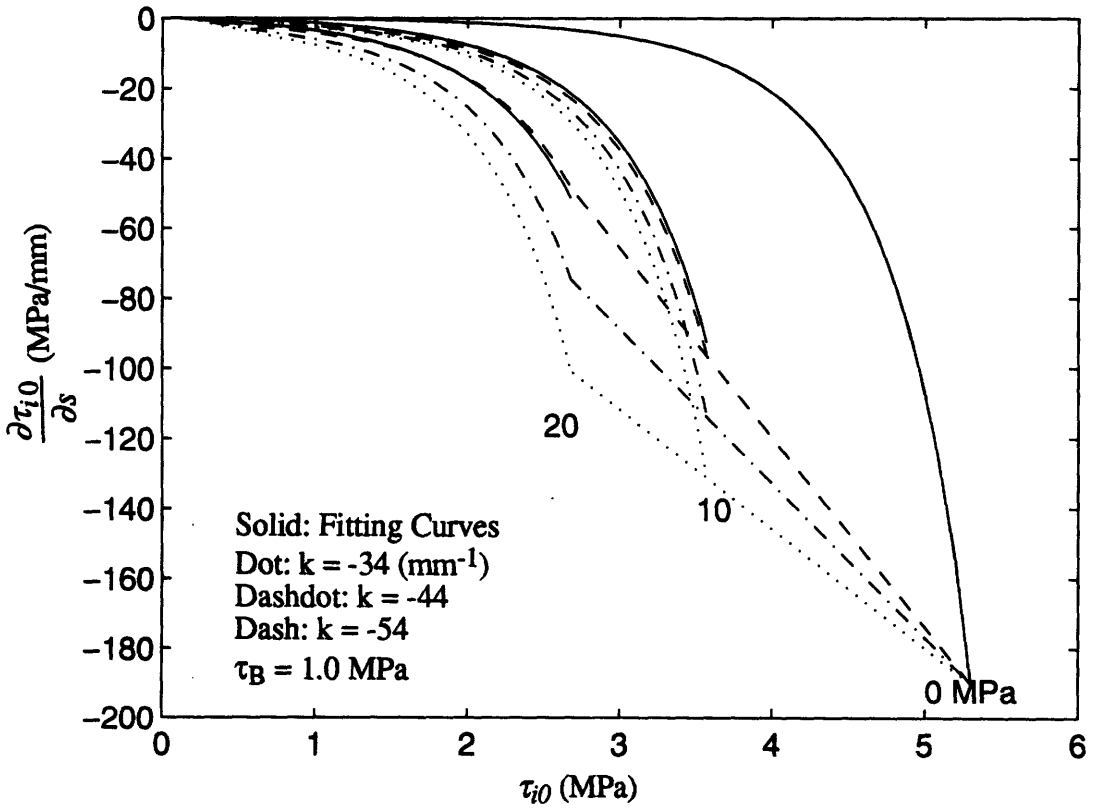

Figure 5.14 Shifting Scheme under Different Value of Slope k

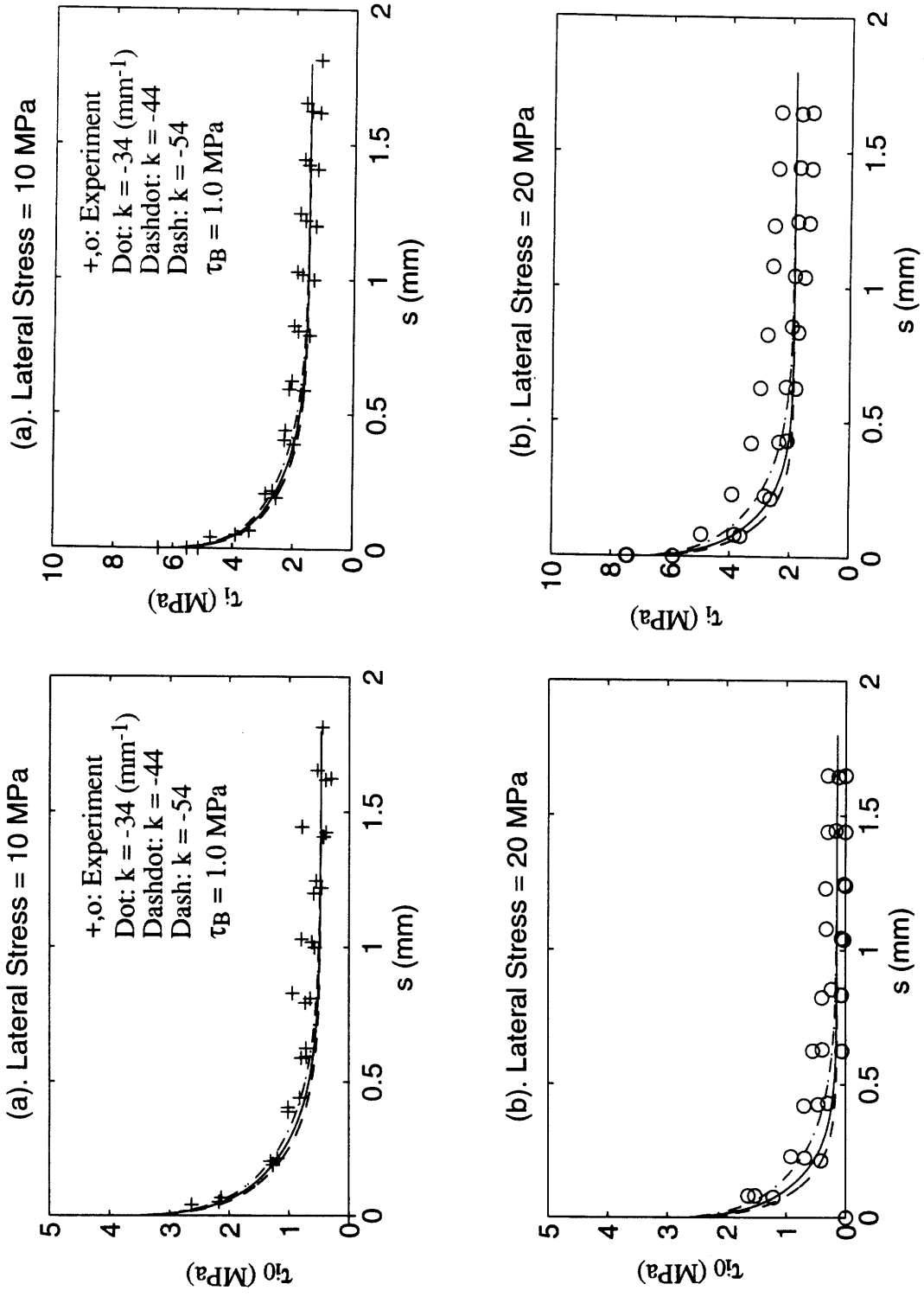

Figure 5.15 Results of τ_i and τ_{i0} vs. s under Different k

5.5.2 Effect of Slope k and Upper Bound of the Late Pullout Stage τ_B

The amount of shifting for curve under non-zero compressive stress is affected by the slope k of the dotted line in Fig. 5.10. Also, at the later pullout stages (τ_{i0} < 1 MPa), the shifted curve is replaced by a straight line using Eq. 5.9. Since both k and τ_B = 1 MPa are chosen from better curve fitting and not physical ground, it is important to carry out a parametric studies to assess the sensitivity of k and τ_B.

Figure 5.14 shows the shifted curves under three different values of k, which results in different $\partial\tau_{i0} / \partial s$, but same initial $\tau_{i0}(0)$ determined by Eq. 5.7. Predicted $\tau_i(s)$ and $\tau_{i0}(s)$ curves for different k values are compared with experimental results in Fig. 5.15. It is clear that the predicted curves are not sensitive to the variation in k. A change in k only slightly affects the amount of shift, although it can significantly change the starting value of $\partial\tau_{i0} / \partial s$. This indicates that the predicted pullout behavior is not sensitive to both k and the starting value $\partial\tau_{i0} / \partial s$.

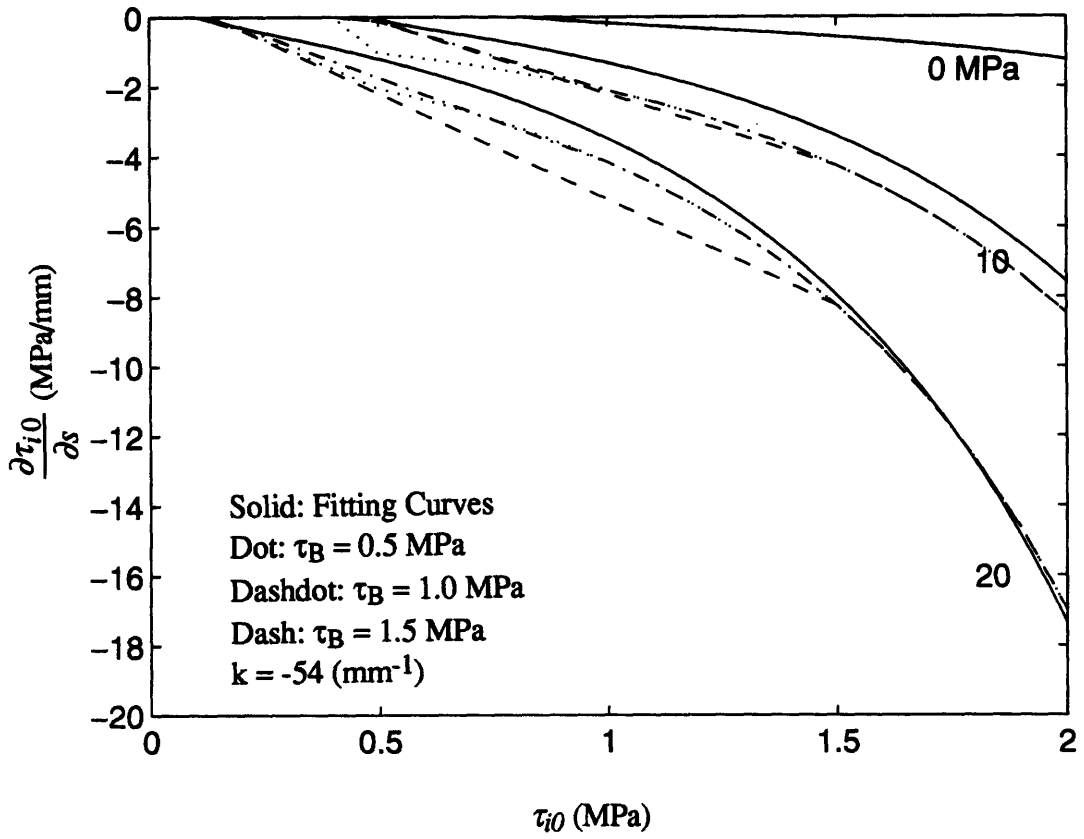

Figure 5.16 Shifting Scheme under Different Value of Upper Bound τ_B

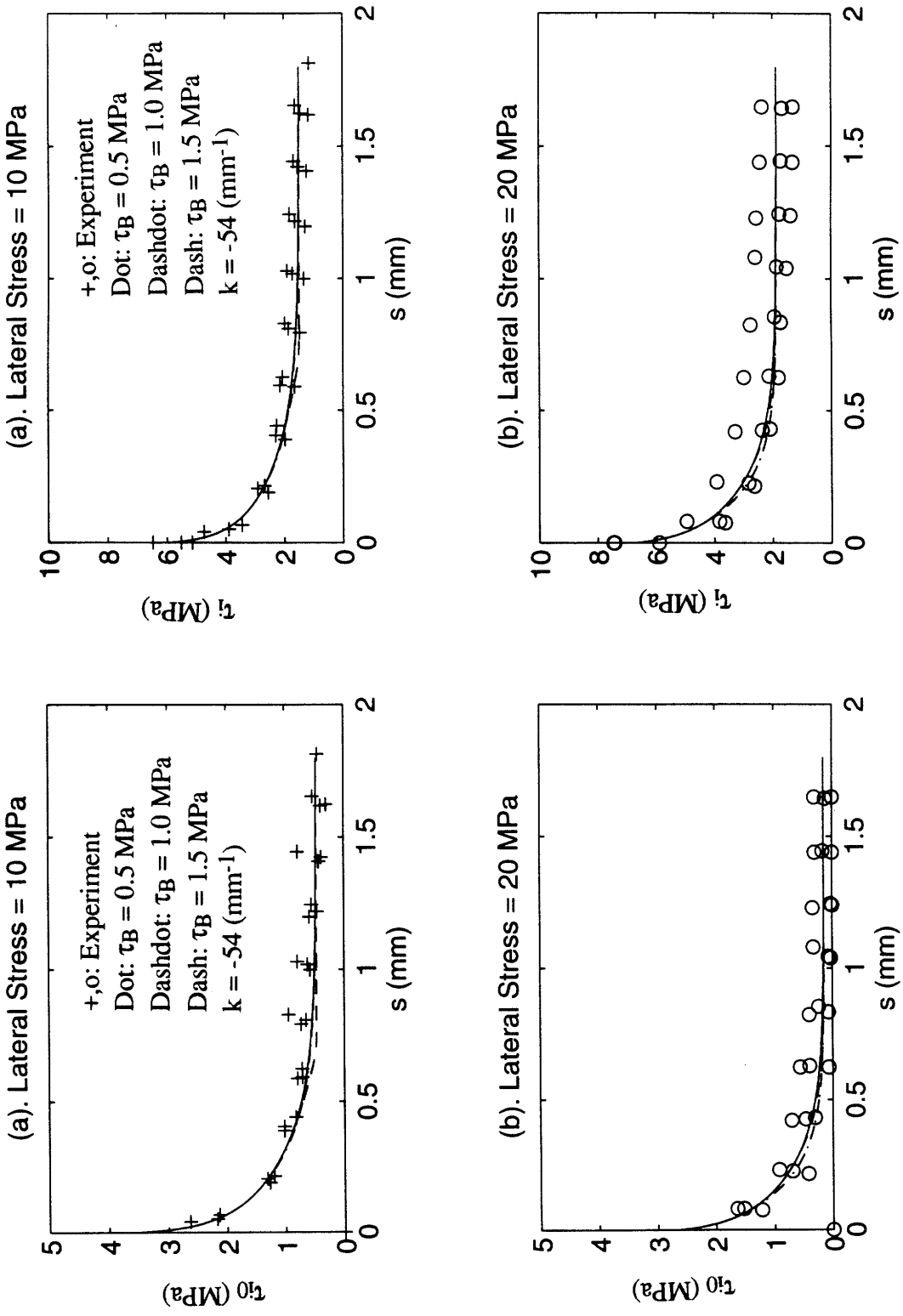

Figure 5.17 Results of τ_i and τ_{i0} vs. s under Different τ_B

The effect of the bound of late pullout stage τ_B is also investigated in a similar way with three different values (Fig. 5.16). Figure 5.17 shows that the variation of bound has very little effect on $\tau_i(s)$ and $\tau_{i0}(s)$, either. Therefore, the shifting scheme of the τ_{i0} vs. $\partial\tau_{i0} / \partial s$ plots can be used reliably to predict the pullout curves.

5.5.3 Experimental verification

In order to verify the model, fiber pullout tests under variable lateral compressive stresses are performed. Three loading histories are employed with each history consisting of five pullout stages. At each stage, a constant lateral compressive stress is applied (Fig. 5.18). Figure 5.19 shows the comparison of the experimental results (solid lines with the interfacial stick-slip effect during fiber pullout) with the damage model prediction (smooth solid lines).

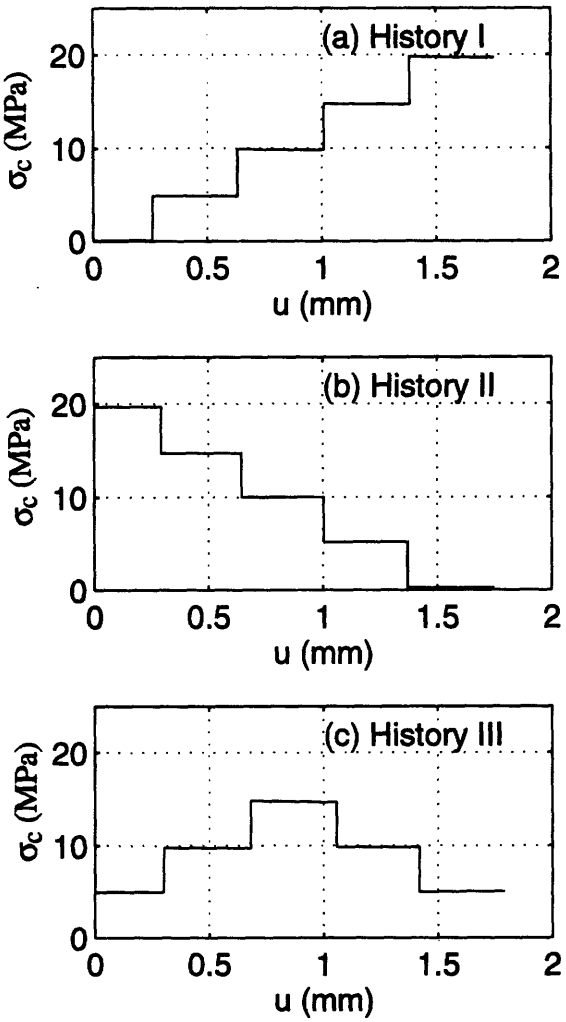

Figure 5.18 Loading History of Lateral Compressive Stress

Because of the difficulty of the test, only five complete curves were obtained at the first trial. For history I, the model does not agree well with the experimental results due to possible fiber surface contamination or material variability. For Histories II & III, the theory and the experiment agrees very well, except some underestimation at the very last stage. The underestimation may be caused by the interfacial spalling of unlocked particles. When lateral compressive stress is unloaded from a higher load and approaches zero, some particles spalled from the severely abraded mortar surface may 'jam' the interface and result in an increase in pullout load at the late pullout stage.

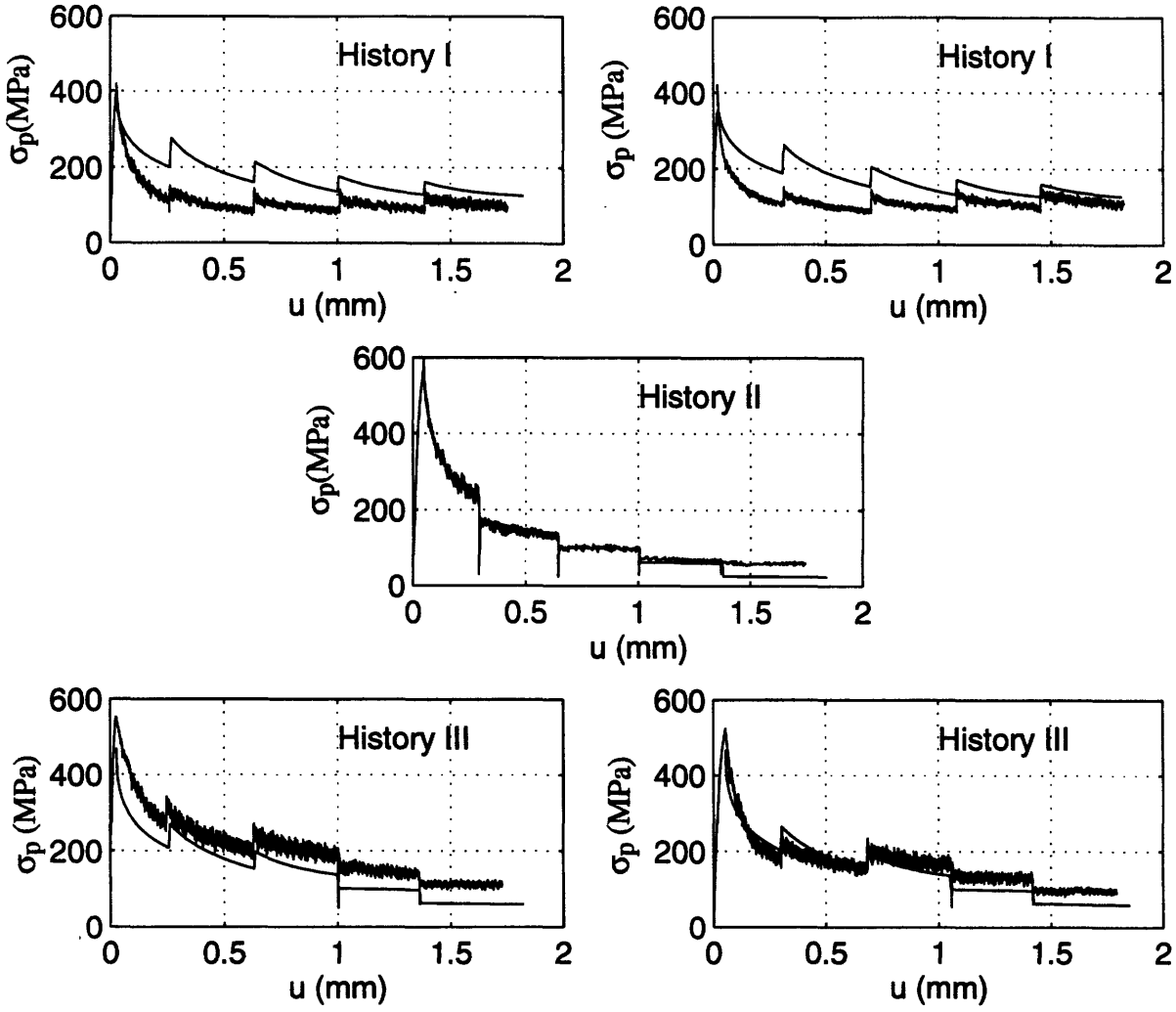

Experimental Results: Solid Lines with Slip-Stick Effect;
Damage Model Prediction: Smooth Solid Lines

Figure 5.19 Experimental Verification (Second Series of Experimental Tests)

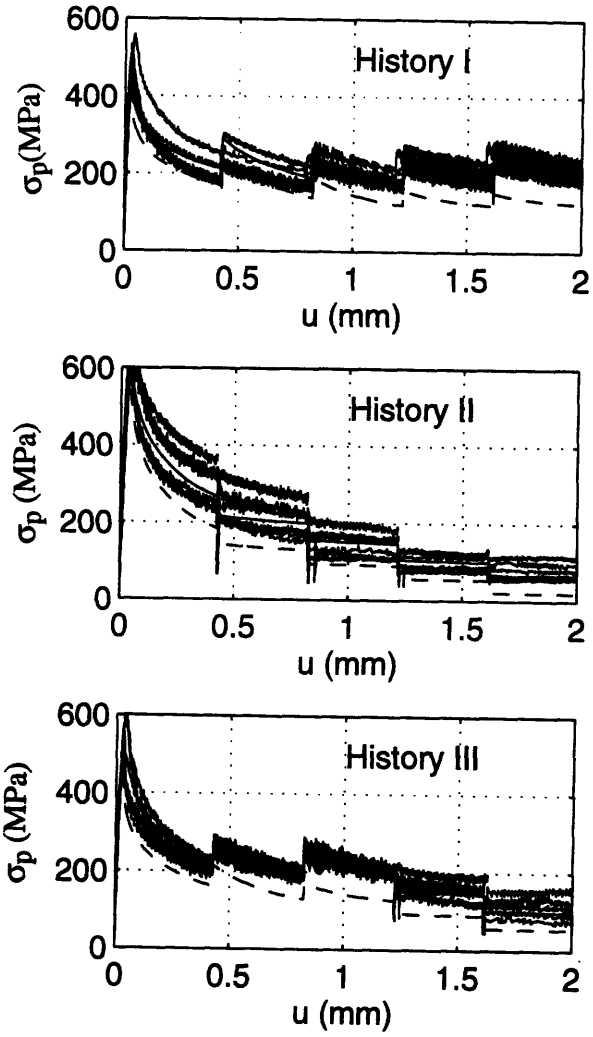

Experimental Results: Solid Lines with Slip-Stick Effect;
Original Damage Model Prediction: Smooth Dashed Lines
Modified Damage Model Prediction ('All-Curve' Shifting): Smooth Solid Lines

Figure 5.20 Experimental Verification (Third Series of Experimental Tests)

Another set of test was done months later with different bags of cement and mortar . The material variability resulted in higher value of the pullout curves and the damage model (dash in Fig. 5.20) based on previous test underestimate the experimental data. In order to count on the material variability which happens in practice, an 'all-curve' shifting scheme is employed in Fig. 5.21. The modified shifting curves (solid) is obtained by shifting all the original shifting curves (dash in Figs. 5.10 and 5.21) by an amount of

$$\Delta\tau = \tau_{i0}(0)|_{Modified} - \tau_{i0}(0)|_{Original} \tag{5.11}$$

where $\tau_{i0(0)/Original}$ = 5.3020 MPa when $\sigma_c = 0$ is the value from the previous test in Eq. 5.7, which established the damage model in Section 5.4; $\tau_{i0(0)/Modified}$ is calculated from the post-peak value of the pullout curves under zero lateral stress when material variability is significant (Eq. 4.1 at $s = 0$ and $\sigma_c = 0$). The pullout curves (solid lines in Fig. 5.20) calculated from the modified scheme (solid line in Fig. 5.21) agree very well with the experiment data.

In practice, material variability is inevitable. Using the 'all-curve' shifting scheme, the only test required is fiber pullout up to total debonding under zero σ_c. From the pullout curve, the post-peak $\sigma_{postpeak}$ can be identified and $\tau_{i0(0)/Modified}$ can be obtained from the post-peak load.

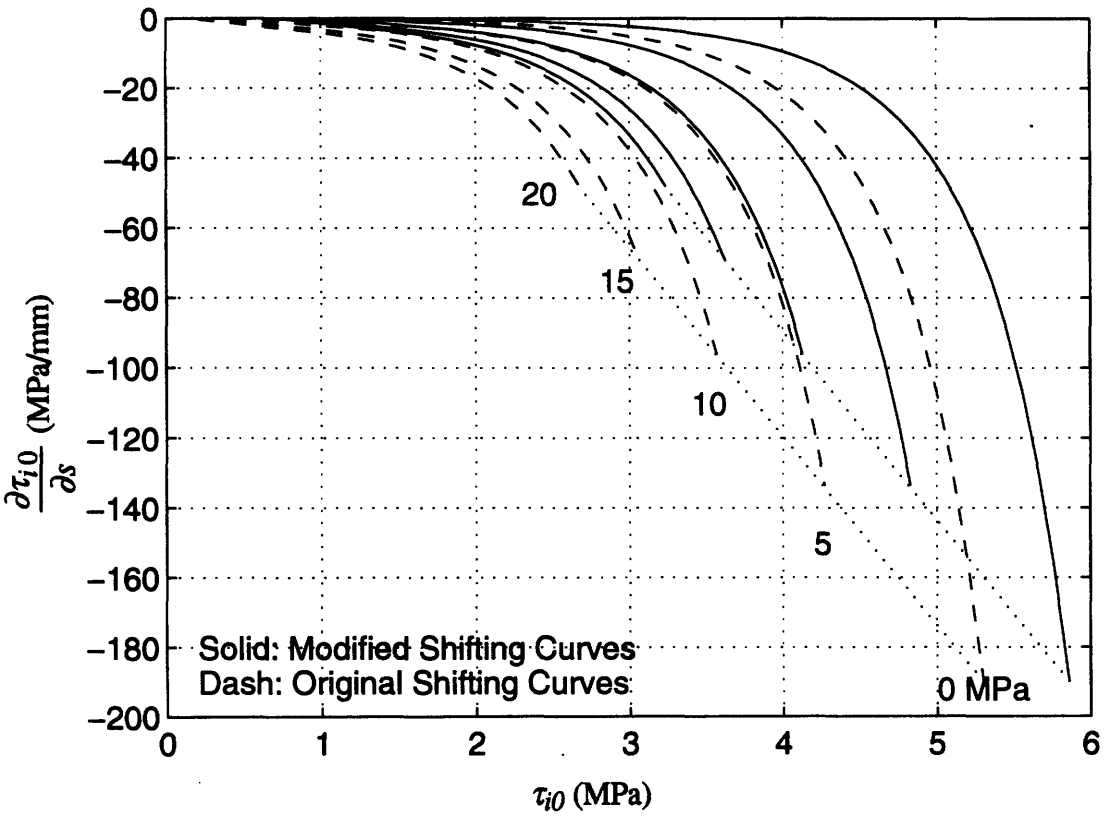

Figure 5.21 'All-Curve' Shifting Scheme for Material Variability

5.6 CONCLUSIONS

The decrease in interfacial residual friction (i.e. fiber/matrix misfit) and the decrease in interfacial roughness (or effective interfacial friction) occurs simultaneously by abrasion

during fiber pullout. Although the abrasion rate may differ under different loading history, $\bar{\mu}$ and τ_{i0} follow a unique linear relationship for same initial interfacial conditions. Since $\partial\tau_{i0} / \partial s$ vs. τ_{i0} curves for different lateral compressive stress levels are similar in shape, the effect of lateral compressive stress on the $\partial\tau_{i0} / \partial s$ vs. τ_{i0} curve can be conveniently modeled with a shifting scheme. The experimental results verifies that the damage model can predict accurately the pullout curves under variable lateral compressive stress history. An 'all-curves' shifting can count material variability for practical applications.

REFERENCES

5.1 Leung, C.K.Y., "Fracture-Based Two-Way Debonding Model for Discontinuous Fibers in Elastic Matrix." ASCE Journal of Engineering Mechanics, Vol. 118, No. 11, pp. 2298-2318 (1992)

5.2 Li, V.C., Y. Wang, and S. Backer, "Effect of Inclining Angle, Bundling and Surface Treatment on Synthetic Fiber Pull-out from a Cement Matrix." Composites, Vol. 21(2), pp. 132-140 (1990)

5.3 Leung, C.K.Y. and V.C. Li, "Effect of Fiber Inclination on Crack Bridging Stress in Brittle Fiber Reinforced Brittle Matrix Composites." J. Mat. Phy. Solid, Vol. 40, No. 6, pp. 1333-1362 (1992)

5.4 Leung, C.K.Y. and J. Chi, "Derivation of Crack Bridging Force in Random Discontinuous Fiber Composites through Micromechanics." in press ASCE J. Eng. Mech (1995)

5.5 Naaman, A.E., G.C. Namur, J.M. Alwan, and H.S. Najm, "Fiber Pullout and Bond Slip. I: Analytical Study." ASCE J. of Structural Engineering, Vol. 117, No. 9, pp. 2769-2790 (1991)

5.6 Naaman, A.E., G.C. Namur, J.M. Alwan, and H.S. Najm, "Fiber Pullout and Bond Slip. II: Experimental Verification." ASCE J. Struct. Eng., Vol. 117, No. 9, pp. 2791-2808 (1991)

5.7 Naaman, A.E., and Shah, S.P., "Pull-out Mechanism in Steel Fiber-Reinforced Concrete." ASCE J. of Structural Division, Vol. 102, ST8, pp. 1537-1548 (1976)

5.8 Pinchin, D.J., and Tabor, D., "Inelastic Behaviour in Steel Wire Pull-out from Portland Cement Mortar." Journal of Material Science, Vol. 13, pp. 1261-1266 (1978)

5.9 Leung, C.K.Y., and Geng, Y., "Effect of Lateral Stresses on Fiber Debonding and Pullout." to appear in J. Comp. Engrg. (1995)

5.10 Geng, Y., and Leung, C.K.Y., "A Microstructural Study of Fiber/Mortar Interfaces during Fiber Debonding and Pullout." to appear in J. Mat. Sci. (1995)

Chapter 6. Fiber Pullout under Mixed Mode Crack Opening

SYNOPSIS

Crack propagation in fiber reinforced concrete is governed by stresses provided by fibers along the crack bridging zone. To predict the behavior of fiber reinforced structural components under general loading conditions (where mixed mode crack propagation is possible), the normal and shear stresses acting on a crack as a function of crack opening and shearing displacements need to be obtained. In this investigation, a mixed mode fiber pullout setup is designed to measure both the opening and shearing bridging forces as a fiber is simultaneously pulled and sheared. Experimental results on steel fiber reinforced mortar reveal (a) the opening and shearing bridging forces are dependent on both the opening and shearing displacements, and (b) the lateral stress on the fiber and the spalling of matrix have important effects on the crack bridging forces.

A micromechanical model is established for the mixed mode crack opening based on a model of an elasto-plastic beam (fiber) on an elastic foundation (matrix) with spalling. The effect of lateral stress on fiber during pullout process (Chapter 5) and a constant matrix pre-spalling depth model are incorporated into the micromechanical model. The modeling results agree well with the experimental data. The work lays the foundation for simulation of FRC structural behavior.

6.1 MODE I CRACK AND MIXED MODE CRACK

Crack propagation in FRC materials is governed by the bridging stresses at the wake of the crack. To assess the effectiveness of fiber bridging, the fiber pullout test is widely used to measure the bridging force provided by the fiber as it is debonded and pulled out of the matrix groove [6.1-6.3]. When fiber is not perpendicular to a crack plane, the pullout mechanism involves both debonding and bending and the extracted interfacial parameters (τ_i and τ_s) in Chapter 4 are not enough to describe the problem. Micromechanical models need to be established to include fiber bending and yielding. Most of the experimental results reported in the literature are on a fiber (perpendicular or

inclined to the crack surface) pulled along a direction normal to the specimen (crack) surface. The results are only applicable to structural failure with pure mode I crack opening under an uniaxial tensile field (Fig. 6.1a). In Section 2.4, research on inclined fiber pullout under Mode I crack opening has been thoroughly reviewed.

In many common failure modes, such as the shear failure of beams (Fig. 1.5), there are both opening and shearing displacements along the crack (Fig. 6.1b). To develop a general model for fracture propagation in FRC, the effects of combined fiber pulling/shearing (hereafter referred to as fiber pullout under mixed mode crack opening) need to be addressed.

In this Chapter, a novel experimental setup which can be employed for mixed mode fiber pullout is first described. Some typical experimental results obtained with the setup is presented. Micromechanical model for mixed mode crack opening is developed based on the experimental findings.

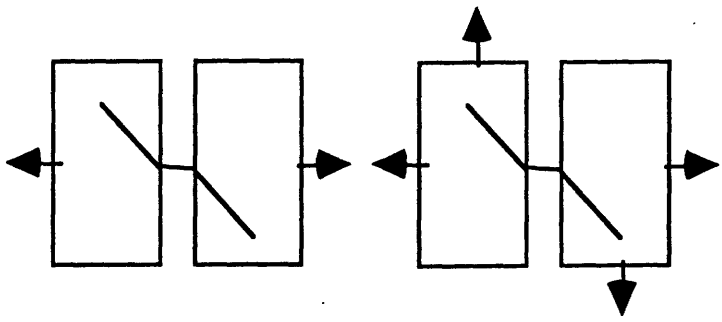

(a) Mode I Crack (b) Mixed Mode Crack

Figure 6.1 Mode I Crack and Mixed Mode Crack

6.2 EXPERIMENTAL PROCEDURE

6.2.1 Experimental Setup

To experimentally measure the bridging forces from a fiber pulled under mixed mode crack opening, the setup should allow independent displacement and load measurements in two orthogonal directions. Moreover, it should provide the capacity to introduce any loading path for the specimen (i.e., any combined histories of opening and shearing). A design of such a setup is shown in Fig. 6.2.

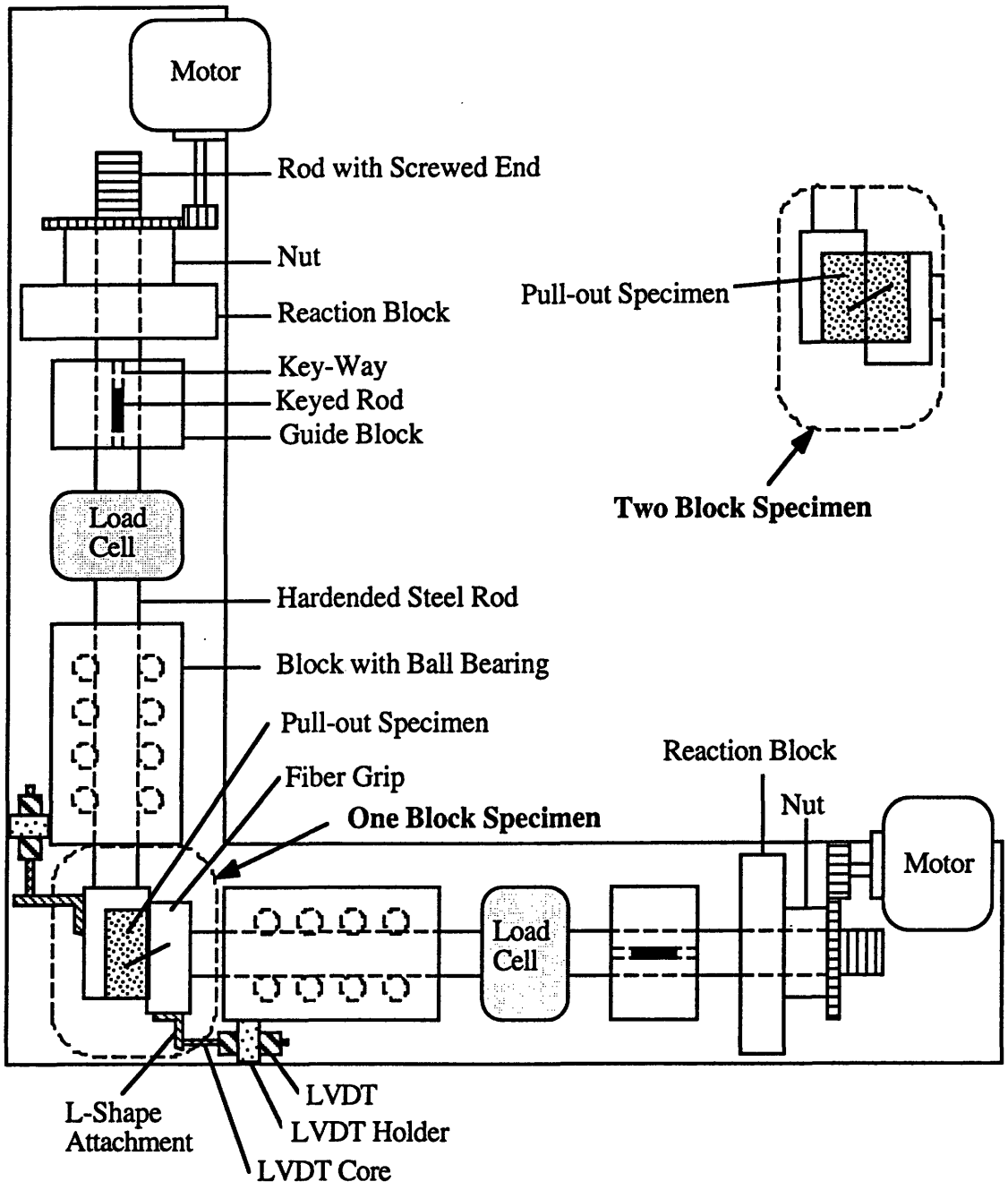

Figure 6.2 A Novel Setup for Mixed Mode Fiber Pullout Test

The setup consists of two orthogonal loading chains. Each chain is composed of several blocks and rods and a load cell. The specimen is glued to specimen holders attached to the load cells through hardened steel rods passing through bearing blocks. The purpose of the bearing blocks are to prevent any bending of the load cell that may affect the accuracy of load measurement. At the other side of the load cell is a specially

designed rod with a key along part of its length. The key goes into a carefully aligned block with a key-way machined to close tolerance. With the key in the key-way, the whole loading chain is constrained to move linearly without any rotation. The other end of the keyed rod (which is screwed) goes through a reaction block into a nut resting on it. By turning the nuts driven by the two motors at the ends of both loading chains, one can introduce any desirable combination of opening and shearing displacements. The friction caused by the ball bearing block is very small (less than 1.4 N) and is subtracted from all load measurements.

Two LVDT's are mounted on each ball bearing block. The displacements along the opening and shearing directions are measured by the movements of the L-shape attachments mounted on the fiber grip and the L-shape specimen holder, respectively.

6.2.2 Specimen Preparation

The procedure of the specimen preparation is the same as that in Section 3.2.1.

Two types of specimens, one-sided and two-sided mortar specimens (Fig. 6.2), are tested. Both have an embedded length of 10 mm. The two-sided specimens are more difficult to prepare and test [6.1]. Due to material variability, the pullout end is the weaker end with lower interfacial friction, but not necessarily the shorter embedded end. As a result, the experimental data show large variation. In this chapter, one-sided specimens are used in the test to ensure better consistency of testing data.

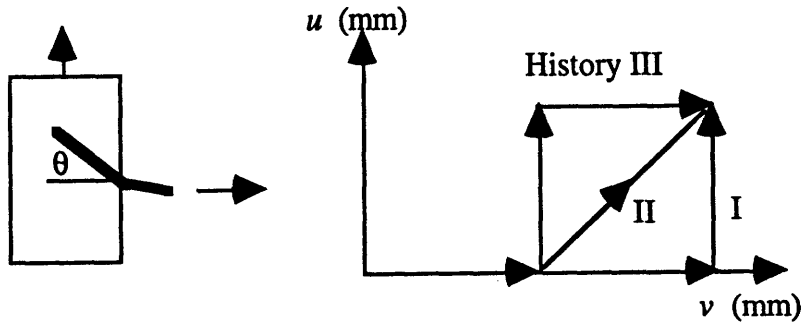

Figure 6.3 Fiber Inclination Angle and Loading Histories

6.2.3 Testing Procedure

Five sets of tests with the fiber inclination angles 0°, 30°, 60°, -30° and -60° are performed. (Note: a positive angle is the one shown in Fig. 6.3 with shearing, which

leads to increasing fiber pullout). For each set, three loading histories are prescribed (Fig. 6.3):

(1). History I: 2.0 mm of pure opening followed by 1.0 mm of pure shearing;

(2). History II: 1.0 mm of pure opening followed by simultaneous opening/shearing at the same rate until the same final displacement as in History I is obtained;

(3). History III: 1.0 mm of pure opening followed by 1.0 mm of pure shearing and a further 1.0 mm of pure opening, are employed.

The three displacement-controlled loading history (opening displacement vs. shearing displacement) recorded from one set of experimental test is shown in Fig. 6.4.

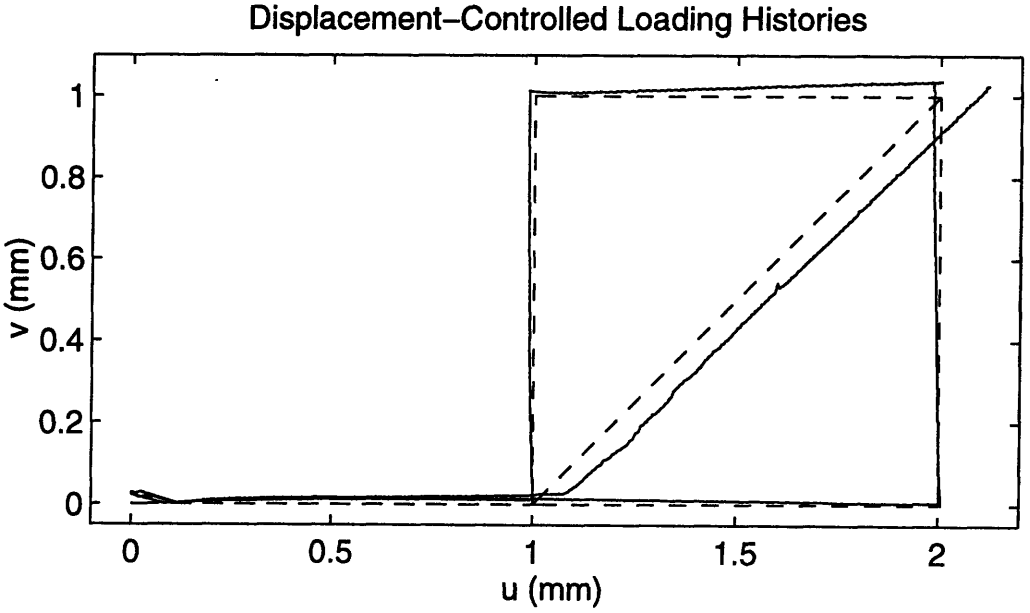

Solid: Actual Loading History in the Test
Dash: Designed Loading History

Figure 6.4 Three Prescribed Loading Histories

The experimental results for each inclination angle are shown in Figs. 6.5-6.9. In each figure, the three rows correspond to the three loading histories. The left column corresponds to the curves of opening load P vs. opening displacement u. The right column corresponds to the curves of shearing load S vs. shearing displacement v.

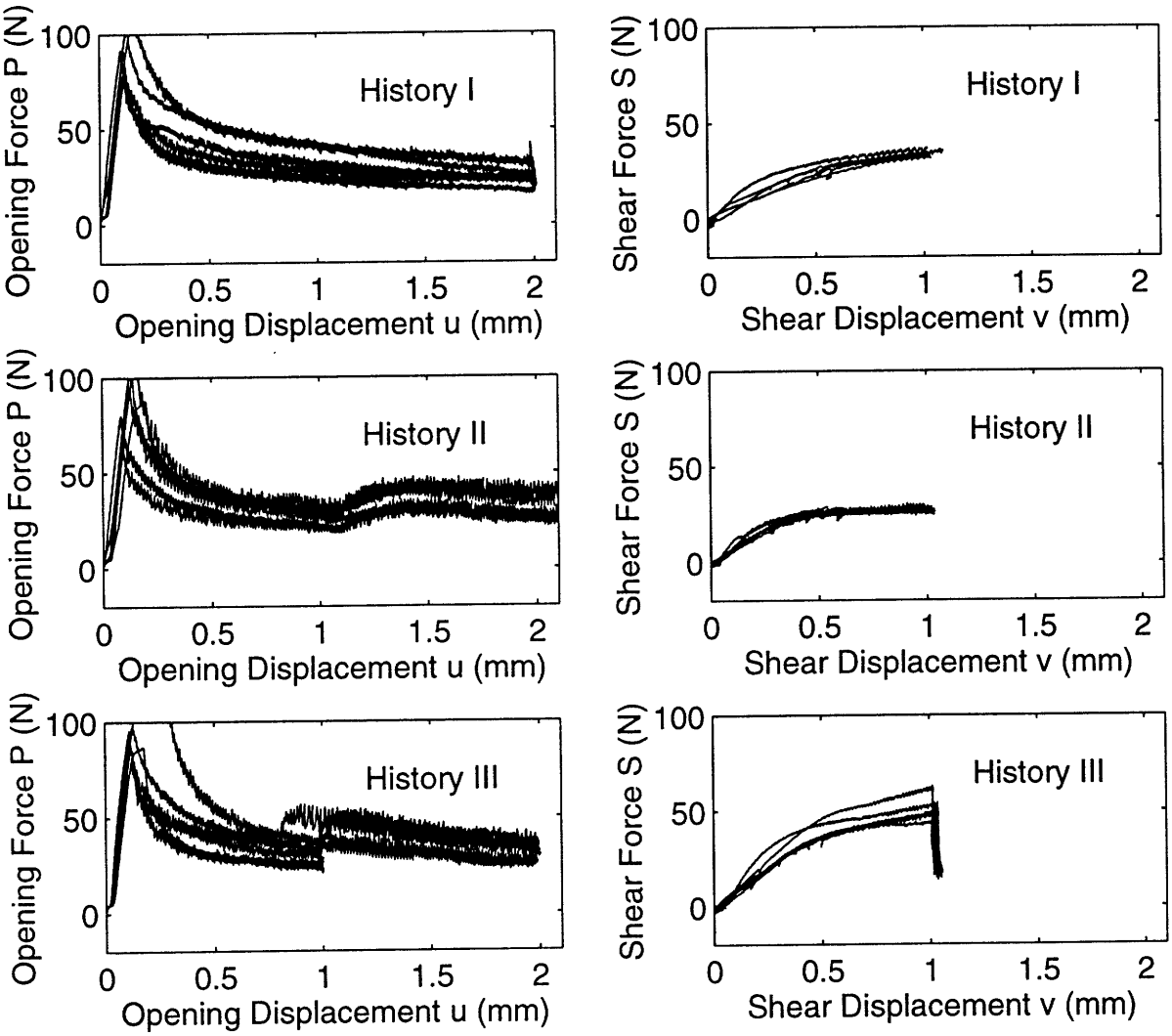

Figure 6.5 Inclination Angle $\theta = 0^o$

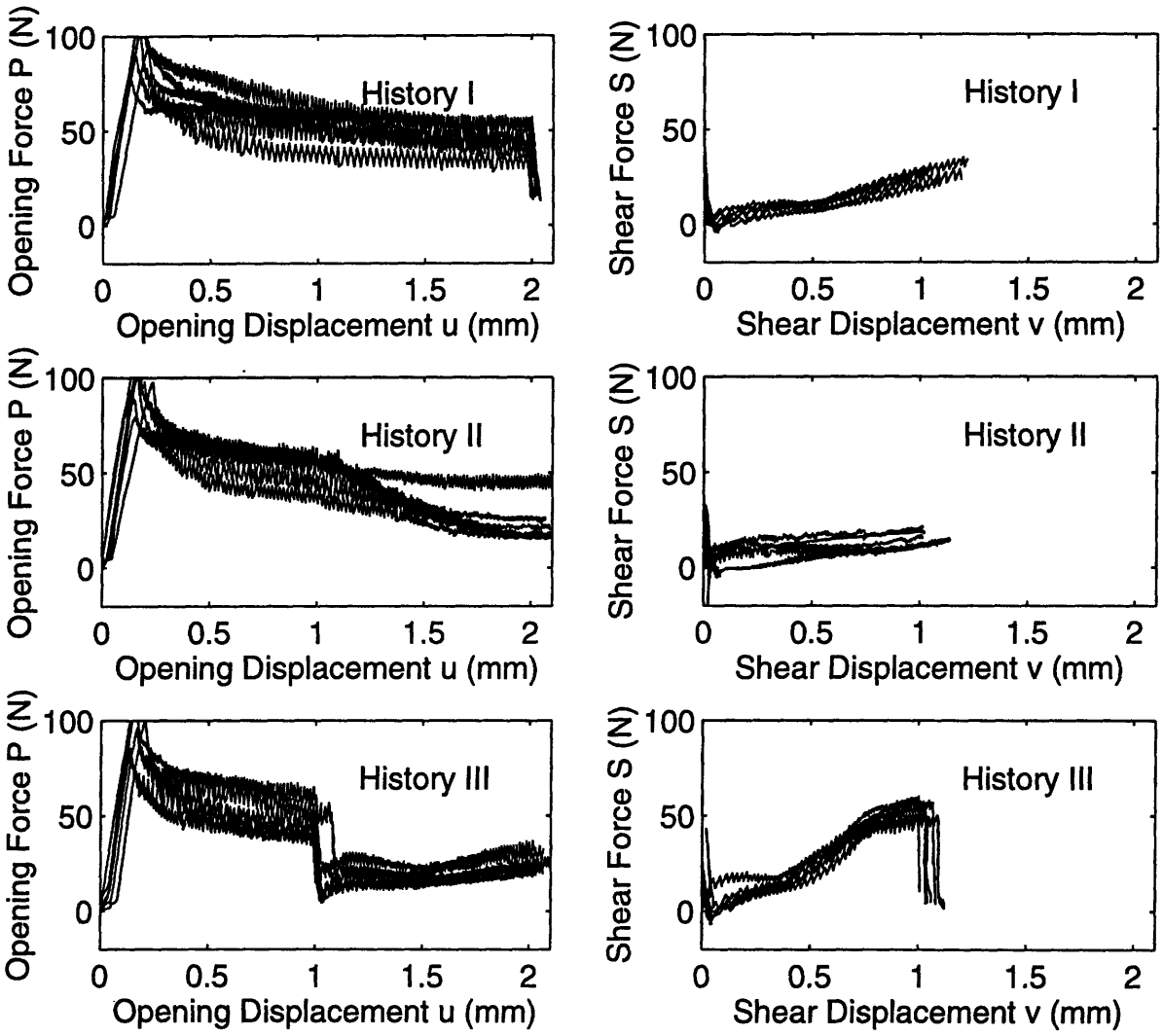

Figure 6.6 Inclination Angle $\theta = 30^{o}$

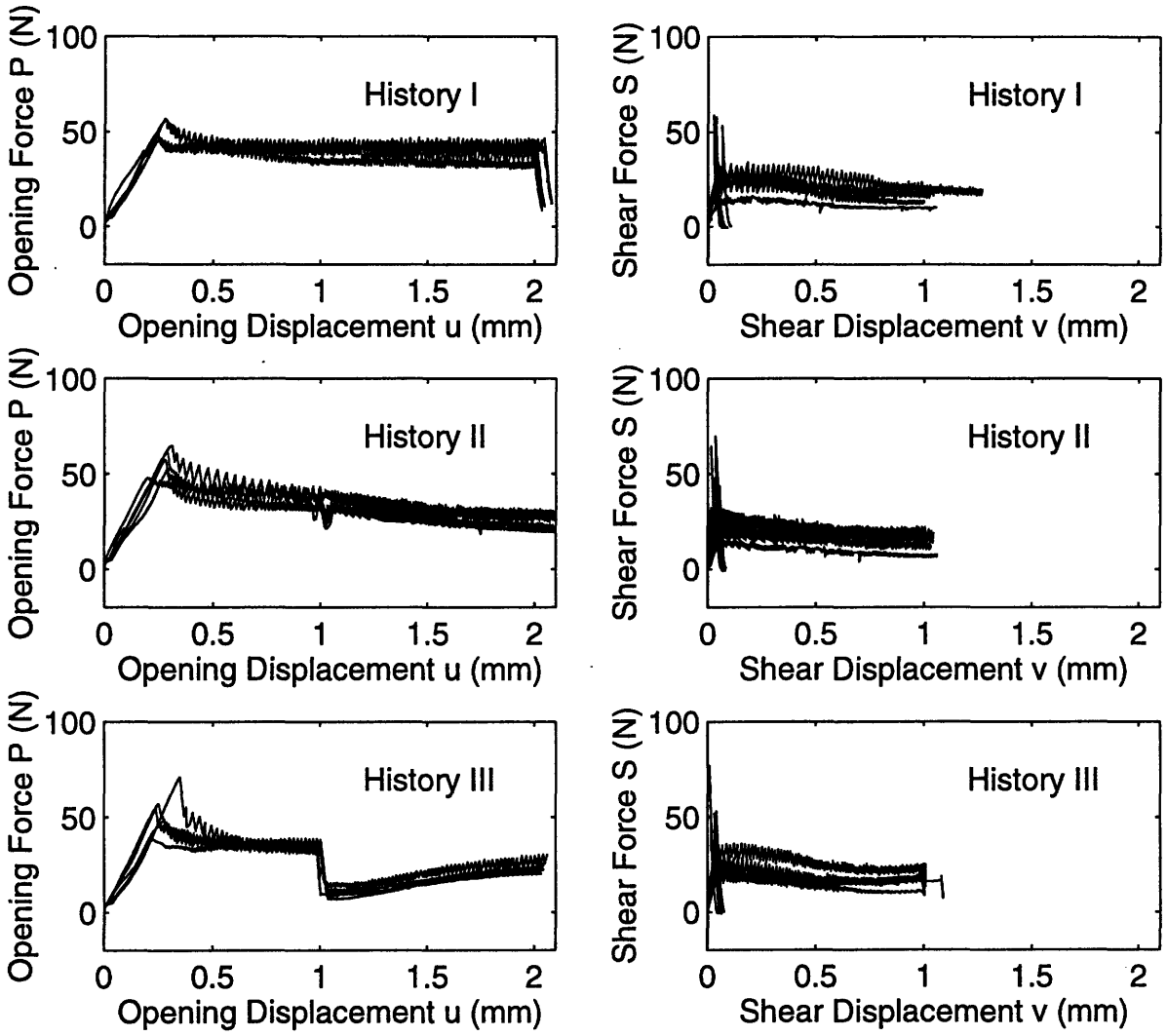

Figure 6.7 Inclination Angle $\theta = 60^{o}$

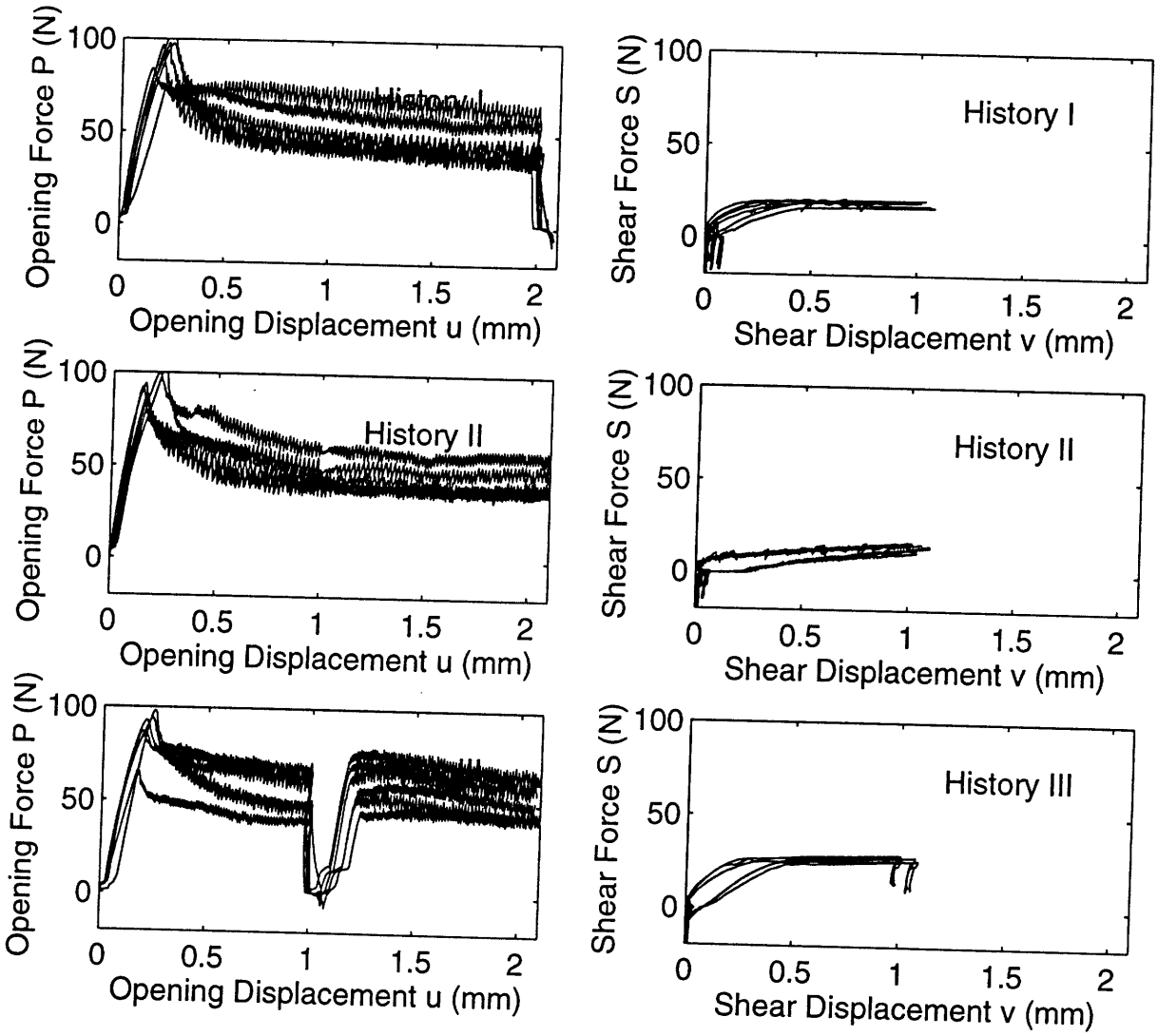

Figure 6.8 Inclination Angle $\theta = -30^{o}$

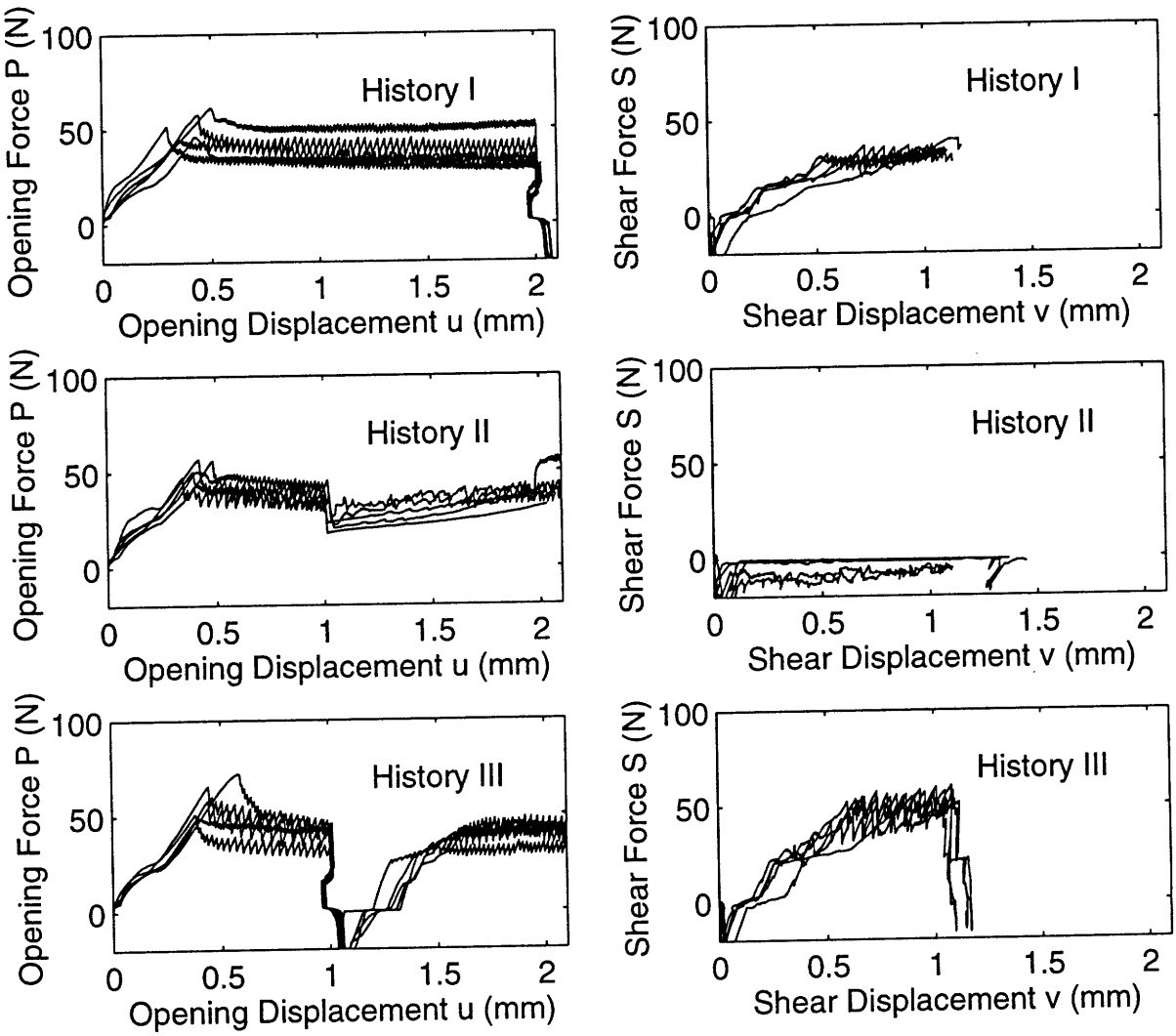

Figure 6.9 Inclination Angle $\theta = -60^{o}$

For the cases with positive angles (0°, 30° and 60°), fibers are subjected to pullout only. For the cases with negative angles (-30° and -60°), fibers are subjected to both pullout and push-in. Micromechanical model is developed for the cases of positive angles in Section 6.3.

6.3 MICROMECHANICAL MODEL

6.3.1 Coupling of Fiber Debonding/Pullout and Fiber Bending

Figure 6.10 shows the configuration of a fiber pulled out under mixed mode crack opening u and v. The model consists of two coupled problems:

(1). Fiber debonding and pullout with the lateral compressive effect (by bending) on the interfacial friction decay;

(2). A nonlinear beam bending on an elastic foundation with tension along axial direction.

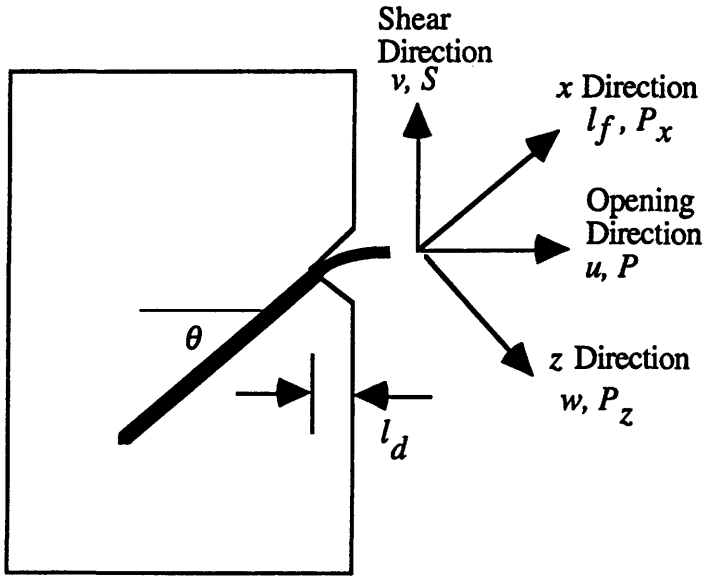

x Direction: Fiber Pullout with Free Length l_f
z Direction: Fiber Bending with Deflection w

Figure 6.10 Geometric Relation of Mixed Mode Crack

For steel fibers, the beam experiences elasto-plastic deformation. For cementitious materials, the matrix experiences spalling at the fiber exit point. l_d is the spalling depth in Fig. 6.10. In addition, the interfacial friction decays during fiber pullout process.

For the mixed mode crack opening, the fiber free length l_f along x-axis and the deflection w along z-axis is hereby defined as

$$w = u\sin\theta - v\cos\theta \tag{6.1a}$$

$$l_f = u\cos\theta + v\sin\theta + R_f\tan\theta \cdot sign(w) \tag{6.1b}$$

where R_f is fiber radius. The third term in Eq. 6.1b is due to the effect of bending which causes fiber/matrix separation or contact. When $w > 0$, l_f increases by $R_f\tan\theta$ due to fiber/matrix separation. When $w < 0$, l_f decreases due to fiber/matrix contact. For $v = 0$ (Mode I case), Eq. 6.1 reduces to the equations proposed by Morton and Groves [6.3]

$$w = u\sin\theta \tag{6.2a}$$

$$l_f = u\cos\theta + R_f\tan\theta \tag{6.2b}$$

where $\theta > 0$. Therefore, Eq. 6.1 is a more general formulation of fiber deflection and free length for mixed mode crack opening.

So far, a micromechanical model based on a decoupled model [6.2] for Mode I crack opening has been developed (Fig. 6.11). Along the direction perpendicular to the fiber (z-axis), fiber/matrix interaction is modeled by an elasto-plastic beam on an elastic foundation with strength-based matrix spalling. Along the fiber direction (x-axis), the fiber can undergo debonding (pre-peak behavior) and pullout (post-peak behavior). The term 'decouple' means that the pullout load along the x-axis is independent of the loading history along the z-axis.

A micromechanical model based on the Mode I model is developed next. Although the fiber pullout load along x direction depends on the lateral stress along z direction (Chapter 5) and the fiber bending and yielding along z direction depends on the tensile load along x direction, the system for mixed mode crack opening is also decoupled. For a given crack opening increment, the interfacial friction and the pullout force are calculated based on the initial fiber/matrix interaction before the crack opening increment. Based on the calculated pullout force, the updated fiber/matrix interaction is calculated.

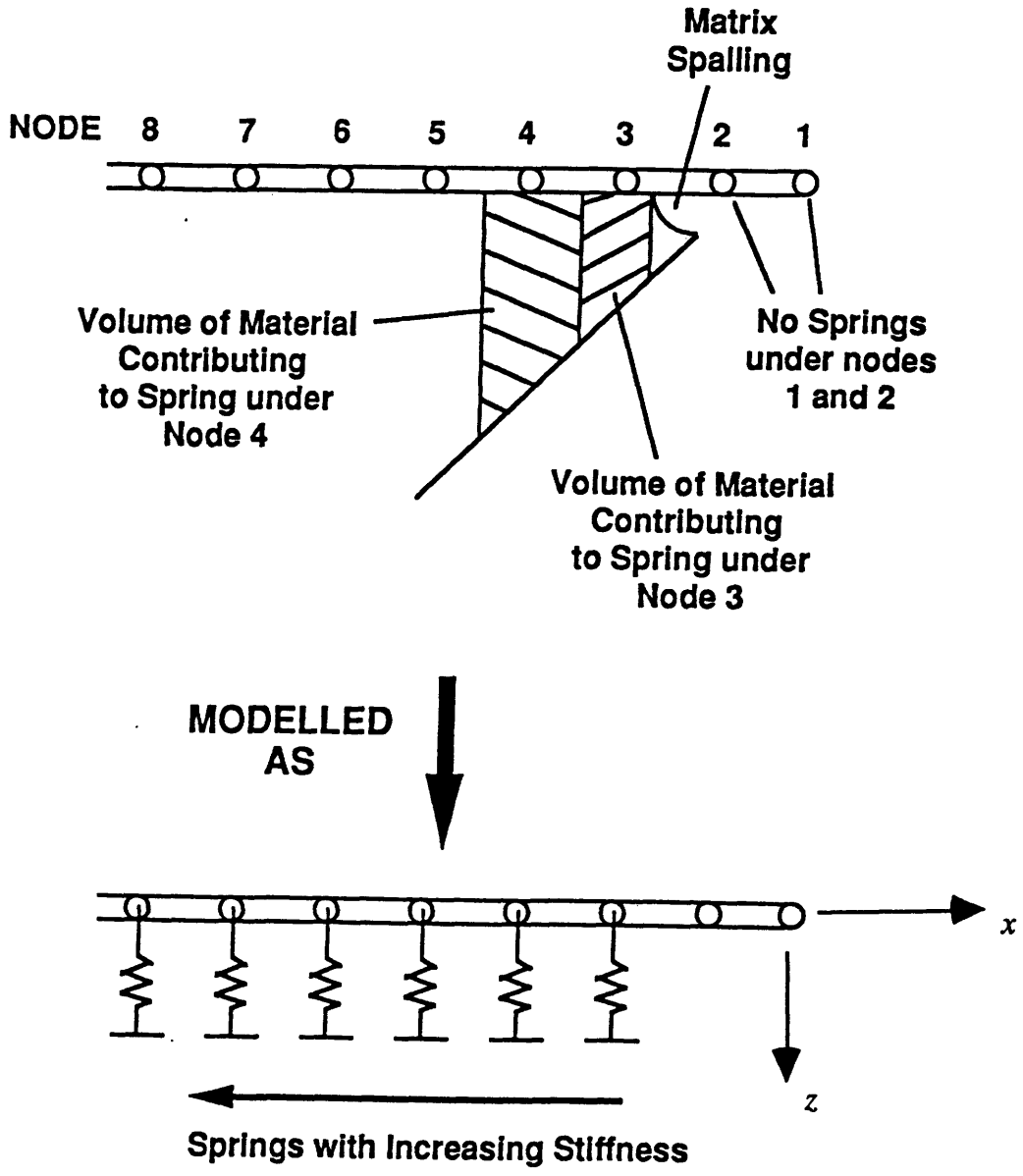

Figure 6.11 Micromechanical Model

6.3.2 Matrix Foundation Properties and Elasto-Plastic Beam Bending Element

The 3-D problem is reduced into a 2-D problem by first simulating the matrix foundation as continuous springs (Fig. 6.12) on top and bottom matrices [6.2]. Figure 6.12 shows FEM modeling of the effective foundation stiffness k_m at the distance h (from the bottom of the fiber to the crack surface, assuming $H_1 = H_2 = 33R_f$).

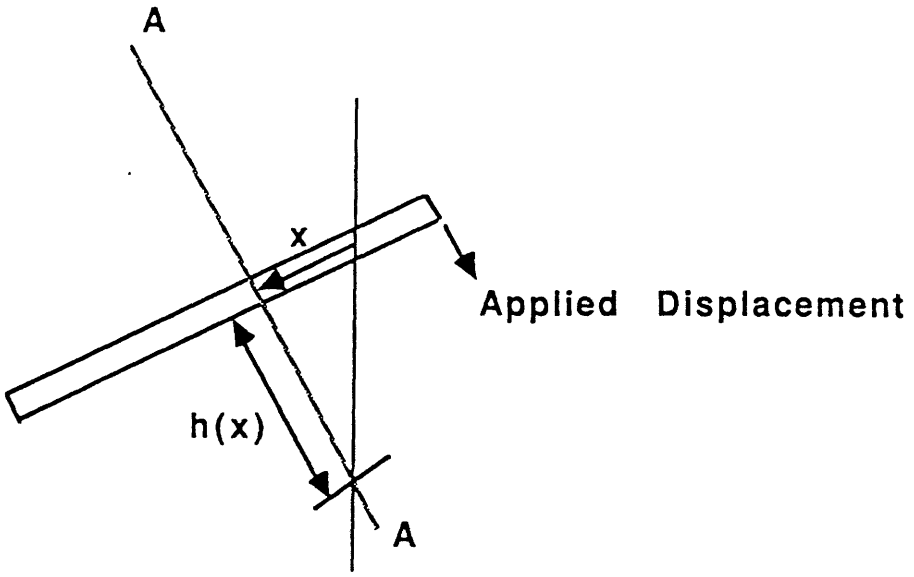

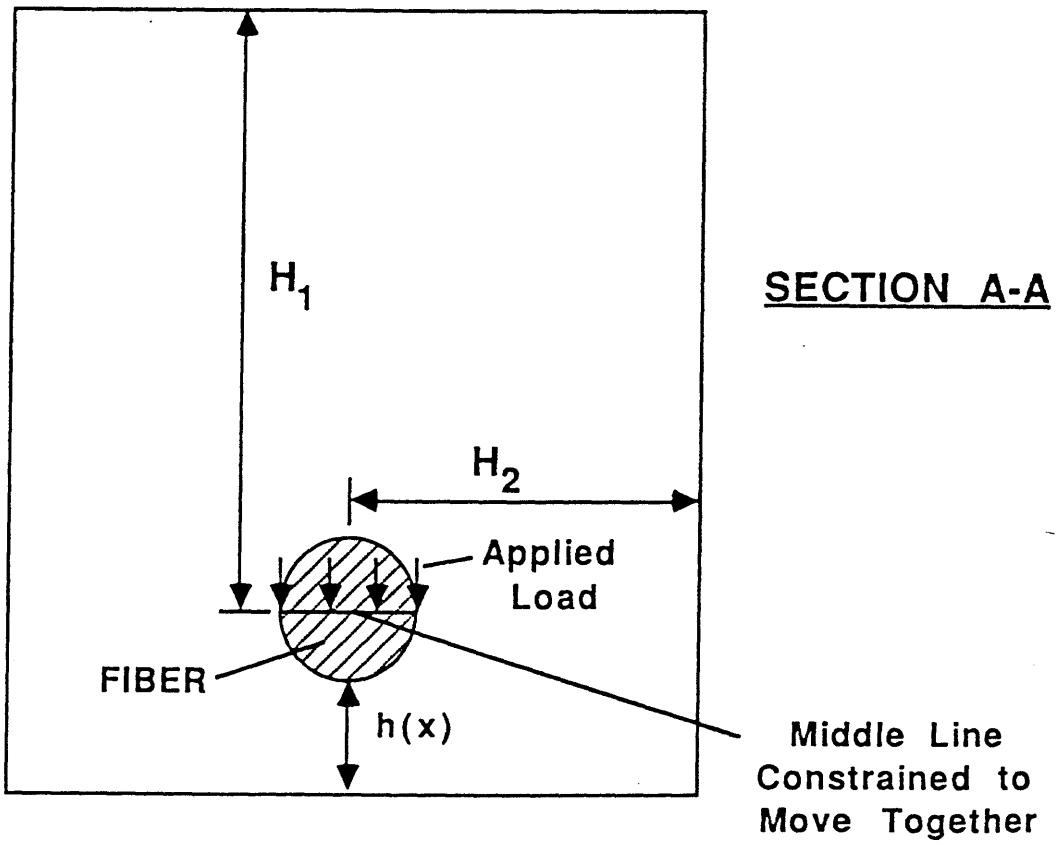

Figure 6.12 FEM Modeling of Foundation Property

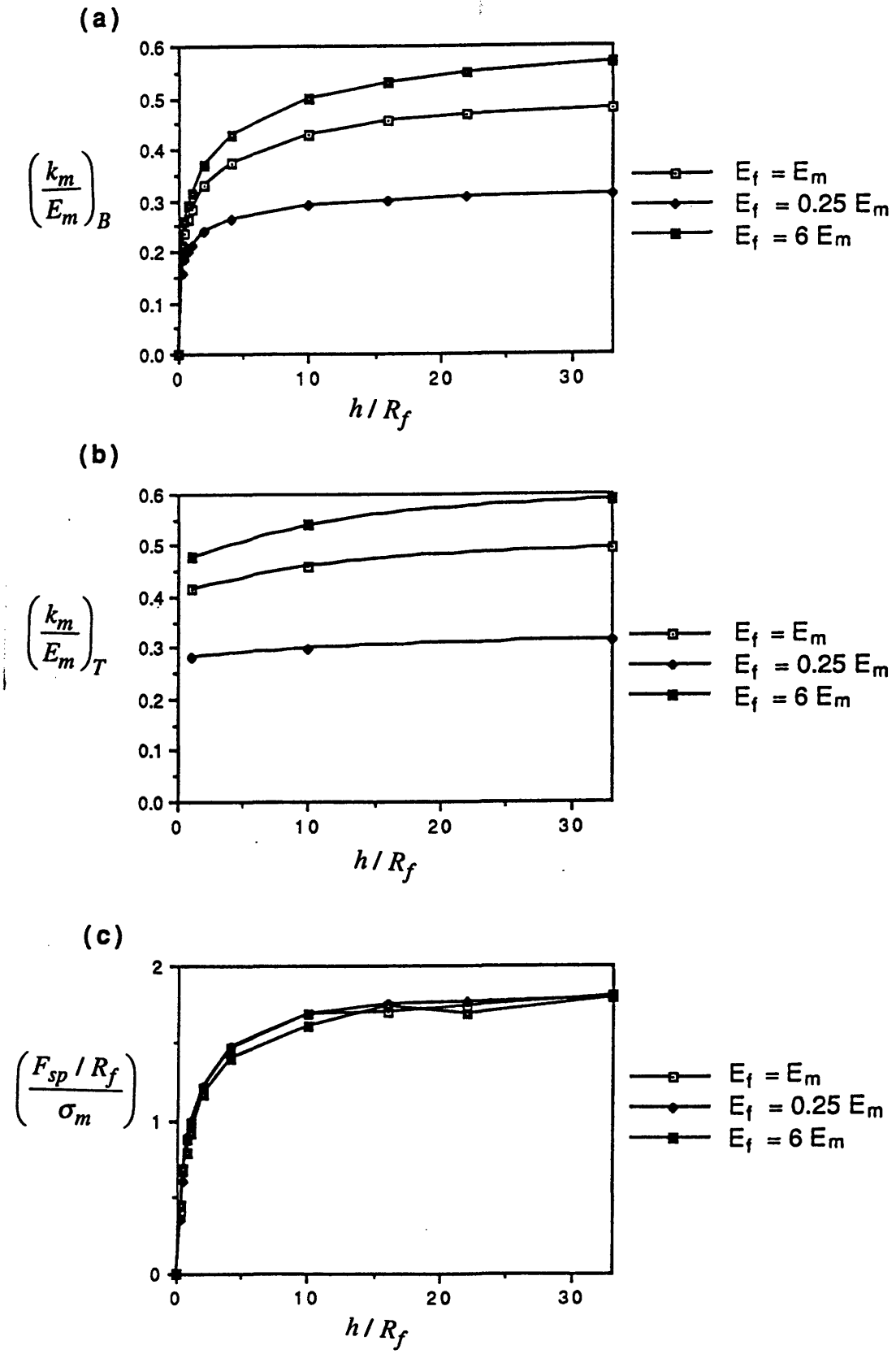

Figure 6.13 Stiffnesses at the Top and Bottom Matrices and Spalling Strength

Based on the finite element analysis, the non-dimensionalized top and bottom stiffnesses and the bottom spalling strength vs. the non-dimensionalized distance are plotted in Fig. 6.13 under different fiber/matrix stiffness ratio. When $E_f/E_m > 6$, the variation of the stiffness from the case of $E_f/E_m = 6$ is negligible and the curve for $E_f/E_m = 6$ is used for all the cases of $E_f/E_m > 6$. For steel/mortar composite in this study, the stiffness ratio is 9 ($E_f/E_m = 200/22.3$).

Having achieved the continuous stiffness along the beam, a series of springs are obtained by lumping the stiffness to the node from each half of the neighboring elements (Fig. 6.11).

The stiffness matrix of the beam element [6.2] is shown in Fig. 6.14. By considering the steel fiber as ideally plastic material without strain hardening after yielding, the moment vs. the curvature (M-κ) can be obtained at each node (Fig. 6.15). Note that the M-κ curve depends on the tensile load along the fiber. For simplicity, the moment-curvature (M-κ) curves are approximated by tri-linear curves. The starting slope follows the slope for the elastic bending up to $M_1 = (M_y+M_u)/2$, where M_y is the moment when yielding starts at the fiber surface and M_u is the ultimate moment capacity. The mid-slope is 1/5 of the starting slope and ended at M_u. The final slope is set to be zero (a very small number in the computer code).

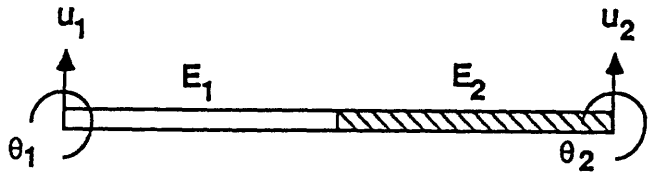

$$\begin{Bmatrix} F_1 \\ M_1 \\ F_2 \\ M_2 \end{Bmatrix} = \frac{E_1^2E_2^2}{E_1^2+E_2^2+14E_1E_2} \begin{bmatrix} \frac{I}{L^3}\left(\frac{96}{E_1}+\frac{96}{E_2}\right) & \frac{I}{L^2}\left(\frac{24}{E_1}+\frac{72}{E_2}\right) & \frac{-I}{L^3}\left(\frac{96}{E_1}+\frac{96}{E_2}\right) & \frac{I}{L^2}\left(\frac{72}{E_1}+\frac{24}{E_2}\right) \\ \frac{I}{L^2}\left(\frac{24}{E_1}+\frac{72}{E_2}\right) & \frac{I}{L}\left(\frac{8}{E_1}+\frac{56}{E_2}\right) & \frac{-I}{L^2}\left(\frac{24}{E_1}+\frac{72}{E_2}\right) & \frac{I}{L}\left(\frac{16}{E_1}+\frac{16}{E_2}\right) \\ \frac{-I}{L^3}\left(\frac{96}{E_1}+\frac{96}{E_2}\right) & \frac{-I}{L^2}\left(\frac{24}{E_1}+\frac{72}{E_2}\right) & \frac{I}{L^3}\left(\frac{96}{E_1}+\frac{96}{E_2}\right) & \frac{-I}{L^2}\left(\frac{72}{E_1}+\frac{24}{E_2}\right) \\ \frac{I}{L^2}\left(\frac{72}{E_1}+\frac{24}{E_2}\right) & \frac{I}{L}\left(\frac{16}{E_1}+\frac{16}{E_2}\right) & \frac{-I}{L^2}\left(\frac{72}{E_1}+\frac{24}{E_2}\right) & \frac{I}{L}\left(\frac{56}{E_1}+\frac{8}{E_2}\right) \end{bmatrix} \begin{Bmatrix} u_1 \\ \theta_1 \\ u_2 \\ \theta_2 \end{Bmatrix}$$

Figure 6.14 Stiffness Matrix of the Beam Element

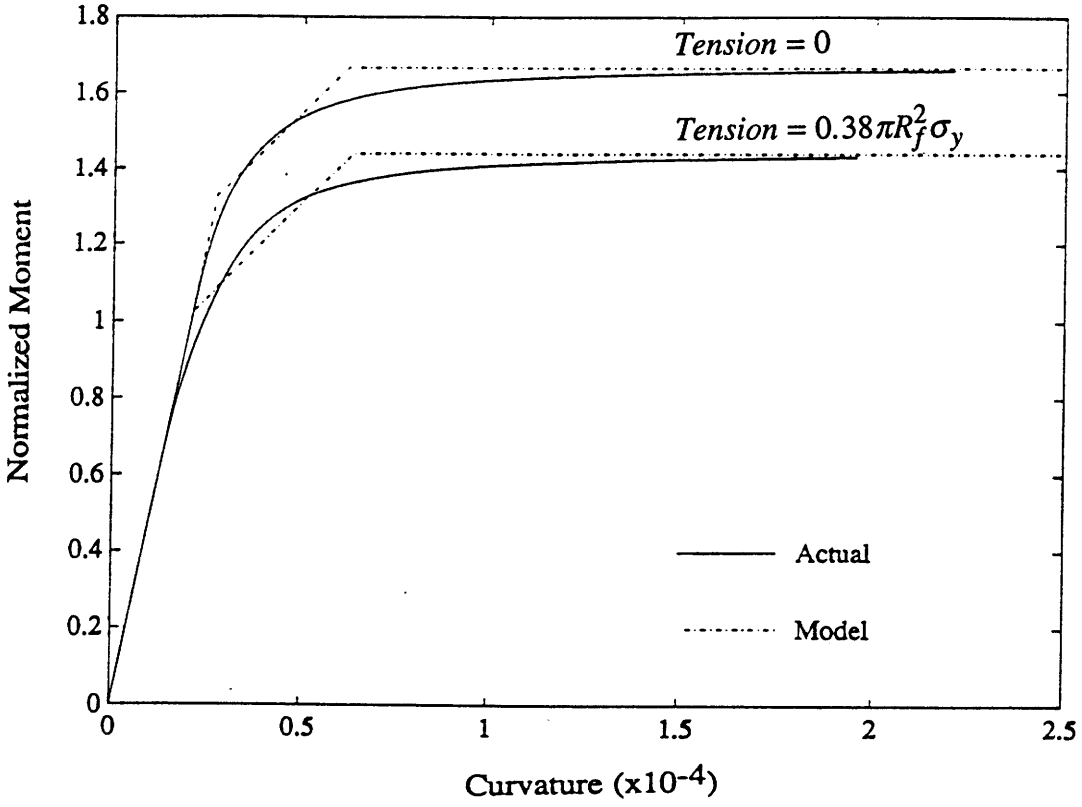

Figure 6.15 Tri-Linear Modeling of Moment-Curvature Relation with Tensile Effect

In [6.2], Leung and Chi assume that spalling occurs when lateral load exceeds a spalling strength, a quantity related to the matrix strength (Fig 6.13c). From the observation of the tested specimen in Section 6.2, it is found that the spalling depth l_d (Fig. 6.10) has no significant differences under different fiber inclination angles, except when $\theta = 0^o$ (Zero inclination case will be discussed separately in the next section). It is also observed from the experiments that spalling occurs very early during the debonding stage, when the pulling load is very low. In the model, an average pre-spalling depth, l_d = 1.2 mm, is used based on the measurements. It is assumed that spalling occurs immediately when loading is applied. With the spalling depth being constant at 1.2 mm, the spalling length along the fiber is given by $l_d/\cos\theta$.

For the case of zero fiber inclination angle ($\theta = 0^o$), few pre-spalling phenomenon is observed. The matrix grove at the fiber exit point is slightly enlarged. It is reasonable that the matrix is more difficult to fracture for zero fiber inclination angle (Fig. 6.10). The grove enlargement at the grove exit point is rather the fiber/matrix interaction (due to matrix shrinkage and fiber misalignment with small angle), which causes matrix surface

abrasion and compaction and has the same damage mechanism of interfacial friction decay during fiber pullout process (discussed in Chapter 5). In the next section, the matrix damage under zero fiber inclination angle is qualitatively modeled by a process of progressive spalling. In the model, instead of the gradual decay of interfacial friction modeled in Chapter 5, the interfacial interaction (friction) drops rigtht to zero (spalling) under certain criterion.

Figure 6.16 shows the numerical procedure. For a given incremental opening from A to B, the calculation follows the path ACDB:

(1). Unload the bending from Point A to Point C based on the fiber tensile load at Point A and record the residual load;

(2). Pull the fiber from Point C to Point D and update the fiber tensile load. The decay of interfacial friction due to fiber/matrix interaction is calculated based on the fiber bending configuration at Point A. The pullout process CD is discussed in Sec. 6.3.3;

(3). Reload the fiber from Point D to Point B and update the bending load due to fiber/matrix interaction.

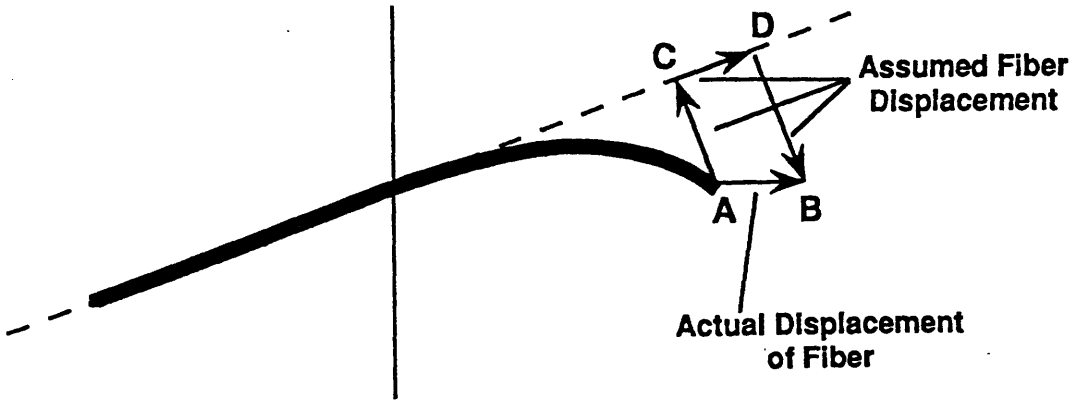

Figure 6.16 Loading History in the Numerical Procedure

6.3.3 Lateral Effect on Fiber Pullout

For simplicity, the calculation of pre-peak behavior uses a model of progressive debonding along the interface at a constant interfacial debonding strength τ_s. By relating the debonding length to both pulling load and debonded length, the relation of P_x vs. l_f is

$$P_x = 2\pi R_f \sqrt{E_f \tau_s l_f R_f} \tag{6.2}$$

In the post-peak regime, Leung and Chi used a constant interfacial friction [6.2]. In this work, the relation of P_x vs. lf at the post-peak regime is calculated using the damage model developed in Chapter 5. The interfacial residual friction can be related to Naaman's formula by neglecting the effect of Poisson's ratio

$$\tau_{i0}(s) = \tau_{i0}(0)\frac{\exp[-s^{\eta}] - \xi \exp[-L^{\eta}]}{1 - \xi \exp[-(L-s)^{\eta}]} \tag{6.3}$$

where ξ=1.0 and η=0.2 are fitting coefficients. $s = lf - \Delta$. is the sliding distance after total debonding (Δ is the pullout length at total debonding in Eq. 6.2). Note that no additional linear terms (Eq. 5.8 in Chapter 5) is used in Eq. 6.3 for the purpose of simplicity.

When the effect of lateral stress on fiber is not considered, $\tau_i(s) = \tau_{i0}(s)$, which is the decay simulated by the Naaman's formula. Otherwise, when the effect of lateral stress on fiber is considered, the damage model developed in Chapter 5 is used. Since only one side of the fiber are under compression, half of the contribution due to lateral stress is included. From Eq. 5.2

$$\tau_i(s) = \tau_{i0}(s) + \frac{1}{2}\bar{\mu}(s)\sigma_c(s) \tag{6.4}$$

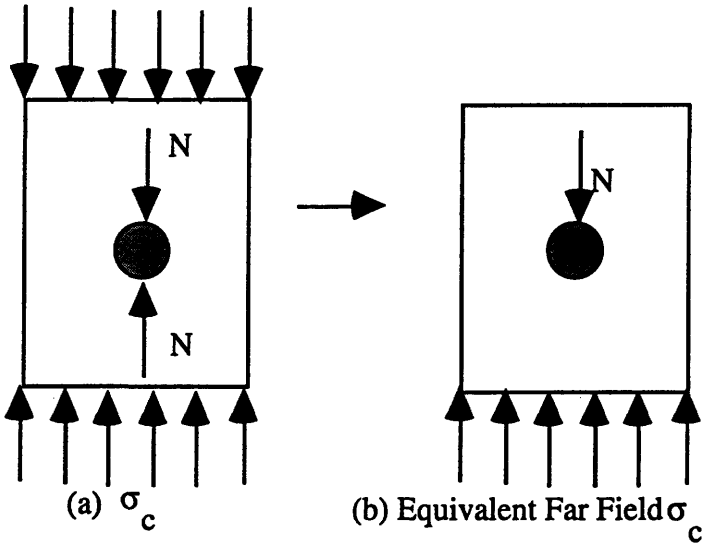

Figure 6.17 Equivalent Lateral Stress

Using an elastic inclusion model (Fig. 6.17a), the total lateral load per unit length N on a fiber is calculated by integrating over the fiber surface and related to the far field lateral stress σ_c [6.4]

$$\sigma_c = \frac{\dfrac{N}{2R\alpha_m\beta}}{\dfrac{1}{2\alpha_f+\beta-1}+\dfrac{2}{1-\beta+4\alpha_m\beta}} = c\cdot\frac{N}{2R} \tag{6.5}$$

where N (lateral force/unit fiber embedded length) is the total load acting on the fiber along the loading (σ_c) direction ; c is a non-dimensional number; and

$$\beta = \frac{G_f}{G_m}; \quad \alpha_f = 1-\nu_f; \quad \alpha_m = 1-\nu_m;$$

Although the equivalent far field lateral stress σ_c can be calculated for each beam element based on the nodal reaction, in this work, σ_c (Fig. 6.17b) is calculated in a simplified way by the average interfacial reaction on fiber surface. N in Eq. 6.5 is, therefore, the summation of the top and bottom reactions (absolute value) at all embedded beam element nodes divided by the embedded fiber length. With the calculated N from Eq. 6.5, the decay of fiber pullout load and the interfacial friction along the path CD in Fig. 6.16 can be calculated.

Based on the material properties in Table 3.1, $c = 0.7$ in Eq. 6.5. However, for good agreement between the experimental results and the micromechanical model, c is found to be 0.2. The overestimation of c is possibly due to the existence of a compliant layer at the interface, which is difficult to estimate quantitatively from experiment. In the following sections and chapters, $c = 0.2$ is used.

6.3.4 Comparisons of Micromechanical Models and Experimental Results

Figures 6.18-6.20 (fiber inclination angles $\theta = 0^o$, 30^o and 60^o) show the comparison of experiment results (solid lines) with different micromechanical models:

(1). When neglecting the effect of lateral compression (using Naaman's formula Eq. 6.3 for interfacial friction decay) and assuming no matrix spalling, the shearing forces S is overestimated (dotted lines);

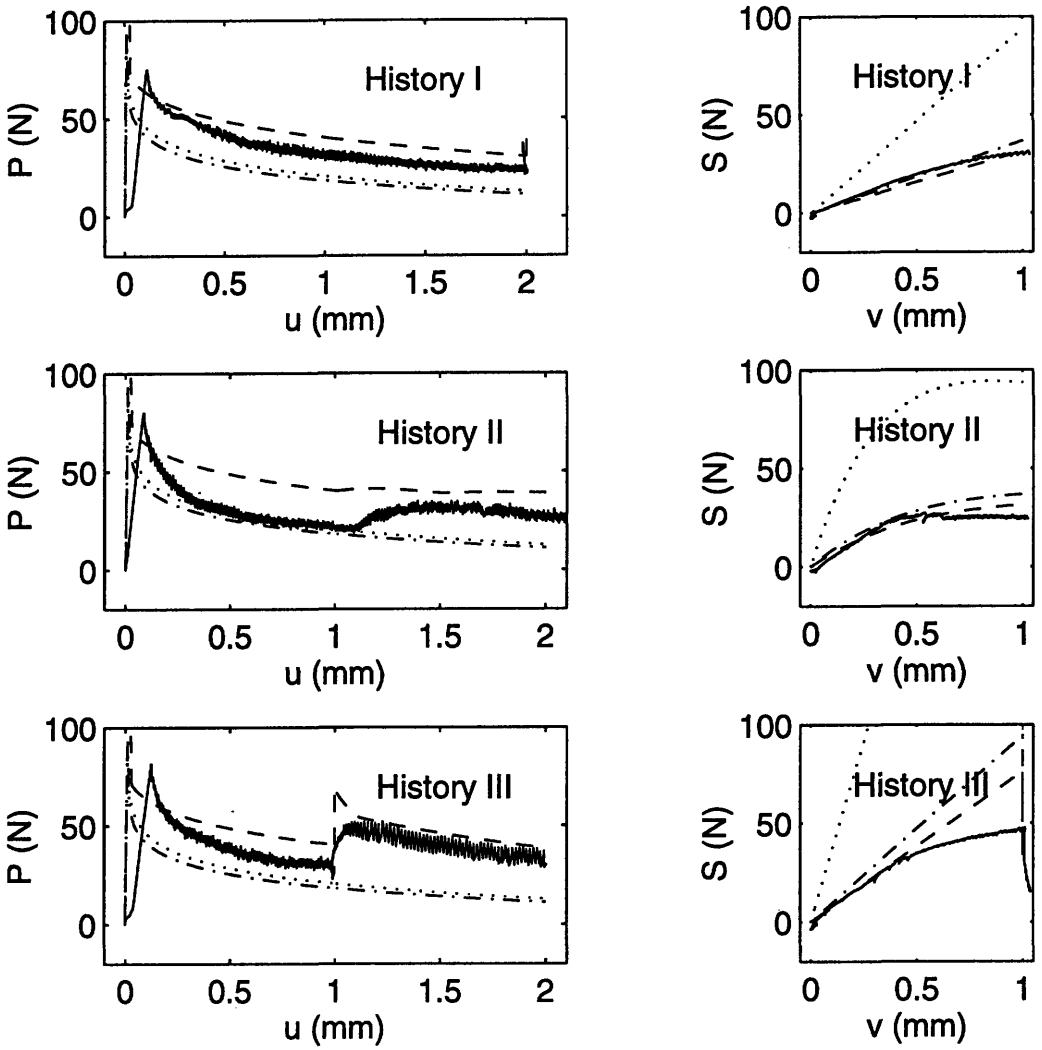

Solid: Experimental Results
Dot: Model without Pre-Spalling and Lateral Compression Effect
Dashdot: Model with Pre-Spalling Depth and without Lateral Compression Effect
Dash: Model with Pre-Spalling Depth and Lateral Compression Effect

Figure 6.18 Comparison with Inclination Angle $\theta = 0^o$

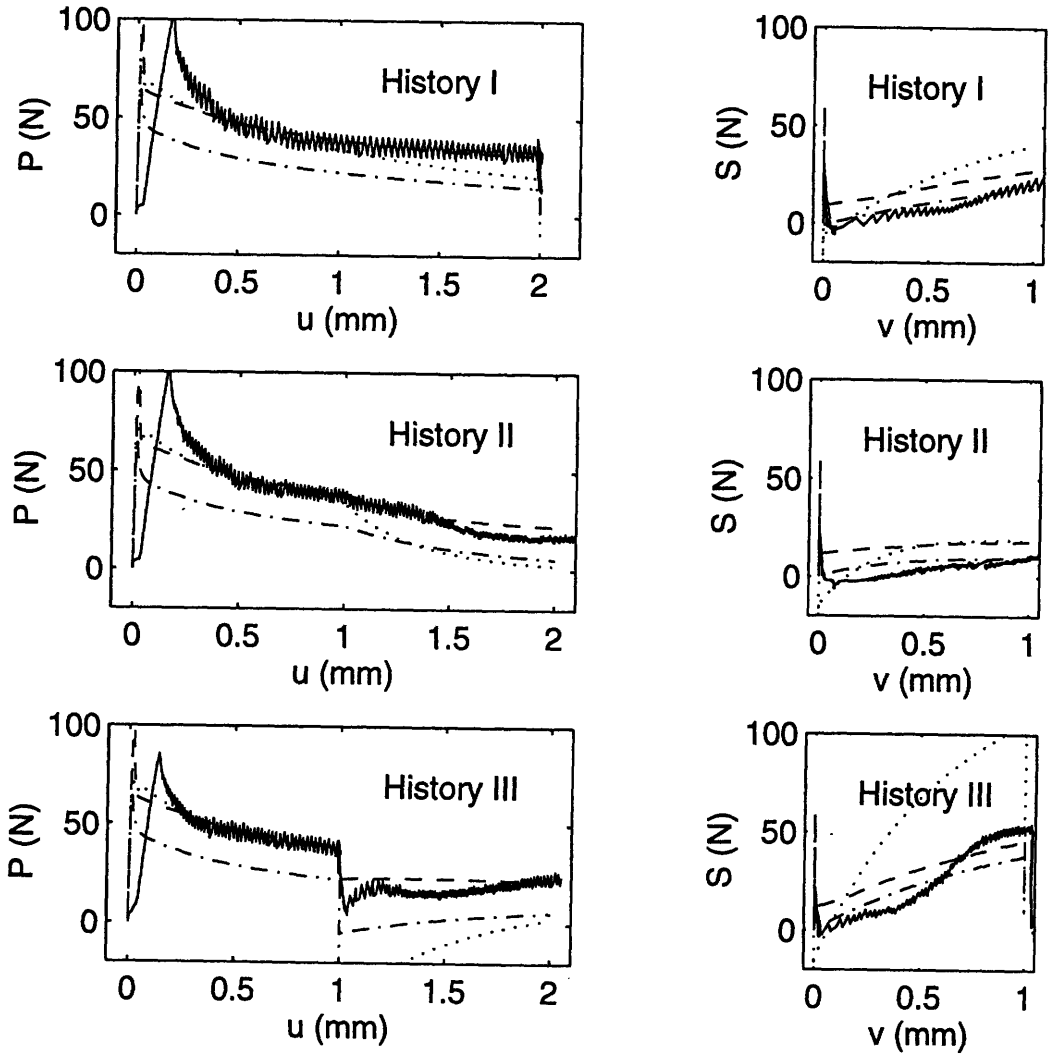

Solid: Experimental Results
Dot: Model without Pre-Spalling and Lateral Compression Effect
Dashdot: Model with Pre-Spalling Depth and without Lateral Compression Effect
Dash: Model with Pre-Spalling Depth and Lateral Compression Effect

Figure 6.19 Comparison with Inclination Angle $\theta = 30^{o}$

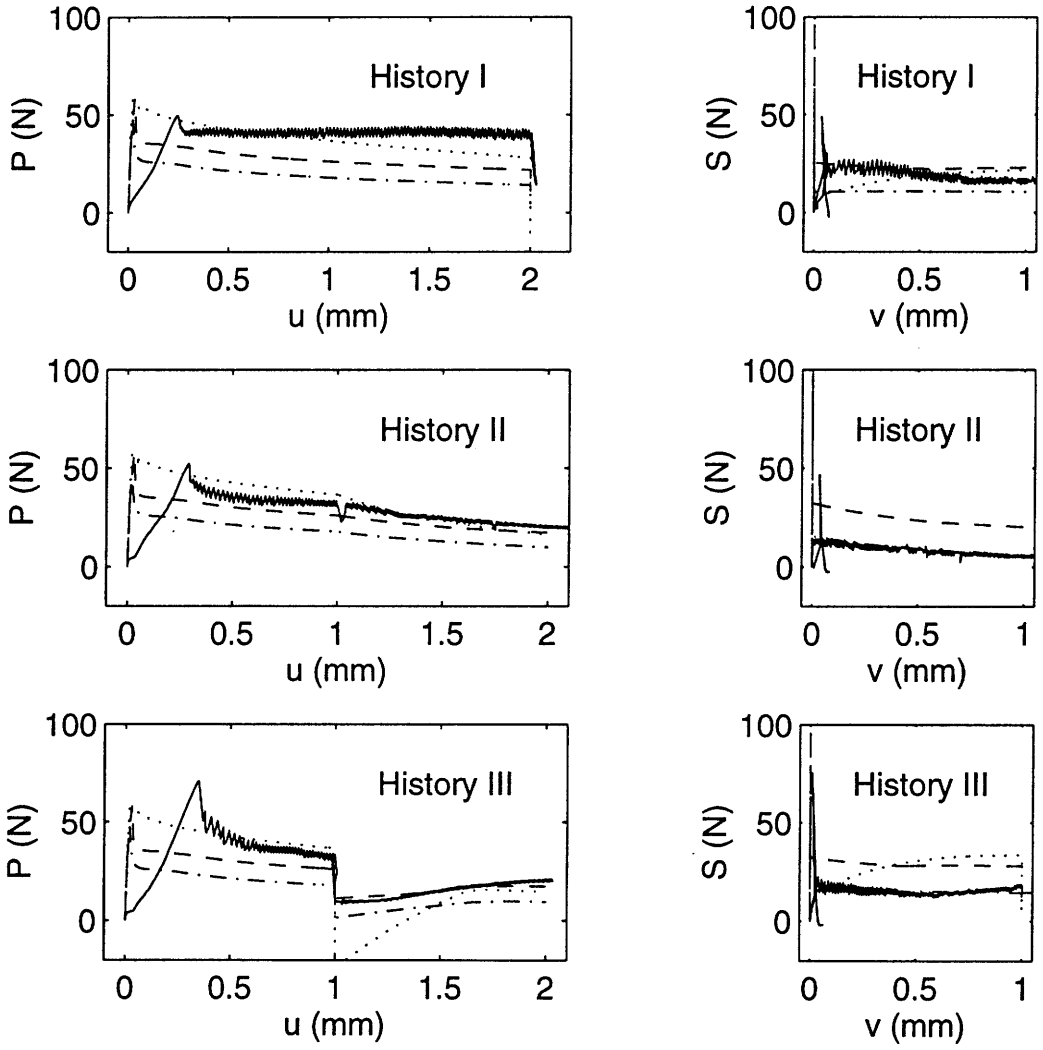

Solid: Experimental Results
Dot: Model without Pre-Spalling and Lateral Compression Effect
Dashdot: Model with Pre-Spalling Depth and without Lateral Compression Effect
Dash: Model with Pre-Spalling Depth and Lateral Compression Effect

Figure 6.20 Comparison with Inclination Angle $\theta = 60^{o}$

(2). By including the pre-spalling depth l_d = 1.2 mm, the simulation of shearing force histories (S vs. v) improved dramatically (dashdotted lines);

(3). By further including the effect of lateral compression N with c = 0.2 in Eq. 6.5, the significant variation of the opening forces P due to shearing displacement (P vs. u in Figures 6.18-6.20) can be predicted well (dashed lines). The final micromechanical model (dashed lines), which includes both the effect of lateral compression and constant pre-spalling depth, can predict the trend of the experimental results well, especially for the case of the P-u curve (history III in Fig. 6.18).

The cases of negative inclination angles (-30° and -60°) is not modeled in this work. Based on the observation of the experimental results in Sec. 6.2, the phenomenon of fiber push-in is expected to be a major factor for the cases of negative inclination angles. It is left for further investigation in the future.

6.4 DISCUSSION

6.4.1 Progressive Spalling at Zero Inclination Angle

When the inclination angle is zero, significant matrix spalling is not observed. However, the matrix groove is found to be enlarged at the fiber exit point. In addition to the factors of fiber misalignment and matrix shrinkage, Fig. 6.18 (solid lines) shows that the increase of the shearing force at large shearing displacement (right column) slows down due to a gradual spalling process and the pre-spalling depth model (dashed lines) over-estimates the shearing forces. Therefore a different matrix damage model is necessary for the zero inclination fiber pullout. This model should be based on interfacial abrasion and compaction (an interfacial decay essentially similar to that in the damage model in Chapter 5), but not on spalling due to bulk matrix fracture.

By simply assuming that spalling occurs gradually and is proportional to the bending force P_Z (Fig. 6.10) and neglecting the effect of fiber misalignment and matrix shrinkage, one can write

$$L_{spall} = kP_z \tag{6.6}$$

With k = 24 μm/Newton, Fig. 6.21 shows that the trend of shearing force (dashed lines in the right column) based on the progressive spalling model agrees well the experimental data.

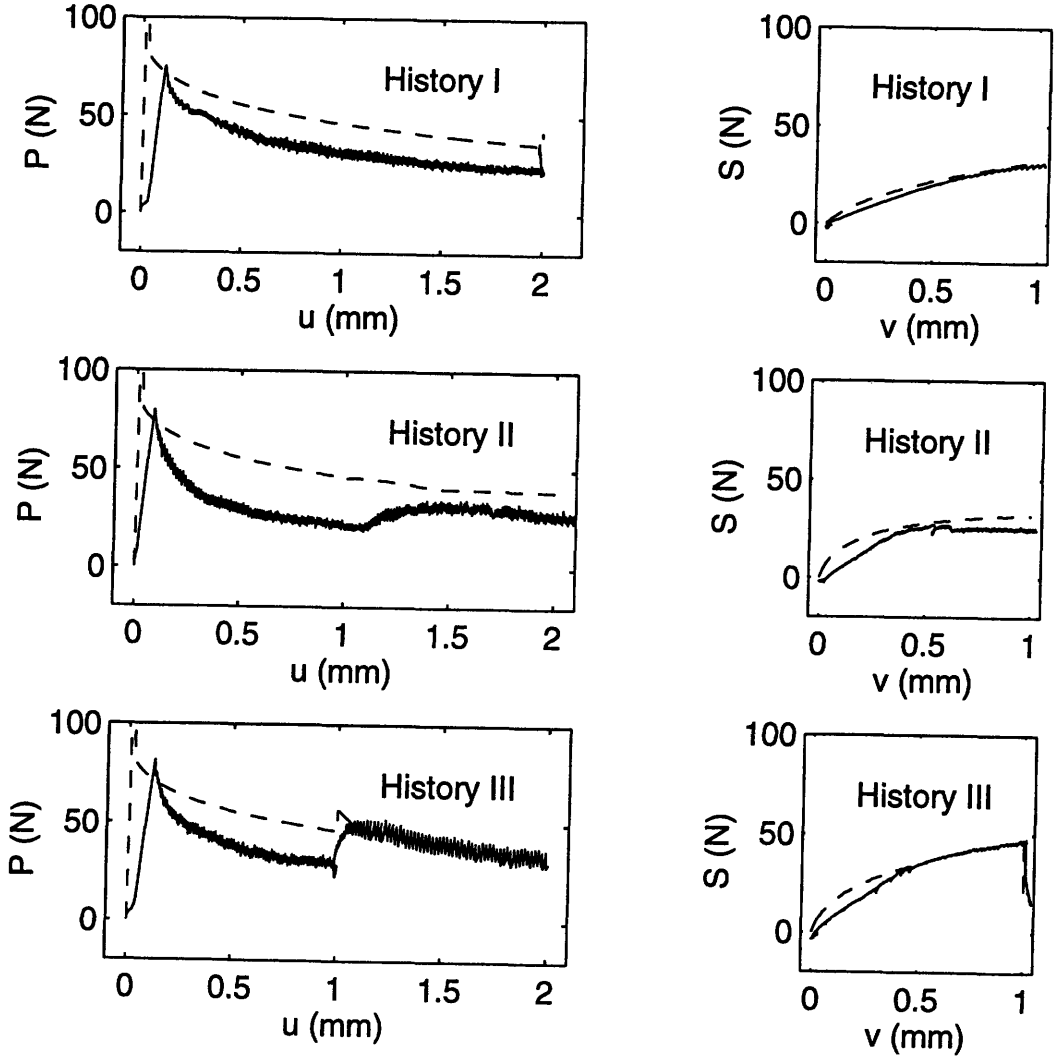

$\theta = 0^o$

Figure 6.21 Effect of Progressive Debonding on S vs. v

However, the overall effect of lateral stress on the opening force reduces. Comparing the "second peak" of the opening load for the cases of History III, the "second peak" is less significant in Fig 6.21. This is due to the fact that the interfacial decay from matrix shrinkage and fiber misalignment are not modeled during the early opening displacement before shearing occurs. Therefore, the real progressive spalling process is much more complicated than Eq. 6.6. It may involve gradual decay of interfacial friction, instead of a sharp drop (spalling) to zero.

For the angled fiber pullout, gradual spalling also occur after the pre-spalling. However, it is the same mechanism of surface abrasion and decay and is included in the damage model by the decay of interfacial friction in Chapter 5 and Eqs. 6.2-6.5. Therefore, no new model is necessary.

In conclusion, two spalling mechanisms exist, pre-spalling of bulk matrix due to fracture and progressive spalling due to surface abrasion and compaction of matrix. When $\theta \sim 0^o$, progressive spalling is dominant. The interfacial transition zone is gradually damaged by compaction and abrasion. When θ is not close to 0^o, pre-spalling is dominant. The whole block of matrix from the interfacial transition zone to the fracture surface is spalled.

For random distribution of fiber angles, only a small portion of the fibers lie around 0^o. As shown in Fig. 6.18, for $\theta = 0^o$, the pre-spalling model can still predict shearing force reasonably well. Therefore, the stress-displacement relation calculated later in Chapter 7 for the prediction of structural behavior will be based on the pre-spalling model.

6.4.2 Pre-Peak Behavior Affected by Experimental Setup

Figures 6.18-6.20 show that the simulated pre-peak behavior along the opening direction (dashed lines in the left column) does not agree well with the experimental data (solid lines). The difference is caused by two factors:

(1). The stiffness of the experimental setup k_u is not high enough which results in an elastic deformation along the opening direction u;

(2). A small adjustment along the negative shearing direction v (Fig. 6.4), especially with cases of non-zero inclination angles (Figs. 6.19 and 6.20), results in an increase of opening displacement when peak load at total debonding u_{debond} is reached (Fig. 6.22).

The opening at the peak load increases from

$$u_{debond} = \frac{\Delta}{\cos\theta} \tag{6.7a}$$

to

$$u_{debond} = \frac{\Delta}{\cos\theta} + v\tan\theta + k_u P_{u,\max} \tag{6.7b}$$

The second term in Eq. 6.7b is attributed to the negative shearing displacement and the third term to the stiffness of the experiment setup along opening direction u.

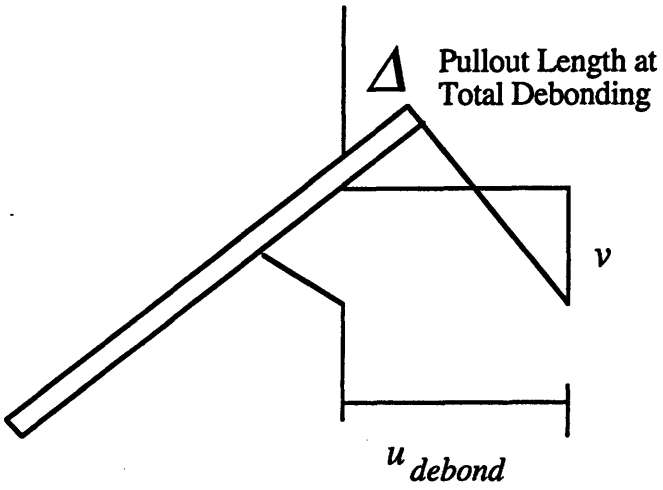

Figure 6.22 Effect of Negative Shear Displacement on Crack Opening at Peak Load

By first measuring the stiffness of the setup from Fig. 6.18 ($\theta = 0^o$) and the negative v for non-zero inclination cases from Figs. 6.19 and 6.20 (right columns) and then including both effects into the micromechanical model, Fig. 6.23 shows that the experimental data (solid lines) and the modified micromechanical model (dashed lines) agree well.

It should be mentioned that the experimental data does not represent the true pre-peak behavior in a real composite, where neither setup stiffness nor negative shearing displacement exists. Therefore, the original micromechanical model (dashed lines in Figs. 6.18-6.20) is used in Chapter 7. This section only serves to explain the discrepancy between the model prediction and the experimental results.

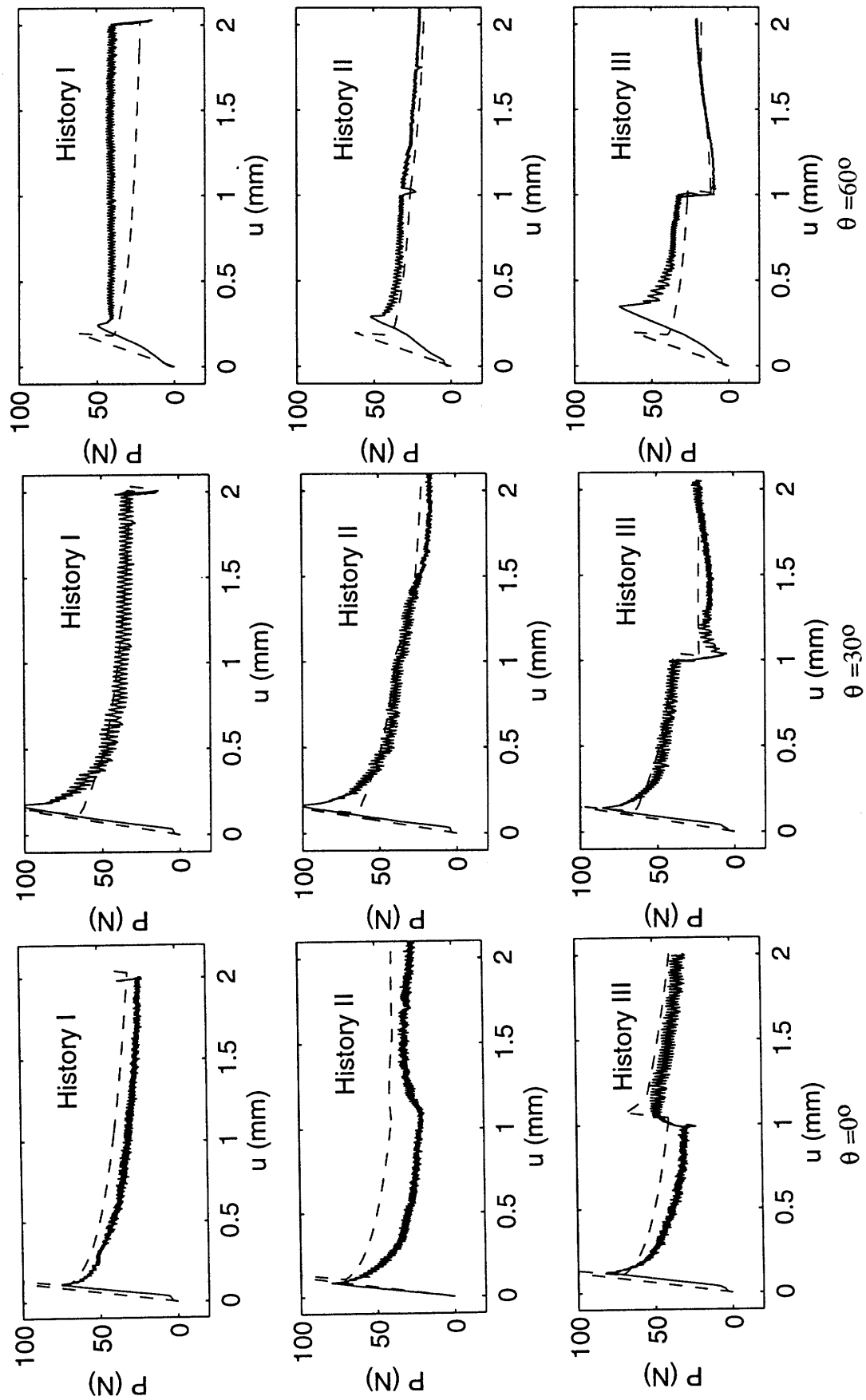

Figure 6.23 Pre-peak Behavior Affected by the Experimental Setup

6.4.3 Reversion from Fiber/Matrix Separation to Contact

In Fig. 6.19 (S vs. v curve for History III), when the shearing displacement is applied, the shearing force (at around v = 0.5 mm) is found to increase suddenly at a higher rate. This increase of shearing force represents a decrease of free length for the fiber. Notice that the fiber has 30° inclination. During the first stage Mode I opening (1 mm) in Fig. 6.4, the fiber contacts the bottom matrix (with spalling). During the following shearing opening (1 mm), fiber/matrix interaction at the fiber exit switches from the bottom matrix to the top one when $v = u \tan 30^o$. Since there is few spalling at the top, the shearing force suddenly increases at a higher rate (Fig. 6.24).

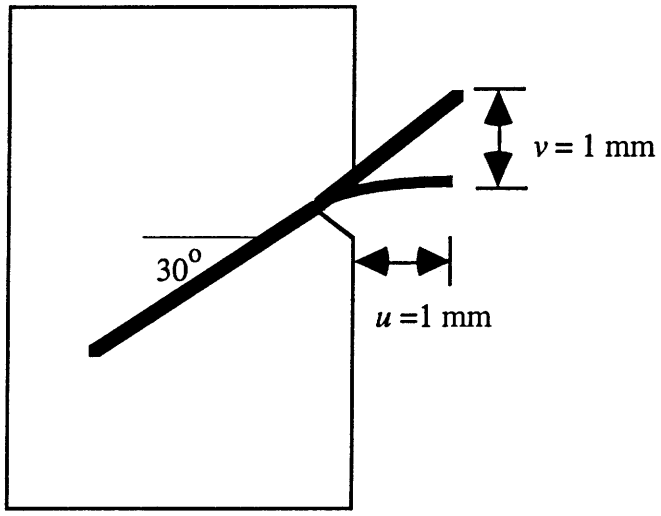

Figure 6.24 Switching Side of Fiber/Matrix Contact During Shearing Displacement v

Although the stiffness change during matrix bottom/top switch is significant, the spalling length is considered to be the same for both the top and bottom matrix in the micromechanical model. The change in spalling length (and hence the free length) during the switch is, therefore, neglected in the model. Even without considering these factors, the pre-spalling depth model simulate the shearing forces reasonably well.

6.5 CONCLUSIONS

From the experimental results obtained with the novel fiber pullout setup, it is observed that fiber crack bridging forces are sensitive to (a) lateral compression, and (b)

both opening and shearing displacement. The matrix spalling depth is fairly constant for different fiber inclination angles. The micromechanical model with the lateral compression effect and constant pre-spalling depth can describe fiber pullout under mixed mode crack opening well. Further work needs to be done for mixed mode crack opening with fiber push-in phenomenon.

REFERENCES

6.1 Leung, C.K.Y., and Y. Geng, "Determination of Crack Bridging Forces in Fiber Reinforced Concrete." Proceedings for US-Europe Workshop on Fracture and Damage of Quasi-Brittle Materials" edited by Z. Bazant and Z. Bittner, Prague (1994)

6.2 Leung, C.K.Y. and J. Chi, "Derivation of Crack Bridging Force in Random Discontinuous Fiber Composites through Micromechanics." in press ASCE J. Eng. Mech. (1995)

6.3 Morton, J., and G.W. Groves, "The Cracking of Composites consisting of Discontinuous Ductile Fibers in a Brittle Matrix--Effect of Fiber Orientation." J. Mat. Sci., Vol. 9, pp. 1436-1445 (1974)

6.4 Timoshenko, S.P., and J.N. Goodier, *Theory of Elasticity.* 3rd edition, McGraw-Hill, New York (1970)

Chapter 7. Micromechanics-Based FEM Simulation of A Bending Beam

SYNOPSIS

The stress-displacement relation along a Mode I crack is established based on the micromechanical model (Chapter 6). Finite element simulation of a beam under four-point bending is performed with the finite element package ADINA. Using the discrete crack approach, strain softening truss elements are used along the cracks. Experiments of beams under four-point bending are performed with specimens containing different fiber volume fractions. The numerical results of the post-cracking behavior of the beams agree well with the experimental results and the procedure for micromechanics-based design and analysis of FRC materials is essentially established.

7.1 CONSTITUTIVE RELATION ALONG MODE I CRACK

7.1.1 Probability Density Functions

At any position along a crack, the bridging contribution of a random distribution of fiber can be derived statistically. For a single fiber of inclination angle θ and embedded length L, the contribution (the bridging force vs. crack opening relation) of the fiber pullout to the overall stress-displacement relation along any position of a crack in a structural member can be obtained from probability density functions. By assuming that the fiber is always pulled out from the shorter embedded end of the fiber, the embedded length of a fiber L can be expressed in terms of the position of the fiber centroid from the crack plane and the fiber inclination angle (Fig. 7.1)

$$L = \frac{L_f}{2} - \frac{\xi}{\cos\theta} \tag{7.1}$$

where L_f is fiber length.

The probability density function for the distance of fiber centroid from the crack surface is uniform

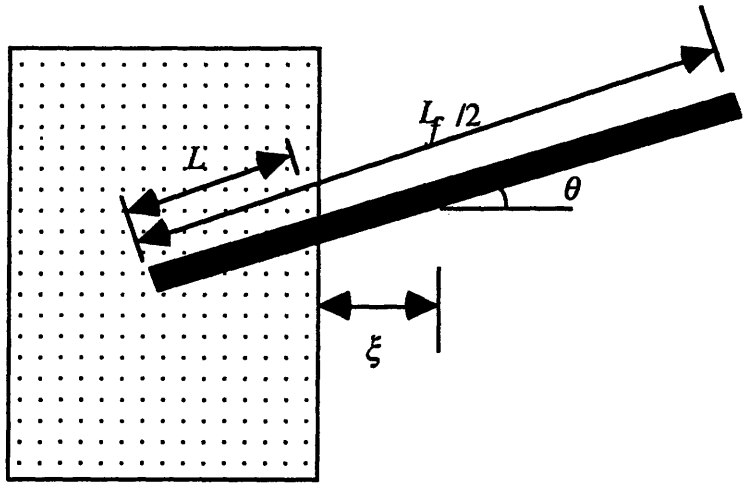

Figure 7.1 A Bridging Fiber across a Matrix Crack

$$p(\xi) = \frac{2}{L_f} \quad for \quad 0 \le \xi \le \frac{L_f}{2} \tag{7.2}$$

The probability density function of the fiber orientation is uniform for 2-D random orientation

$$p(\theta) = \frac{2}{\pi} \quad for \quad 0 \le \theta \le \frac{\pi}{2} \tag{7.3a}$$

and non-uniform for 3-D random orientation

$$p(\theta) = \sin\theta \quad for \quad 0 \le \theta \le \frac{\pi}{2} \tag{7.3b}$$

The derivation of Eq. 7.3b is illustrated in Fig. 7.2.

7.1.2 Bridging Force

The bridging force of a random fiber at certain crack opening u can, therefore, be obtained by integrating the contribution over inclination angle θ and centroidal position from the crack surface ξ

$$F(u) = \int_{\theta=0}^{\pi/2} \{ \int_{\xi=0}^{(L_f \cos\theta)/2} P(\xi,\theta,u)p(\xi)d\xi \} p(\theta)d\theta \tag{7.4}$$

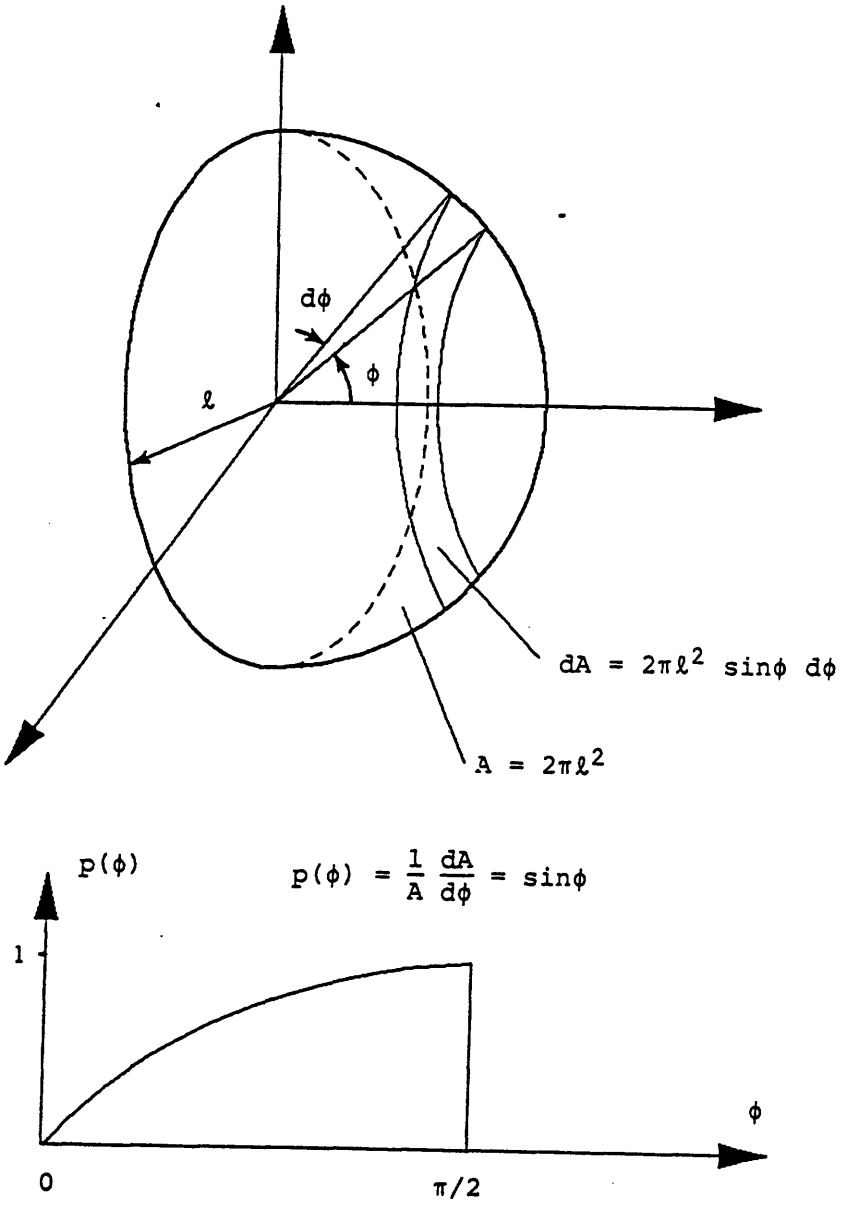

Figure 7.2 3-D Random Fiber Inclination Angle Distribution [7.1]
(*A* is the surface area of the hemisphere with a radius ℓ)

where $P(\xi_i, \theta, u)$ is the pullout force at the given ξ_i, θ, and u. The variable integration limit excludes the cases when fibers do not cross the crack surface. Although Eq. 7.4 is

different in form from those in [7.1-7.3], they are equivalent in mathematics. Equation 7.4 is used for the convenience of calculating the integration numerically.

By transforming the integration variable ξ into L using Eq. 7.1, Eq. 7.4 becomes

$$\begin{aligned} F(u) &= \int_{\theta=0}^{\pi/2} \{ \int_{L=0}^{L_f/2} P'(L,\theta,u) p'(L) \cos\theta dL \} p(\theta) d\theta \\ &= \int_{\theta=0}^{\pi/2} \{ \int_{L=0}^{L_f/2} P'(L,\theta,u) p'(L) dL \} p'(\theta) d\theta \\ &= \int_{\theta=0}^{\pi/2} F_L(\theta,u) p'(\theta) d\theta \end{aligned} \tag{7.5a}$$

where $F_L(\theta,u)$ is the average pullout force over all possible embedded lengths for a given inclination angle θ

$$F_L(\theta,u) = \int_{L=0}^{L_f/2} P'(L,\theta,u) p'(L) dL \tag{7.5b}$$

and the probability density functions are

$$\begin{aligned} p'(L) &= \frac{2}{L_f} \quad for \quad 0 \le L \le \frac{L_f}{2} \\ p'(\theta) &= \frac{2}{\pi}\cos\theta \quad for \quad 0 \le \theta \le \frac{\pi}{2} \end{aligned} \tag{7.5c}$$

note that the lower bound of L is zero, instead of a negative value (A negative value of L means that fiber does not cross the crack plane, the exclusion has already been considered in Eq. 7.4). Equation 7.5 can be explained directly from the physical ground with the $\cos\theta$ in Eq. 7.5c represents a reduction of bridging force due to some of the inclining fibers not crossing the crack surface.

Using the micromechanical model developed in Chapter 6, the pullout forces $P(L,\theta,u)$ are computed at L = 0~10 mm with 1.0 mm increment and θ = 0~90° with 5° increment. The curves calculated from Eq. 7.5b are shown in Fig. 7.3 at different inclination angles. The pullout force vs. Mode I crack opening for a single fiber under 2-D random orientation is then calculated by Eq. 7.5a (Fig. 7.4). In order to simulate the structural behavior using the finite element program (ADINA), the pullout curve is simplified by a piece-wise linear curve with five straight lines.

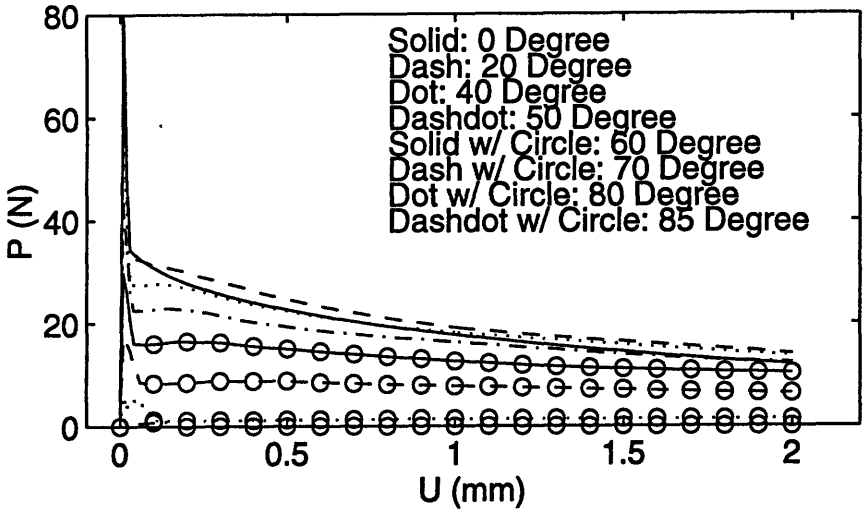

Figure 7.3 Average Pullout Curves over Embedded Length at a Given Angle

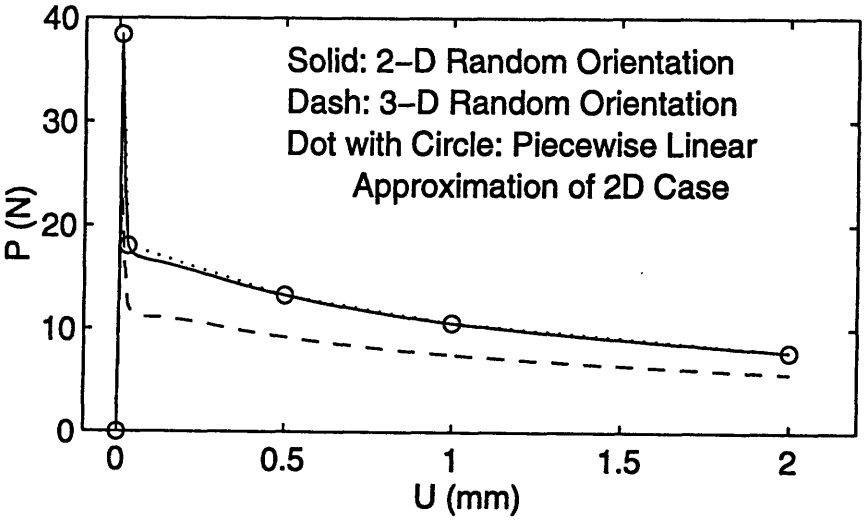

Figure 7.4 Mode I Pullout Curve of a Single Fiber at 2-D Random Orientation

The bridging stress can be calculated from bridging force $F(u)$ (Eq 7.5) and fiber volume fraction V_f

$$\sigma_B(u) = \frac{P(u)}{\pi R_f^2} V_f \tag{7.6}$$

where R_f is fiber radius. Three volume fractions V_f = 0.5%, 1.0% and 1.5% are considered, and the results are shown in Fig. 7.5.

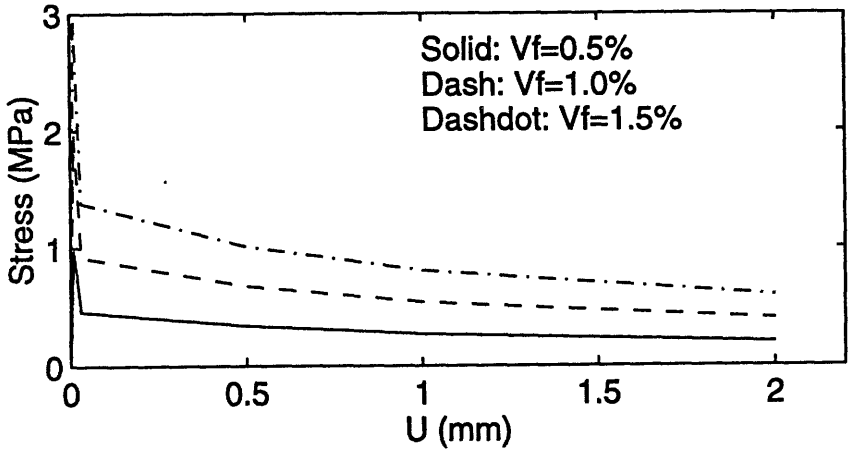

Figure 7.5 Fictitious Bridging Stress along Crack

7.2 FINITE ELEMENT SIMULATION

7.2.1 Numerical Approach

In order to simulate the softening behavior of structural members caused by the fiber bridging force during crack propagation and opening, FEM analysis is needed for a structural member with general geometric and loading configuration.

In uncracked areas, 2-D or 3-D solid elements can be used as usual. Along cracks, there have been two approaches to model the bridging forces, discrete crack approach (softening spring element across the crack [7.4-7.6]) and smeared crack approach (softening solid element across the crack [7.7-7.8]). Section 2.4 reviews both approaches in detail. In this work, the discrete crack approach is used with a prescribed crack path.

7.2.2 First Cracking Strength

Since the structural member is uncracked before loading and the bridging curves in Fig. 7.5 are obtained from the experiments and models of pre-existing cracks, first cracking strength has to be considered in the relation of bridging stress vs. crack opening.

In this work, a simple approximation is used. Based on the tensile strength of the cement mortar (3.6 MPa), the pullout curve in the early stage in Fig. 7.5 is modified as follows: instead of reaching the peak load along the original initial slope, the bridging

stresses reach the tensile strength (3.6 MPa) along a steeper slope of the value of stiffness of the mortar matrix (E_m = 22.3 GPa). After reaching the tensile strength, the pullout curves are described by lines between the tensile strength and the original peak pullout loads (dotted line in Fig. 7.6). Beyond this original peak pullout load, the softening behaviors follow the predicted curves by the micromechanical model.

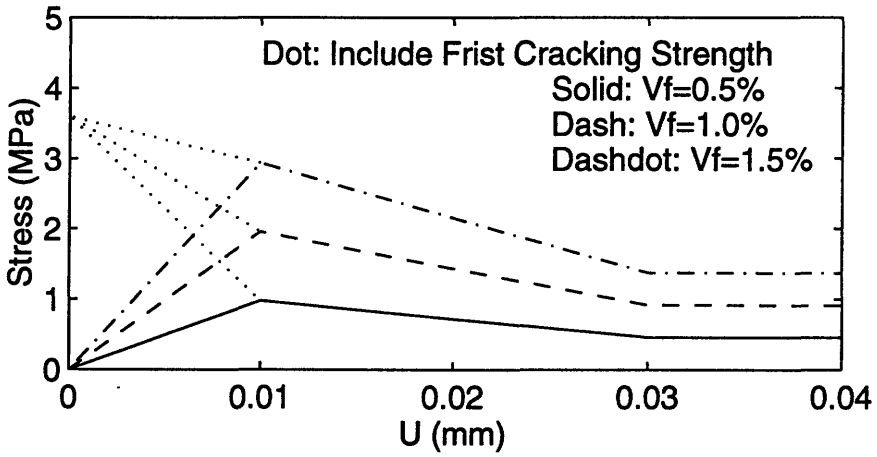

Figure 7.6 Bridging Stress with Pre-Crack Failure Criterion

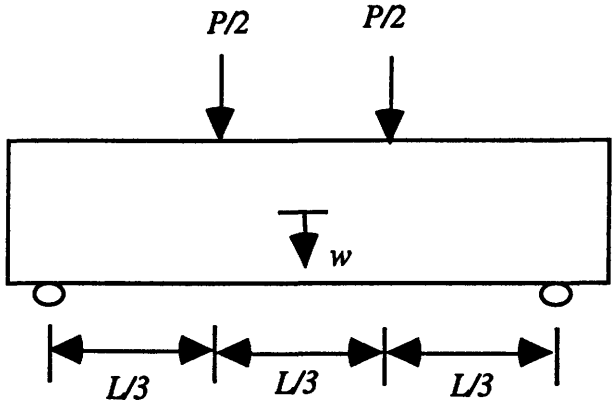

Figure 7.7 Beam under Four-Point Bending (L = 18", h = 4.5" b = 3")

7.2.3 Examples of Beams under Four Point Bending

Beams under four-point bending are studied (Fig. 7.7). Half of the beam is modeled with 162 2-D solid elements (9 nodes, 18 columns x 9 rows). Discrete crack approach is

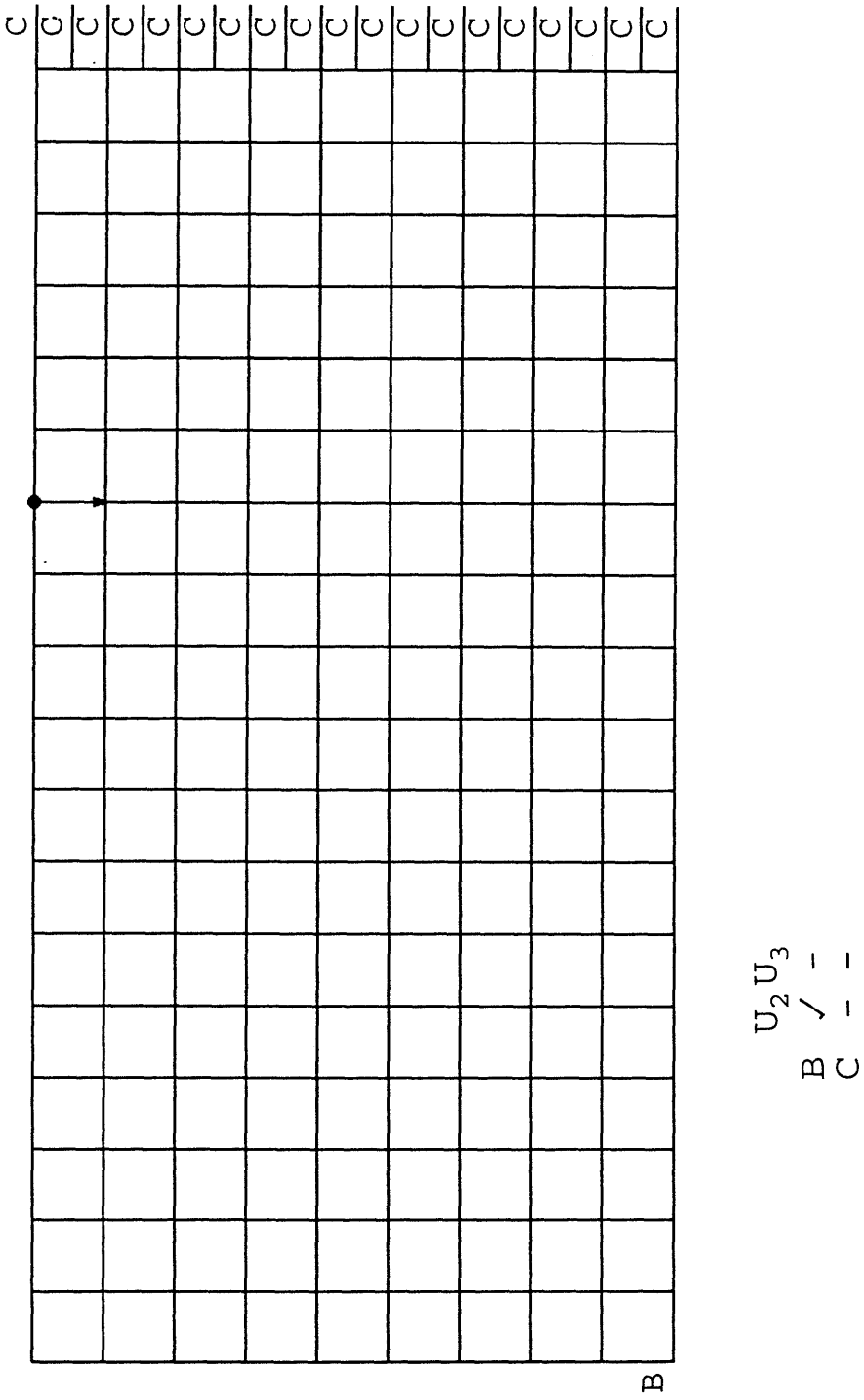

Figure 7.8 FEM Mesh

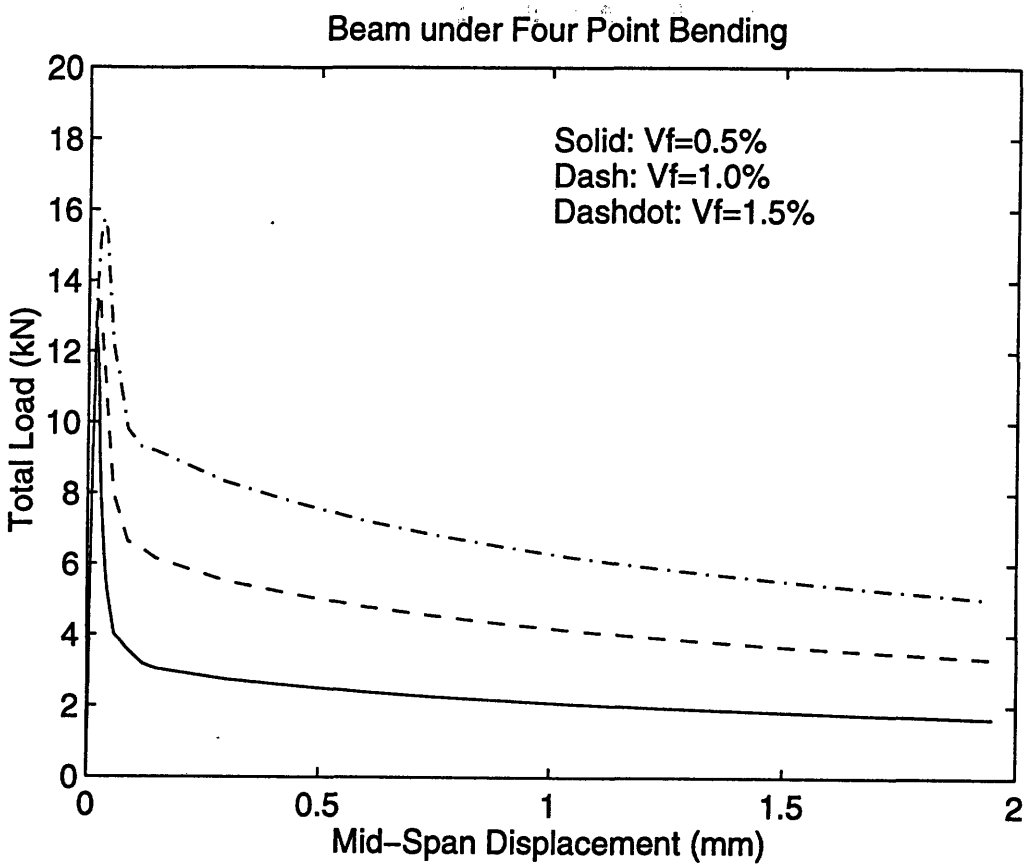

Figure 7.9 Beam Behavior (P vs. w) for Different Fiber Volume Fractions

used with the assumption of the crack path along the mid-span. For the case of four-point bending, this assumption is reasonable (from the experiments in the next section) since generally only one crack is initiated and the crack occurs within the mid-span. Two-node truss elements with prescribed tensile behavior are used as the softening springs along the crack. The length of the truss elements is chosen to be very small (10 μm) so that the presence of the elements will not affect the overall behavior of the structural member.

Three types of fiber volume fractions are used (V_f= 0.5%, 1.0 % and 1.5%), resulting in three stress-displacement relations along the crack surface given in Fig. 7.6. The softening truss elements with the behaviors in Fig. 7.6 are placed at each node across the crack.

The FEM mesh is shown in Fig. 7.8. With displacement controlled loading in the analysis, the relations of loading (P) vs. mid-span deflection (w) at the three fiber volume fractions are shown in Fig. 7.9.

One can see that the addition of fibers results in a favorable post-peak behavior. Without the fibers, the beam will separate into two pieces with little mid-span displacement (< 0.1 mm). Also, the increase in post-peak load is roughly proportional to the increase in fiber volume fraction.

7.3 EXPERIMENTAL VERIFICATION AND DISCUSSION

7.3.1 Testing Equipment and Specimen Preparations

Compression test and splitting test of FRC cylinders are performed to estimate the Young's modulus, compressive strength and tensile strength of the FRC composites. Four-point bending test of beam is performed to evaluate the flexural strength of the specimens and to compare with the numerical results. A 60 kips Instron machine is used to perform all the above tests (Fig. 7.10). The data acquisition system used is the same as the one shown in Fig. 3.9.

The same kinds of steel fiber, type III Portland cement and mortar sand used in the fiber pullout tests in Chapters 3-6 (Sec. 3.2) are employed here with the same water/cement/sand ratio (0.5:1:2). The volume fractions of steel fiber are the same as those in the numerical simulation in the previous section (0%, 0.5%, 1.0% and 1.5%).

Two types of FRC specimens, cylinders and beams, are prepared. The cylinders are 3 inches in diameter and 6 inches in length (Fig. 7.11). The beams are 21 inches in length, 4.5 inches in depth and 3 inches in width (Fig. 7.7). In order to produce a beam with fiber aligned in a random 2-D distribution in the loading plane, a layer by layer casting procedure is used. During the casting of each layer, the mold is vibrated to induce fibers to fall onto the loading plane.

7.3.2 Compression Test and Splitting Test

Compression test is performed to estimate Young's Modulus and compressive strength of FRC materials of different fiber volume fractions. The cylindrical specimens are first loaded to about half of the compressive strength to measure the slope of the loading curves, as shown in Fig. 7.11. Figure 7.12 shows the stress-strain relations of FRC materials under different fiber volume fractions.

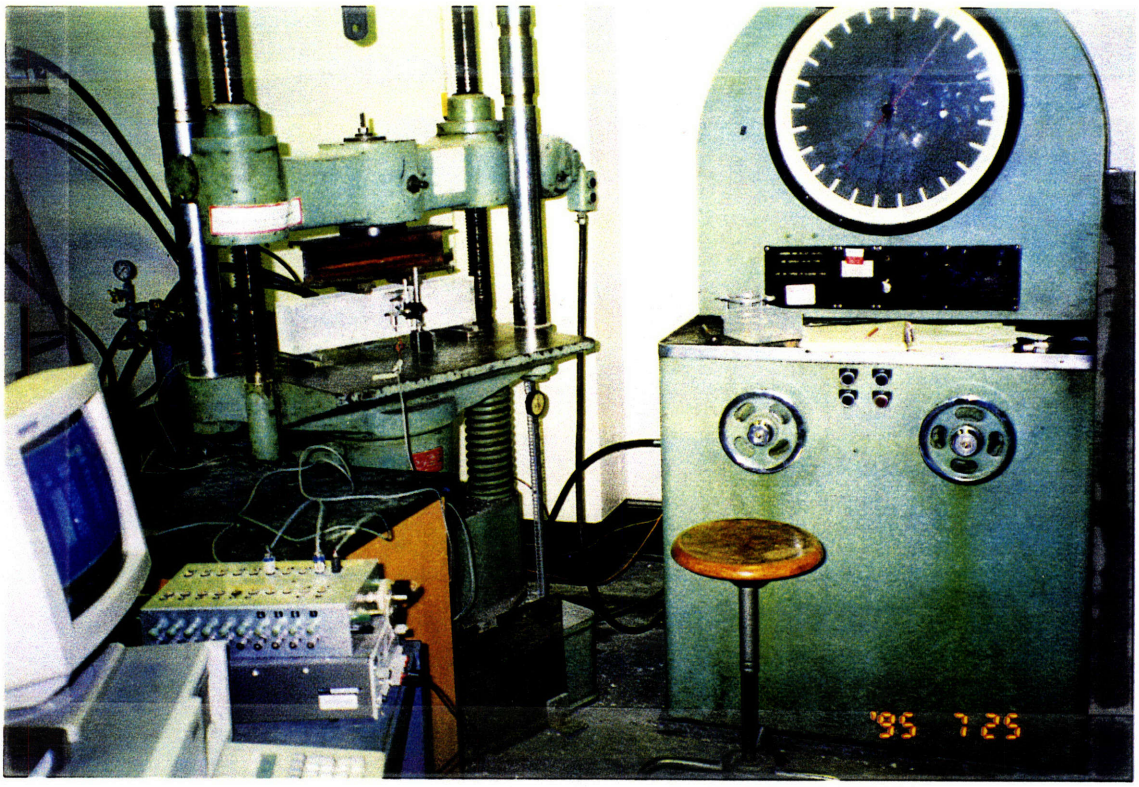

Figure 7.10 60 kips Instron Machine

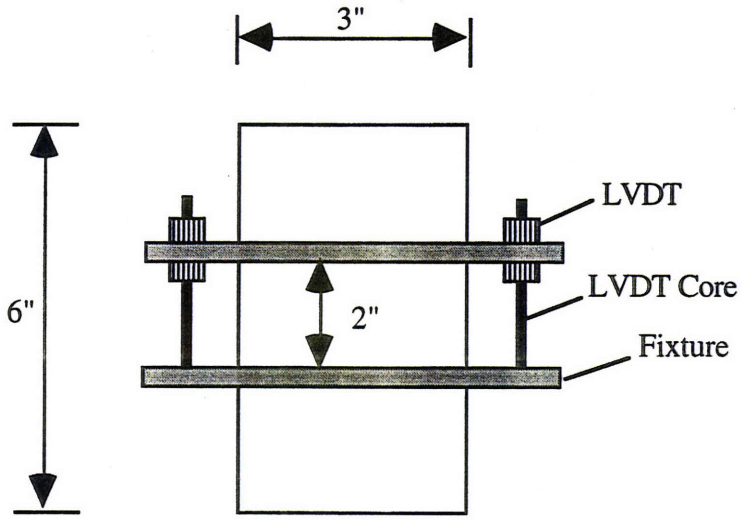

Figure 7.11 Compression Test for Measuring Young's Modulus

Because of the lower fiber volume fraction (< 2%), the Young's modulus of FRC does not vary significantly with respect to the fiber volume fraction, which is expected according to the rule of mixture. The Young's modulus of the cement mortar matrix and the FRC composite is about 18 GPa.

For each specimen, once the stress-strain curve is obtained, the compression is unloaded. The LVDT's and the fixtures for displacement measurement are removed. The cylinder is reloaded until it fails. The maximum load is recorded and the compressive strengths under different fiber volume fractions are calculated from the maximum load and cross-section of the cylinder. From Fig. 7.13, it is interesting to see that the compressive strength decreases when fiber volume fraction increases. This is probably due to increased porosity of the concrete with the addition of fibers.

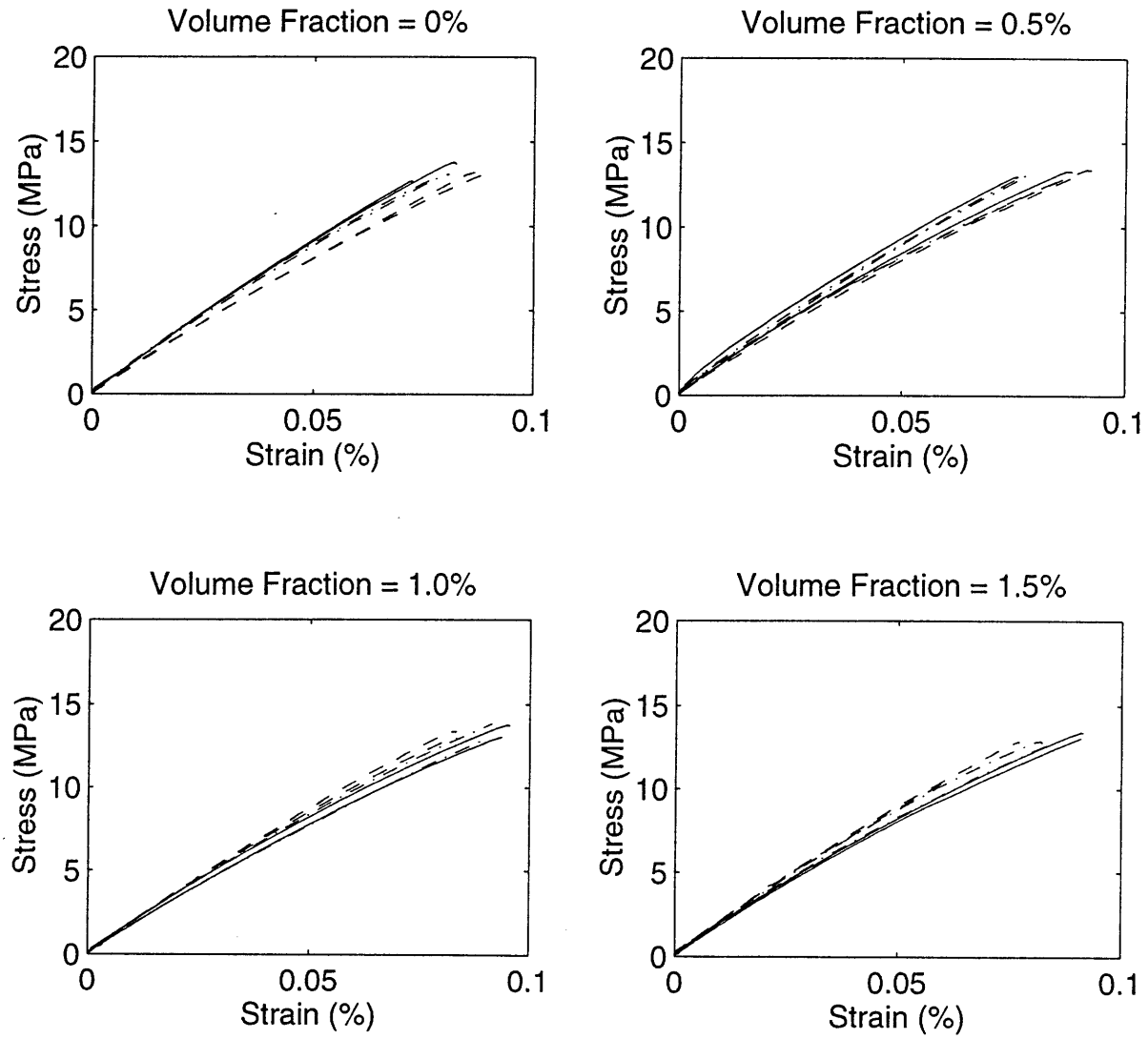

Figure 7.12 Stress-Strain Curves under Various Fiber Volume Fractions

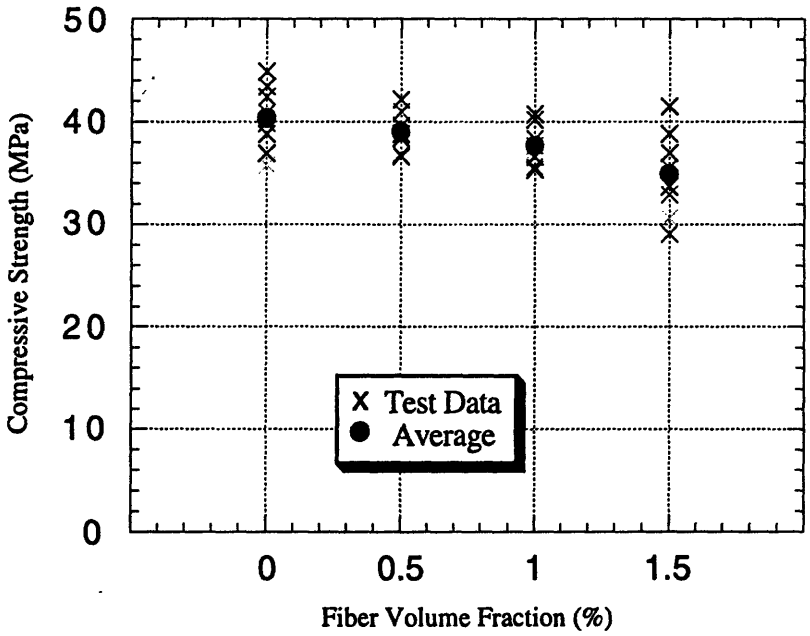

Figure 7.13 FRC Compressive Strength vs. Fiber Volume Fraction

Splitting test is performed to estimate the tensile strength of FRC materials. Figure 7.14 shows the configuration of the test. The cylinder is compressed along its length and an LVDT is mounted at the end of the cylinder to detect the splitting crack. With the measured load when splitting crack occurs, the tensile strength can be estimated by

$$f_t = \frac{2P}{\pi l d} \tag{7.7}$$

where P is the compressive load when split occurs. $l = 6$ inch is the length of the cylinder and $d = 3$ inch is the diameter of the cylinder.

Figure 7.16 shows the compressive loading curves of the splitting tests up to the peak load. It should be mentioned that the first splitting crack may occur before the maximum load is reached, especially for the cases of non-zero V_f. In addition, when fibers are added to the cylinder, the distribution of the fibers are not uniform along the length of the cylinder due to the mixing procedure with shaking table. The end of the cylinder with less fiber splits first and the other end with more fiber splits later with multiple cracks (Fig. 7.15).

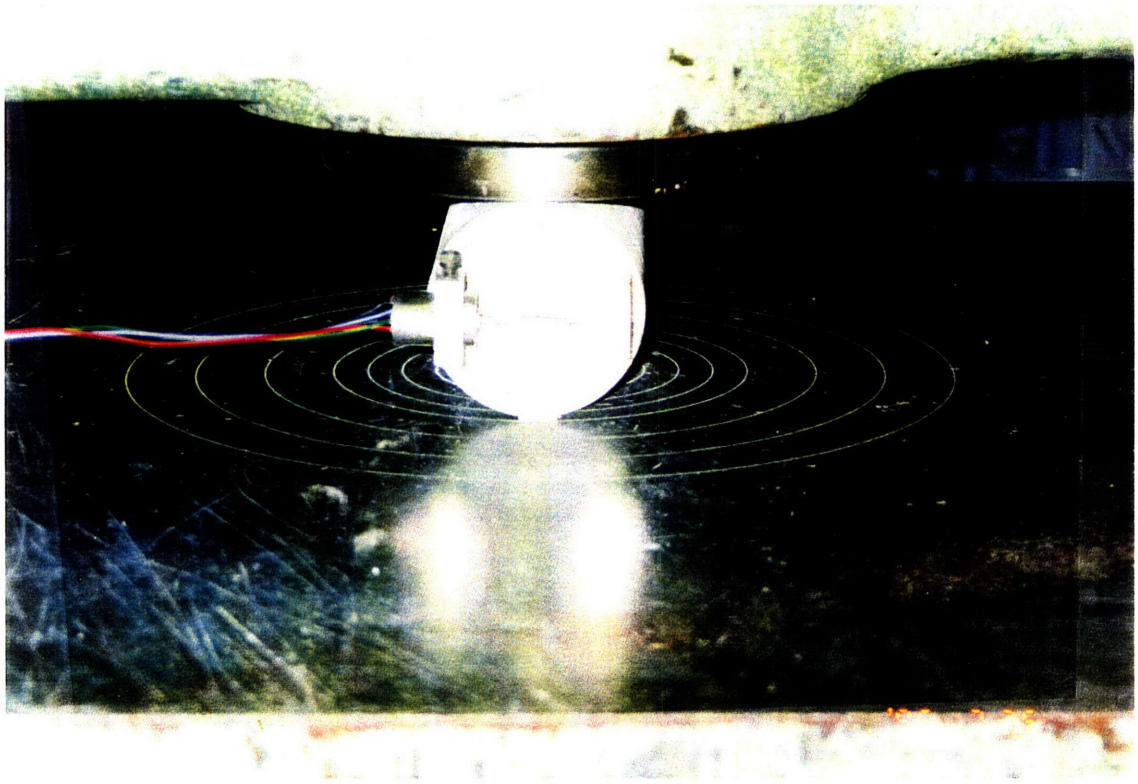

Figure 7.14 Splitting Test

Figure 7.15 FRC Cylinders after Splitting Test

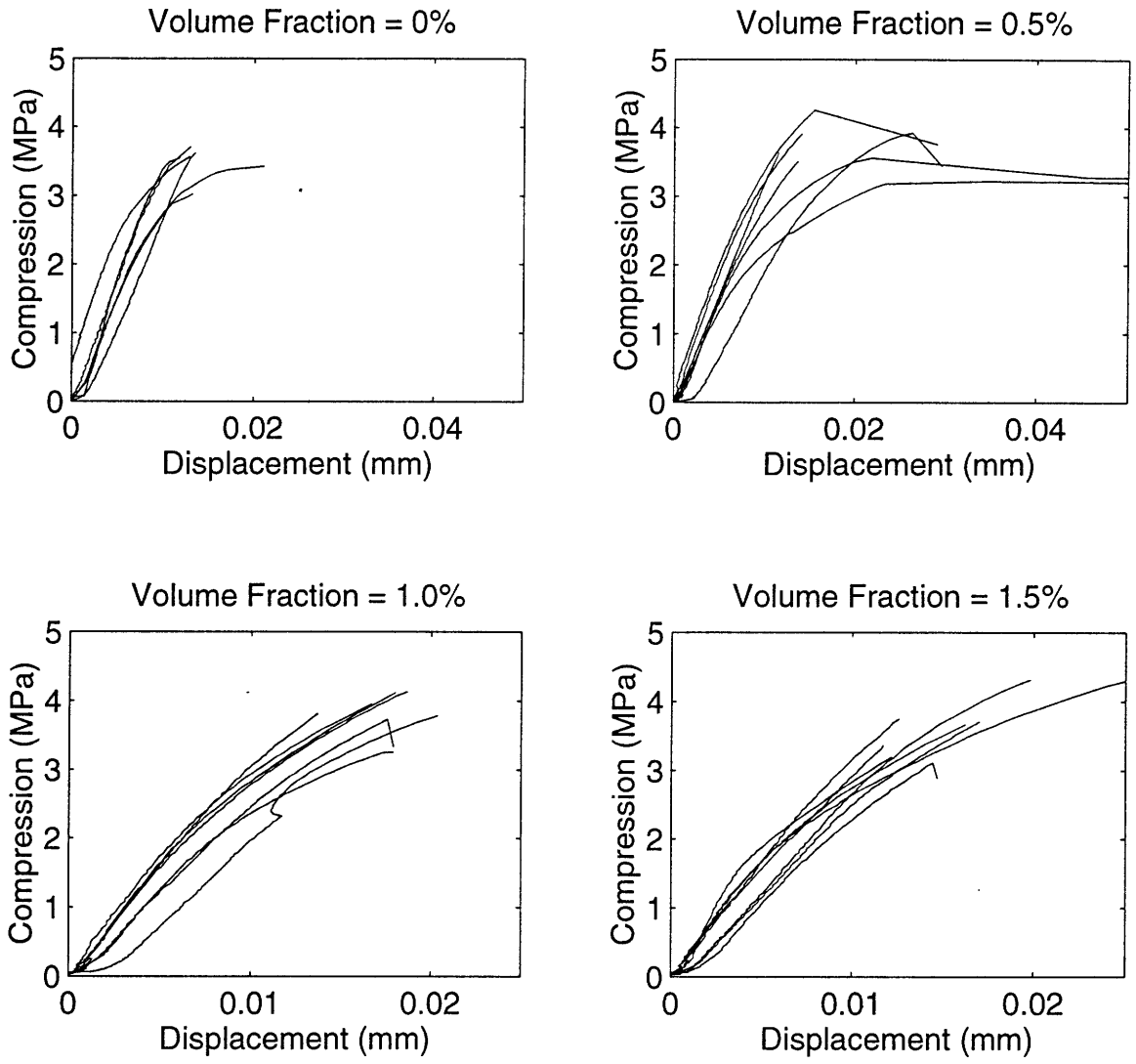

Figure 7.16 Compressive Loading Curves of Splitting Tests

Given the uncertainty discussed above, the tensile strength under different fiber volume fractions is only a rough estimation from the maximum load or the load when splitting is detected using Eq. 7.7. From Fig. 7.17, one can see that the average value does not vary significantly with respect to the (low) fiber volume fraction. The tensile strength is approximately f_t = 3.6 MPa for all fiber volume fractions (V_f< 2%).

7.3.3 Four-Point Bending Test

Figure 7.18 shows the configuration of the four-point bending test. The beam size is the same as that shown in Fig. 7.7. Two LVDT's are mounted on the mid-span of each

side of the beam. For each fiber volume fraction, six specimens made from 3 sets of mixes are tested. All of the tested beams are shown in Fig. 7.19.

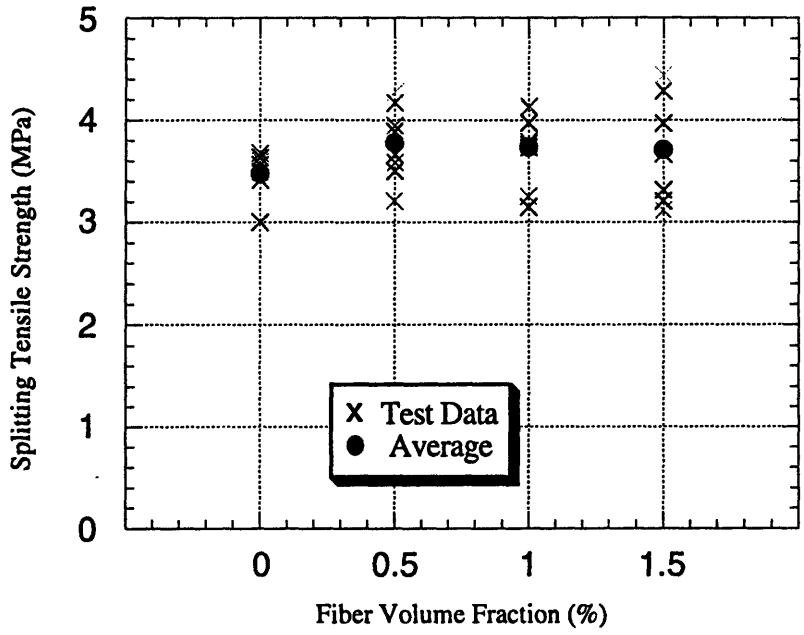

Figure 7.17 Splitting Tensile Strength vs. Fiber Volume Fraction

Figure 7.20 shows the loading curves with fiber volume fractions V_f = 0%, 0.5%, 1.0% and 1.5%. Different line types (dash, dot, and dashdot) represent different sets of mix. The flexural strength of a beam can be obtained from the peak loads in Fig. 7.20

$$f_r = \frac{PL}{bh^2} \tag{7.8}$$

where P is the total maximum loads (Fig. 7.7). L = 18 inch is the span between the two supports. b = 3 inch is the beam width and h = 4.5 inch is the beam depth.

For plane cement mortar (V_f = 0), the flexural strength f_r = 4.5 MPa. For FRC beams (non-zero fiber volume fraction), the flexural strength does not vary significantly from that of the plane cement mortar. From Fig. 7.20, one can see clearly that the peak load (which determines the flexural strength of the beam) does not vary significantly with respect to fiber volume fraction, whereas the post-peak load increases significantly when fiber volume fraction increases.

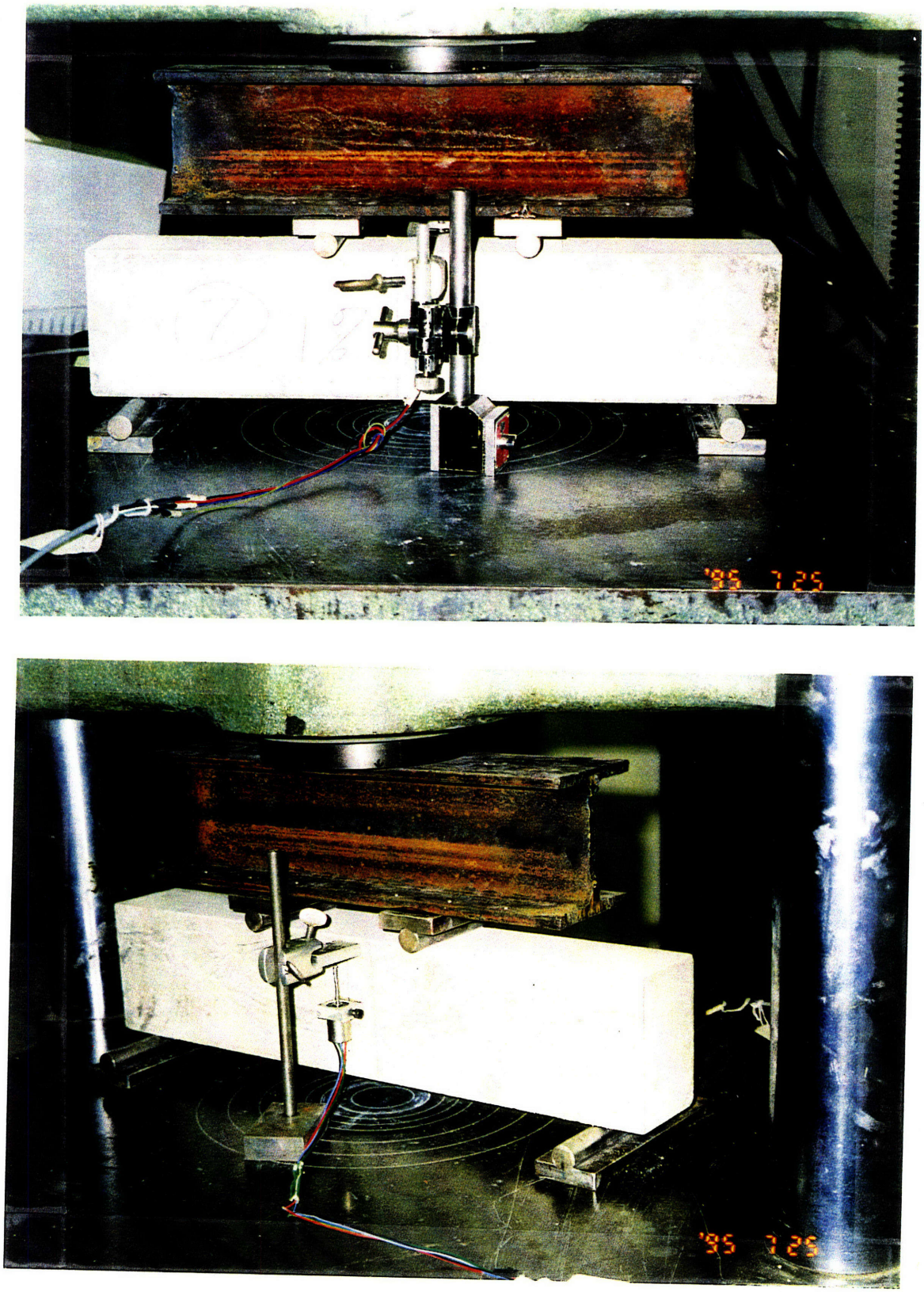

Figure 7.18 Beam under Four-Point Bending

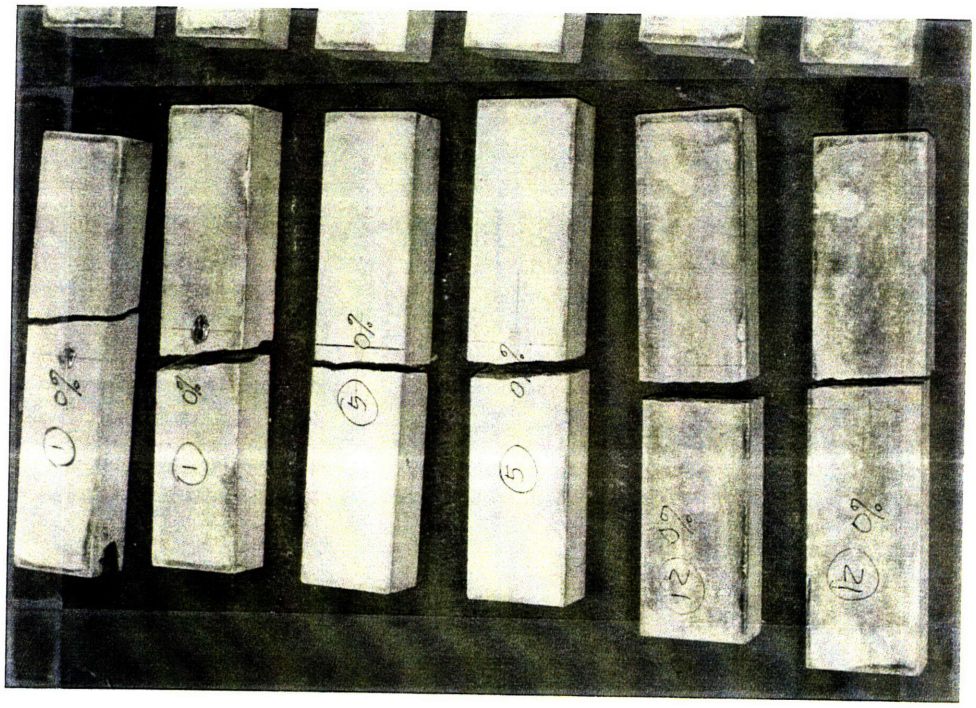

(a) $V_f = 0$

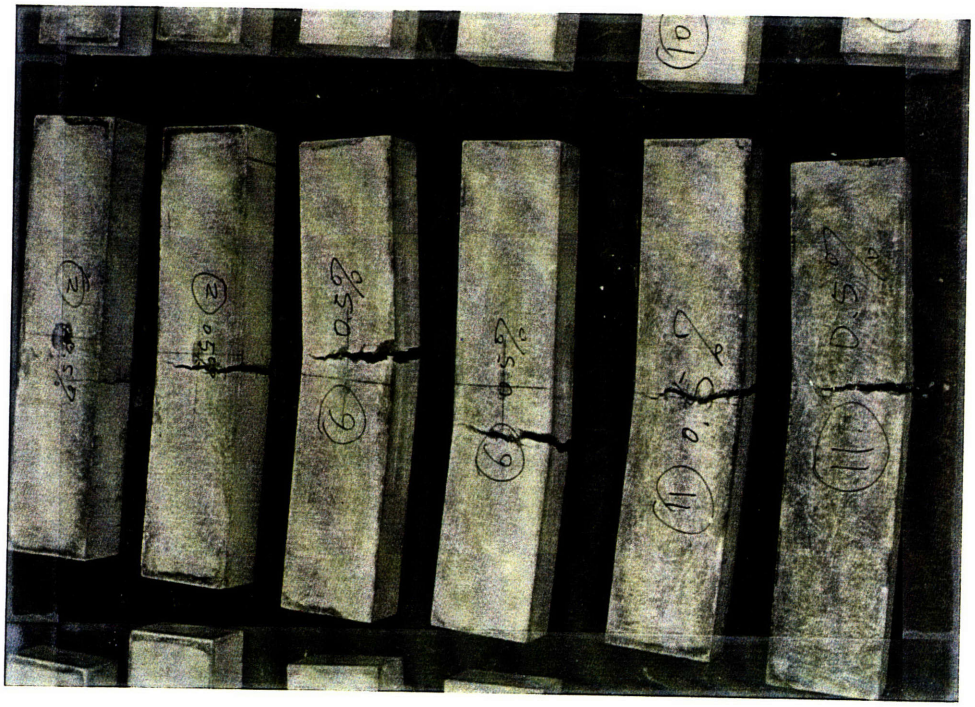

(b) $V_f = 0.5\%$

Figure 7.19 Tested Beam Specimens

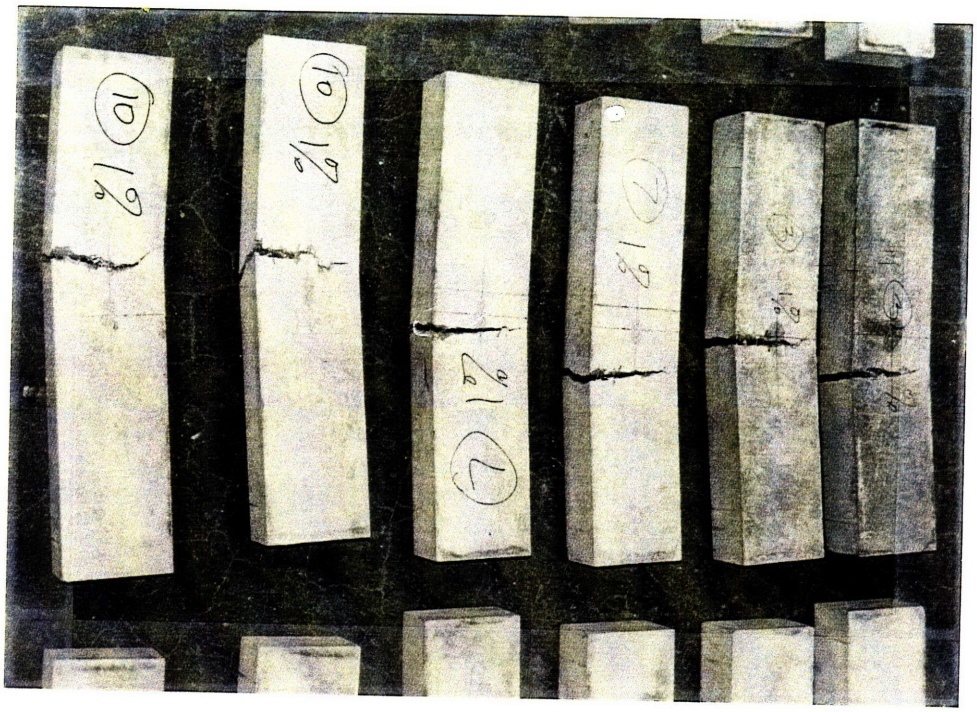

(c) $V_f = 1.0\%$

(d) $V_f = 1.5\%$

Figure 7.19 Tested Beam Specimens

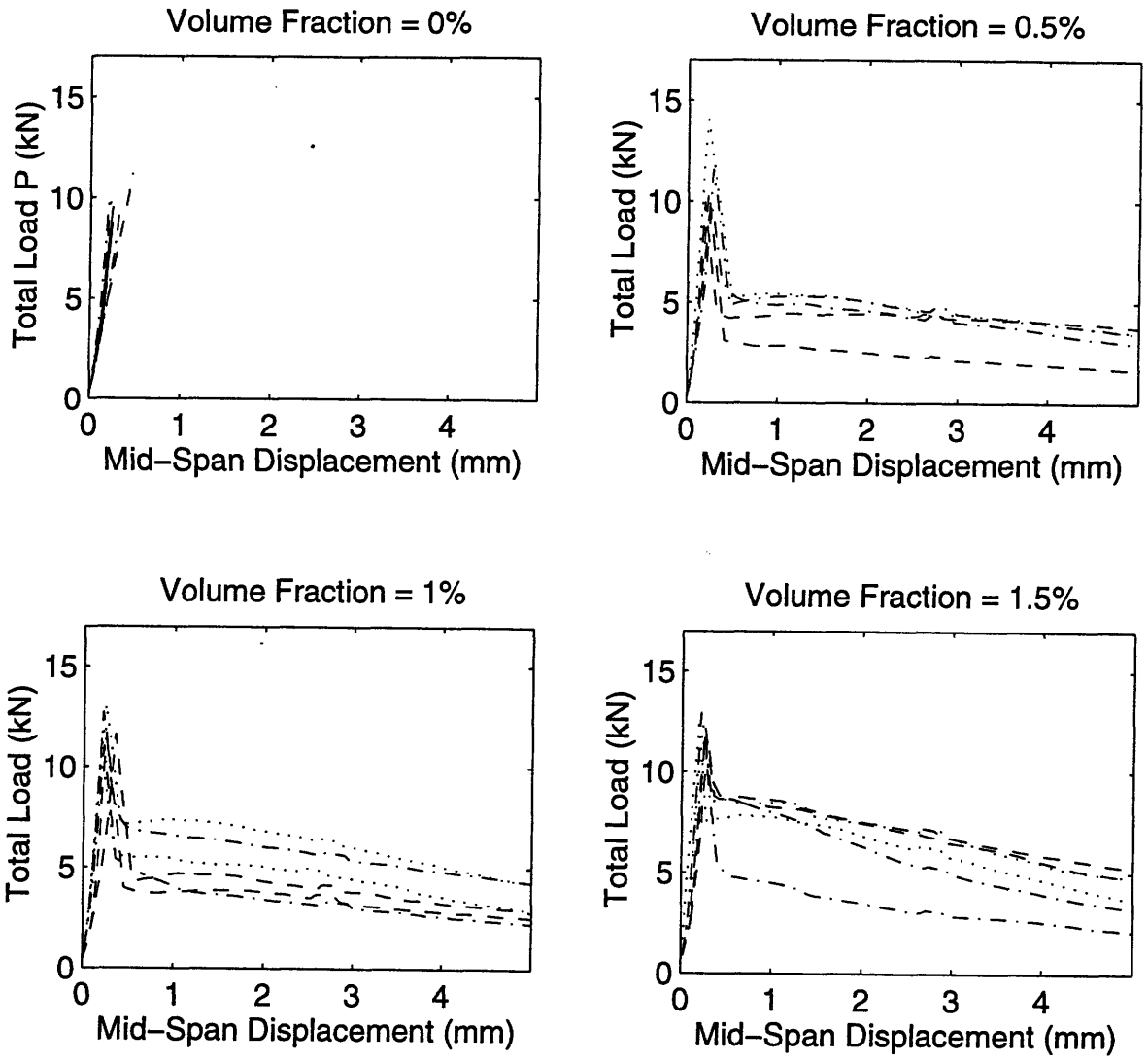

Figure 7.20 Total Loads vs. Mid-Span Deflection

7.3.4 Comparison and Discussion

Figure 7.21 compares the experimental data with the numerical results from the micromechanical model and FEM simulation (solid lines), one can see that micromechanical modeling can predict the post-peak behavior reasonably well. Since the relation of bridge stress vs. crack opening was calculated up to 2 mm crack opening based on the micromechanical model in Chapter 6, the FEM simulation reaches this limit when the mid-span deflection w reaches about 2.1 mm.

The micromechanical model tends to underestimate the experimental data (Fig. 7.21). One possible cause is the mixing procedure. Since fibers are managed to lay in the 2-D plane, fresh mix (concrete with fibers) is added layer by layer on a shaking table. This process may result in more fibers in one side of beams than the other. The high volume fraction of fiber in one side of beams may results in higher load in the experimental data.

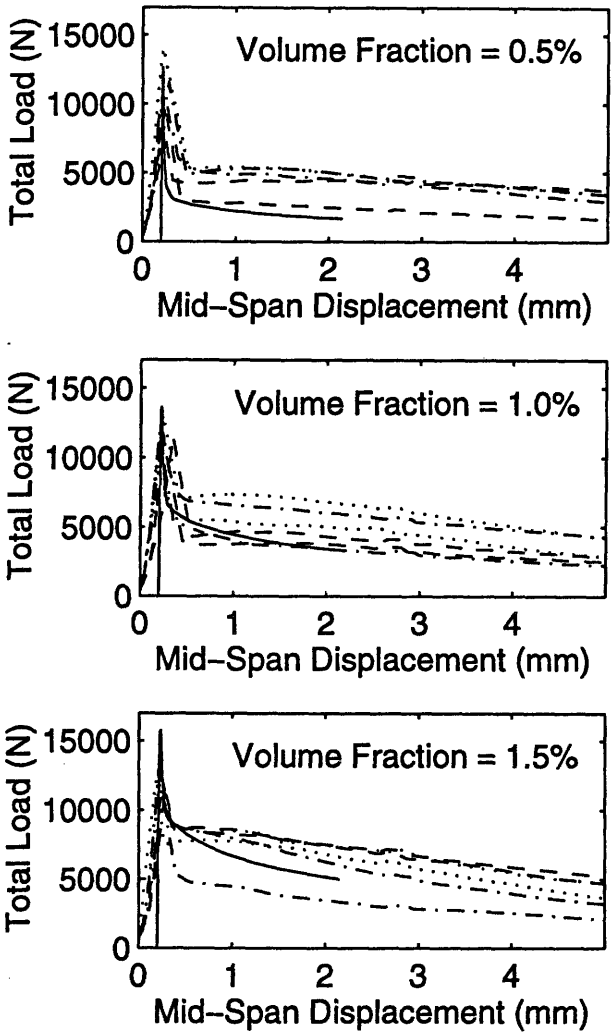

Solid: Numerical Simulation (ADINA)
Others: Different Sets of Experimental Results

Figure 7.21 Comparison of Experimental results with Micromechanics-Based Numerical Results

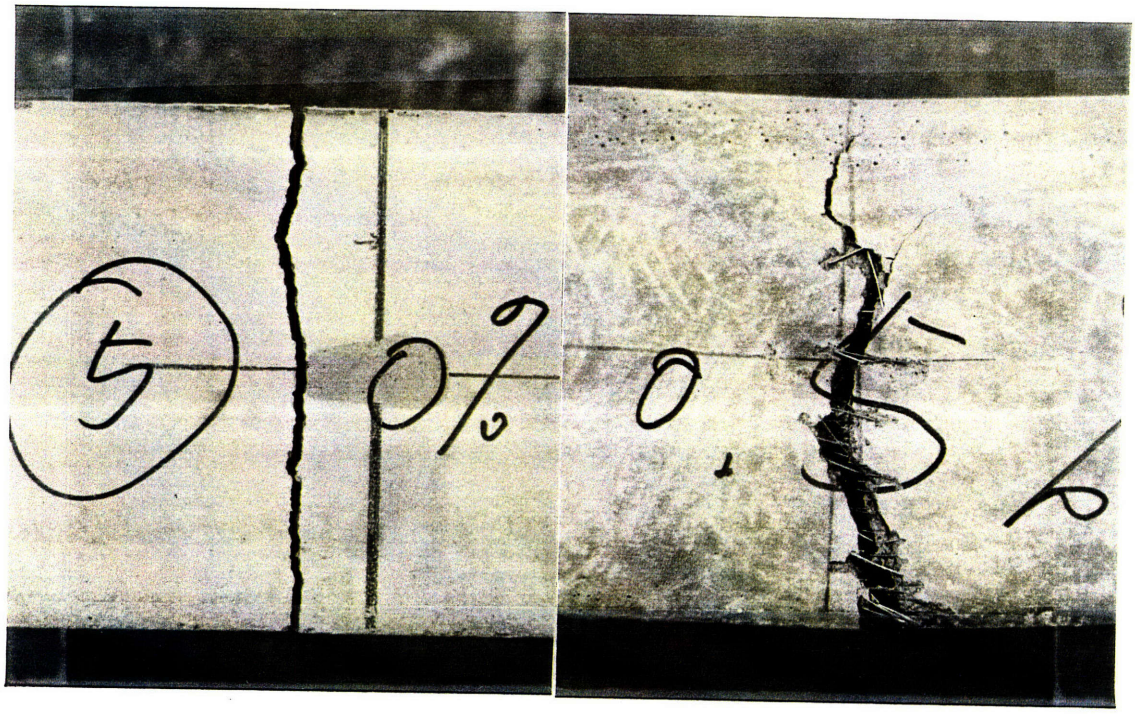

(a) $V_f = 10$ (b) $V_f = 0.5\%$

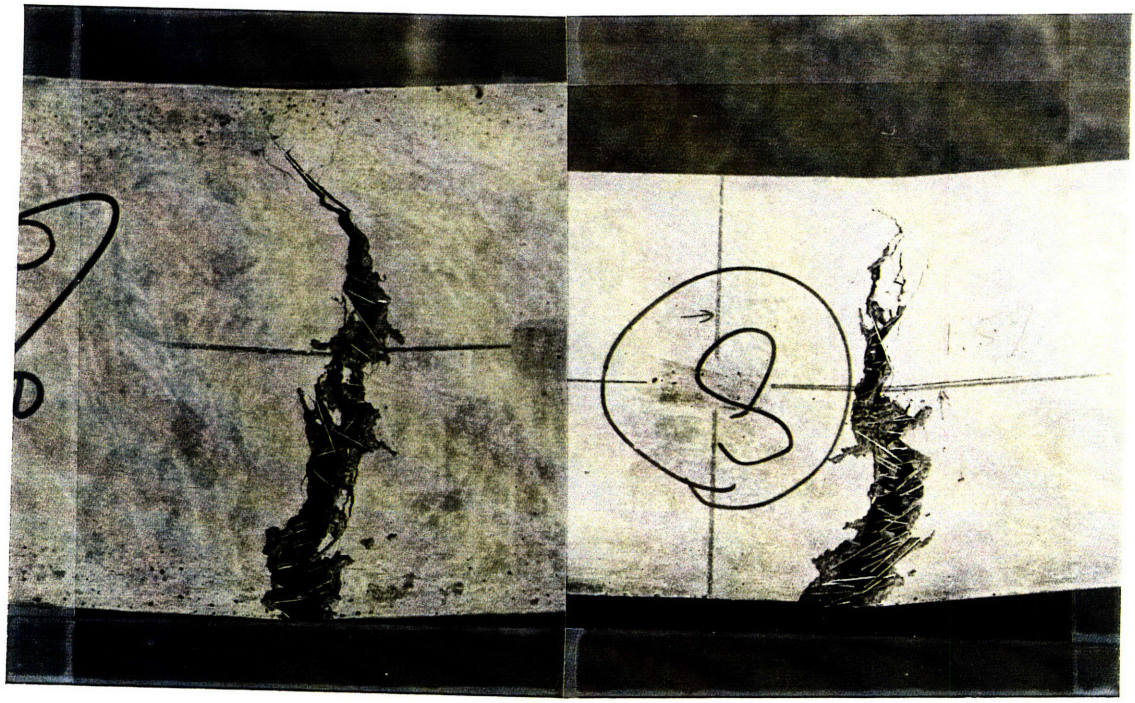

(c) $V_f = 1.0\%$ (d) $V_f = 1.5\%$

Figure 7.22 Cracks at Mid-Span of Four-Point Bending Beam

In Sec. 7.3.2, the Young's modulus of the mortar is found to be 18 GPa. However, the Young's modulus of the mortar used in earlier pullout tests is 22.3 GPa, which is used in the micromechanical models and the FEM models in Sec. 7.2. The difference is attributed to material variability of different sand bags and cement bags ordered at different time and possibly the scale of the mixing procedure. Since Young's modulus is less important to the post-peak behavior, the variation will not affect the comparison significantly. With micromechanical model using Young's modulus of 22.3 GPa, the results of FEM modeling with Young's moduli of 18 GPa and 22.3 GPa gives no significant difference.

The material variability does not affect the splitting tensile strength (3.6 MPa for both the pullout test in Chapters 3-6 and the beam test in this chapter) and compressive strength (40 MPa for both tests). However, it is interesting to see that the compressive strength decreases moderately with respect to the fiber volume fraction (Fig. 7.13). This is probably due to the scale of defects and porosity introduced by fiber addition. Because fiber length (20 mm) is much larger than the fine aggregates size (< 2.362 mm), potential cracks along the interface and potential defects near the interfacial transition zone are larger. Fortunately, compressive strength is not a significant factor in failure of FRC materials. In both the micromechanical model (using the constant spalling length for matrix spalling, Chapter 6) and FEM model (using the splitting tensile strength only), the compressive strength is used for neither plane cement mortar nor FRC composites.

Figure 7.20a shows that the beam fails catastrophically without fiber addition. The mode I (opening) cracks propagate through the beam section in a split of a second (Fig. 7.22a). However, by adding less than 2% of fibers, the post-peak behavior changes dramatically. Figure 7.22b-d shows that fiber addition bridges the cracks and prevent the crack propagates through the cross-section. The post-peak behavior with fiber addition is, therefore, much more favorable than the case of plane concrete mortar (Fig. 7.20). This better post-peak behavior can lead to the reduction of steel reinforcement and allow easier fabrication and mixing procedure in many construction applications, such as: dam, airport pavement, nuclear shield, etc.

7.4 CONCLUSIONS

Based on the results in Fig. 7.21, the post-peak behavior of structural beam members is predicted reasonably well based on micromechanical modeling. At this stage, a preliminary methodology for micromechanics-based design and analysis is established.

REFERENCES

7.1 Wang, Y., *Mechanics of Fiber Reinforced Cementitious Composites*, Ph.D. Thesis, MIT, pp. 183-191 (1989)

7.2 Li, V.C., Wang, Y and Backer, S. "A Micromechanical Model of Tension-Softening and Bridging Toughening of Short Fiber Reinforced Brittle Matrix Composites." J. Mech. Phys. Solids, Vol.39, No.5, pp. 607-625 (1991)

7.3 Aveston, J. , and A. Kelly, "Theory of Multiple Fracture of Fibrous Composites." J. of Materials Science, Vol. 8, pp. 352-362 (1973)

7.4 Hillerborg, A., "Analysis of One Single Crack." *Fracture Mechanics of Concrete*, ed. F.H. Wittmann, Elsevier Science, Amsterdam, pp. 223-249 (1983)

7.5 Ingraffea, A.R., and V. Saouma, "Numerical Modeling of Discrete Crack Propagation in Reinforced and Plain Concrete." *Fracture Mechanics of Concrete: Structural Applications and Numerical Calculations*, ed. G. Sih and A. DiTommaso, Martinus Nijhoff, pp. 171-225 (1984)

7.6 Gustafsson, P.J., "Fracture Mechanics Studies of Non-yielding Materials like Concrete", Report TVBM-1007, Div. of Building Materials, Lund Institute of Technology, Sweden (1985)

7.7 Bazant, Z.P., and B.H. Oh, "Crack Band Theory for Fracture of Concrete." RILEM Mat. & Struct., Vol. 16, pp. 55-177 (1983)

7.8 Rots, J.G., and R. de Borst, "Analysis of Mixed-mode Fracture in Concrete." ASCE J. Eng. Mech., Vol. 113, No. 11, pp. 1739-1758 (1987)

Chapter 8. Thesis Conclusions and Comments on Future Work

8.1 THESIS CONCLUSIONS

This thesis involves microstructural study, micromechanical modeling and structural analysis. Through these three steps, a micromechanics-based design methodology is established.

In Chapter 3, the microstructural features of the steel, nylon and polypropylene fiber/mortar interfaces during fiber debonding and pullout are studied. It is found that the different trends of post-peak behavior are due to the different interfacial damage mechanisms. The damage at the steel fiber/mortar interface includes mortar abrasion and steel surface plastic deformation, which causes drastic decrease of the post-peak load in the early stage of fiber pullout. The damage at the nylon and polypropylene fiber/mortar interfaces is fiber surface peeling with the mortar surface experiencing very little damage, resulting in increase of friction in the post-peak stage.

By applying lateral compression to the mortar during fiber pullout, the matrix abrasion (steel fiber/mortar) and the fiber peeling (polymer fiber/mortar) effects are more severe; it also confirms that the steel mortar surface damage is caused mostly by abrasion, instead of compaction.

In Chapter 4, the sensitivity of steel fiber debonding behavior to both applied lateral compression and tension is established. At the onset of debonding, the initial interfacial friction and the effective interfacial shear strength increase with lateral compression. For post-peak behavior, a higher lateral compression also results in a more rapid decrease in the interfacial friction during steel fiber pullout. Therefore, while lateral compression can significantly increase the peak pullout load, the energy absorption capacity does not increase to the same degree.

Lateral tension imposes opposite effects to lateral compression. Quantitatively, a small lateral tension can result in changes in interfacial properties comparable in magnitude to those caused by a much higher lateral compression.

For polypropylene and nylon fibers pullout under lateral compression, while the peak load of polymer fibers is about an order lower than that of steel fiber, the energy absorption capacities for polymer and steel fibers are comparable.

In Chapter 5, the behavior of fiber pullout and the non-linear decay of interfacial friction under far field variable lateral compressive stress are studied. This thesis proves experimentally that, for a given interface, a unique relationship exists between τ_{i0} and $\bar{\mu}$, which is independent of the histories of sliding distance and lateral compressive stress σ_c, i.e. independent of the interfacial abrasion rate (affected by lateral compression or pulling rate) during the fiber pullout process. This phenomenon agrees with the physical postulation that the degree of damage of surface abrasion (decrease in the interfacial misfit and τ_{i0}) is uniquely related to the degree of damage of surface asperity (decrease of surface roughness and $\bar{\mu}$). In this thesis, the relation between τ_{i0} and $\bar{\mu}$ is linear although τ_{i0} and $\bar{\mu}$ vary non-linearly with respect to the sliding distance.

With the relation between τ_{i0} and $\bar{\mu}$, a damage model, which evaluates the interfacial residual stress τ_{i0} only, is developed to predict the pullout curves under variable lateral compressive stress. The model uses a forward difference formula over sliding distance increment and a τ_{i0} vs. $\partial\tau_{i0} / \partial s$ plot with a shifting scheme to predict the decay of interfacial residual friction when variable lateral compressive stress exists.

Experimental verification shows that the model predicts the pullout curves under variable compressive stress well. A modified shifting scheme is developed to account for material variability and can be applied to practical problems without generating new τ_{i0} vs. $\partial\tau_{i0} / \partial s$ plots.

In Chapter 6, a novel fiber pullout setup is designed to measure both the normal and shearing bridging forces as a fiber is simultaneously pulled and sheared. The experimental results of steel fiber pulled out of cement mortar indicate the dependence of opening bridging forces on the lateral fiber/matrix interaction, and shearing bridging forces on matrix spalling length.

A micromechanical model is established for the mixed mode fiber pullout. The pullout process is modeled with a series of elasto-plastic beams (as fiber) on a series of elastic spring (as matrix). The effect of lateral stress on fiber developed in Chapter 5 and a constant matrix pre-spalling depth model are incorporated into the micromechanical model. The modeling result agrees well with the experimental result, which lays the foundation for simulation of FRC structural behavior.

Based on the micromechanical model in Chapter 6, the stress-displacement relation along a Mode I crack is established in Chapter 7. Using the discrete crack approach, finite element simulation (ADINA) of four-point bending FRC beams of different volume fractions are performed. Similar experiment is performed for verification. The numerical results of the post-cracking behavior agree well with the experimental results and the procedure of micromechanics-based design and analysis of FRC materials is essentially established.

8.2 COMMENTS ON FUTURE WORK

In Chapter 3, although the surface damage evolution during fiber pullout stage is studied and understood in detail, the surface damage evolution during fiber debonding stage is known in less detail due to the limitation of the experimental techniques and can only be speculated through micromechanics (Fig. 4.15). Investigation of the debonding process is still at the stage of developing reliable experimental techniques. Some techniques, such as Moiré interferometry [8.1] and environmental SEM may be useful for such investigations.

In Chapters 4 and 5, the effects of lateral stress on the interfacial parameters during fiber debonding and pullout are studied in detail for steel FRC. Further work should be extended to micromechanical modeling of the debonding and pullout process of polymer FRC's.

In Chapter 6, mixed mode crack opening with positive fiber inclination angles (fiber experiencing pullout only) are modeled. For the negative fiber inclination angles, other important mechanisms such as fiber push-in may occur. A new model is, therefore, necessary for mixed mode crack opening with negative fiber inclination angles.

In Chapter 7, the post-peak behavior of FRC structural members due to Mode I crack opening is simulated. With future development of micromechanical models for the fiber push-in effect, one will be able to establish the stress-displacement relation for mixed mode crack opening and simulate more general FRC structures with both opening and shearing cracks.

For fracture of structural members, the prediction of crack path also needs to be addressed.

REFERENCE

8.1 S.P. Shah, and Y. Shao, "Fiber-Matrix Interface in Cement Composites." *1st International Conference on Composite Engineering*, pp. 477-478 (1994)

4671-28